

# Characterisation of Metal-Organic Frameworks with Inherent Functionalisation for Carbon Capture Methods

**CRAIG ALAN MCANALLY**

THESIS SUBMITTED TO THE UNIVERSITY OF STRATHCLYDE FOR THE DEGREE OF  
DOCTOR OF PHILOSOPHY

DEPARTMENT OF CHEMICAL AND PROCESS ENGINEERING  
UNIVERSITY OF STRATHCLYDE

2017

# DECLARATION OF AUTHENTICITY AND AUTHOR'S RIGHTS

‘This thesis is the result of the author’s original research. It has been composed by the author and has not been previously submitted for examination which has led to the award of a degree.’

‘The copyright of this thesis belongs to the author under the terms of the United Kingdom Copyright Acts as qualified by University of Strathclyde Regulation 3.50. Due acknowledgement must always be made of the use of any material contained in, or derived from, this thesis.’

Signed:

Date:

# ACKNOWLEDGEMENTS

I have many people to thank for their help and support in completing this thesis and project, making this one of the most enjoyable and memorable experiences I have had; the list is by no means exhaustive.

My utmost thanks go to my supervisor, Dr Ashleigh Fletcher, whose unwavering support has helped me get through some of the most difficult moments, with the occasional ‘unconventional’ encouragement. I cannot thank you enough for all the help and guidance you have given me, not just in my research, and helping me gain more confidence in myself.

Thanks also go to my second supervisor, Dr Eddie Cussen, for his support, and introducing me to the ‘wonderful world of MOFs’ during my undergraduate research project, which led me to undertake my postgraduate studies.

To Stewart Taylor, former PhD student/Post-Doc of the Fletcher group, for being a constant source of support and making sure I remembered ‘it will all be fine!’ To Colin McKinstry, for being the only other student who understood the pains of working with MOFs, and for all our chats in the lab. To everyone in the Fletcher group past and present: Ivan, Martin, Andrea, Mohammed, Maryam, Abdul, Francesca, Ese, Bing, and Sher Leen; and to the members of the Cussen Group: Heather, Irene, Marco, Hany, and Alex. To those project students that helped me in the lab, Emma, Stuart, and Jennifer, it was a pleasure to work with you.

To the members of academic and technical staff that helped within the lab: Dr Alan Kennedy, for single crystal X-ray analysis, Dr Len Berlouis for letting me invade his lab to use the IGA, Jim Murphy, Ian Airdrie, Lindsay McCulloch, Dr Fiona Sillars,

and Alex Clunie. Also thanks to the office staff: Caroline, Laura, Megan, Jacqueline, and Nic.

To the many friends I have made in the last 3.5 years; Scott, David Connell, Alessia, Javier, Paul, Joy, Onorio, Vincenzo, Rab, Dorin, Calum, Joe, Declan, Fraser, Daria, Alexandra, Ruben, Andrew, Chris, Hrvojka, Francesco, Vitor, David McKechnie, and Marta, thanks for making my time so enjoyable.

To my family and friends, thanks for your support and understanding, I promise that's the last time you'll have to listen to my lengthy ramblings about my research.

Finally, to my wife-to-be, Laura, for always being there for me. Thank you for putting up with me for the last 3.5 years (in addition to the previous 7.5 years), and providing the support and encouragement I needed to reach the end.

# ABSTRACT

Carbon Capture offers potential remediation for greenhouse gases from industrial point sources, and physical sorbents are an economically viable option, but one that requires optimisation. Here, materials were investigated to assess the effect of incorporation of functionalised ligands, which utilise a Lewis basic character, on the potential of such materials for Carbon Capture applications. Materials were investigated for their structural and adsorptive properties, allowing analysis and evaluation of the selective capture of carbon dioxide. Characterisation included single crystal X-ray diffraction, powder X-ray diffraction, infrared spectroscopy, thermogravimetric analysis, and elemental analysis. Adsorption properties were evaluated using volumetric nitrogen adsorption at 77 K, which showed all three materials experienced activated diffusion, and gravimetric carbon dioxide adsorption at 273 K. Further gravimetric adsorption analysis was performed at various temperatures using carbon dioxide, methane, and nitrogen gases, to analyse the performance of these materials under simulated conditions for carbon capture processes. Thermodynamic and kinetic properties were determined in order to provide an indication of the underlying processes governing diffusion and equilibration of adsorption.

Three materials were investigated;  $\text{Cu}(\text{bpetha})_2\text{SiF}_6$  (bpetha = 1,2-bis(4-pyridyl)ethane),  $[\text{Cu}(\text{TPT})]\text{BF}_4 \cdot 0.75\text{H}_2\text{O}$  and  $[\text{Cu}(\text{TPT})]\text{NO}_3 \cdot \text{MeOH}$  (TPT = 1,3,5-tris(4-pyridyl)-2,4,6-triazine).  $\text{Cu}(\text{bpetha})_2\text{SiF}_6$  showed promising results for carbon dioxide adsorption ( $0.6 \text{ mmol g}^{-1}$  at 100 kPa and 333 K), having kinetically selective behaviour for nitrogen and methane at timescales that are suitable for pressure swing adsorption processing (90 %/5 % of equilibrium uptake for carbon dioxide vs. nitrogen in under 3 min). The material also showed enhanced adsorption interactions towards carbon

dioxide as a consequence of electronegative fluorine atoms within the structure, and also exhibited flexibility of the framework towards carbon dioxide. [Cu(TPT)]BF<sub>4</sub>·0.75H<sub>2</sub>O showed poor adsorption capabilities for carbon dioxide (0.15 mmol g<sup>-1</sup> at 100kPa and 333 K), which is ascribed to pore blocking effects of the anion within the structure. [Cu(TPT)]NO<sub>3</sub>·MeOH showed moderate uptakes for CO<sub>2</sub> at low temperatures (1.96 mmol g<sup>-1</sup> maximum capacity at 273 K), but demonstrated better adsorption capabilities for methane at higher temperatures (1.54 mmol g<sup>-1</sup> at 100 kPa and 333 K). The framework experienced a large structural change upon adsorption, which was probed using methane at different temperatures.

The results of this study showed that materials synthesised with inherent functionalisation could be developed to enhance carbon dioxide adsorption for Carbon Capture applications. However, other structural effects of the materials must be considered as the complexity of Metal-Organic Framework structures can influence the adsorption properties via a variety of mechanisms.

# DISSEMINATION

## PUBLICATIONS

*Solvent-Switchable Continuous-Breathing Behaviour in a Diamondoid Metal–Organic Framework and its Influence on CO<sub>2</sub> versus CH<sub>4</sub> Selectivity*, **2017**, E. J. Carrington, C. A. McAnally, A. J. Fletcher, S. P. Thompson, M. Warren & L. Brammer. Nature Chemistry

*“A Family of Nitrogen-Enriched Metal-Organic Frameworks with CCS Potential”*, **2016**, E. Dooris, C. A. McAnally, E. J. Cussen, A. R. Kennedy & A. J. Fletcher, Crystals 6(1), 14

## PRESENTATIONS

*“A Joint Experimental and Computational Study of a SIFSIX MOF Demonstrating Flexible Properties”*

5th International Conference on Multifunctional, Hybrid and Nanomaterials, Lisbon, March 2017

Craig A. McAnally, Christopher Campbell, Miguel Jorge, Ashleigh J. Fletcher

*“Adsorption Studies of Metal-Organic Frameworks for use in Carbon Capture Technologies”*

Research Presentation Day, University of Strathclyde, Glasgow, June 2016

Craig A. McAnally, Ashleigh J. Fletcher, Edmund J. Cussen

*“Unexpected Adsorption Behaviour for ‘Non-porous’ SIFSIX MOF”*

12th International Conference on the Fundamentals of Adsorption (FOA12), Friedrichshafen, May 2016

Craig A. McAnally, Ashleigh J. Fletcher, Edmund J. Cussen

*“Strategies for CO<sub>2</sub> Mitigation – A Holistic Approach”*

Scottish Carbon Capture & Storage (SCCS) Conference, Edinburgh, Oct 2015

Ivan A. Principe, Craig A. McAnally, Ashleigh J. Fletcher.

*“New Materials for Gas Storage and Selective Separation”*

Research Presentation Day, University of Strathclyde, Glasgow, June 2015

Craig A. McAnally, Ashleigh J. Fletcher, Edmund J. Cussen

*“Evaluation of MOF Textural Parameters - Lessons for Materials Screening”*

RSC Solid State Chemistry Group (SSCG) Christmas Meeting, Glasgow, Dec 2014

Craig A. McAnally, Ashleigh J. Fletcher, Edmund J. Cussen

*“Development of New Metal-Organic Frameworks for Carbon Capture”*

Research Presentation Day, University of Strathclyde, Glasgow, June 2014

Craig A. McAnally, Ashleigh J. Fletcher, Edmund J. Cussen

*“Developing Crystalline Materials with Potential for CO<sub>2</sub>/CH<sub>4</sub> Sieving”*  
RSC Solid State Chemistry Group (SSCG) Christmas Meeting, Bath Dec 2013  
Craig A. McAnally, Ashleigh J. Fletcher, Edmund J. Cussen

# TABLE OF CONTENTS

Declaration of Authenticity and Author's Rights .....	i
Acknowledgements .....	ii
Abstract .....	iv
Dissemination .....	vi
Table of Contents .....	viii
1 Introduction.....	2
1.1 Intergovernmental Panel on Climate Change.....	4
1.2 Science of Climate Change and Opportunities for Mitigation.....	4
1.3 Environment and Climate Change .....	11
1.3.1 Mitigation .....	11
1.3.2 Carbon Capture and Sequestration.....	12
1.3.3 Amine Scrubbing.....	17
1.4 Porous Materials .....	22
1.4.1 Activated Carbons .....	22
1.4.2 Zeolites .....	24
1.5 Porous Coordination Polymers/Metal-Organic Frameworks.....	27
1.5.1 Structure and Properties of MOFs .....	28
1.5.2 Reticular Synthesis.....	29
1.5.3 Nodes .....	29
1.5.4 Linkers .....	31
1.5.5 Linker Types .....	32
1.5.6 Interpenetration .....	33
1.5.7 Functionalisation and Post Synthetic Modification .....	34
1.5.8 Flexibility.....	36
1.6 References .....	40
2 Aims and Objectives .....	50
2.1 Overall Objectives .....	51
2.2 Specific Objectives .....	51

2.2.1	Synthesis of MOFs to Study Their Adsorption Potential.....	51
2.2.2	Characterisation of MOF Materials .....	52
2.2.3	Study of Single Component Adsorption Characteristics .....	52
2.2.4	Study of the Competitive Adsorption Characteristics .....	52
2.3	Thesis Outline.....	53
3	Principles of Adsorption.....	56
3.1	Definition of Adsorption .....	56
3.2	Physisorption and Chemisorption.....	59
3.3	Porosity.....	62
3.4	Pore classification.....	64
3.4.1	Microporosity.....	64
3.4.2	Mesoporosity.....	66
3.4.3	Macroporosity .....	67
3.5	Interpreting Adsorption.....	68
3.5.1	IUPAC Isotherm Classification .....	68
3.5.2	Hysteresis Loops .....	71
3.6	Adsorption Theories.....	74
3.6.1	Henry's Law.....	74
3.6.2	Virial Equation.....	74
3.6.3	Langmuir Isotherm Equation .....	75
3.6.4	Brunauer-Emmett-Teller (BET) Theory.....	78
3.6.5	Polanyi Potential Theory .....	81
3.6.6	Dubinin-Radushkevich Model – Theory of Volume Filling of Micropores.....	83
3.6.7	Determination of surface area.....	88
3.7	Adsorption Phenomena .....	90
3.7.1	Capillary Condensation .....	90
3.7.2	Activated Diffusion .....	91
3.8	Adsorption Kinetics .....	94
3.8.1	Diffusion Mechanisms.....	94
3.8.2	Linear Driving Force Model (Case II) .....	98
3.8.3	Non-Fickian / Anomalous Diffusion Models .....	100
3.8.4	Stretched Exponential.....	100
3.8.5	Avrami Model .....	101
3.8.6	Nested Kinetic Models .....	102

3.9	Adsorption Thermodynamics .....	104
3.9.1	Clausius-Clapeyron Equation .....	104
3.9.2	Arrhenius Equation for Activation Energy of Reaction Rate.....	106
3.10	References .....	108
4	Crystallography .....	114
4.1	Diffraction by Crystalline Solids.....	114
4.1.1	Bragg's Law .....	115
4.1.2	Miller Indices .....	116
4.1.3	Crystal Systems .....	118
4.1.4	X-ray Generation.....	122
4.1.5	X-ray Diffraction Techniques .....	122
4.1.6	Rietveld Refinement and Le Bail method .....	127
4.2	References .....	130
5	Experimental Methods.....	132
5.1	Materials Used .....	132
5.1.1	Synthesis Components.....	132
5.1.2	Adsorptive Gases Used.....	134
5.2	Synthesis Techniques .....	137
5.2.1	Solvent Diffusion .....	137
5.2.2	Solvothermal .....	139
5.2.3	Direct Addition (Batch Crystallisation) .....	140
5.3	Analytical Techniques.....	141
5.3.1	Single Crystal X-ray Diffraction.....	141
5.3.2	Powder X-ray Diffraction.....	142
5.3.3	Thermogravimetric Analysis .....	143
5.3.4	Fourier Transform Infrared Spectroscopy .....	145
5.4	Gas Adsorption Analysis.....	146
5.4.1	Volumetric Adsorption Apparatus .....	146
5.4.2	Intelligent Gravimetric Analyser .....	150
5.5	References .....	160
6	Characterisation of MOF Structures .....	163
6.1	Synthesis & Characterisation of $\text{Cu}(\text{bpetha})_2\text{SiF}_6$ .....	163
6.1.1	Preparation of Single Crystals of $\text{Cu}(\text{bpetha})_2\text{SiF}_6$ .....	163

6.1.2	Non-Porous [Cu(bpetha)(OH <sub>2</sub> ) <sub>3</sub> (NO <sub>3</sub> )]SiF <sub>6</sub> •(H <sub>2</sub> O)•0.5(CH <sub>3</sub> OH)	165
6.1.3	Structural determination of Porous Cu(bpetha) <sub>2</sub> (SiF <sub>6</sub> )	168
6.1.4	Thermal Studies of Cu(bpetha) <sub>2</sub> (SiF <sub>6</sub> )	172
6.1.5	Elemental Analysis of Cu(bpetha) <sub>2</sub> SiF <sub>6</sub>	174
6.2	Synthesis & Characterisation of [Cu(TPT)]BF <sub>4</sub> •0.75H <sub>2</sub> O	176
6.2.1	Thermal Studies of [Cu(TPT)]BF <sub>4</sub> •0.75H <sub>2</sub> O	181
6.2.2	Elemental analysis of [Cu(TPT)]BF <sub>4</sub> •0.75H <sub>2</sub> O	182
6.3	Synthesis and Characterisation of [Cu(TPT)]NO <sub>3</sub> •MeOH	184
6.3.1	Thermal Studies of [Cu(TPT)]NO <sub>3</sub> •MeOH	188
6.3.2	Elemental analysis of [Cu(TPT)]NO <sub>3</sub> •MeOH	189
6.4	Porous Characterisation	190
6.4.1	Adsorption Analysis of Cu(bpetha) <sub>2</sub> SiF <sub>6</sub>	190
6.4.2	Adsorption Analysis of [Cu(TPT)]BF <sub>4</sub> •0.75H <sub>2</sub> O	193
6.4.3	Adsorption Analysis of [Cu(TPT)]NO <sub>3</sub> •MeOH	196
6.5	Discussion	200
6.5.1	Structural Analysis of Cu(bpetha) <sub>2</sub> SiF <sub>6</sub>	200
6.5.2	Structural Analysis of [Cu(TPT)]BF <sub>4</sub> •0.75H <sub>2</sub> O	209
6.5.3	Structural Analysis of [Cu(TPT)]NO <sub>3</sub> •MeOH	213
6.6	References	216
7	Adsorption Analysis of MOF Structures	220
7.1	Adsorption on Cu(bpetha) <sub>2</sub> SiF <sub>6</sub>	220
7.1.1	CO <sub>2</sub> Adsorption Isotherms	220
7.1.2	Thermodynamics of Adsorption	223
7.1.3	Pure Component Adsorbate Isotherms	225
7.1.4	Adsorption Kinetics	227
7.1.5	Competitive Adsorption Isotherms	237
7.2	Adsorption on [Cu(TPT)]BF <sub>4</sub> •0.75H <sub>2</sub> O	239
7.2.1	Adsorption Isotherms	239
7.2.2	Adsorption Kinetics	240
7.3	Adsorption on [Cu(TPT)]NO <sub>3</sub> •MeOH	242
7.3.1	Adsorption Isotherms	242
7.3.2	Thermodynamics of Adsorption	244
7.3.3	Adsorption Kinetics	246
7.3.4	Activation Energies	251
7.4	Discussion	253

7.4.1	Adsorption on $\text{Cu}(\text{bpetha})_2\text{SiF}_6$ .....	253
7.4.2	Adsorption on $[\text{Cu}(\text{TPT})]\text{BF}_4 \cdot 0.75\text{H}_2\text{O}$ .....	262
7.4.3	Adsorption on $[\text{Cu}(\text{TPT})]\text{NO}_3 \cdot \text{MeOH}$ .....	265
7.5	References .....	270
8	Conclusions .....	274
	References .....	278
9	Further Work .....	280
9.1	Further work on $\text{Cu}(\text{bpetha})_2\text{SiF}_6$ .....	280
9.2	Further work on $[\text{Cu}(\text{TPT})]\text{BF}_4 \cdot 0.75\text{H}_2\text{O}$ .....	281
9.3	Further work on $[\text{Cu}(\text{TPT})]\text{NO}_3 \cdot \text{MeOH}$ .....	281
9.4	References .....	283
10	Appendix .....	285
10.1	Bond Valence Calculations .....	285
10.2	Determination of Components Lost During TGA .....	286
10.2.1	$\text{Cu}(\text{bpetha})_2\text{SiF}_6$ .....	286
10.2.2	$[\text{Cu}(\text{TPT})]\text{BF}_4 \cdot 0.75\text{H}_2\text{O}$ .....	286
10.2.3	$[\text{Cu}(\text{TPT})]\text{NO}_3 \cdot \text{MeOH}$ .....	287
10.3	Single Crystal X-ray Diffraction Structural Data of $[\text{Cu}(\text{bpetha})(\text{OH}_2)_3(\text{NO}_3)]\text{SiF}_6 \cdot (\text{H}_2\text{O}) \cdot 0.5(\text{CH}_3\text{OH})$ .....	288
10.4	Single Crystal X-ray Diffraction Structural Data of $[\text{Cu}(\text{TPT})]\text{BF}_4 \cdot 0.75\text{H}_2\text{O}$ .....	290
10.5	Single Crystal X-ray Diffraction Structural Data of $[\text{Cu}(\text{TPT})]\text{BF}_4$ After $\text{CO}_2$ Adsorption .....	294
10.6	Buoyancy Correction of Gravimetric Adsorption Data .....	298
10.6.1	Error Analysis .....	305
10.7	References .....	309

## List of Figures

Figure 1.1 Temperature variability over the last 800,000 years taken from Antarctic ice cores. <sup>8</sup> .....	5
Figure 1.2: Plot of the Global mean temperature anomaly from 1880 – Present (°C). Plot shows the difference in temperature between recorded values and the predicted temperature from climate models, which is expected from natural variations over the last decade, (■) shows the annual mean recorded each year, line (red) gives the 5-year mean showing the general upwards trend (Data obtained from <sup>10</sup> ). .....	6
Figure 1.3: Data collected by the IPCC showing (a) the annual ice extent of north polar ice cap, (b) yearly ice coverage between 1990 – 2010, (c) annual ice thickness, (d) global mean sea levels from 1950 – 2010, (e) heat content of the upper ocean surface (ZJ), and (f) the annual salinity difference between 1950's – 2010 taking the difference of highest and lowest recorded salinities <sup>6</sup> . .....	7
Figure 1.4: Concentrations of Greenhouse Gases CO <sub>2</sub> and N <sub>2</sub> O in ppm, and CH <sub>4</sub> in ppb, over the last 2005 years. Increasing trend occurs during the last 300 years, at the commencement of the industrial era <sup>7</sup> . .....	8
Figure 1.5: Radiation spectrum from incident energy from the Sun. Spectra given for incident radiation on atmosphere (Yellow) and sea level (Blue), and approximation for Sun's spectrum as a black body emitter with temperature 5800 K (Data obtained from <sup>12</sup> ). .....	10
Figure 1.6: Examples of Primary, Secondary and Tertiary alkanolamine structures used for CO <sub>2</sub> capture in amine scrubbing <sup>29</sup> .....	18
Figure 1.7: Process flow diagram of an amine scrubber unit for industrial processing of acid gases. Process' main unit operations are the absorber where CO <sub>2</sub> /H <sub>2</sub> S is chemically absorbed by liquid amines, CO <sub>2</sub> rich solution is taken to the regenerator where high temperatures are used to break the bond between amine and CO <sub>2</sub> , releasing pure CO <sub>2</sub> for processing and storage <sup>32</sup> .....	20
Figure 1.8: Diagrammatical depiction of nodes and linkers having different functional sites which determines the overall coordination and geometry of the resulting MOF structure <sup>67</sup> .....	30
Figure 1.9: Structure of MOF-5 shown in different topological descriptions. (a) gives the crystal structure showing Zn <sub>4</sub> O tetrahedral units (blue polyhedra) which coordinate with the oxygen atoms (red) of the benzenedicarboxylate ligands (grey), (b) node and linker diagram showing metal clusters as spherical nodes (red) and ligands as rods (blue), (c) detailed node/linker diagram showing metal clusters as polyhedra (red) and ligands shown as slats (blue) which indicates ligand positioning within crystal structure <sup>73</sup> .....	30
Figure 1.10: Structures of 12 non-interpenetrated isorecticular MOFs (IRMOFs) showing increase in pore volume with increase in ligand length <sup>75</sup> .....	31
Figure 1.11: Typical organic ligands used in the synthesis of Metal-Organic Frameworks.....	32

Figure 1.12: Interpenetration of 2-dimensional nets to form a 3-dimensional structure. Separate nets form independently within the space between coordinated atoms of another net. Interpenetrated structures cannot be separated without collapse of the entire structure <sup>81</sup> .....	33
Figure 1.13: Scheme of different mechanisms by which MOFs can show flexibility <sup>99</sup> .....	37
Figure 3.1: Leonard-Jones Potential Diagram shows the potential energy , E, between two particles which are a distance r apart. $\sigma$ represents the minimum distance where a stable energy minimum is obtained, and $\epsilon$ is the minimum energy potential .....	57
Figure 3.2: Mechanism of adsorption of a gas molecule onto a surface. In the gas phase, molecules are able to move in 3-dimensions, once adsorbed onto the surface the molecule is able to move 2-dimensionally across the surface, creating a ‘pseudo-liquid’ like phase .....	60
Figure 3.3: Different Types of Porosity. Legend indicates the types of porosity and the symbols which correspond to the symbols on the diagram .....	62
Figure 3.4: Change in adsorption potential between (a) macropores, (b) mesopores, and (c) micropores. Adsorbate molecules interact more strongly with narrow pores due to the overlap of wall potentials. Wider pores have less overlap, therefore energy wells are seen at two distinct regions in the energy plot, where the central channel of the pore is less stable. Macropores are in essence plane surfaces as there is no overlap of potentials due to the large pore width <sup>18</sup> .....	66
Figure 3.5: IUPAC Classification for adsorption isotherms plotted as amount adsorbed against relative pressure $(P/P_0)$ <sup>1</sup> .....	68
Figure 3.6: IUPAC Classification for adsorption hysteresis loops, plotted as amount adsorbed against relative pressure $(P/P_0)$ <sup>1</sup> .....	71
Figure 3.7: BET isotherm model, showing a range of C values and the subsequent impact on the isothermal curve obtained.....	80
Figure 3.8: Representation of Polanyi’s theory. Cross-section of the adsorbed phase showing energy levels increasing with a decrease in the distance to the surface <sup>18</sup> .....	81
Figure 3.9: Diagrammatic representation of the deviations from linearity seen in the D-R Equation, and how this relates to pore-size distribution <sup>34</sup> . (Image courtesy of Dr. Ashleigh J. Fletcher <sup>35</sup> ).....	87
Figure 3.10: Capillary condensation mechanism, (a) monolayer adsorption, (b) multilayer formation, (c) stabilised adsorbate molecules within the central core of the pore, (d) condensation of liquid-like adsorbate, (e) complete pore filling at $P/P_0 = \sim 1$ , (f) altered desorption mechanism with core adsorbed liquid desorbing from pore first	90
Figure 3.11: Mechanisms of diffusion based upon the mean free path of the molecule.	95
Figure 4.1: Simplified diagrammatic representation of Bragg’s Law. Incident radiation of wavelength, $\lambda$ , interacts with a set of parallel planes at an angle of incidence, $\theta$ , which are separated by a distance, $d_{hkl}$ . X-rays are scattered and if the path length	

difference between two waves is a positive integer, then constructive interference occurs. Adapted from Stout <i>et al.</i> <sup>2</sup> .....	115
Figure 4.2: Series of 2-dimensional lattice planes, showing the corresponding miller indices (hkl), c-axis is perpendicular to the ab plane, therefore $l = 0$ . Adapted from Stout <i>et al.</i> <sup>2</sup> .....	117
Figure 4.3: Definition of Unit Cell, showing lengths a, b and c, with corresponding angles $\alpha$ , $\beta$ and $\gamma$ <sup>3</sup> .....	118
Figure 4.4: Crystal structure of Sodium Chloride (NaCl). Na <sup>+</sup> (green), Cl <sup>-</sup> (red) <sup>4</sup> .....	121
Figure 5.1: Chemical Structure of 2,4,6-tris(4-pyridyl)-1,3,5-triazine .....	133
Figure 5.2: (a) plot of liquid density vs. temperature for gases CO <sub>2</sub> (red), CH <sub>4</sub> (grey), and N <sub>2</sub> (blue). (b) linear extrapolation from Equation (5-3) determined by Camacho <i>et al.</i> <sup>5</sup> , density plotted on natural log scale. It should be noted, that due to CO <sub>2</sub> subliming at low temperatures, liquid data was unavailable below the triple point; therefore values used for the boiling point in the calculation were taken from the triple point of CO <sub>2</sub> .	136
Figure 5.3: Schematic of a Parr <sup>®</sup> Autoclave <sup>8</sup> .....	140
Figure 5.4: Schematic of Volumetric measurement setup. Two volume chambers V1+V2 connected by valve A, connection to gas supply through valve B and vacuum through valve C. Sample is contained in chamber V <sub>2</sub> which is temperature controlled using a thermostat (T) <sup>11</sup> .....	146
Figure 5.5: IGA unit within Chemical and Process Engineering Department. From left to right; Computer user interface with IGA unit hosting IGASwin software, sample chamber, temperature controlling units, gas cylinders and external valves, Mass flow controllers and furnace controller .....	151
Figure 5.6: Internal components of IGA system. From left to right; computer module, stainless steel microbalance chamber, gas dosing pipework.....	151
Figure 5.7: IGA microbalance chamber, and simplified diagram of the compensating beam balance.....	153
Figure 5.8: Pressure dosing system containing pressure transducers, automated admit and exhaust valves, and pipework for delivery of gas/vapours to IGA chamber.....	154
Figure 6.1: Structure of [Cu(bpetha)(OH <sub>2</sub> ) <sub>3</sub> (NO <sub>3</sub> )]SiF <sub>6</sub> •(H <sub>2</sub> O)•0.5(CH <sub>3</sub> OH). Cu (light blue), Si (yellow), F (green) O (red), N (blue), C (grey). Uncoordinated solvents and H's on ligands omitted for clarity. Depicts polymeric chains of Cu-bpetha, Cu coordinated to water molecules which interact with SiF <sub>6</sub> <sup>2-</sup> through hydrogen bonding to link chains.....	165
Figure 6.2: (a) One network formed by coordination of [SiF <sub>6</sub> ] <sup>2-</sup> units to chains of Cu(bpetha). (b) Structure is 8-fold interpenetrated shown by intertwined chains of different colours.....	166
Figure 6.3: Hydrogen bonding present between coordinated water molecules and nitrate groups, and methanol molecule to nitro groups on bpetha ligands. ....	167

Figure 6.4: Powder X-ray diffraction data collected for samples of $\text{Cu}(\text{bpetha})_2\text{SiF}_6$ using different Cu metal salts. ....	168
Figure 6.5: Organic ligand structures and the associated distances between the terminal nitrogen atoms of the ligand <sup>2,5-8</sup> . Used for comparison with bpetha ligand used in this work. ....	170
Figure 6.6: GSAS Le Bail refinement of powder diffraction data collected on $\text{Cu}(\text{bpetha})_2\text{SiF}_6$ . Pattern was fit to the P4 space group. Collected data (red), Calculated peaks (green), Difference curve (pink), allowed reflections of the P4 space group (l)	171
Figure 6.7: Powder diffraction data collected during heating of the sample $\text{Cu}(\text{bpetha})_2\text{SiF}_6$ . The sample diffraction pattern was measured at 20 K intervals from 353 K to 453 K. ....	172
Figure 6.8: Thermogravimetric analysis of $\text{Cu}(\text{bpetha})_2\text{SiF}_6$ . Initial mass loss shows 9.75 % solvent content up to 473 K. Structure begins to degrade after 473 K. ....	173
Figure 6.9: FT-IR Spectra for $\text{Cu}(\text{bpetha})_2\text{SiF}_6$ . Measurements of three synthesised materials using metal salts, $\text{Cu}(\text{SO}_4)$ (green), $\text{Cu}(\text{NO}_3)_2$ (red), and $\text{Cu}(\text{BF}_4)_2$ (black). ....	174
Figure 6.10: Structure of $[\text{Cu}(\text{TPT})]\text{BF}_4 \cdot 0.75\text{H}_2\text{O}$ . Cu (light blue), F (green), O (red), N (blue), C (grey), B (orange), H (white). Framework H's were omitted for clarity. ....	177
Figure 6.11: asymmetric unit of $[\text{Cu}(\text{TPT})]\text{BF}_4 \cdot 0.75\text{H}_2\text{O}$ . Cu (light blue), F (green), O (red), N (blue), C (grey), B (orange), H (white). Framework H's were omitted for clarity. ....	178
Figure 6.12: Extended framework of structure $[\text{Cu}(\text{TPT})]\text{BF}_4 \cdot 0.75\text{H}_2\text{O}$ , with space filling model of included $[\text{BF}_4]^-$ anions within the pores. Interpenetrated networks shown by different colours. ....	179
Figure 6.13: Powder diffraction data of synthesised $[\text{Cu}(\text{TPT})]\text{BF}_4 \cdot 0.75\text{H}_2\text{O}$ samples, additional pattern (black) shows diffraction data from synthesised TPT ligand. ....	180
Figure 6.14: Thermogravimetric analysis of $[\text{Cu}(\text{TPT})]\text{BF}_4 \cdot 0.75\text{H}_2\text{O}$ . Shows small solvent loss of 4.55 % upto 473 K, with degradation of the material at 573 K. ....	181
Figure 6.15: FT-IR spectra for $[\text{Cu}(\text{TPT})]\text{BF}_4 \cdot 0.75\text{H}_2\text{O}$ , TPT ligand, and starting material for organic ligand synthesis, 4-cyanopyridine. ....	182
Figure 6.16: Structure of $[\text{Cu}(\text{TPT})]\text{NO}_3 \cdot \text{MeOH}$ . Cu (light blue), O (red), N (blue), C (grey), H (white). Framework H's were omitted for clarity. ....	185
Figure 6.17: 4-fold interpenetrated framework of $[\text{Cu}(\text{TPT})]\text{NO}_3 \cdot \text{MeOH}$ . View down b-axis of the porous structure, H atoms and methanol molecules removed for clarity. ..	186
Figure 6.18: Hydrogen bonding present between methanol solvent molecules and coordinated nitrate groups. ....	187
Figure 6.19: Powder diffraction data of synthesised samples of $[\text{Cu}(\text{TPT})]\text{NO}_3$ . Tick marks shown for space group $\text{P2}_1/\text{n}$ . ....	187
Figure 6.20: Thermogravimetric analysis of $[\text{Cu}(\text{TPT})]\text{NO}_3 \cdot \text{MeOH}$ . Shows solvent loss of 4.32 % up to 453 K. Degradation of the material begins at 513 K. ....	188

Figure 6.21: FT-IR spectra of [Cu(TPT)]NO <sub>3</sub> .MeOH, TPT, and 4-cyanopyridine.....	189
Figure 6.22: N <sub>2</sub> adsorption isotherm at 77 K on Cu(bpetha) <sub>2</sub> SiF <sub>6</sub> .....	190
Figure 6.23: Analysis of BET linear equation to determine surface area of Cu(bpetha) <sub>2</sub> SiF <sub>6</sub> .....	191
Figure 6.24: CO <sub>2</sub> adsorption isotherm at 273 K on Cu(bpetha) <sub>2</sub> SiF <sub>6</sub> , Ads (■) and Des (□). Shows Type I isotherm classification. Presence of hysteresis, however mild conditions for outgassing removes guest species. ....	191
Figure 6.25: Langmuir linear plot of CO <sub>2</sub> isotherm at 273 K for the determination of monolayer capacity of Cu(bpetha) <sub>2</sub> SiF <sub>6</sub> .....	192
Figure 6.26: D-R linear equation of CO <sub>2</sub> isotherm at 273 K to determine the micropore volume of Cu(bpetha) <sub>2</sub> SiF <sub>6</sub> .....	192
Figure 6.27: N <sub>2</sub> adsorption isotherm at 77 K on [Cu(TPT)]BF <sub>4</sub> .0.75H <sub>2</sub> O. Linear trend in isotherm does not correspond to classical isotherm type, suggested to be the result of activated diffusion occurring in very narrow micropores. ....	193
Figure 6.28: CO <sub>2</sub> adsorption at 273 K on [Cu(TPT)]BF <sub>4</sub> .0.75H <sub>2</sub> O. Shows Type I isotherm classification. Presence of hysteresis, use of mild conditions for outgassing removes guest species. ....	194
Figure 6.29: Langmuir linear plot of CO <sub>2</sub> isotherm at 273 K for the determination of monolayer capacity of [Cu(TPT)]BF <sub>4</sub> .0.75H <sub>2</sub> O .....	194
Figure 6.30: D-R linear equation of CO <sub>2</sub> isotherm at 273 K to determine the micropore volume of [Cu(TPT)]BF <sub>4</sub> .0.75H <sub>2</sub> O .....	195
Figure 6.31: N <sub>2</sub> adsorption isotherm (cm <sup>3</sup> g <sup>-1</sup> ) over relative pressure range (P/P <sub>0</sub> ) at 77 K on [Cu(TPT)]NO <sub>3</sub> .MeOH.....	196
Figure 6.32: Analysis of BET linear equation to determine surface area of [Cu(TPT)]NO <sub>3</sub> .MeOH. (a) shows plot of V(1-P/P <sub>0</sub> ) vs. P/P <sub>0</sub> used to determine the appropriate linear region for the BET equation. (b) shows the plot of P/P <sub>0</sub> /[V(1-P/P <sub>0</sub> )] vs. P/P <sub>0</sub> to obtain the linear plot of the BET equation. Monolayer capacity and C constant are determined from the gradient and intercept of the line and used to determine the surface area .....	197
Figure 6.33: CO <sub>2</sub> adsorption at 273 K on [Cu(TPT)]NO <sub>3</sub> .MeOH. Shows Type I isotherm classification. Inset: log(P) plot showing sharp increase in adsorption amount at 20 kPa .....	198
Figure 6.34: Langmuir plot of P/n (kPa g mmol <sup>-1</sup> ) vs. pressure (kPa) to obtain linear plot of CO <sub>2</sub> adsorption isotherm at 273 K for the determination of monolayer capacity of [Cu(TPT)]NO <sub>3</sub> .MeOH. Monolayer capacity calculated from gradient as 1.976 mmol g <sup>-1</sup> .....	198
Figure 6.35: Plot of log(n) vs log <sup>2</sup> (P <sub>0</sub> /P) to obtain linear function of D-R equation for CO <sub>2</sub> adsorption isotherm at 273 K to determine the micropore volume of [Cu(TPT)]NO <sub>3</sub> .MeOH. Micropore volume was determined from intercept of line to obtain a value of 0.1015 cm <sup>3</sup> g <sup>-1</sup> .....	199

Figure 7.1: CO <sub>2</sub> adsorption analysis on Cu(bpetha) <sub>2</sub> SiF <sub>6</sub> at 273 K and 298 K. (a) Pressure range 0 – 700 kPa, (b) Pressure range 0 – 100 kPa. ‘step’ in 298 K isotherm observed at 7.5 – 10 kPa.....	221
Figure 7.2: CO <sub>2</sub> adsorption isotherms in temperature range 273 K – 333 K for Cu(bpetha) <sub>2</sub> SiF <sub>6</sub> over pressure range 0 – 100 kPa.....	222
Figure 7.3: (a) Plot of isosteric enthalpy of adsorption (kJ mol <sup>-1</sup> ) and (b) plot of isosteric entropy of adsorption (J mol <sup>-1</sup> K <sup>-1</sup> ) against CO <sub>2</sub> molar uptake (mmol g <sup>-1</sup> ) for Cu(bpetha) <sub>2</sub> SiF <sub>6</sub> . Isosteres taken from isotherms to obtain pressures, which were plotted as the ln(P) against 1/T. Linear regression of the points for each isostere gave values for the gradient and intercept which could be used to obtain the enthalpy and entropy values, respectively. Errors were obtained from the least squares regression analysis. ....	223
Figure 7.4: Adsorption isotherms for CO <sub>2</sub> (red ■), CH <sub>4</sub> (grey ○), and N <sub>2</sub> (blue ▲), at temperatures 298 K (a), and 333 K (b). Pressure range 10 – 15 kPa is highlighted (grey) to show the adsorption capacities for each gas at typical CO <sub>2</sub> concentrations. ....	225
Figure 7.5: Adsorption kinetic rate constants, k (s <sup>-1</sup> ), for CO <sub>2</sub> adsorption against pressure (kPa). CO <sub>2</sub> is modelled to a Double Exponential, giving two rate constants, k <sub>1</sub> having values of 10 <sup>-2</sup> s <sup>-1</sup> , k <sub>2</sub> having values of 10 <sup>-4</sup> s <sup>-1</sup> . ....	228
Figure 7.6: Adsorption kinetic rate constants, k (s <sup>-1</sup> ), for CO <sub>2</sub> adsorption against No. of CO <sub>2</sub> molecules per unit cell. CO <sub>2</sub> is modelled to a Double Exponential, giving two rate constants, k <sub>1</sub> having values of 10 <sup>-2</sup> s <sup>-1</sup> , k <sub>2</sub> having values of 10 <sup>-4</sup> s <sup>-1</sup> .....	229
Figure 7.7: Pre-exponential factor, A <sub>2</sub> , for CO <sub>2</sub> adsorption kinetics from DE model for temperatures from range 273 – 333 K. Only A <sub>2</sub> is shown for clarity, the combination of A <sub>1</sub> + A <sub>2</sub> = 1.....	229
Figure 7.8: Kinetic mass profiles vs time (s) of CO <sub>2</sub> adsorption pressure steps 5 – 7.5 kPa (a), 7.5 – 10 kPa (b), and 12.5 – 15 kPa (c). Plot (b) corresponds to the point at which the ‘step’ in the 298 K isotherm occurs, and shows an increase from 20000 s to 200000 s equilibration time. Plots are shown with their residuals for the fits, showing good agreement to the DE model.....	231
Figure 7.9: Plot of CH <sub>4</sub> adsorption kinetics at 298 K and 333 K. Data for k (left-axis) and β (right axis) for the SE model used to fit the data. Data fits closely to a LDF model with exponent values ranging between 0.8 – 1.2.....	232
Figure 7.10: Comparison of adsorption kinetic rate constants, k (s <sup>-1</sup> ), against pressure (kPa) for CO <sub>2</sub> (red), k <sub>1</sub> (●) and k <sub>2</sub> (□), CH <sub>4</sub> (grey ○), and N <sub>2</sub> (blue ▷) at (a) 298 K and (b) 333 K. CO <sub>2</sub> fits to a DE model, whereas CH <sub>4</sub> and N <sub>2</sub> fit to a SE model. Dashed lines signify the pressure at which the volume filling reaches one molecule of CO <sub>2</sub> per unit cell. ....	233
Figure 7.11: Mass-time profiles for CO <sub>2</sub> (red), CH <sub>4</sub> (grey), and N <sub>2</sub> (blue) at pressures before (a), during (b), and after (c) the ‘step’ in the CO <sub>2</sub> isotherm at 298 K. Inset figures show initial change in profile. Plots show CO <sub>2</sub> has quickest initial rate at all three pressures, but experiences a much slower rate at the ‘step’ in the isotherm. CH <sub>4</sub> and N <sub>2</sub> do not show the same change in profile .....	235

Figure 7.12: Mass Profiles for CO <sub>2</sub> at 333 K over pressure range 200 – 350 kPa. Profiles show a long equilibration time for 250 and 300 kPa, which is not witnessed during pressures before or after, suggesting the ‘step’ in 333 K isotherm may occur at higher pressure, which corresponds to one CO <sub>2</sub> molecule per unit cell. ....	236
Figure 7.13: Competitive adsorption isotherm for CO <sub>2</sub> vs. N <sub>2</sub> at 333 K (black ▲), with desorption curve (black △). Pressure was maintained at 100 kPa with a total flow of gas of 200 ml min <sup>-1</sup> . Ratio of flow rates was changed to alter the partial pressure of CO <sub>2</sub> within the system. Second curve shows pure component adsorption (red ●) and desorption (red ○) isotherm for CO <sub>2</sub> at 333 K under flowing conditions to compare with competitive adsorption uptake. Plots show mixed flow has similar uptake to pure CO <sub>2</sub> indicating minimal uptake of N <sub>2</sub> . Presence of N <sub>2</sub> causes a suppression of the isotherm at low CO <sub>2</sub> partial pressures, suggesting mean free path is altered. ....	237
Figure 7.14: Pure component mass profiles vs. equilibration time (min) for CO <sub>2</sub> (red) and N <sub>2</sub> (blue) at 333 K. CO <sub>2</sub> plot shown for a pressure step of 10 kPa, and N <sub>2</sub> plot shown for a pressure step of 90 kPa. Plots show CO <sub>2</sub> reaches 90 % of the equilibrated mass uptake within 3 min, with N <sub>2</sub> having very low uptake at this time.....	238
Figure 7.15: Adsorption isotherms for CO <sub>2</sub> (red), CH <sub>4</sub> (grey), and N <sub>2</sub> (blue) on [Cu(TPT)]BF <sub>4</sub> .0.75H <sub>2</sub> O at 333 K from 0 – 100 kPa. Grey band shows pressure range between 10 – 15 kPa which indicates the concentration of CO <sub>2</sub> within a post-combustion flue gas stream, showing adsorption of CH <sub>4</sub> is higher in this region. ....	239
Figure 7.16: Adsorption kinetic parameters, (a) rate constant, <i>k</i> (s <sup>-1</sup> ), against pressure (kPa) and (b) exponent β against pressure (kPa) for CO <sub>2</sub> (red), CH <sub>4</sub> (grey), and N <sub>2</sub> (blue) at 333 K. ....	240
Figure 7.17: Adsorption isotherms for (a) CO <sub>2</sub> (red) and CH <sub>4</sub> (grey) at 298 K, and (b) CO <sub>2</sub> (red), CH <sub>4</sub> (grey), and N <sub>2</sub> (blue) at 333 K.....	242
Figure 7.18: CH <sub>4</sub> adsorption isotherms measured at 298 – 333 K, over pressure range 0 – 100 kPa. Second axis given showing number of CH <sub>4</sub> molecules per unit cell. Isotherm ‘step’ observed for volume filling of one CH <sub>4</sub> molecule per unit cell .....	243
Figure 7.19: Virial plot of ln( <i>n</i> / <i>p</i> ) (lnmol g <sup>-1</sup> Pa <sup>-1</sup> ) vs. <i>n</i> (mol g <sup>-1</sup> ) for CH <sub>4</sub> uptake over temperature range 298 – 333 K. Two measured linear plots were taken at positions before and after the ‘step’ in the isotherm .....	244
Figure 7.20: Plot of virial function constant <i>A</i> <sub>0</sub> (lnmol g <sup>-1</sup> Pa <sup>-1</sup> ) vs <i>1/T</i> (K <sup>-1</sup> ) for CH <sub>4</sub> adsorption on [Cu(TPT)]NO <sub>3</sub> .MeOH. Shows values before step (■) and after the step (□) giving enthalpy values from the gradient of the lines of 5.29 ± 6.60 kJ mol <sup>-1</sup> and 11.16 ± 3.66 kJmol <sup>-1</sup> , respectively. ....	245
Figure 7.21: Comparison of adsorption kinetic rate constants vs. Pressure (kPa) for (a) CO <sub>2</sub> (red) and CH <sub>4</sub> (grey) at 298 K, and (b) CO <sub>2</sub> (red), CH <sub>4</sub> (grey), and N <sub>2</sub> (blue) at 333 K .....	246
Figure 7.22: Adsorption kinetic exponent, β, vs pressure (kPa) for SE model of CO <sub>2</sub> (□), CH <sub>4</sub> (○), and N <sub>2</sub> (△)at a temperature of 333 K for material [Cu(TPT)]NO <sub>3</sub> .MeOH. Values vary between 0.8 – 1.1 for all three gases, with the exception of N <sub>2</sub> below 10 kPa where te value decreases to 0.5. ....	247

Figure 7.23: Mass profiles vs. time (s) for CH <sub>4</sub> adsorption at 298 K for pressure steps (a) 2.5 – 5 kPa, (b) 5 – 7.5 kPa, and (c) 7.5 – 10 kPa, where the ‘step’ occurs in (b). The corresponding residual plots shows the accuracy of the fit, the red lines show the projection of the equilibrated uptake. ....	247
Figure 7.24: Kinetic rate constant, k, for CH <sub>4</sub> adsorption at temperatures from 298 – 333 K, using the SE model. (a) shows kinetic plots on a pressure basis, (b) shows kinetic plots on a molar uptake basis. A reduction in rate occurs within the region 0.8 – 1 mmol g <sup>-1</sup> , with the exception of the plot for 323 K, which does not show a decrease as the isotherm shows a large increase in uptake between 0.4 – 1 mmol g <sup>-1</sup> .....	248
Figure 7.25: Kinetic exponent parameter, β, plotted against pressure for CH <sub>4</sub> at temperatures from 298 – 333 K. Plot shows exponent varies between 0.8 – 1.1, suggesting the kinetics follow a linear driving force process. ....	249
Figure 7.26: Mass profiles of CH <sub>4</sub> adsorption at temperatures from 298 – 333 K, showing five pressure steps at points along the adsorption isotherms. The plots in black show that the pressure at which the step occurs shows an increasing trend from 298 – 333 K, at pressures ranging from 20 – 40 kPa. ....	250
Figure 7.27: Mass profile for CH <sub>4</sub> adsorption at 328 K for pressure step 32.5 – 35 kPa, and shows the uptake within the step increasing in successive levels . The consecutive steps in the kinetic plot were not modelled as this mechanism cannot be adequately fit to the nested set of kinetic equations .....	251
Figure 7.28: (a) Plot of Activation Energy (kJ mol <sup>-1</sup> ) against amount adsorbed (mmol g <sup>-1</sup> ), (b) plot of frequency factor ln(A) (ln(s <sup>-1</sup> )) against activation energy (kJ mol <sup>-1</sup> ), for CH <sub>4</sub> adsorption on [Cu(TPT)]NO <sub>3</sub> .MeOH. Activation energy shows decrease in value with increasing uptake, large change in energy after ‘ step’ in the isotherm, energy experiences gradual increase after this point. Pre-exponential factor decreases with decreasing activation energy, which corresponds to a larger frequency of molecules at the pore opening when the barrier to activation is high. ....	252
Figure 10.1: Forces acting on an object of mass, M <sub>s</sub> , in a fluid of density, ρ <sub>g</sub> . Force contributions are from weight of sample, f <sub>w</sub> , and buoyancy due to displacement of fluid by volume of object, f <sub>b</sub> , and outlined in Equation (10-2).....	298
Figure 10.2: Example of unequilibrated mass profile. Data is normalise from 0 to 1 in the range M <sub>0</sub> to M <sub>t</sub> , calculation using the kinetic models provides a value for parameter A which is >1 if equilibrium is not reached during the experiment. A correction is made to find the maximum uptake M <sub>e</sub> using the information from the graph .....	304
Figure 10.3: Plot of M <sub>t</sub> /M <sub>e</sub> against time (s) for a fully equilibrated pressure step. Analysis of the profile was performed using a DE model, taking percentages of the total equilibrated profile data between 10 – 100 %. The values of A from the kinetic model gave an indication of the deviation from the calculated equilibrium mass using 100 % of the profile data .....	306
Figure 10.4: Plot of the values of A <sub>1</sub> , A <sub>2</sub> , and A <sub>1</sub> + A <sub>2</sub> against the percentage of collected data used to determine the kinetic fit. Plot shows that reasonable errors are achieved when a minimum of 40 % of the equilibrium curve data is collected .....	307

## List of Tables

Table 1.1: Concentration of Gases within Earth's atmosphere in ppmv, percentages (%) given for major constituents <sup>11</sup> .....	9
Table 3.1: Definitions of Key Components in Adsorption Process.....	56
Table 3.2: Properties relating to physisorption and chemisorption processes .....	59
Table 3.3: Size Classification for the Categories of Porosity .....	64
Table 3.4: Size Classification for the Categories of Microporosity .....	64
Table 4.1: Unit cell configurations, unique cell dimensions and possible Bravais lattices .....	119
Table 4.2: Examples of possible symmetry elements within unit cells.....	120
Table 5.1: Solvothermal synthesis conditions of 1,3,5-tris(4-pyridyl)-2,4,6-triazine..	133
Table 5.2: Physical Properties of Gases .....	134
Table 6.1: Conditions used for the synthesis of Cu(bpetha) <sub>2</sub> SiF <sub>6</sub> , as adapted from Zaworotko <i>et al.</i> <sup>2</sup> .....	164
Table 6.2: Collection of Crystal structures of similar Cu(ligand) <sub>2</sub> SiF <sub>6</sub> containing structures <sup>2,5-8</sup> .....	169
Table 6.3: Key Infrared peaks for samples of Cu(bpetha) <sub>2</sub> SiF <sub>6</sub> , and associated bond vibrations .....	175
Table 6.4: CHN analysis of Cu(bpetha) <sub>2</sub> SiF <sub>6</sub> for structures synthesised from Cu(NO <sub>3</sub> ) <sub>2</sub> and Cu(BF <sub>4</sub> ) <sub>2</sub> .....	175
Table 6.5: Key Infrared peaks for [Cu(TPT)]BF <sub>4</sub> ·0.75H <sub>2</sub> O, and their associated bond vibrations .....	183
Table 6.6: CHN analysis of [Cu(TPT)]BF <sub>4</sub> ·0.75H <sub>2</sub> O.....	183
Table 6.7: CHN analysis of [Cu(TPT)]NO <sub>3</sub> ·MeOH.....	189
Table 7.1: Results of CO <sub>2</sub> , CH <sub>4</sub> , and N <sub>2</sub> adsorption at specified pressure intervals ....	226
Table 7.2: Equilibration times (s) before, during, and after the 'step' for temperature range 273 – 333 K.....	236
Table 7.3: Virial parameters for CH <sub>4</sub> adsorption at temperatures 298 – 333 K.....	244
Table 7.4: Minimum molecular dimensions of adsorptives <sup>10</sup> .....	258
Table 10.1: Crystal data and structure refinement for [Cu(bpetha)(OH <sub>2</sub> ) <sub>3</sub> (NO <sub>3</sub> )]SiF <sub>6</sub> ·(H <sub>2</sub> O)·0.5(CH <sub>3</sub> OH).....	288
Table 10.2: Fractional atomic coordinates and isotropic or equivalent isotropic displacement parameters (Å <sup>2</sup> ) for [Cu(bpetha)(OH <sub>2</sub> ) <sub>3</sub> (NO <sub>3</sub> )]SiF <sub>6</sub> ·(H <sub>2</sub> O)·0.5(CH <sub>3</sub> OH)	289
Table 10.3: Crystal data and structure refinement for [Cu(TPT)]BF <sub>4</sub> ·0.75H <sub>2</sub> O .....	290

Table 10.4: Atomic coordinates ( $\times 10^4$ ) and equivalent isotropic displacement parameters ( $\text{\AA}^2 \times 10^3$ ) for $[\text{Cu}(\text{TPT})]\text{BF}_4 \cdot 0.75\text{H}_2\text{O}$ . $U(\text{eq})$ is defined as one third of the trace of the orthogonalized $U^{ij}$ tensor.....	291
Table 10.5: Crystal data and structure refinement for $[\text{Cu}(\text{TPT})]\text{BF}_4$ after $\text{CO}_2$ . .....	294
Table 10.6: Atomic coordinates ( $\times 10^4$ ) and equivalent isotropic displacement parameters ( $\text{\AA}^2 \times 10^3$ ) for $[\text{Cu}(\text{TPT})]\text{BF}_4$ after $\text{CO}_2$ . $U(\text{eq})$ is defined as one third of the trace of the orthogonalized $U^{ij}$ tensor.....	295
Table 10.7: Balance components and their associated weights, densities, and temperatures as used in the buoyancy correction calculations.....	300

# Chapter I

# 1 INTRODUCTION

---

As of 4<sup>th</sup> November 2016, the United Nations Framework Convention on Climate Change (UNFCCC) entered into force The Paris Agreement <sup>1</sup>, which brings together 197 ‘Parties’ (Governments), and unites them under a common cause; to reduce the impact of climate change by implementing a global plan for emissions mitigation <sup>2</sup>. The long-term goal of the Agreement is to minimise average global temperature increases to below 2 °C of pre-industrial levels, and thereafter reduce emissions through further ambitious targets, with the EU committed to decreasing emissions by 20% of 1990 levels by 2020, and 40% by 2030 <sup>3</sup>. The Agreement was put into effect when 55 countries, accounting for at least 55 % of global greenhouse gas emissions, had endorsed the proposal.

Since 1979, an international response has been set up to address the issue of greenhouse gas (GHG) emissions, with the establishment, in 1988, of the Intergovernmental Panel on Climate Change (IPCC), a scientific board dedicated to gathering observations on climate change <sup>4</sup>. This led to the United Nations founding the UNFCCC and setting in place the Kyoto Protocol in 1997, with implementation in 2005.

The Kyoto Protocol was an agreement to which 37 countries, which include the European states, agreed to commit to undertake a 5 % emission reduction below 1990 levels, for the period 2008 - 2012. The 192 Parties which were part of the Kyoto Protocol were divided into Annex I and Non-Annex I groups; developed countries which have contributed to 55 % of the global GHG emissions were asked to agree upon stringent emissions targets, and developing countries, whose compliance with the

Protocol could harm their economic growth, were set less strict targets or were allowed to increase emissions. Unfortunately, the three countries with the highest emissions, China, India and USA, did not accept the treaty on the grounds of potential negative impacts on economic growth (with the USA raising concerns over economic competition with the other two countries), as a consequence, GHG emission reductions made by all other Parties involved failed to slow the increasing trend in carbon dioxide (CO<sub>2</sub>) levels during the first commitment period<sup>5</sup>. As of 2016, the USA is the only Party yet to ratify the Kyoto Protocol.

Several amendments have been added to the Kyoto Protocol since it came into force in 2005, with a new commitment period set for 2013 – 2020, which features higher targets. The most recent update, The Paris Agreement, incorporates a need to support developing countries, and those vulnerable to the effects of climate change, to meet their defined targets. Therefore, all 197 Parties of the Convention have common, but differentiated, responsibility towards emissions reduction, a point that previously led to disagreement with the Kyoto Protocol by some developed nations. A number of measures have been considered to help reduce emissions and support communities with adaptation, as effects such as drought, desertification and flooding are seen across the globe, the effects of which are the impact of the global input to emissions. It is apparent that research and development into low carbon technologies is becoming increasingly necessary to achieve the goals set by the Paris Agreement, therefore, further knowledge of the science behind the effects of increasing GHG emissions on the climate is required to obtain an understanding of how to reverse the effects of climate change.

## 1.1 INTERGOVERNMENTAL PANEL ON CLIMATE CHANGE

The IPCC assesses scientific literature to provide governments with a complete evaluation of the current understanding of climate change. The panel reports on three main aspects through working groups that focus on: (i) the physical science behind climate change (WGI), (ii) the social and economic impacts of climate change on communities and natural systems, including an assessment of possible adaptations to environment, social and economic impacts (WGII), and (iii) the potential options for mitigation, from changes in current practice to limit emissions to new technologies that can be implemented to prevent further emissions (WGIII)<sup>6</sup>. The development of the UNFCCC was based upon the work that the IPCC performs, therefore, the IPCC continues to play an important role in decision making by the parties involved in the Kyoto Protocol and Paris Agreement.

## 1.2 SCIENCE OF CLIMATE CHANGE AND OPPORTUNITIES FOR MITIGATION

The IPCC assessment reports give a detailed response on the current knowledge of climate change within our global environment. Many factors have been analysed, with data being collected from across the globe and collated by the IPCC from a number of sources to define the current understanding of what is happening to our environment<sup>7</sup>.

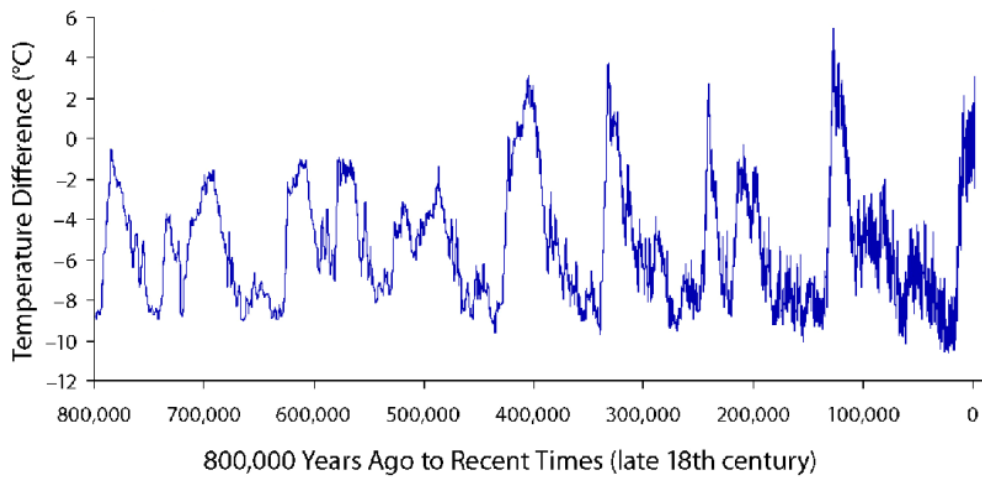


**Figure 1.1 Temperature variability over the last 800,000 years taken from Antarctic ice cores.**<sup>8</sup>

Studies performed on ice cores from the Antarctic, were used to measure the trend in global temperature change from the last 800,000 years<sup>8</sup>. Figure 1.1 shows the cycle in temperature due to ice age events, up to the late 18<sup>th</sup> century (pre-industrial). The fluctuating behaviour of the temperature is the result of glacial periods occurring in cycles; the temperature changes show that the minimum and maximum temperatures have not changed over the course of 800,000. Data collected from a number of sources, including meteorological stations, over the past ~140 years has shown an increasing trend in temperature, which is inconsistent with historic trends<sup>9,10</sup>. The plot in Figure 1.2 shows the global mean temperature variation, between 1880 – present, that is observed from data collected in the field and compared with predicted climate models<sup>10</sup>; the plot shows the increasing trend in temperature anomalies compared with the predicted temperature expected from natural variations alone. A number of other environmental impacts have been recorded within this timeframe, which are inexplicable through naturally occurring events. Data have been collected regarding the extent of sea ice, glaciers and snow cover, showing a loss in ice content over recent years (Figure 1.3), which has contributed to increased sea levels that affect low lying communities with increased flooding events<sup>6</sup>. As these increasing trends continue, the

associated impacts on humans and the environment will become more extreme and increasingly difficult to correct:

- Increasing temperatures will lead to difficulties with growing crops, as lands become more dry and desertification increases
- Increased temperatures can lead to impacts on human health with increased incidences of heat waves
- Reduction in sea ice is impacting wildlife, increasing the number of endangered species
- Rising sea levels, from melting ice, means many areas are experiencing increased levels of flooding
- Changes in sea currents and weather patterns are producing more extreme weather occurrences.

All these changes will ultimately lead to economic difficulties across the globe, as countries must deal with the consequences of climate change.

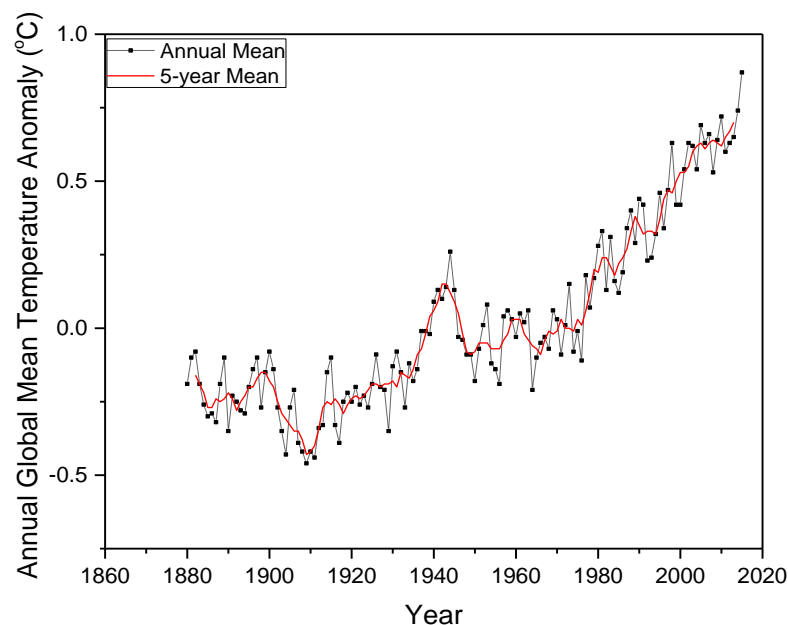


**Figure 1.2: Plot of the Global mean temperature anomaly from 1880 – Present (°C). Plot shows the difference in temperature between recorded values and the predicted temperature from climate models, which is expected from natural variations over the last decade, (■) shows the annual mean recorded each year, line (red) gives the 5-year mean showing the general upwards trend (Data obtained from <sup>10</sup>).**

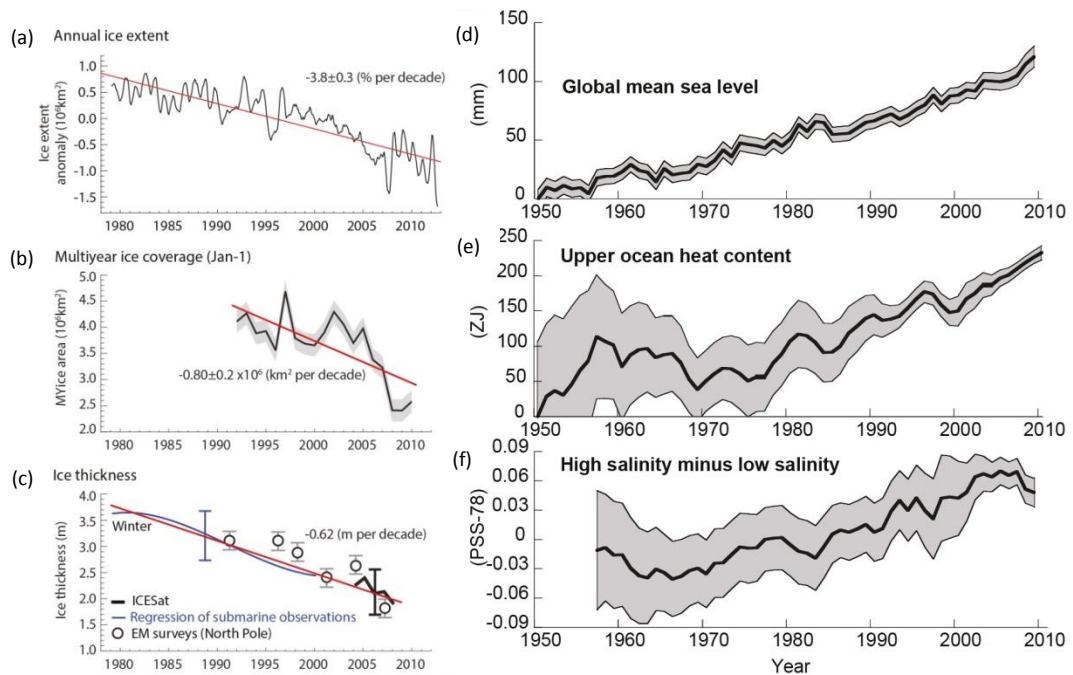


**Figure 1.3: Data collected by the IPCC showing (a) the annual ice extent of north polar ice cap, (b) yearly ice coverage between 1990 – 2010, (c) annual ice thickness, (d) global mean sea levels from 1950 – 2010, (e) heat content of the upper ocean surface (ZJ), and (f) the annual salinity difference between 1950's – 2010 taking the difference of highest and lowest recorded salinities <sup>6</sup>.**

It has been accepted, by most within the scientific community, that the anomalies in global temperatures are the consequence of more than just naturally occurring events. The unexpected changes in the climate have been seen to correspond with growing levels of anthropogenic GHG emissions, which have been recorded within our atmosphere since the start of the industrial era (~1750's). Figure 1.4 shows the increasing concentrations of carbon dioxide (CO<sub>2</sub>), methane (CH<sub>4</sub>), and nitrous oxide (N<sub>2</sub>O), the most prominent contributors to GHG emissions, for the past 2000 years. GHG emissions have been observed to increase proportionally with the increase in global temperatures; additionally, the rate of increase in both GHGs and temperature is significantly higher than historical trends have previously suggested <sup>7</sup>.

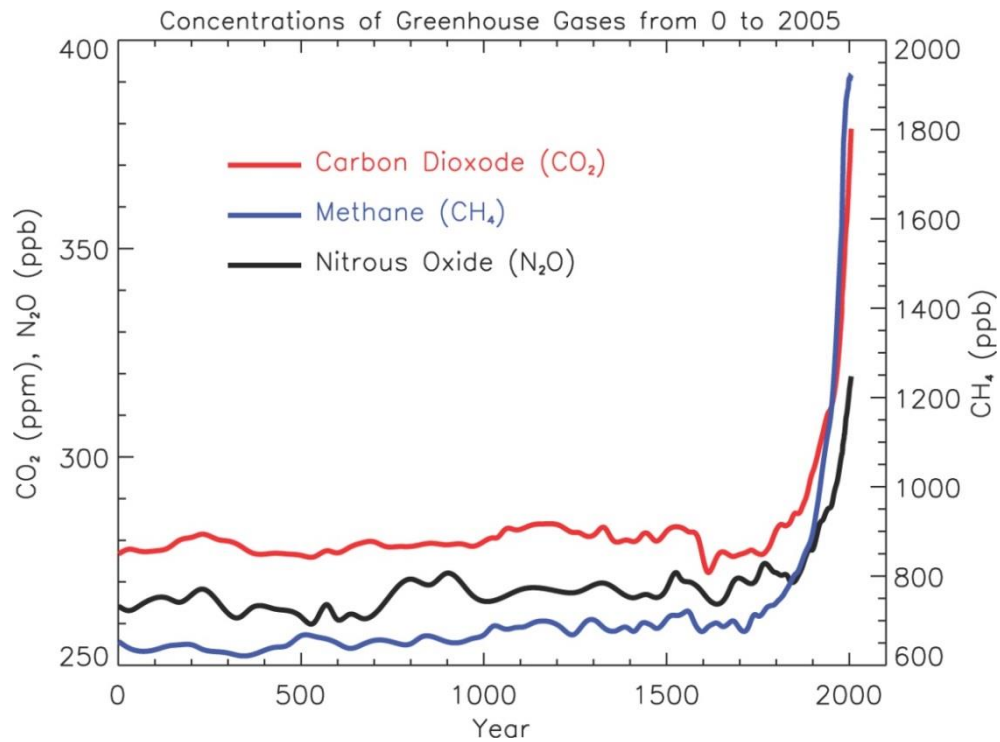


**Figure 1.4: Concentrations of Greenhouse Gases CO<sub>2</sub> and N<sub>2</sub>O in ppm, and CH<sub>4</sub> in ppb, over the last 2005 years. Increasing trend occurs during the last 300 years, at the commencement of the industrial era <sup>7</sup>.**

This has led many to believe that human impact on the environment has influenced the climate system. Other evidence indicates that the increase in CO<sub>2</sub> emissions has impacted the carbon and water cycles; as CO<sub>2</sub> content within oceans has increased, this has resulted in lower pH (more acidic) and increased surface water temperatures, leading to: faster dissolution of sea ice, and deviations in water salinity through higher rates of evaporation (high salinity) and higher precipitation rates (low salinity) at different regions across the globe. The higher levels of GHG emissions within our atmosphere are leading to increased radiative forcing, resulting in higher energy content in the atmosphere, oceans, and land masses <sup>7</sup>. The Earth's ability to maintain conditions suitable for life is dependent upon its atmosphere, and small perturbations in gas concentrations can have a massive influence on environmental conditions.

**Table 1.1: Concentration of Gases within Earth's atmosphere in ppmv, percentages (%) given for major constituents <sup>11</sup>**

<b>Gas</b>	<b>Concentration (ppmv)</b>	<b>Concentration (%)</b>
<b>N<sub>2</sub></b>	780840	78.08
<b>O<sub>2</sub></b>	209460	20.95
<b>Ar</b>	9340	0.93
<b>CO<sub>2</sub></b>	350*	0.035*
<b>H<sub>2</sub>O</b>	0 – 40000*	0 – 4*
<b>Ne</b>	18	-
<b>He</b>	5.2	-
<b>CH<sub>4</sub></b>	1.7	-
<b>H<sub>2</sub></b>	0.53	-
<b>N<sub>2</sub>O</b>	0.3	-
<b>CO</b>	0.04 - 0.2	-
<b>NH<sub>3</sub></b>	<0.01	-
<b>H<sub>2</sub>S</b>	10 <sup>-4</sup>	-
<b>SO<sub>2</sub></b>	10 <sup>-4</sup>	-
<b>O<sub>3</sub></b>	0 – 10	-

\*signifies a variable quantity

Table 1.1 lists the composition of gases found within the Earth's atmosphere <sup>11</sup>. With the advent of biological organisms early in the Earth's history, the atmosphere has been highly altered compared to other planets within our solar system, giving increased oxygen levels at lower altitudes, thereby supporting life on the planet <sup>11</sup>. As solar energy is incident on the atmosphere, a portion is reflected by gas molecules and other particulates, whereby some energy is absorbed by these gases, reducing the energy that reaches the surface. The Sun emits a broad spectrum of radiation, as shown in Figure 1.5 <sup>12</sup>. The formation of ozone (O<sub>3</sub>) in the lower stratosphere has allowed life to be protected from the harmful UV rays emitted by the Sun <sup>13</sup>. The oxygen (O<sub>2</sub>) and O<sub>3</sub> present within our atmosphere can absorb radiation from the Sun at wavelengths less than 400 nm, preventing these high energy wavelengths from reaching the Earth's surface and reducing the total energy that arrives at the lower atmosphere; hence, the spectrum of wavelengths is reduced once it reaches the Earth's surface. The emission spectrum of the Sun can be estimated as a black body with a temperature of 5800 K (as illustrated by the black dashed line in Figure 1.5), and the temperature of the Earth's surface can be estimated as a black body emitter with a

temperature of 256 K. As the average global temperature is 288 K, the Earth's surface is being heated from an additional source <sup>14</sup>.

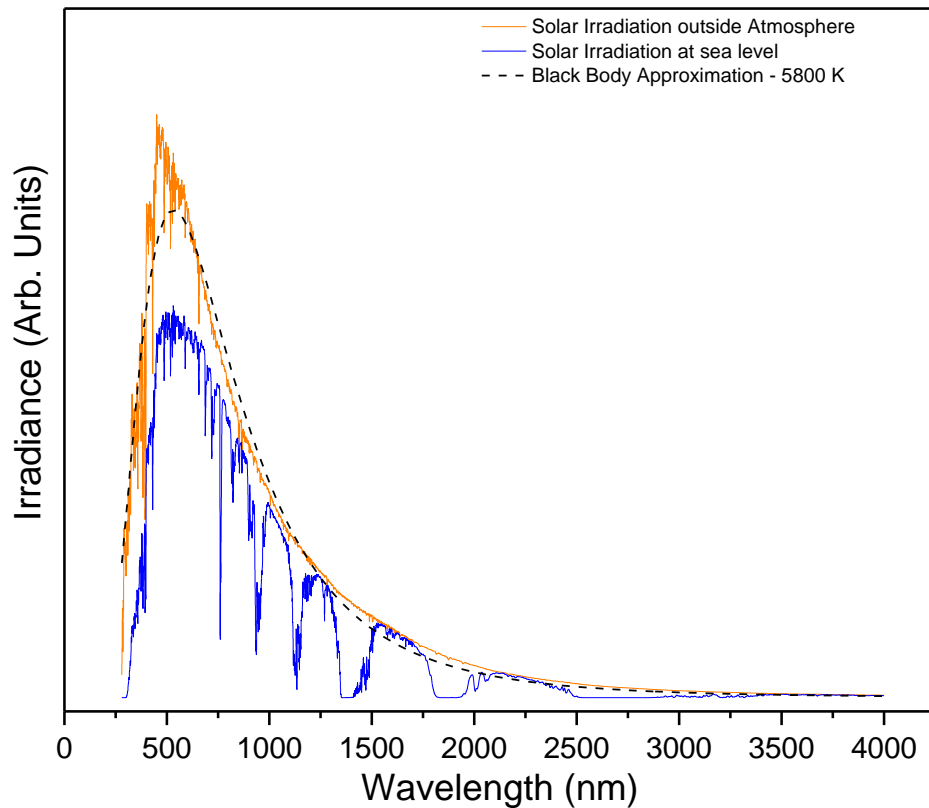


**Figure 1.5: Radiation spectrum from incident energy from the Sun. Spectra given for incident radiation on atmosphere (Yellow) and sea level (Blue), and approximation for Sun's spectrum as a black body emitter with temperature 5800 K (Data obtained from <sup>12</sup>)**

As the emission spectrum from the Earth's surface is within the infrared (IR) region, gas molecules absorb energy via vibrational and rotational energy states; emission of this energy is radiated back to the Earth's surface, providing the aforementioned additional heating. This phenomenon, which allows the Earth to maintain a viable climate for the existence of life is known as the 'Greenhouse Gas Effect', as the absorbing gases have the same effect as a greenhouse, which traps heat energy by transmission of the sun's energy through glass and reflection internally to increase the temperature. Gas molecules that possess an asymmetric stretching and bending are the principle absorbers of this IR radiation; therefore, water (H<sub>2</sub>O), CO<sub>2</sub> and O<sub>3</sub> are the most dominant species affecting global temperatures <sup>14</sup>. However, the

increasing use of fossil fuels for power generation and transportation has caused higher atmospheric concentrations of these absorbing species, and so the amount of heat retained by the atmosphere is increased, resulting in higher land and ocean temperatures. With the onset of the industrial revolution, the release of other gases such as CH<sub>4</sub>, N<sub>2</sub>O and chlorofluorocarbons (CFCs) has impacted the radiation region known as the ‘infrared window’; a portion of the emission spectrum through which a large portion of the heat energy from the Earth’s surface is released without absorption by species with naturally high concentrations in the atmosphere. These ‘man-made’ products are strongly absorbing in this region and so allowing their concentration to increase will result in higher temperatures in coming years, and will increase temperatures towards the 2 °C upper limit that must be avoided in order to prevent extreme harm to the environment.

## 1.3 ENVIRONMENT AND CLIMATE CHANGE

### 1.3.1 MITIGATION

It has been well established that methods to reduce carbon emissions must be implemented to prevent further impact on the global climate and environment. Our high demand for energy contributes heavily to carbon emissions, with an estimated 80% of the World’s energy being supplied by the combustion of fossil fuels in 2014 <sup>15</sup>; therefore, changes are required in the way we generate power, moving towards the use of low carbon intensive fuels, such as natural gas, and renewable energy sources, such as wind, solar, etc. Additional strategies are necessary across all sectors that release GHG emissions, as well as changing our behaviour, lifestyle, and culture in terms of energy use <sup>16</sup>. Individuals can help improve their own ‘carbon footprint’, the equivalent CO<sub>2</sub> produced either directly or indirectly by an individual, by using solar panels to

supplement energy demands in homes, and adding adequate insulation to reduce heat loss; as well as using less emission intensive forms of transport. However, with energy demands continuing to rise, the prevention of carbon emissions must also be focussed at major point sources, such as power plants and heavy industry, which requires new methods of capturing the CO<sub>2</sub> produced by burning fossil fuels. Carbon Capture and Sequestration (CCS) is seen as the best solution to meet these objectives, while allowing current methods of energy production, from fossil fuels, to be sustained.

### 1.3.2 CARBON CAPTURE AND SEQUESTRATION

Yang *et al.*<sup>17</sup> state three possible scenarios that can be implemented to reduce carbon emissions to the atmosphere from large point sources: (i) reducing overall energy consumption by using methods to improve efficiency, (ii) reducing the carbon content of fuels to avoid production of large quantities of CO<sub>2</sub>, such as using hydrogen or renewable energy, and finally (iii) enhancing methods of sequestration, the act of storing carbon long-term in a solid or liquid form, most commonly by injection into depleted oil reservoirs. In each scenario, further research and development is required before it can provide a long term solution. Reducing energy intensity would require better methods of energy storage to prevent waste at times of low energy consumption; hydrogen (H<sub>2</sub>) storage remains a topic of on-going research, and reliance on renewable energy will take time before they are mature enough to be relied upon to handle the World's energy demands. The UK Government has announced plans to move all fossil fuel power generation to gas, owing to the high carbon intensity of using coal, which will be phased-out by 2025<sup>18</sup>. The use of carbon sequestration provides an intermediate solution to allow fossil fuels to continue to be used of as part of a wider energy mix, helping to mitigate the impacts of climate change and meet the UK's emission targets, in line with the Paris Agreement, while allowing renewable

technologies, and energy storage solutions, to advance to a level where energy provision is no longer reliant on coal, oil or gas. Currently, there are three technologies that can be implemented for the purpose of carbon capture; pre-combustion, oxy-fuel combustion and post-combustion.

### *1.3.2.1 PRE-COMBUSTION CAPTURE*

Pre-combustion capture involves the production of a concentrated stream of CO<sub>2</sub> and H<sub>2</sub>, where H<sub>2</sub> is burned as a fuel to generate only H<sub>2</sub>O as a product, and the CO<sub>2</sub> is separated prior to combustion<sup>19</sup>. This method has been suggested as the most effective approach to capturing CO<sub>2</sub> from coal powered sources, by partial oxidation of coal to synthesis Gas (syngas) via a gasification step, and further treating the gas mixture by oxidising carbon monoxide to CO<sub>2</sub> via the water gas shift reaction<sup>20</sup>. The subsequent separation is, therefore, between CO<sub>2</sub>/H<sub>2</sub> only, and proves to be easier than other separation mixtures, as there are strong differences in the chemical properties of the two species, such as polarisability, quadrupole moment, and kinetic diameter<sup>21</sup>. The high concentration of CO<sub>2</sub> in the flue gas is beneficial as it improves capture efficiency and lowers the energy penalties for regeneration of the sorbent<sup>20</sup>. Pre-combustion provides the benefit of flexibility in terms of the type of fuel used, including coal, natural gas, and biomass, as examples<sup>22</sup>. The combustion process is in-effect a carbonless process, and has the added advantage of performing the separation of impurities prior to combustion, which would improve fuel efficiency. However, the capital costs required to construct a power plant with integrated capture facilities would be high when compared with other technologies and, due to the capture plant being located within the body of the process, retrofitting of existing plants would be limited. The improvements gained on the regeneration efficiency could actually be negated due to efficiency losses from the shift reaction, as this process is endothermic<sup>23</sup>.

The use of natural gas as a fuel source is still in high demand, and plays a key role in global energy production. This has led suppliers to re-evaluate discovered gas reserves that contain large amounts of contaminants, which renders the gas economically unviable. CO<sub>2</sub> is often an impurity of natural gas which must first be removed before transport is possible, due to corrosion of pipelines. Its presence reduces the heating value of natural gas streams, and concentrations are often required to be less than 3 % before it can be used by the public. Therefore processing of gas streams (natural gas sweetening) using pre-combustion techniques is required to bring impurities of CO<sub>2</sub> and other acidic/sour gases to minimum levels<sup>24</sup>. Amine scrubbing (Section 1.3.3) is a possible technique for removal of CO<sub>2</sub> from natural gas; however methods involving porous media have also been studied. The presence of polar functional groups has been found to enhance the CO<sub>2</sub> capture ability of adsorbent materials due to the preference for the quadrupole moment of CO<sub>2</sub> over the non-polar CH<sub>4</sub> molecule<sup>25</sup>.

#### *1.3.2.2 OXY-FUEL COMBUSTION CAPTURE*

The process of oxy-fuel combustion involves the burning of fuel using a pure stream of O<sub>2</sub> instead of air<sup>20</sup>. This requires the separation of O<sub>2</sub>/N<sub>2</sub> prior to the combustion stage; the final flue gas has a high concentration of CO<sub>2</sub> allowing for easy separation from other flue gases. The process is suitable for retrofitting to existing power plants, assuming a recycle of CO<sub>2</sub> to the fuel burner is added to reduce the temperature of the flame to levels equal to air-fuel combustion conditions, eliminating the need for more robust construction materials<sup>19</sup>. The separation of N<sub>2</sub> reduces the possibility of NO<sub>x</sub> impurities within the exhaust stream, reducing the need for large treatment units<sup>19</sup>; however, the disadvantages of this technology lie in the processes required to separate O<sub>2</sub> and N<sub>2</sub>. The current technique used to purify and separate air

components is cryogenic distillation, used in the large scale commercial production of pure gases. The process is very resource intensive, requiring large amounts of energy for refrigeration of feed air to reduce its temperature to the boiling point of O<sub>2</sub>. Distillation of O<sub>2</sub> from N<sub>2</sub> proves difficult as their boiling points are relatively close (90.17 K and 77.35 K, respectively)<sup>21</sup> requiring stringent control of the temperature during separation. Other methods, such as pressure swing adsorption, are used with zeolites; however these are only suitable at scales smaller than those required for oxy-fuel<sup>19</sup>. With further research into solid sorbents, it may be possible to improve the efficiency of separation, making this method viable in the future.

### *1.3.2.3 POST-COMBUSTION CAPTURE*

Post-combustion capture is the separation of CO<sub>2</sub> from flue gases after combustion of a carbon fuel<sup>20</sup>. Post-combustion capture methods are easily retrofitted into existing plant designs, as the exhaust gases from the combustion process can be siphoned off to an additional unit for capture<sup>26</sup>. Several test facilities and pilot plants have been built for the study of post-combustion capture using solvent based methods, which provides a large body of knowledge<sup>27</sup>. With large amounts of research focussed on developing this technology, it is expected that the majority of early CCS projects will be post-combustion, with the World's first commercial scale CCS facility, Boundary Dam, started in 2014, capturing approximately 1 million metric tons of CO<sub>2</sub> per year<sup>28</sup>. However, the design of new unit operations for CO<sub>2</sub> capture can have a similar footprint to the existing power plant due to the limits of the current technologies used for capture<sup>22</sup>. As CO<sub>2</sub> is captured following combustion, the major components of the flue gas will be CO<sub>2</sub> and inert N<sub>2</sub> from air. However, the partial pressure of CO<sub>2</sub> within the flue gas is relatively low compared with other capture processes, and depends on the type of fuel used; natural gas (3-4% vol) or coal/oil (11-14% vol). This requires large volumes of gas to be treated and sorbents to have a strong chemical interaction with CO<sub>2</sub> in order to achieve high capture efficiencies. There are similarities in the physical properties of CO<sub>2</sub> and N<sub>2</sub>, both molecules having similar kinetic diameters (3.3 Å and 3.64-3.8 Å, respectively)<sup>21</sup>; CO<sub>2</sub> has a larger quadrupole moment making it possible to separate using chemical interactions, such as the Lewis acid-Lewis base chemistry exploited in amine scrubbing, described in Section 1.3.3.

### 1.3.3 AMINE SCRUBBING

The development of techniques used for large scale carbon capture stems from historical use of gas absorption processes which have been in use for more than 60 years within industrial processing<sup>25</sup>. Its use has been well studied for natural gas sweetening, where acid gases such as hydrogen sulphide (H<sub>2</sub>S) and carbon dioxide (CO<sub>2</sub>) are present within the crude mixture extracted from reservoirs, and must be removed to improve not only the odour of the fuel gas, but more importantly improves the heating content and reduces pipe corrosion during transport<sup>29</sup>. Many other industries use gas absorption as a means of purifying product or exhaust streams, a list of which is given by Yildirim *et al.*<sup>30</sup>. The process of absorption involves contacting a solvent with a flue gas which has impurities which are soluble (or chemically react) within the solvent, and the product components are insoluble or unreactive. For CO<sub>2</sub> removal from natural gas, or low concentration flue streams such as those from post-combustion processing, amine solutions are used due to their good selectivity for reaction with the acid gases.

#### 1.3.3.1 CHEMISTRY OF AMINE SCRUBBING

Aqueous alkanolamine solutions are currently considered the most feasible component for use in large scale CO<sub>2</sub> capture systems, with a number of commercially available absorption processes which could be designed for scale-up<sup>16</sup>. The molecules are a combination of hydrocarbon chains, with at least one hydroxyl group and one amino group, examples of which are shown in Figure 1.6<sup>29</sup>. Due to the acidity of CO<sub>2</sub>, strong reactions are found to occur with alkaline components, making the amino group responsible for absorption of the CO<sub>2</sub> molecules; the requirement of the hydroxyl groups is to improve the solubility of the alkanolamine in water, and reduce the vapour

pressure of the solution<sup>29</sup>. The smallest and most commonly studied amine<sup>17</sup> is monoethanolamine (MEA), a primary amine; secondary and tertiary amines are also considered to fine tune the properties of the solution.

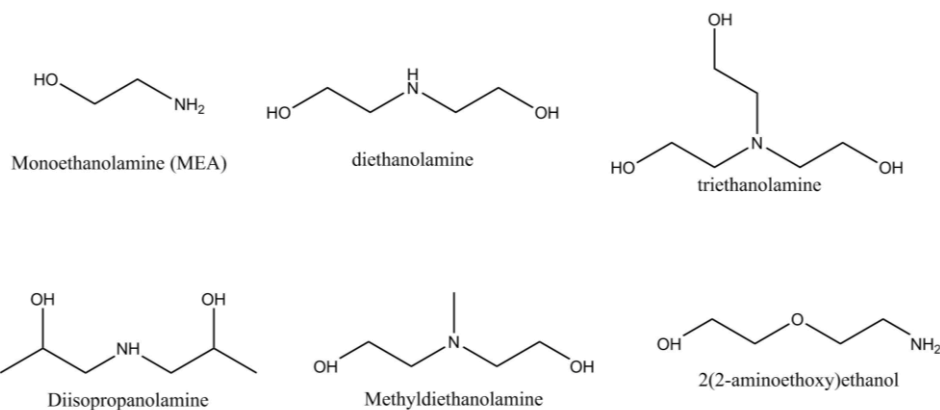
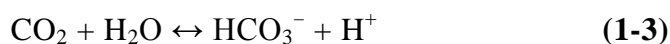


**Figure 1.6: Examples of Primary, Secondary and Tertiary alkanolamine structures used for CO<sub>2</sub> capture in amine scrubbing<sup>29</sup>**

The principal reaction, **(1-1)**, which occurs with primary amines is the formation of a carbamate ion with a CO<sub>2</sub> molecule, with other side reactions occurring with the amine and water shown in the equations below;



The product forms via a Lewis acid-Lewis base interaction, with the lone pair of electrons from the nitrogen atom donating to the carbon of CO<sub>2</sub> which has a positive dipole. Carbamates are stable in solution when formed by reaction using primary amines<sup>29</sup>, with tertiary amines not able to react through reaction **(1-1)** to form a carbamate, due to it being unable to undergo deprotonation. Therefore, the maximum capacity of CO<sub>2</sub> capture for primary amines is 0.5 mol CO<sub>2</sub> mol<sup>-1</sup> amine, giving a maximum possible uptake of 8 mmol g<sup>-1</sup> MEA. The capacity will be much less due to factors limiting the reaction, such as temperature and pressure, the amount of MEA

which is soluble in water, additional components use to prevent degradation of the solution of inhibit corrosion, and any recycled MEA which is still in a carbamate form with CO<sub>2</sub>. The capture capacity can be improved by using tertiary amines, as the formation of a carbamate is not possible. The nitrogen atom of the amine group has no hydrogen atoms bonded, therefore reaction with a CO<sub>2</sub> molecule through Equation (1-1) is not possible. With no free hydrogen atoms present in the reaction mixture, the second amine molecule required for Equation (1-2) is free to react with a second CO<sub>2</sub> molecule, therefore the maximum capture capacity possible from tertiary amines is 1 mol CO<sub>2</sub> mol<sup>-1</sup> amine. Limitations to using either secondary or tertiary amines arise from slower rates of reaction compared with primary amines, and lower selectivity for CO<sub>2</sub>, resulting in a much lower capture capacity than the theoretical 1 mol CO<sub>2</sub> mol<sup>-1</sup> amine<sup>31</sup>.

#### *1.3.3.2 PROCESS OF AMINE SCRUBBING*

Processing of the reaction is performed on industrial scale using an absorption and regeneration column as shown in Figure 1.7<sup>32</sup>, a typical description of the flow diagram is given below. Flue gas from the process is fed to an absorber column, where it is contacted with lean amine solvent being discharged down the column. Mass transfer limitations require the columns to be designed so that there is a large gas-liquid interface, therefore plates or packed beds are used and flow is counter-current to maximise mixing of the flue gas and solvent<sup>27</sup>. The treated gas is washed to remove any entrained solvent and is vented to the atmosphere. The CO<sub>2</sub> rich solvent is pumped to the regeneration tower, and is passed through a heat exchanger to transfer heat from the recycled lean solvent to the rich solvent, to bring it to temperatures close to the regeneration column temperature.



solutions must be considered, where MEA solutions are normally limited to concentrations up to 30 %, to avoid highly corrosive mixtures; the use of secondary and tertiary amines limits the corrosive ability of the solution, but suffers from lower capacities due to lower selectivity for CO<sub>2</sub>, therefore mixtures are also considered to obtain the best balance of properties from both types of solvent <sup>17</sup>.

Aside from the wealth of knowledge on amine scrubbing showing its use as a means of capturing CO<sub>2</sub>, there are numerous shortcomings which must be improved through developing new solvent mixtures, to make amine scrubbing a viable option for all capture processes. On-going research within the adsorption community has looked into the use of solid adsorbent materials which have appreciable and reversible uptake of CO<sub>2</sub> <sup>35</sup>. These adsorbents are capable of providing a means of lowering the energy penalty for regeneration, and providing large improvements on the capture capacity and selectivity for the process.

## 1.4 POROUS MATERIALS

### 1.4.1 ACTIVATED CARBONS

Carbons have been used extensively throughout history as adsorbent materials; historically charcoal has been used for the purpose of medical treatments of poisoning<sup>36</sup> and purification of drinking water. Currently, activated carbons are used domestically for the removal of colour, odour, and taste, as well as the removal of volatile organic components (VOCs) and inorganic impurities industrially. Activated carbons are considered a low cost adsorbent and widely available, due to their production methods.

The structure of activated carbon is an amorphous arrangement of carbon graphene sheets, which are randomly stacked together, giving rise to an internal porous structure. Around 85-95 % of the material is comprised of carbon atoms, with other elements such as hydrogen, oxygen and sulphur present as impurities in the carbon sheets<sup>37</sup>. Activated carbons are commercially produced from sources such as lignite, peat, wood and coconut shell<sup>38,39</sup>; the list is extensive, and large variation in properties can be seen between carbons derived from different sources, allowing a range of different adsorption conditions to be covered<sup>40</sup>. In addition to changing the precursor of the carbon, the method of synthesising the activated material can have a large impact on the properties of the final product<sup>41</sup>.

Two methods are most often used for the formation of activated carbons, which help to develop their internal porosity: physical and chemical activation<sup>42</sup>. Initially, the carbon precursor undergoes a carbonisation step, where it is heated in an inert atmosphere at temperatures below 1073 K to thermally decompose the structure and remove impurities. Physical activation of a carbon involves performing a partial

gasification of the structure using CO<sub>2</sub>, steam, or air at temperatures up to 1273 K<sup>38,42</sup>; chemical activation involves adding reagents to either of the steps above, allowing reduced temperatures to be used<sup>42</sup>. The processes used for synthesis of activated carbon materials, by taking a solid structure and developing porosity, create the amorphous nature of the material, and limit the methods of characterisation that can be used, compared with zeolites and metal-organic frameworks. Additionally, as the starting materials come from natural sources, the pore size, distribution, and shape of the final product can vary widely across samples<sup>43</sup>; generally speaking, activated carbons exhibit high levels of porosity, and have the advantage of high surface areas (reaching 1000 – 3000m<sup>2</sup>g<sup>-1</sup>) , resulting in large adsorption capacities<sup>43</sup>.

Within carbon capture processes, activated carbons can be treated to improve their affinity for CO<sub>2</sub>. The surface chemistry of a carbon material has a major impact on its adsorption capabilities; the presence of functional groups on the carbon surface, from heteroatoms, and the amount of delocalised electrons on the carbon sheets will influence the acidic or basic nature of the carbon material, and the overall performance of CO<sub>2</sub> adsorption<sup>44,45</sup>. Many studies on enhancing carbons for CO<sub>2</sub> adsorption have reported that surface modification with basic groups (ammonia, amines, etc.) will increase interactions with CO<sub>2</sub>, but can be at a cost of reducing the porosity<sup>46-51</sup>. Untreated carbons will have a much weaker interaction with CO<sub>2</sub>, from van der Waals forces, resulting in low adsorption at low pressure and high temperatures, however the large surface areas typically offered by activated carbons allow for large uptakes at high pressure; this will be reduced if the post-activation material has a high number of acidic surface groups, which will have the opposite effect to adding basic groups<sup>44</sup>.

## 1.4.2 ZEOLITES

Zeolites are naturally occurring porous crystalline materials, which have been comprehensively studied in the literature<sup>52</sup>. Over 40 natural zeolites have been discovered, but many more synthetic structures have been developed<sup>53</sup>. Synthetic zeolites have found extensive use in many systems for purification and gas separation<sup>35</sup>, industrial catalysis<sup>54</sup>, and are commonly used in the petrochemical and refining industries<sup>55</sup>.

The structure of all zeolites consists of a number of oxygen sharing  $[\text{SiO}_4]$  and  $[\text{AlO}_4]^-$  tetrahedra, forming an extended 3-dimensional framework<sup>56</sup>. The mixture of 4+ and 3+ silicon and aluminium ( $\text{Si}^{4+}$  and  $\text{Al}^{3+}$ ) cationic charges causes the entire framework to have an unbalanced negative charge; as such, cations of Group I and II elements are included during the formation of the material to counterbalance the charge<sup>35</sup>. The arrangement of  $[\text{SiO}_4]$  and  $[\text{AlO}_4]^-$  units produces a regularly repeating structure, which introduces voids that have regular, discrete sizes extending in 3-dimensions, where the cationic species reside; this clearly defines zeolites as having advantageous properties over carbons, which have irregular amorphous structures that cannot be characterised using crystallographic techniques.

The rigid framework of zeolites and their internal pore cavities make them effective materials to perform separations by size exclusion (molecular sieving). The uniform size and shape of the pores allows the material to exclude molecules that have larger dimensions than the pore size, resulting in differentiation between molecules that have similar chemical characteristics (hydrocarbon molecules), with zeolitic structures being capable of precisions  $<1 \text{ \AA}$ <sup>57</sup>. Pore sizes of zeolites can range from 5 to 12  $\text{\AA}$ <sup>35</sup>, therefore careful tuning of the pore size using, for example metal cation exchange<sup>35</sup>,

can make materials that are effective for the separation of CO<sub>2</sub>. This takes advantage of the quadrupole moment of the gas, therefore, gas-solid interactions can be enhanced through the negative charge of the framework and exchange with cationic species<sup>56</sup>; however, strong interactions with the surface can lead to chemisorption of the gas resulting in the formation of carbonate species, which are strongly bonded to the zeolite surface<sup>58</sup>, requiring regeneration temperatures around 573 K<sup>52</sup>, higher than those currently used in traditional absorption techniques.

Zeolites that have been studied for CO<sub>2</sub> adsorption have shown capacities of 0.15 – 5.5 mmol g<sup>-1</sup> (mmol CO<sub>2</sub> g<sup>-1</sup> of zeolite)<sup>56</sup>; zeolite 13X has been considered a benchmark material for CO<sub>2</sub> adsorption, with comparisons to many other new solid adsorbents being performed<sup>59</sup>. Zeolites can suffer from a lack of selectivity for CO<sub>2</sub> over other gases, which cannot be separated by virtue of their molecular sieving properties. With the presence of large quantities of N<sub>2</sub> within the flue gas stream of post-combustion processes, low CO<sub>2</sub>/N<sub>2</sub> selectivities have been observed<sup>60</sup> as the kinetic diameters of the two gases are very closely matched (3.3 Å and 3.6 Å respectively)<sup>53</sup>, and the presence of a weak quadrupole moment in nitrogen removes the possibility of selectivity by utilising the electric field of the zeolite structure<sup>61</sup>. The presence of water has also been observed to limit the adsorption capacity of zeolites<sup>56</sup>, as it preferentially binds to the cationic adsorption sites within the porous structure<sup>62</sup>.

Their consideration for use in carbon capture processes stems from their well-studied traits and previous use by the oil and gas industry; they are characterised as having high structural and thermal stability making them amenable to harsh conditions, which may occur during processing. Although zeolites will continue to be promising adsorbent materials for use in other types of gas separations (and other processes mentioned previously), carbon capture remains elusive due to the negative effects of

other common components within the flue gas streams of power plants. The limited number of components that form zeolites means there is limited scope for tuneable properties, due to the constraints of Si/Al-O chemistry. Newer, ordered materials have been developed which ‘swap’ the Si and Al ions of the structure with other elements, and these recently developed rigid materials <sup>63</sup> will continue to gather interest in a range of applications, including adsorption.

## 1.5 POROUS COORDINATION POLYMERS/METAL-ORGANIC FRAMEWORKS

The International Union of Pure and Applied Chemistry (IUPAC) defined Coordination Polymers (CPs) and Metal-Organic Frameworks (MOFs) as two distinct materials <sup>64</sup>:

“A coordination compound with a repeating coordination entity extending in 1, 2 or 3 dimensions”

And,

“A Metal-Organic Framework, abbreviated to MOF, is a Coordination Network with organic ligands containing potential voids”.

The use of these two terms has been interchangeable in the literature over the last 20 years to refer to compounds that exist as extended structures composed of a metal ion centre and organic bridging ligands, which form polymeric chains (1D), layers (2D), or frameworks (3D) <sup>65,66</sup>. MOFs have been suggested, in some circles, to define CPs with porosity <sup>65</sup> (as defined in the IUPAC recommendations), but other researchers have coined the phrase Porous Coordination Polymers (PCPs) <sup>67</sup>, thus continuing the ambiguity with regards to naming these compounds. For the purposes of this thesis, the terminology, MOFs, will be used exclusively to define any metal-organic coordinating compound that displays a repeating structural unit giving it a crystalline form, and the presence of sorption properties.

## 1.5.1 STRUCTURE AND PROPERTIES OF MOFS

As stated previously, MOFs are compounds containing both metal ions and organic bridging units, which form open frameworks with voids. Additional components, such as counter-ions and guest/template molecules, can be contained within the void spaces of the framework, and the structure may exhibit permanent porosity when the guest species are removed and the structural integrity is retained. The guests and templating molecules are usually molecules of the solvent used in synthesis of the material to dissolve the reactants; weak interactions with the framework allow these guests to be easily removed by vacuum at low temperatures, generating an open framework with accessible porosity. To be considered a MOF structure, the metal ions of the framework must extend in at least one dimension through the bridging ligands and these must contain at least one carbon atom between the coordinating atoms; this defines MOFs as distinct compounds from classical organometallics<sup>68</sup>. Overall, the extended structure is periodic and crystalline<sup>69</sup>, making them similar to zeolites, but having the ability to tune the structure, through careful selection of the type of metal and ligand<sup>70</sup>. These suggestions for designable materials were first applied by Hoskins and Robson in 1990<sup>70</sup>, but interest in tuneable structures did not gain momentum until the discovery of HKUST-1<sup>71</sup> and MOF-5<sup>72</sup> in 1999. The establishment of the term “reticular synthesis” by Yaghi *et al.*<sup>73</sup> paved the way for targeted structures that could be designed to have desired properties for a multitude of applications.

## 1.5.2 RETICULAR SYNTHESIS

Reticular synthesis is the design of predetermined structures through the use of rigid building blocks, which retain their structural integrity<sup>73</sup>. The resulting framework is easily defined by a set of secondary building units (SBUs), which are inorganic or organic fragments defined as nodes or linkers. With a large variety of SBUs, the number of possible crystal structures is vast; having prior knowledge of the coordination of a building block allows for overall control of the topology of the framework.

## 1.5.3 NODES

Nodes act as vertices at the connecting points between linkers. In order to produce 3-dimensional structures, this requires each node to have a high coordination number, making metal cations the most suitable choice in a MOF framework. Often the metal centre is formed of a transition metal, due to their versatility in forming a number of coordination modes as a consequence of variable oxidation states, which can help tailor the geometry of the resulting framework<sup>67</sup>. Figure 1.8 shows nodes with coordination numbers from 2 to 6, with 7 being the highest possible coordination value. This can give rise to a number of geometries such as linear, T-shaped, tetrahedral and octahedral, to name a few<sup>67</sup>. The SBUs of metal ions are often described as metal clusters, which utilise the coordinated atoms from the bridging linkers to form polyhedra.

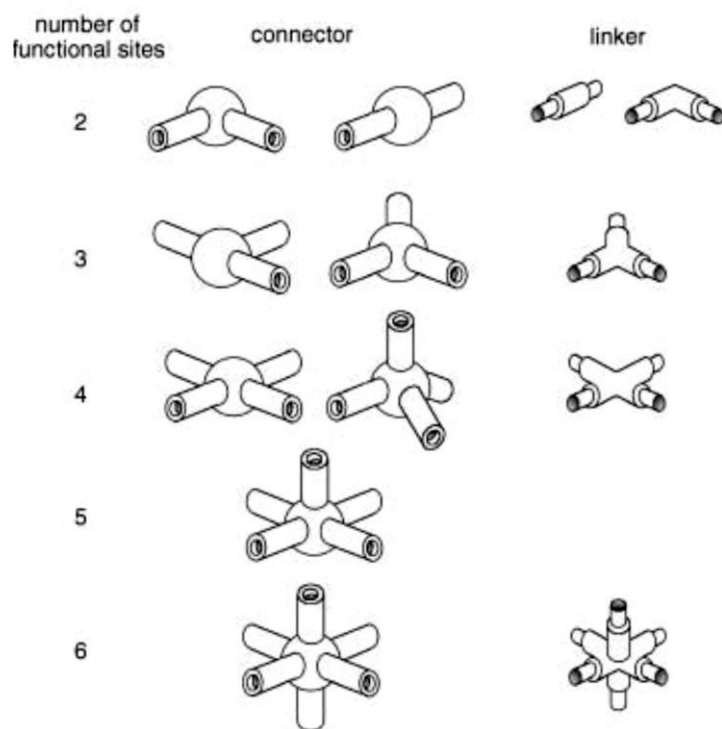


**Figure 1.8: Diagrammatical depiction of nodes and linkers having different functional sites which determines the overall coordination and geometry of the resulting MOF structure** <sup>67</sup>

In the example of MOF-5, the framework is composed of  $Zn^{2+}$  metal ions and 1,4-benzenedicarboxylate (BDC) organic ligands, as shown in Figure 1.9; the vertices of the structure can be described as  $Zn_4O$  tetrahedral clusters linked to O-C-O bonded atoms of the straight BDC units, giving the red SBU polyhedra, linked by straight slats <sup>73</sup>.

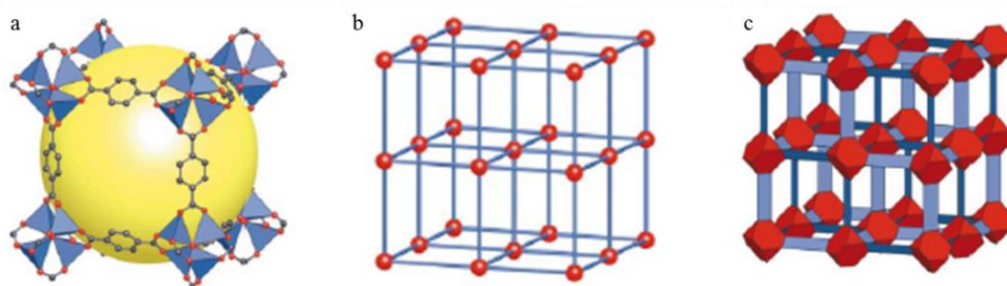


**Figure 1.9: Structure of MOF-5 shown in different topological descriptions. (a) gives the crystal structure showing  $Zn_4O$  tetrahedral units (blue polyhedra) which coordinate with the oxygen atoms (red) of the benzenedicarboxylate ligands (grey), (b) node and linker diagram showing metal clusters as spherical nodes (red) and ligands as rods (blue), (c) detailed node/linker diagram showing metal clusters as polyhedra (red) and ligands shown as slats (blue) which indicates ligand positioning within crystal structure** <sup>73</sup>

## 1.5.4 LINKERS

Linkers are formed from organic fragments of the MOF structure, and bridge between the nodes, forming an extended framework. Linkers must be able to coordinate to at least two metal centres; therefore, their structures can be multi-dentate and must have Lewis basic sites (such as a lone pair of electrons or negative charge) in order to form coordination bonds with the metal cation (Lewis acid), which are required to produce the resulting structure<sup>74</sup>. Their structures are typically rigid, planar molecules that give rise to linear bridges between nodes; however, more research has shown a variety of flexible, chiral and functionalised linkers, which give rise to interesting framework geometries and surface properties<sup>74</sup>. As a consequence of reticular synthesis, linkers chosen with similar coordination geometries, but having longer chain lengths or functionalities, will give rise to the same framework topology. This is best described by the isorecticular series, IRMOF, which is based on the MOF-5 (IRMOF-1) structure<sup>75</sup>. As shown in Figure 1.10, changes in the number of aromatic rings lead to a variation in pore size and pore volume, which demonstrates the ability of MOFs to be tailored to specific applications<sup>75</sup>. The result of changing the size and shape of these linkers, has led to the development of MOFs with accessible surface areas in excess of  $7000 \text{ m}^2 \text{ g}^{-1}$ <sup>76</sup>.

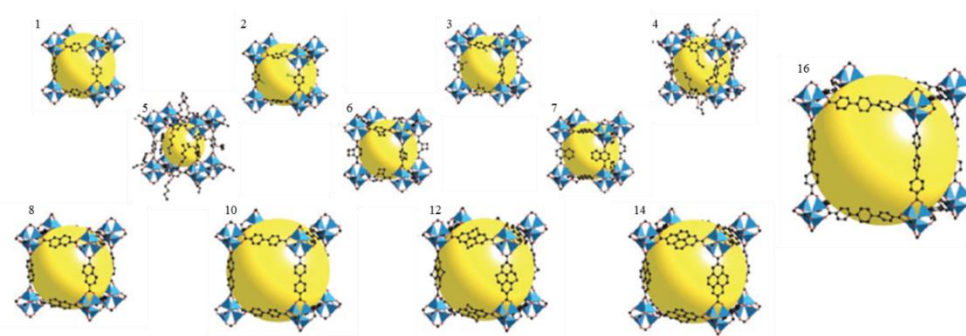


**Figure 1.10: Structures of 12 non-interpenetrated isorecticular MOFs (IRMOFs) showing increase in pore volume with increase in ligand length<sup>75</sup>**

## 1.5.5 LINKER TYPES

Typical donor moieties are carboxylate or heterocyclic nitrogen organics.

Examples of both types of ligands are shown in Figure 1.11.

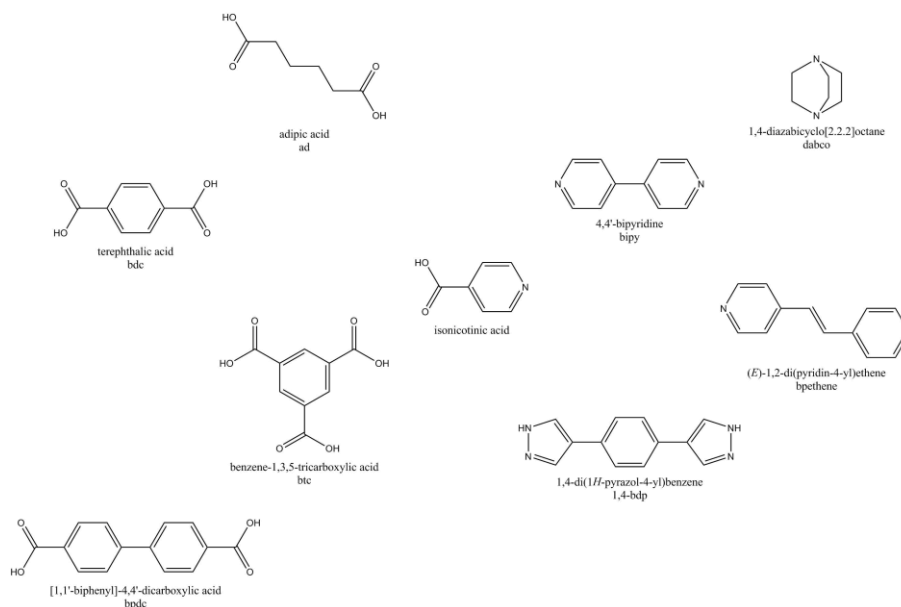


**Figure 1.11: Typical organic ligands used in the synthesis of Metal-Organic Frameworks.**

Neutral nitrogen donor ligands bond to metal ions via the sharing of lone pair electrons, resulting in a cationic framework, which requires anions for charge balance. These counter-ions can often block pore volume, leading to low adsorption capacities, however they have been shown to promote different network topologies<sup>77</sup>. N-donor ligands, such as the prototypical 4,4'-bipyridine have been shown to produce 3-dimensional frameworks that exhibit porosity<sup>78,79</sup>.

Oxygen donor ligands have been constructed from a variety of aliphatic and aromatic hydrocarbon structures, with carboxylate functional groups allowing for coordination to metal centres. Carboxylate ligands have the ability to form interesting geometries with metal centres, such as the  $Zn_4O$  tetrahedra in MOF-5 and the copper paddle-wheel motif in HKUST-1<sup>71,72</sup>. The ligands are anionic, carrying a negative charge on the oxygen donor atoms, therefore the overall charge of a MOF will be

neutral, with no additional counter ions required <sup>77</sup>. The synthesis of pure compounds can be hindered by the need for deprotonating reagents, such as trimethylamine, as a variety of coordination arrangements can be obtained <sup>80</sup>.

### 1.5.6 INTERPENETRATION

As described previously, the coordination of metal cations and ligands results in highly ordered structures, capable of generating spacious voids that can be beneficial for a number of applications. The voids, cavities, and channels present within MOFs are often filled with highly disordered solvent molecules <sup>81</sup>, which can be removed via heating or vacuum, leading to the either generation of a porous structure or the irreversible collapse of the framework <sup>82</sup>. However, it is possible that within these large void spaces, identical frameworks can form that become interwoven through the initial framework, forming an interpenetrated structure.

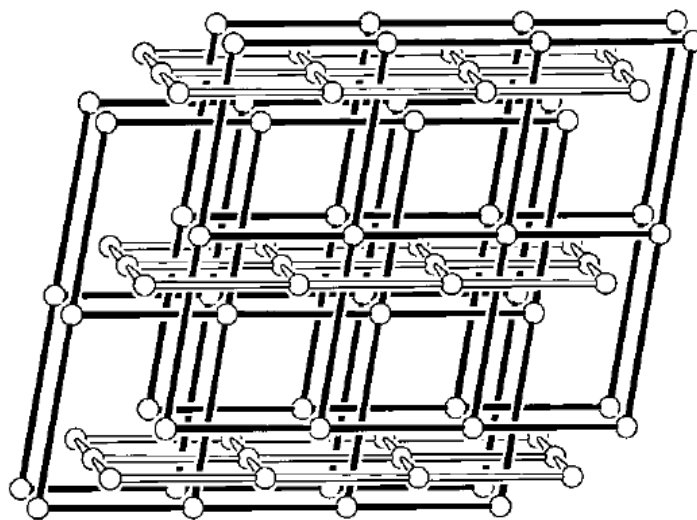


**Figure 1.12: Interpenetration of 2-dimensional nets to form a 3-dimensional structure. Separate nets form independently within the space between coordinated atoms of another net. Interpenetrated structures cannot be separated without collapse of the entire structure <sup>81</sup>**

Figure 1.12 shows the result of a 2-dimensional interpenetrated structure, showing how two identical networks are entwined, without any interaction between the structures, making them completely independent of one another. Additionally, attempting to remove the interpenetrated framework from the pore space will require the breaking of one or more of the framework bonds for all independent structures, resulting in complete breakdown of the framework <sup>81</sup>.

It has been observed that increasing the ligand length can increase the likelihood of interpenetration within a framework, with higher orders of interpenetration resulting from longer ligand molecules <sup>65</sup>. Interpenetration does not always prevent the formation of a porous structure <sup>83</sup>; interpenetrated MOFs have been synthesised with a pore size range that enhances selectivity for CO<sub>2</sub> adsorption at low pressures <sup>84</sup>, but such occupation of the void space can have disadvantageous effects on the maximum capacity <sup>52</sup>. The use of longer heterocyclic ligands has produced interpenetrated structures on a more frequent basis than similar carboxylate ligands, due to the more favourable  $\pi$ - $\pi$  interactions between the ligands <sup>77</sup>. A number of methods have been suggested for the control of interpenetration, such as changing the ligand design or including bulky functional groups <sup>65,85</sup>, in addition to altering reaction conditions, such as lowering the concentration of reactants or reducing temperature <sup>86</sup>.

### 1.5.7 FUNCTIONALISATION AND POST SYNTHETIC MODIFICATION

Similar to activated carbons or mesoporous silicas, interactions between MOFs and adsorptive molecules can be enhanced through the inclusion of functional groups on their surface. The presence of organic components allows for modification of the ligands and, in addition to the ability to tune the porous structure by choice of ligand length, MOFs can be used to suit a variety of applications.

Functionalisation of the MOF material is not limited to the ligand components. In materials where carboxylate linkers are used, full coordination of the metal is not always achieved, and partial coordination of guest species, such as solvent molecules, can occur. On activation of the material by vacuum or heating, the coordinated solvent molecules can be removed, leaving an unsaturated metal site, known as an open metal site<sup>87</sup>. This allows for Lewis acid sites to interact with the oxygen atom of CO<sub>2</sub> molecules in an 'end-on' fashion<sup>88</sup>. The strong potential of these sites increases adsorption at low pressure, making them beneficial for adsorption of CO<sub>2</sub> from flue gas streams; however this also increases the heat of adsorption<sup>25</sup>.

The incorporation of functional groups can be achieved by a variety of methods. In addition to using ligands already functionalised and reacting them directly with other reagents to form the functionalised MOF, the method of Post-Synthetic Modification (PSM) can be utilised to introduce functionality after formation of the original MOF material. This process has the benefit of introducing functional groups that, under typical reaction conditions, could result in their degradation, or coordination with the metal, rendering them useless in host-guest interactions<sup>89</sup>. Simple modifications can be performed via changing the anionic species present in balancing positively charged frameworks, as these inorganic species have been shown to improve adsorption interaction and selectivity<sup>90</sup>.

To this end, many researchers have utilised the addition of NH<sub>2</sub> functionalities to the framework surface to enhance interactions with CO<sub>2</sub>. Such surface groups have advantageous effects on the interaction with CO<sub>2</sub> molecules, via a Lewis acid-Lewis base interaction<sup>91-94</sup>. A unique method of incorporating a di-amine onto an open metal site via PSM of a MOF has yielded excellent properties for high capacity and selectivity of CO<sub>2</sub><sup>94</sup>. However, an amine functional group can increase the interaction strength of

the MOF with CO<sub>2</sub> which can result in a chemisorptive interaction, making the regeneration procedure more energy intensive. The incorporation of N,N'-dimethylethylenediamine (mmen) into H<sub>3</sub>[(Cu<sub>4</sub>Cl)<sub>3</sub>(BTTri)<sub>8</sub>] resulted in a heat of adsorption of -96 kJ mol<sup>-1</sup> <sup>93</sup>.

Post-synthetic ligand exchange has also been performed, where functionalised ligands have been used to replace the same non-functionalised analogues <sup>95</sup>. The addition of UiO-66 (Zr<sub>6</sub>O<sub>4</sub>(OH)<sub>4</sub>(BDC)<sub>6</sub>) to a solution of the functionalised ligand, BDC-NH<sub>2</sub>, resulted in ~50% exchange of BDC from the already formed framework <sup>96</sup>.

In addition to functionalising MOFs to improve surface properties, added functionalisation has been studied to improve the chemical stability of MOF structures, for example the addition of hydrophobic methyl groups to MOF-5 was found to improve its water stability compared with non-functionalised MOF-5 <sup>97</sup>.

### 1.5.8 FLEXIBILITY

In contrast to the structures of carbons and zeolites, the hybrid nature of MOFs allows for a significant amount of structural flexibility, through a number of different mechanisms <sup>98</sup>. Through the influence of external stimuli, movement of the coordinated bonds and ligands can result in changes in the physical properties of MOFs <sup>99,100</sup>. As seen in the MOF structure MIL-88, the changes in structure caused by flexibility can be as large as 200 % in terms of volume changes <sup>101</sup>. These flexible transitions occur via crystalline phases, in contrast to those seen in porous polymers which are amorphous <sup>99</sup>. The transitions to other crystalline phases occur via a number of different possible phase changes, which is dependent upon the MOF crystal and its structural connectivity

being analysed <sup>102</sup>. Figure 1.13 shows the different mechanisms by which structural transitions can occur <sup>99</sup>.

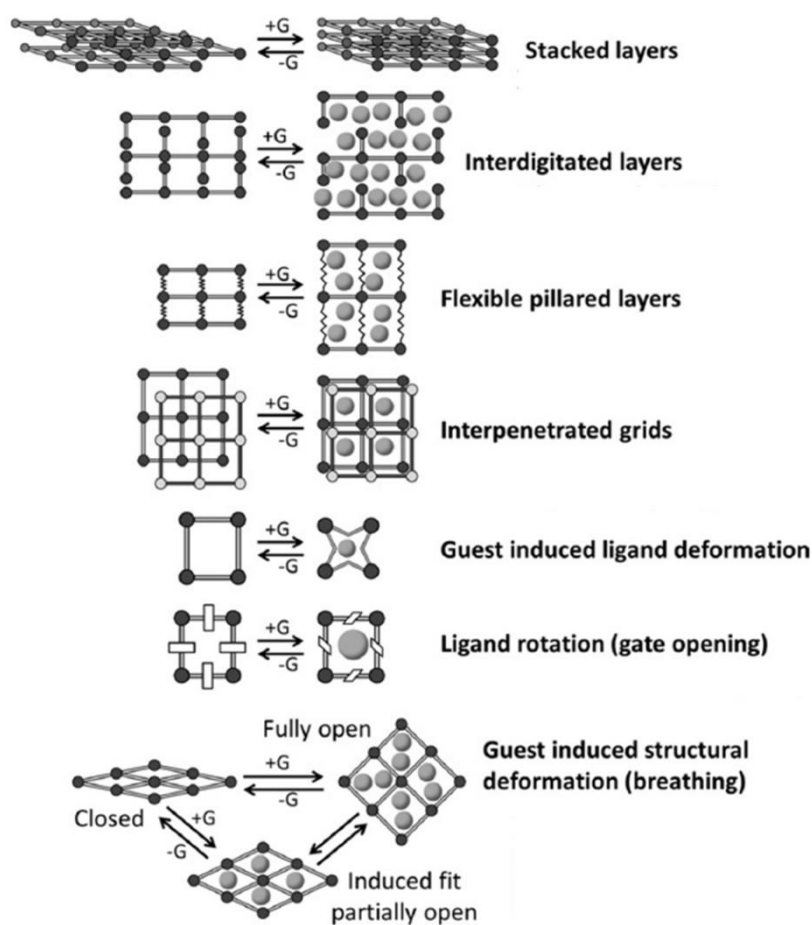


**Figure 1.13: Scheme of different mechanisms by which MOFs can show flexibility <sup>99</sup>**

2-dimensional stacked layers are metal-organic coordinated structures, which exhibit weak intermolecular interactions between adjacent layers. These can either be in a parallel stacked arrangement or staggered, and have been observed to interchange reversibly between the two structures via the removal of guest species <sup>103</sup>.

Interdigitated layers interact more strongly than stacked layer through the protrusions of coordinated groups around the metal centres of separate layers generating an inter-locking pattern of ridges and hollows. The framework reversibly expands upon guest inclusion, separating the inter-locking of the initial structure <sup>78,104,105</sup>.

Flexible pillared layers exhibit a reversible elongation and shortening of non-rigid ligands within the structure, which open to include guest species, and relax upon removal<sup>106</sup>.

The inclusion of interpenetration can often lead to smaller pore sizes and reduction of the adsorption capacity. However the introduction of guests to some frameworks have resulted in reversible change from a densely packed structure to one with open cavities, termed a 'sponge-like' behaviour<sup>105,107</sup>.

Changes in the guest species of some MOFs can lead to structural flexing by the ligands to change the pore size and shape to accommodate the new guest, resulting in changes in the unit cell axis lengths<sup>108</sup>.

Ligand rotation is the mechanism of guest adsorption through the flexing of a ligand which restricts part of the framework until a certain pressure is applied which instigates a gate-opening of the structure. Fairen-Jimenez *et al.*<sup>109</sup> noted the small windows of ZIF-8 could potentially allow for molecular sieving of larger molecules than the size of the pore window; however adsorption of species larger than the pore windows achieved large adsorption capacities, suggesting the presence of a structural change, which was investigated by simulations.

Guest-induced breathing of a MOF structure is one of the most highly studied flexible transitions, owing to the discovery of the MIL-53 structures<sup>110,111</sup>. The framework undergoes structural transformation between different narrow pore (np) and large pore (lp) forms. The structural changes have been characterised to occur as a flexing of both the organic ligand, and the inorganic metal SBU, by alteration of the angles between the metals and coordinated oxygens<sup>100</sup>; this is a completely different

mechanism to the previously stated transitions, which do not typically undergo flexing of the SBU unit.

The impact of flexibility on the adsorption properties of MOFs has been studied in a number of review articles<sup>82,112,113</sup>. Analysis of the isotherm of a gas can generate unusual 'steps' in the isotherm, which makes classification to standard isotherms impractical. It has been suggested that use of *In-situ* X-ray diffraction is necessary for unequivocal determination of the structural changes in a MOF material<sup>114</sup>, however analysis of adsorption isotherm data gives information regarding the presence of structural changes in a material, if not their exact mechanism.

## 1.6 REFERENCES

1. United Nations Framework Convention on Climate Change. *Landmark Climate Change Agreement to Enter into Force*, <<http://newsroom.unfccc.int/unfccc-newsroom/landmark-climate-change-agreement-to-enter-into-force/>> (2016), *Accessed on: 12/10/2016*
2. United Nations Framework Convention on Climate Change. *The Paris Agreement*, <[http://unfccc.int/paris\\_agreement/items/9485.php](http://unfccc.int/paris_agreement/items/9485.php)> (2016), *Accessed on: 12/10/2016*
3. Latvian Presidency of the Council of the European Union. *Intended Nationally Determined Contribution of the EU and its Member States*. (2015), <<http://www4.unfccc.int/ndcregistry/PublishedDocuments/European%20Union%20First/LV-03-06-EU%20INDC.pdf>>, *Accessed on: 24/04/2017*.
4. United Nations Framework Convention on Climate Change. *The Essential Background*, <[http://unfccc.int/essential\\_background/items/6031.php](http://unfccc.int/essential_background/items/6031.php)> (2016), *Accessed on: 13/10/2016*
5. Clark, D. *Has the Kyoto protocol made any difference to carbon emissions?* , <<https://www.theguardian.com/environment/blog/2012/nov/26/kyoto-protocol-carbon-emissions>> (2012), *Accessed on: 30/05/2017*
6. Intergovernmental Panel on Climate Change. *Intergovernmental Panel on Climate Change (IPCC) Fifth Assessment Report: Climate Change 2014*. (2014).
7. Intergovernmental Panel on Climate Change. (eds T.F. Stocker *et al.*) *1535* (Cambridge University Press, Cambridge, United Kingdom and New York, NY, USA, 2013).
8. Jouzel, J., Masson-Delmotte, V., Cattani, O., Dreyfus, G., Falourd, S., Hoffmann, G., Minster, B., Nouet, J., Barnola, J. M., Chappellaz, J., Fischer, H., Gallet, J. C., Johnsen, S., Leuenberger, M., Loulergue, L., Luethi, D., Oerter, H., Parrenin, F., Raisbeck, G., Raynaud, D., Schilt, A., Schwander, J., Selmo, E., Souchez, R., Spahni, R., Stauffer, B., Steffensen, J. P., Stenni, B., Stocker, T. F., Tison, J. L., Werner, M. & Wolff, E. W. *Orbital and millennial Antarctic climate variability over the past 800,000 years. Science* **317**, 793-6 (2007).
9. Hansen, J., Ruedy, R., Sato, M. & Lo, K. *Global Surface Temperature Change. Reviews of Geophysics* **48**, n/a-n/a (2010).
10. GISTEMP Team. *GISS Surface Temperature Analysis (GISTEMP)*, <<http://data.giss.nasa.gov/gistemp/>> ( 2016), *Accessed on: 14<sup>th</sup> Oct/2016*
11. Holloway, A. M. & Wayne, R. P. *Atmospheric Chemistry*. (The Royal Society of Chemistry, 2010).
12. National Renewable Energy Laboratory. *Solar Spectral Irradiance: ASTM G-173*, <<http://rredc.nrel.gov/solar/spectra/am1.5/ASTMG173/ASTMG173.html>> (*Accessed on: 15/11/2016*)

13. Hobbs, P. V. *Introduction to Atmospheric Chemistry*. (Cambridge University Press, 2000).
14. Graedel, T. E. & Crutzen, P. J. *Atmospheric Change: An Earth System Perspective*. (W. H. Freeman, 1993).
15. International Energy Agency. Key CO<sub>2</sub> Emissions Trends Excerpt from: CO<sub>2</sub> Emissions from Fuel Combustion. (2016), <<http://www.iea.org/publications/freepublications/publication/KeyCO2EmissionsTrends.pdf>>, Accessed on: 24/04/2017.
16. Metz, B., Davidson, O., de Coninck, H., Loos, M. & [Working Group III of the Intergovernmental Panel on Climate Change]. *IPCC: Special Report on Carbon Dioxide Capture and Storage*. (Cambridge University Press, 2005).
17. Yang, H., Xu, Z., Fan, M., Gupta, R., Slimane, R. B., Bland, A. E. & Wright, I. Progress in carbon dioxide separation and capture: A review. *Journal of Environmental Sciences-China* **20**, 14-27 (2008).
18. Loughhead, J. *Securing the UK's Energy Future: the role of gas*, <<https://decc.blog.gov.uk/2015/12/15/securing-the-uks-energy-future-the-role-of-gas/>> (2015), Accessed on: 24/04/2017
19. Sumida, K., Rogow, D. L., Mason, J. A., McDonald, T. M., Bloch, E. D., Herm, Z. R., Bae, T.-H. & Long, J. R. Carbon Dioxide Capture in Metal-Organic Frameworks. *Chemical Reviews* **112**, 724-81 (2012).
20. Olajire, A. A. CO<sub>2</sub> capture and separation technologies for end-of-pipe applications – A review. *Energy* **35**, 2610-28 (2010).
21. Li, J.-R., Kuppler, R. J. & Zhou, H.-C. Selective gas adsorption and separation in metal-organic frameworks. *Chemical Society Reviews* **38**, 1477-504 (2009).
22. Haszeldine, R. S. Carbon Capture and Storage: How Green Can Black Be? *Science* **325**, 1647-52 (2009).
23. Gibbins, J. & Chalmers, H. Carbon capture and storage. *Energy Policy* **36**, 4317-22 (2008).
24. Rufford, T. E., Smart, S., Watson, G. C. Y., Graham, B. F., Boxall, J., Diniz da Costa, J. C. & May, E. F. The removal of CO<sub>2</sub> and N<sub>2</sub> from natural gas: A review of conventional and emerging process technologies. *Journal of Petroleum Science and Engineering* **94-95**, 123-54 (2012).
25. Bae, Y.-S. & Snurr, R. Q. Development and Evaluation of Porous Materials for Carbon Dioxide Separation and Capture. *Angewandte Chemie-International Edition* **50**, 11586-96 (2011).
26. Songolzadeh, M., Ravanchi, M. T. & Soleimani, M. Carbon dioxide capture and storage: a general review on adsorbents. *World Academy of Science, Engineering and Technology* **70**, 225-32 (2012).

27. MacDowell, N., Florin, N., Buchard, A., Hallett, J., Galindo, A., Jackson, G., Adjiman, C. S., Williams, C. K., Shah, N. & Fennell, P. An overview of CO<sub>2</sub> capture technologies. *Energy & Environmental Science* **3**, 1645-69 (2010).
28. Stéphenne, K. Start-up of World's First Commercial Post-combustion Coal Fired CCS Project: Contribution of Shell Cansolv to SaskPower Boundary Dam ICCS Project. *Energy Procedia* **63**, 6106-10 (2014).
29. Kohl, A. L. & Nielsen, R. B. in *Gas Purification (Fifth Edition)* pp. 40-186 (Gulf Professional Publishing, 1997).
30. Yildirim, O., Kiss, A. A., Huser, N., Lessmann, K. & Kenig, E. Y. Reactive absorption in chemical process industry: A review on current activities. *Chemical Engineering Journal* **213**, 371-91 (2012).
31. Boot-Handford, M. E., Abanades, J. C., Anthony, E. J., Blunt, M. J., Brandani, S., Mac Dowell, N., Fernandez, J. R., Ferrari, M. C., Gross, R., Hallett, J. P., Haszeldine, R. S., Heptonstall, P., Lyngfelt, A., Makuch, Z., Mangano, E., Porter, R. T. J., Pourkashanian, M., Rochelle, G. T., Shah, N., Yao, J. G. & Fennell, P. S. Carbon capture and storage update. *Energy & Environmental Science* **7**, 130-89 (2014).
32. Abu-Zahra, M. R. M., Schneiders, L. H. J., Niederer, J. P. M., Feron, P. H. M. & Versteeg, G. F. CO<sub>2</sub> capture from power plants. Part I. A parametric study of the technical-performance based on monoethanolamine. *International Journal of Greenhouse Gas Control* **1**, 37-46 (2007).
33. Pirngruber, G. D. & Llewellyn, P. L. in *Metal-Organic Frameworks* pp. 99-119 (Wiley-VCH Verlag GmbH & Co. KGaA, 2011).
34. Rochelle, G. T. Amine Scrubbing for CO<sub>2</sub> Capture. *Science* **325**, 1652-4 (2009).
35. Samanta, A., Zhao, A., Shimizu, G. K. H., Sarkar, P. & Gupta, R. Post-Combustion CO<sub>2</sub> Capture Using Solid Sorbents: A Review. *Industrial & Engineering Chemistry Research* **51**, 1438-63 (2012).
36. Derlet, R. W. & Albertson, T. E. Activated Charcoal—Past, Present and Future. *Western Journal of Medicine* **145**, 493-6 (1986).
37. Roy, G. M. *Activated Carbon Applications in the Food and Pharmaceutical Industries*. (Technomic Publishing Company Inc., 1995).
38. Yang, T. & Lua, A. C. Textural and chemical properties of zinc chloride activated carbons prepared from pistachio-nut shells. *Materials Chemistry and Physics* **100**, 438-44 (2006).
39. Marsh, F., Rodriguez-Reinoso, F. *Activated Carbon*. (Elsevier Ltd, 2006).
40. Rodríguez-Reinoso, F. & Molina-Sabio, M. Activated carbons from lignocellulosic materials by chemical and/or physical activation: an overview. *Carbon* **30**, 1111-8 (1992).

41. Sircar, S., Golden, T. C. & Rao, M. B. Activated carbon for gas separation and storage. *Carbon* **34**, 1-12 (1996).
42. Ahmadpour, A. & Do, D. D. The preparation of active carbons from coal by chemical and physical activation. *Carbon* **34**, 471-9 (1996).
43. Morris, R. E. & Wheatley, P. S. Gas storage in nanoporous materials. *Angewandte Chemie-International Edition* **47**, 4966-81 (2008).
44. Silvestre-Albero, J. & Rodríguez-Reinoso, F. in *Novel Carbon Adsorbents* pp. 583-603 (Elsevier, 2012).
45. Lee, Z. H., Lee, K. T., Bhatia, S. & Mohamed, A. R. Post-combustion carbon dioxide capture: Evolution towards utilization of nanomaterials. *Renewable & Sustainable Energy Reviews* **16**, 2599-609 (2012).
46. Pevida, C., Drage, T. & Snape, C. E. Silica-templated melamine-formaldehyde resin derived adsorbents for CO<sub>2</sub> capture. *Carbon* **46**, 1464-74 (2008).
47. Plaza, M. G., Pevida, C., Arenillas, A., Rubiera, F. & Pis, J. J. CO<sub>2</sub> capture by adsorption with nitrogen enriched carbons. *Fuel* **86**, 2204-12 (2007).
48. Pevida, C., Plaza, M., Arias, B., Feroso, J., Rubiera, F. & Pis, J. Surface modification of activated carbons for CO<sub>2</sub> capture. *Applied Surface Science* **254**, 7165-72 (2008).
49. Sevilla, M., Valle-Vigón, P. & Fuertes, A. B. N-Doped Polypyrrole-Based Porous Carbons for CO<sub>2</sub> Capture. *Advanced Functional Materials* **21**, 2781-7 (2011).
50. Bezerra, D. P., Oliveira, R. S., Vieira, R. S., Cavalcante Jr, C. L. & Azevedo, D. C. Adsorption of CO<sub>2</sub> on nitrogen-enriched activated carbon and zeolite 13X. *Adsorption* **17**, 235-46 (2011).
51. Hao, G. P., Li, W. C., Qian, D. & Lu, A. H. Rapid Synthesis of Nitrogen-Doped Porous Carbon Monolith for CO<sub>2</sub> Capture. *Advanced Materials* **22**, 853-7 (2010).
52. D'Alessandro, D. M., Smit, B. & Long, J. R. Carbon Dioxide Capture: Prospects for New Materials. *Angewandte Chemie-International Edition* **49**, 6058-82 (2010).
53. Aguilar-Armenta, G., Hernandez-Ramirez, G., Flores-Loyola, E., Ugarte-Castaneda, A., Silva-Gonzalez, R., Tabares-Munoz, C., Jimenez-Lopez, A. & Rodriguez-Castellon, E. Adsorption Kinetics of CO<sub>2</sub>, O<sub>2</sub>, N<sub>2</sub>, and CH<sub>4</sub> in Cation-Exchanged Clinoptilolite. *The Journal of Physical Chemistry B* **105**, 1313-9 (2001).
54. Corma, A. From microporous to mesoporous molecular sieve materials and their use in catalysis. *Chemical Reviews* **97**, 2373-419 (1997).
55. Vermeiren, W. & Gilson, J. P. Impact of Zeolites on the Petroleum and Petrochemical Industry. *Topics in Catalysis* **52**, 1131-61 (2009).
56. Bonenfant, D., Kharoune, M., Niquette, P., Mimeault, M. & Hausler, R. Advances in principal factors influencing carbon dioxide adsorption on zeolites. *Science and Technology of Advanced Materials* **9** (2008).

57. Davis, M. E. & Lobo, R. F. Zeolite and Molecular-Sieve Synthesis. *Chemistry of Materials* **4**, 756-68 (1992).
58. Wang, Q., Luo, J., Zhong, Z. & Borgna, A. CO<sub>2</sub> capture by solid adsorbents and their applications: current status and new trends. *Energy & Environmental Science* **4**, 42-55 (2011).
59. Bae, T.-H., Hudson, M. R., Mason, J. A., Queen, W. L., Dutton, J. J., Sumida, K., Micklash, K. J., Kaye, S. S., Brown, C. M. & Long, J. R. Evaluation of cation-exchanged zeolite adsorbents for post-combustion carbon dioxide capture. *Energy & Environmental Science* **6**, 128-38 (2013).
60. Sayari, A., Belmabkhout, Y. & Serna-Guerrero, R. Flue gas treatment via CO<sub>2</sub> adsorption. *Chemical Engineering Journal* **171**, 760-74 (2011).
61. Breck, D. W. *Zeolite molecular sieves: structure, chemistry, and use*. (R.E. Krieger, 1984).
62. Li, G., Xiao, P., Webley, P., Zhang, J., Singh, R. & Marshall, M. Capture of CO<sub>2</sub> from high humidity flue gas by vacuum swing adsorption with zeolite 13X. *Adsorption* **14**, 415-22 (2008).
63. Davis, M. E. Ordered porous materials for emerging applications. *Nature* **417**, 813-21 (2002).
64. Batten, S. R., Champness, N. R., Chen, X.-M., Garcia-Martinez, J., Kitagawa, S., Ohrstrom, L., O'Keeffe, M., Suh, M. P. & Reedijk, J. Terminology of metal-organic frameworks and coordination polymers (IUPAC Recommendations 2013). *Pure and Applied Chemistry* **85**, 1715-24 (2013).
65. James, S. L. Metal-organic frameworks. *Chemical Society Reviews* **32**, 276-88 (2003).
66. Ferey, G. Hybrid porous solids: past, present, future. *Chemical Society Reviews* **37**, 191-214 (2008).
67. Kitagawa, S., Kitaura, R. & Noro, S. Functional porous coordination polymers. *Angewandte Chemie-International Edition* **43**, 2334-75 (2004).
68. Janiak, C. Engineering coordination polymers towards applications. *Dalton Transactions*, 2781-804 (2003).
69. Rowsell, J. L. C. & Yaghi, O. M. Metal-organic frameworks: a new class of porous materials. *Microporous and Mesoporous Materials* **73**, 3-14 (2004).
70. Hoskins, B. F. & Robson, R. Design and Construction of a New Class of Scaffolding-Like Materials Comprising Infinite Polymeric Frameworks OF 3D-Linked Molecular Rods - a Reappraisal of the Zn(CN)<sub>2</sub> and Cd(CN)<sub>2</sub> Structures and the Synthesis and Structure of the Diamond-Related Frameworks [N(CH<sub>3</sub>)<sub>4</sub>][Cu<sup>I</sup>Zn<sup>II</sup>(CN)<sub>4</sub>] and Cu<sup>I</sup>[4,4',4'',4'''-Tetracyanotetraphenylmethane]BF<sub>4</sub>.x C<sub>6</sub>H<sub>5</sub>NO<sub>2</sub>. *Journal of the American Chemical Society* **112**, 1546-54 (1990).

71. Chui, S. S. Y., Lo, S. M. F., Charmant, J. P. H., Orpen, A. G. & Williams, I. D. A chemically functionalizable nanoporous material  $\text{Cu}_3(\text{TMA})_2(\text{H}_2\text{O})_3(\text{n})$ . *Science* **283**, 1148-50 (1999).
72. Li, H., Eddaoudi, M., O'Keeffe, M. & Yaghi, O. M. Design and synthesis of an exceptionally stable and highly porous metal-organic framework. *Nature* **402**, 276-9 (1999).
73. Yaghi, O. M., O'Keeffe, M., Ockwig, N. W., Chae, H. K., Eddaoudi, M. & Kim, J. Reticular synthesis and the design of new materials. *Nature* **423**, 705-14 (2003).
74. Robin, A. Y. & Fromm, K. M. Coordination Polymer Networks with O- and N-donors: What They Are, Why and How They Are Made. *Coordination Chemistry Reviews* **250**, 2127-57 (2006).
75. Eddaoudi, M., Kim, J., Rosi, N., Vodak, D., Wachter, J., O'Keeffe, M. & Yaghi, O. M. Systematic design of pore size and functionality in isorecticular MOFs and their application in methane storage. *Science* **295**, 469-72 (2002).
76. Farha, O. K., Eryazici, I., Jeong, N. C., Hauser, B. G., Wilmer, C. E., Sarjeant, A. A., Snurr, R. Q., Nguyen, S. T., Yazaydin, A. O. & Hupp, J. T. Metal-Organic Framework Materials with Ultrahigh Surface Areas: Is the Sky the Limit? *Journal of the American Chemical Society* **134**, 15016-21 (2012).
77. Aakeroy, C. B., Champness, N. R. & Janiak, C. Recent advances in crystal engineering. *CrystEngComm* **12**, 22-43 (2010).
78. Fletcher, A. J., Cussen, E. J., Prior, T. J., Rosseinsky, M. J., Kepert, C. J. & Thomas, K. M. Adsorption dynamics of gases and vapors on the nanoporous metal organic framework material  $\text{Ni}_2(4,4\text{'-bipyridine})_3(\text{NO}_3)_4$ : Guest modification of host sorption behavior. *Journal of the American Chemical Society* **123**, 10001-11 (2001).
79. Noro, S., Kitagawa, S., Kondo, M. & Seki, K. A new, methane adsorbent, porous coordination polymer  $\{\text{CuSiF}_6(4,4\text{'-bipyridine})_2\}(\text{n})$ . *Angewandte Chemie-International Edition* **39**, 2082-4 (2000).
80. Yaghi, O. M., Davis, C. E., Li, G. M. & Li, H. L. Selective guest binding by tailored channels in a 3-D porous zinc(II)-benzenetricarboxylate network. *Journal of the American Chemical Society* **119**, 2861-8 (1997).
81. Batten, S. R. & Robson, R. Interpenetrating nets: Ordered, periodic entanglement. *Angewandte Chemie-International Edition* **37**, 1460-94 (1998).
82. Horike, S., Shimomura, S. & Kitagawa, S. Soft porous crystals. *Nature Chemistry* **1**, 695-704 (2009).
83. Reineke, T. M., Eddaoudi, M., Moler, D., O'Keeffe, M. & Yaghi, O. M. Large free volume in maximally interpenetrating networks: The role of secondary building units exemplified by  $\text{Tb}_2(\text{ADB})_3[(\text{CH}_3)_2\text{SO}]_4 \cdot 16[(\text{CH}_3)_2\text{SO}]$ . *Journal of the American Chemical Society* **122**, 4843-4 (2000).

84. Yao, Q., Su, J., Cheung, O., Liu, Q., Hedin, N. & Zou, X. Interpenetrated metal-organic frameworks and their uptake of CO<sub>2</sub> at relatively low pressures. *Journal of Materials Chemistry* **22**, 10345-51 (2012).
85. Prasad, T. K. & Suh, M. P. Control of Interpenetration and Gas-Sorption Properties of Metal-Organic Frameworks by a Simple Change in Ligand Design. *Chemistry-a European Journal* **18**, 8673-80 (2012).
86. Jiang, H. L., Makal, T. A. & Zhou, H. C. Interpenetration control in metal-organic frameworks for functional applications. *Coordination Chemistry Reviews* **257**, 2232-49 (2013).
87. Campbell, C., Ferreira-Rangel, C. A., Fischer, M., Gomes, J. R. B. & Jorge, M. A. Transferable Model for Adsorption in MOFs with Unsaturated Metal Sites. *The Journal of Physical Chemistry C* **121**, 441-58 (2017).
88. Dietzel, P. D. C., Johnsen, R. E., Fjellvag, H., Bordiga, S., Groppo, E., Chavan, S. & Blom, R. Adsorption properties and structure of CO<sub>2</sub> adsorbed on open coordination sites of metal-organic framework Ni<sub>2</sub>(dhtp) from gas adsorption, IR spectroscopy and X-ray diffraction. *Chemical Communications*, 5125-7 (2008).
89. Cohen, S. M. Postsynthetic Methods for the Functionalization of Metal–Organic Frameworks. *Chemical Reviews* **112**, 970-1000 (2012).
90. Forrest, K. A., Pham, T., Hogan, A., McLaughlin, K., Tudor, B., Nugent, P., Burd, S. D., Mullen, A., Cioce, C. R., Wojtas, L., Zaworotko, M. J. & Space, B. Computational Studies of CO<sub>2</sub> Sorption and Separation in an Ultramicroporous Metal-Organic Material. *Journal of Physical Chemistry C* **117**, 17687-98 (2013).
91. Wang, X., Li, H. & Hou, X.-J. Amine-Functionalized Metal Organic Framework as a Highly Selective Adsorbent for CO<sub>2</sub> over CO. *Journal of Physical Chemistry C* **116**, 19814-21 (2012).
92. Vaidhyanathan, R., Iremonger, S. S., Dawson, K. W. & Shimizu, G. K. H. An amine-functionalized metal organic framework for preferential CO<sub>2</sub> adsorption at low pressures. *Chemical Communications*, 5230-2 (2009).
93. McDonald, T. M., D'Alessandro, D. M., Krishna, R. & Long, J. R. Enhanced carbon dioxide capture upon incorporation of N,N'-dimethylethylenediamine in the metal-organic framework CuBTTri. *Chemical Science* **2**, 2022-8 (2011).
94. McDonald, T. M., Lee, W. R., Mason, J. A., Wiers, B. M., Hong, C. S. & Long, J. R. Capture of Carbon Dioxide from Air and Flue Gas in the Alkylamine-Appended Metal-Organic Framework mmen-Mg<sub>2</sub>(dobpdc). *Journal of the American Chemical Society* **134**, 7056-65 (2012).
95. Kim, M. & Cohen, S. M. Discovery, development, and functionalization of Zr(IV)-based metal-organic frameworks. *CrystEngComm* **14**, 4096-104 (2012).
96. Kim, M., Cahill, J. F., Su, Y. X., Prather, K. A. & Cohen, S. M. Postsynthetic ligand exchange as a route to functionalization of 'inert' metal-organic frameworks. *Chemical Science* **3**, 126-30 (2012).

97. Yang, J., Grzech, A., Mulder, F. M. & Dingemans, T. J. Methyl modified MOF-5: a water stable hydrogen storage material. *Chemical Communications* **47**, 5244-6 (2011).
98. Férey, G. & Serre, C. Large breathing effects in three-dimensional porous hybrid matter: facts, analyses, rules and consequences. *Chemical Society Reviews* **38**, 1380-99 (2009).
99. Llewellyn, P., Maurin, G. & Rouquerol, J. in *Adsorption by Powders and Porous Solids (Second Edition)* pp. 565-610 (Academic Press, 2014).
100. Schneemann, A., Bon, V., Schwedler, I., Senkowska, I., Kaskel, S. & Fischer, R. A. Flexible metal-organic frameworks. *Chemical Society Reviews* **43**, 6062-96 (2014).
101. Serre, C., Mellot-Draznieks, C., Surblé, S., Audebrand, N., Filinchuk, Y. & Férey, G. Role of Solvent-Host Interactions That Lead to Very Large Swelling of Hybrid Frameworks. *Science* **315**, 1828 (2007).
102. Kitagawa, S. & Uemura, K. Dynamic porous properties of coordination polymers inspired by hydrogen bonds. *Chemical Society Reviews* **34**, 109-19 (2005).
103. Li, D. & Kaneko, K. Hydrogen bond-regulated microporous nature of copper complex-assembled microcrystals. *Chemical Physics Letters* **335**, 50-6 (2001).
104. Fletcher, A. J., Cussen, E. J., Bradshaw, D., Rosseinsky, M. J. & Thomas, K. M. Adsorption of gases and vapors on nanoporous  $\text{Ni}_2(4,4'\text{-bipyridine})_3(\text{NO}_3)_4$  metal-organic framework materials templated with methanol and ethanol: Structural effects in adsorption kinetics. *Journal of the American Chemical Society* **126**, 9750-9 (2004).
105. Kitaura, R., Seki, K., Akiyama, G. & Kitagawa, S. Porous coordination-polymer crystals with gated channels specific for supercritical gases. *Angewandte Chemie-International Edition* **42**, 428-31 (2003).
106. Kitaura, R., Fujimoto, K., Noro, S., Kondo, M. & Kitagawa, S. A pillared-layer coordination polymer network displaying hysteretic sorption:  $\text{Cu}_2(\text{pzdc})_2(\text{dpyg})_n$  (pzdc = pyrazine-2,3-dicarboxylate; dpyg=1,2-di(4-pyridyl)glycol). *Angewandte Chemie-International Edition* **41**, 133-5 (2002).
107. Carlucci, L., Ciani, G., Moret, M., Proserpio, D. M. & Rizzato, S. Polymeric layers catenated by ribbons of rings in a three-dimensional self-assembled architecture: A nanoporous network with spongelike behavior. *Angewandte Chemie-International Edition* **39**, 1506-10 (2000).
108. Nelson, A. P., Parrish, D. A., Cambrea, L. R., Baldwin, L. C., Trivedi, N. J., Mulfort, K. L., Farha, O. K. & Hupp, J. T. Crystal to Crystal Guest Exchange in a Mixed Ligand Metal–Organic Framework. *Crystal Growth & Design* **9**, 4588-91 (2009).
109. Fairen-Jimenez, D., Moggach, S. A., Wharmby, M. T., Wright, P. A., Parsons, S. & Düren, T. Opening the Gate: Framework Flexibility in ZIF-8 Explored by Experiments and Simulations. *Journal of the American Chemical Society* **133**, 8900-2 (2011).

110. Hamon, L., Llewellyn, P. L., Devic, T., Ghoufi, A., Clet, G., Guillerm, V., Pirngruber, G. D., Maurin, G., Serre, C., Driver, G., van Beek, W., Jolimaître, E., Vimont, A., Daturi, M. & Férey, G. Co-adsorption and Separation of CO<sub>2</sub>-CH<sub>4</sub> Mixtures in the Highly Flexible MIL-53(Cr) MOF. *Journal of the American Chemical Society* **131**, 17490-9 (2009).
111. Llewellyn, P. L., Bourrelly, S., Serre, C., Vimont, A., Daturi, M., Hamon, L., De Weireld, G., Chang, J.-S., Hong, D.-Y., Hwang, Y. K., Jhung, S. H. & Férey, G. High uptakes of CO<sub>2</sub> and CH<sub>4</sub> in mesoporous metal-organic frameworks MIL-100 and MIL-101. *Langmuir* **24**, 7245-50 (2008).
112. Fletcher, A. J., Thomas, K. M. & Rosseinsky, M. J. Flexibility in metal-organic framework materials: Impact on sorption properties. *Journal of Solid State Chemistry* **178**, 2491-510 (2005).
113. Rosseinsky, M. J. Recent developments in metal-organic framework chemistry: design, discovery, permanent porosity and flexibility. *Microporous and Mesoporous Materials* **73**, 15-30 (2004).
114. Bourrelly, S., Moulin, B., Rivera, A., Maurin, G., Devautour-Vinot, S., Serre, C., Devic, T., Horcajada, P., Vimont, A., Clet, G., Daturi, M., Lavalley, J.-C., Loera-Serna, S., Denoyel, R., Llewellyn, P. L. & Férey, G. Explanation of the Adsorption of Polar Vapors in the Highly Flexible Metal Organic Framework MIL-53(Cr). *Journal of the American Chemical Society* **132**, 9488-98 (2010).

# Chapter II

## 2 AIMS AND OBJECTIVES

---

Attention from the global community to the on-going issue of climate change is driving the power generation industry to consider options for technologies that capture carbon dioxide (CO<sub>2</sub>) from effluent gas streams. Metal-Organic Frameworks (MOFs) are seen as a promising class of materials for developing more efficient CO<sub>2</sub> capture, through tuning their structures to optimise thermodynamic and kinetic adsorption properties.

MOFs can be tuned to enhance their potential for adsorption through a number of different alterations to their structure. In order to study their performance relative to current carbon capture technologies, MOFs with inherent functionalities which utilise Lewis acid-Lewis base interactions similar to amines are examined, to determine their potential for selective capture of CO<sub>2</sub>.

By determination and subsequent interpretation of the kinetics and thermodynamics involved in the adsorption of CO<sub>2</sub>, with different Lewis basic character, it may be possible to tailor the pore structure and surface chemistry of a MOF to enhance the selectivity and adsorption times for technologies which require fast adsorption/desorption cycles to have economic viability.

Three materials were considered as part of this investigation. The first material, Cu(bpetha)<sub>2</sub>SiF<sub>6</sub>, was chosen from the SIFSIX series of materials, due to their known capabilities towards CO<sub>2</sub> capture. The synthesis and analysis of the bpetha analogue (1,2-Bis(4-pyridyl)ethane) has not been detailed within the known literature, therefore it was deemed a candidate of interest for further investigation. The incorporation of fluorine atoms from the [SiF<sub>6</sub>]<sup>2-</sup> anion are thought to enhance the

adsorption of CO<sub>2</sub> through Lewis acid – Lewis base interactions, and the introduction of a flexible component from the ligand was also of interest to the adsorption properties.

Further development of the SIFSIX materials was considered through the incorporation of a 3-coordinate organic ligand, 2,4,6-Tris(4-pyridyl)-1,3,5-triazine (TPT). Synthesis methods using this ligand and [SiF<sub>6</sub>]<sup>2-</sup> were unsuccessful, however two additional structures were obtained, [Cu(TPT)]BF<sub>4</sub>·0.75H<sub>2</sub>O and [Cu(TPT)]NO<sub>3</sub>·MeOH. [Cu(TPT)]NO<sub>3</sub>·MeOH was a known literature structure, however analysis of its adsorption properties was not performed, therefore it was considered an interesting material to study. Both materials include three uncoordinated nitrogen atoms which were proposed as possible sites for enhancing CO<sub>2</sub> adsorption.

## 2.1 Overall Objectives

The overall objective of this research is to study whether MOFs with inherent Lewis basic functionalities can offer potential for Carbon Capture and Sequestration (CCS) applications. To improve the understanding of the role of the inherent functionality to the adsorption/desorption characteristics of CO<sub>2</sub>, the kinetics associated with the processes and the factors affecting the kinetics of adsorption are investigated.

## 2.2 SPECIFIC OBJECTIVES

### 2.2.1 SYNTHESIS OF MOFs TO STUDY THEIR ADSORPTION POTENTIAL

- i. Synthesis of 1,3,5-tris(4-pyridyl)-2,4,6-triazine ligand containing Lewis base functionality
- ii. Determination of most appropriate MOF synthesis techniques
- iii. Development of MOF synthesis procedure by analysis of different reactant variations

## 2.2.2 CHARACTERISATION OF MOF MATERIALS

- i. Evaluation of crystalline materials synthesised using Single Crystal X-ray Diffraction
- ii. Evaluation of bulk properties of materials through Powder X-ray Diffraction
- iii. Evaluation of elemental properties through characterisation using Infrared Spectroscopy and Elemental (CHN) Analysis
- iv. Evaluation of the thermal stability of materials and temperatures of guest loss
- v. Analysis of the porous characteristics by adsorption of nitrogen at 77 K
- vi. Evaluation of micropore volume by CO<sub>2</sub> adsorption at 273 K

## 2.2.3 STUDY OF SINGLE COMPONENT ADSORPTION CHARACTERISTICS

- i. Evaluation of adsorption potential of pure gases by gravimetric analysis
- ii. Determination of equilibrium capacities of pure gases
- iii. Evaluation of kinetics of adsorption of CO<sub>2</sub> over a range of temperatures and establishing appropriate kinetic models
- iv. Determination of thermodynamic parameters related to equilibrium and kinetic processes

## 2.2.4 STUDY OF THE COMPETITIVE ADSORPTION CHARACTERISTICS

- i. Evaluation of performance of promising materials for CO<sub>2</sub>/N<sub>2</sub> selectivity
- ii. Determination of overall capacity of synthesised porous material

## 2.3 THESIS OUTLINE

Chapter I provided a detailed outline of the motivation for studying Metal-Organic Frameworks for Carbon Capture processes due to the impacts of climate change. Included is the background to CCS techniques, current methods of capture, classical adsorbents, and a detailed description of the structure of Metal-Organic Frameworks.

Chapter III gives the theory of adsorption, detailing the different types of adsorption, porosity and classification of porous materials. The interpretation of isotherms using a variety of theories is described, and the interpretation of adsorption kinetics using model equations.

Chapter IV gives the basic theory of crystallography required for analysis and understanding Metal-Organic Frameworks structures. The methods for analysing crystal structures through single crystal and powder X-ray diffraction are discussed, and the methods of analysis of the data to obtain a model of the structure.

Chapter V details the experimental methods used within this work, detailing the methods of synthesis, and analytical techniques used for the elucidation of the materials properties. A detailed description of the instruments used for adsorption analysis is given, due to the intricate methods used for the kinetic analysis of adsorption systems.

Chapter VI gives the results of the textural properties for the three materials studied,  $\text{Cu}(\text{bpetha})_2\text{SiF}_6$ ,  $[\text{Cu}(\text{TPT})]\text{BF}_4 \cdot 0.75\text{H}_2\text{O}$  and  $[\text{Cu}(\text{TPT})]\text{NO}_3 \cdot \text{MeOH}$ . Structural analysis of the products, using SCXRD and PRXD, are discussed; the chemical analysis is given from data collected using IR, TGA and CHN analysis.

Finally, analysis of the porous properties is described using  $N_2$  and  $CO_2$  adsorption at standard isotherms of 77 K and 273 K, respectively.

Further analysis of the materials adsorption properties, with a focus on the capabilities for Carbon Capture processes, is given in Chapter VII. Analysis of the  $CO_2$ ,  $CH_4$ , and  $N_2$  adsorption capabilities is performed, and analysis of the thermodynamic properties is performed on the best performing adsorbate. Adsorption kinetics of the isotherms are investigated, to provide a deeper understanding of the mechanisms for adsorption processes.

In Chapters VIII and IX, a summary of the key conclusions is given, and recommendations for future studies are provided

# Chapter III

# 3 PRINCIPLES OF ADSORPTION

---

## 3.1 DEFINITION OF ADSORPTION

The process of adsorption is the enrichment of molecules, atoms or ions at an interface between two phases, gas/solid, liquid/solid, liquid/liquid or gas/liquid. For a gas/solid system, as commonly experienced in a porous solid adsorbent, molecules of a gas or vapour are accumulated on the internal surface of the solid <sup>1</sup>. This process is distinct in nature to absorption, which is the bulk penetration of a fluid into a liquid or solid's internal structure. The components of an adsorption system are defined by the following standard classifications in Table 3.1:

Name	Definition
Adsorptive	Component in the fluid phase of the system capable of adsorption at the interface
Adsorbate	Component that is in the adsorbed state at the interface
Adsorbent	Solid on whose surface adsorption occurs

The physical description of adsorption is the balancing of intermolecular forces <sup>2</sup>; when an adsorptive species is at a minimum distance from a solid surface, the attractive and repulsive forces are such that a minimum potential energy is achieved, and the adsorbate-adsorbent interaction is favoured <sup>3</sup>. The potential energy can be described by the Lennard-Jones potential shown in Figure 3.1, when physical interactions are present only.

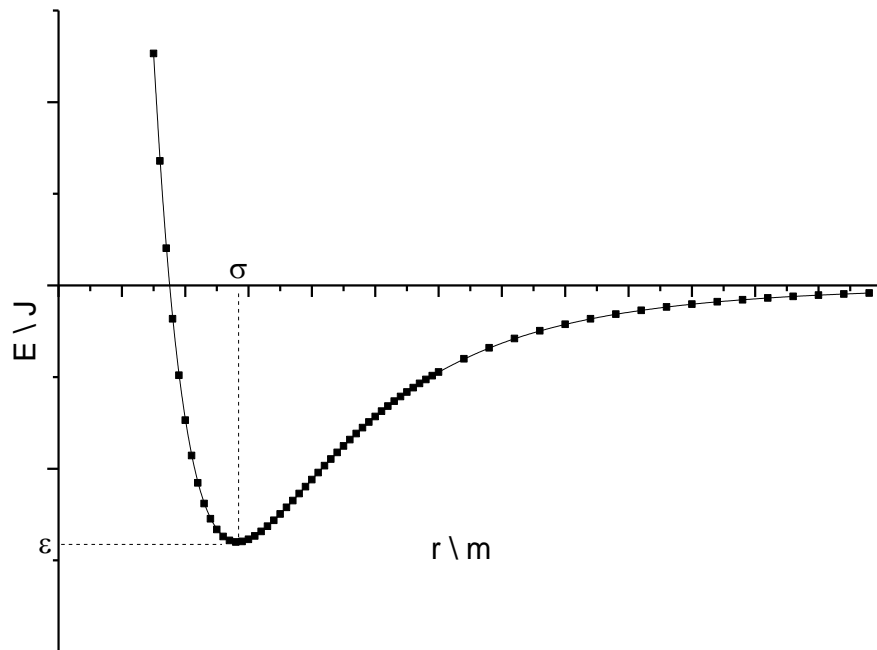


**Figure 3.1: Leonard-Jones Potential Diagram shows the potential energy , E, between two particles which are a distance r apart.  $\sigma$  represents the minimum distance where a stable energy minimum is obtained, and  $\varepsilon$  is the minimum energy potential**

The energy function is expressed in terms of the distance between each atom of the adsorbate and adsorbent by (3-1):

$$E(r) = 4\varepsilon \left[ \left( \frac{\sigma}{r} \right)^{12} - \left( \frac{\sigma}{r} \right)^6 \right] \quad (3-1)$$

Where:

- $E(r)$  = energy potential (J)
- $r$  = distance between the adsorptive and adsorbent (m)
- $\varepsilon$  = minimum energy potential (J)
- $\sigma$  = minimum distance between the two components where a stable minimum energy potential is favoured (m).

Attractive forces are influential at long distance and are therefore proportional to  $r^{-6}$ , while repulsive forces become dominant at close range and are proportional to  $r^{-12}$ . Attractive forces result from non-specific dispersion forces, generated from the fluctuations in the electron cloud of the constituent particles of each component to a position where an atom/molecule produces a short-lived dipole, known as a London

dispersion force. Depending on the nature of the adsorbent and adsorbate molecules, other forces can arise which strengthen the interaction with the surface, such as, dipole-dipole interactions caused by a charged adsorbate and surface, or polarisation interaction where a charged surface can induce a dipole on an adsorbate (dipole-induced dipole). Repulsive forces are produced from overlapping of electron density clouds of the adsorbate and adsorbent atoms, hence the short range required for their effects to be observed. By contrast, specific forces arise from chemical interactions between species, such as Lewis acid-Lewis base interactions, and these, therefore, give rise to the distinction between physisorption and chemisorption.

## 3.2 PHYSISORPTION AND CHEMISORPTION

As stated by the differences in interaction strength with the surface, adsorption can be described by two distinct processes; physical adsorption (physisorption) or chemical adsorption (chemisorption). Table 3.2 outlines the differences between the two processes.

**Table 3.2: Properties relating to physisorption and chemisorption processes**

Properties	Physical Adsorption	Chemical Adsorption
<b>Heat of Adsorption</b> $\text{kJmol}^{-1}$	20 - 40 <i>c.f.</i> heats of vaporisation	> 80 <i>c.f.</i> bulk-phase chemical reactions
<b>Rate of Adsorption</b> (at 273K)	Fast	Slow
<b>Temperature Dependence of Uptake</b>	Decreases	Increases when interaction is endothermic
<b>Desorption</b>	Easy By reduced pressure or increased temperature	Difficult High temperature required to break bonds
<b>Desorbed Species</b>	Adsorbate unchanged	May be different to original adsorptive
<b>Specificity</b>	Non-specific	Very Specific
<b>Monolayer Coverage</b>	Mono or multilayer depending on conditions	Monolayer

Physisorption occurs through non-specific interactions and is present in all adsorbate-adsorbent systems; the process is dynamic and an equilibrium exists between the adsorbed phase on the surface and the bulk gas phase in contact with the interfacial layer. Whether chemisorption is possible or not, the adsorbate molecules are initially weakly adsorbed onto the surface before further chemical bonding occurs. The interaction strength is of low energy, and has no directional chemical bonding. The physical interaction of a gas molecule on a surface is long range and, therefore, weak, as only intermolecular forces (dispersion/ van der Waals) are dominant. The process is analogous to the condensation of vapour molecules on a surface, where condensed molecules are in a lower energy state, produced by their coalescence on the surface

forming a liquid; therefore the interaction energy between the adsorbate and adsorbent surface is comparable to the enthalpy of vaporisation of the adsorbate. Like condensation, physical adsorption is always an exothermic process, as ordering of the adsorbate on the surface decreases entropy, and according to the Gibbs Free energy equation:

$$(\Delta G)_T = (\Delta H)_T - T(\Delta S)_T \quad (3-2)$$

A spontaneous process results in a negative free energy, therefore  $\Delta H$  must be negative. As a result, physisorptive processes will increase with decreasing temperature and increasing pressure (a consequence of Le Chatelier's principle, where increased concentration in the gas phase shifts the equilibrium to the adsorbed phase). Within a porous medium, the surface available for adsorption can be heterogeneous, due to the presence of heteroatoms, or sites where more than one surface are in close proximity, thus adsorption occurs into these sites of higher adsorption potential first. Adsorption then follows the mechanism of filling into progressively larger (or less energetic) pores, until the volume is completely filled which, dependent upon the nature of the adsorbent, occurs at varying pressures.

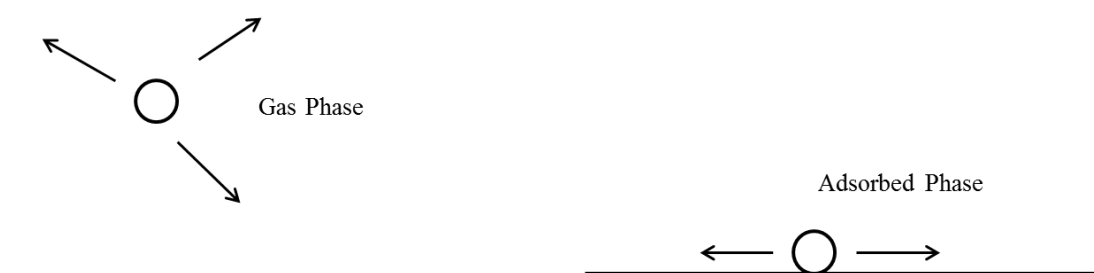


**Figure 3.2: Mechanism of adsorption of a gas molecule onto a surface. In the gas phase, molecules are able to move in 3-dimensions, once adsorbed onto the surface the molecule is able to move 2-dimensionally across the surface, creating a 'pseudo-liquid' like phase**

The reduction in entropy of the adsorbate molecules on the surface is a result of the reduction in the degrees of freedom, as shown in Figure 3.2. Within the gas phase, a molecule close to the surface has 3-dimensions of movement; once adsorbed

onto the surface, the molecules have 2-dimensional movement, being bound to the surface preventing it from moving into the gas phase (at an instantaneous point in time). This highly compressed state under which adsorbate molecules are confined within pores (detailed later), can be defined as a 'pseudo-liquid' like layer of adsorbed molecules on a surface. This intermediate state was theorised by the contrast between the physical properties of the adsorbed phase with those of the gas phase <sup>4</sup>.

Chemisorption is a specific interaction and results in a formal bond between the adsorbate and surface through the donation of electrons. This induces a higher energy of interaction through adhesion onto the adsorbent surface, and prevents the adsorbate from being easily removed. Through the process of dissociative chemisorption, the desorbed species can be chemically different to the initial adsorptive. This gives rise to the use of adsorbents as effective catalysts for a number of reactions. Often the input of additional heat energy is required to break the bond between the surface and the adsorbate; as a consequence, degradation of the adsorbent can occur through loss of the adsorbed species, or thermal effects due to the high temperatures required for regeneration.

### 3.3 POROSITY

*Porosity is antithesis to Aristotle's proposition "Nature abhors a vacuum" <sup>5</sup>*

Adsorption can occur on any surface that is exposed to a bulk gas or vapour; enhanced adsorption occurs only within materials where internal surfaces are present. Porous solids are defined as solids that contain pores, cavities, channels, or interstices. A pore, or porosity, is a term that describes the small channels within a porous solid, which can allow the passage of gases and vapours from the external surface of a solid, through the internal structure, and allow the process of adsorption to occur on internal surfaces. Porous solids are composed of several classes of pores, which make up the internal surface area, and may often be in excess of the external surface area. The porosity provides a volume of space within the adsorbent, which is accessible to gases and vapours to transport them to the surface interaction sites; therefore porosity only provides a means to access a large amount of internal surface area, and does not contribute to the adsorption directly. The terms external and internal surfaces are important in order to understand when enhanced adsorption can occur on porous solids; often external surfaces are defined as all imperfections on a particle that are wider than they are deep, and internal surfaces are therefore inferred as imperfections that are deeper than they are wide <sup>6</sup>.



**Figure 3.3: Different Types of Porosity. Legend indicates the types of porosity and the symbols which correspond to the symbols on the diagram**

Porosity of a material is described by the accessibility of the pore by an adsorbate molecule, and is defined by four different terms:

- open pores* - a pore connected to the external surface of a solid allowing passage of adsorbate molecules through the solid
- closed pores* - a void within the solid not connected to the external surface and is isolated; not suitable for adsorption
- transport pores* - internal pores that connect different pores, allowing gas molecules to pass from one external surface to another
- blind pores* - pore with only one open end that is connected to transport pores and do not lead to any other pore or surface.

Figure 3.3 shows a diagrammatic representation of the types of porosity found within a typical porous solid. The total pore volume can therefore be defined as the sum of open pore volume and closed pore volume; however, in the case of adsorption, the term total pore volume is usually assigned to the accessible volume of the material, namely the open pore volume, as closed pores are not accessible to adsorbate molecules. According to Gurvitsch's Rule <sup>7</sup>, the total pore volume is independent of the adsorbate molecule used, providing there are no selective interactions. The volume can be expressed as a liquid volume (due to the pseudo-liquid state of the adsorbate within the pores), in  $\text{cm}^3\text{g}^{-1}$ .

## 3.4 PORE CLASSIFICATION

The sizes of pores are not specific set values, but vary across a wide range. Porosity is classified based on a set of arbitrary regions defined by IUPAC <sup>8</sup>, but it must be noted that there is no definitive line between each class, and regions of overlap in terms of properties does occur. The accepted classifications are shown in Table 3.3:

**Table 3.3: Size Classification for the Categories of Porosity**

<b>Name</b>	<b>Definition</b>
Micropores	Width less than 2 nm
Mesopores	Width between 2 and 50 nm
Macropores	Width greater than 50 nm

Microporosity is then sub-categorised into three distinct variants:

**Table 3.4: Size Classification for the Categories of Microporosity**

<b>Name</b>	<b>Definition</b>
Ultramicropores	Width less than 0.7 nm
Micropores	Width between 0.7 - 1.4 nm
Supermicropores	Width between 1.4 - 2.0 nm

Depending upon the adsorbent material under study, the porosity can be a distribution of several types of pores, but often in the case of Metal-Organic Frameworks (MOFs) this is limited to one or two specific sizes, which are inherited by the framework's topology.

### 3.4.1 MICROPOROSITY

As stated above, micropores can be classified into three separate groups:

*Ultramicroporosity*: range of pores whose characteristic widths are less than 0.7 nm, they are usually responsible for activated diffusion effects <sup>9</sup>(Section 3.7.1), having widths comparable to the two or three molecular diameters of adsorbate molecules <sup>1</sup>.

*Microporosity:* the mid-range micropores, having characteristic widths between 0.7 – 1.4 nm. Pores are filled at low pressure, and have relatively quick kinetics dependent upon the choice of adsorbate <sup>10-12</sup>. The presence of an overlap in pore wall potentials provides additional stability of the adsorbate molecules within such pores, and produces a pore filling mechanism that is specific to micropores <sup>13-15</sup>.

*Supermicroporosity:* having pore sizes ranging from 1.4 – 2.0 nm, the filling process occurs at higher pressures than micropores, and can extend into the region of multilayer formation (Section 3.4.2) <sup>16</sup>. In such pores, a secondary process for adsorption, known as co-operative pore filling, is theorised <sup>17</sup>. With pore widths more than a few molecules wide, formation of more than one adsorbed layer is possible. Once molecules in the monolayer are adsorbed onto the surface, this creates a ‘reduction’ in the effective pore size; this enhances the formation of further layers by the co-operative effects of the adsorbate molecules already on the surface of the adsorbent.

The pore walls within micropores are in closer proximity to each other than in other pore types, therefore an overlap and interaction of the Polanyi wall potentials (Section 3.6.5) can occur, and as a result can form a deep potential energy well, which provides enhanced adsorption with adsorbates, shown in Figure 3.4. The deep potential well can also induce large activation energies for diffusion into the pore structure.

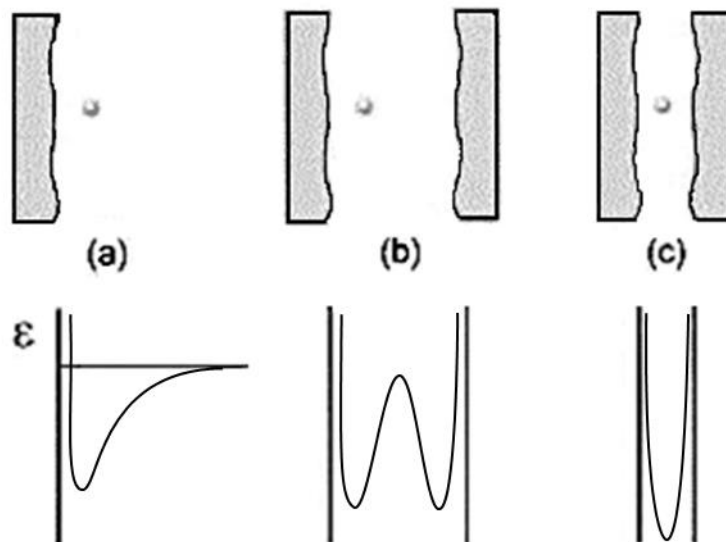


**Figure 3.4: Change in adsorption potential between (a) macropores, (b) mesopores, and (c) micropores. Adsorbate molecules interact more strongly with narrow pores due to the overlap of wall potentials. Wider pores have less overlap, therefore energy wells are seen at two distinct regions in the energy plot, where the central channel of the pore is less stable. Macropores are in essence plane surfaces as there is no overlap of potentials due to the large pore width <sup>18</sup>**

### 3.4.2 MESOPOROSITY

Mesopores are most commonly described by the classical mechanisms of adsorption, having three distinct stages of physisorption onto the pore surface:

- i) Monolayer formation
- ii) Multilayer formation
- iii) Capillary condensation

Mesopores begin to fill at low pressures through formation of a monolayer on the adsorbent surface, followed by the formation of multiple layers adsorbing onto the surfaces of the previously adsorbed molecules. Mesopores reach a critical point at high relative pressure where interaction between layers on either side of the pore form ‘links’, which nucleate further adsorption within the central column of the pore, resulting in ‘condensation’ of the adsorbate into a liquid-like volume of adsorbate. The

result of capillary condensation is different depending on the shape of the mesopore, and gives rise to hysteresis within the adsorption isotherm through the process of adsorbate removal.

### 3.4.3 MACROPOROSITY

Due to the size of macropores being greater than 50 nm, they bear little effect on the adsorption process within a material. Their large size compared to the size of the adsorbate molecule makes the interaction with the surface more like an open, external surface. This is shown in comparison to the interaction experienced by mesopore and micropores in Figure 3.4. Macropores are important as transport pores within a material, to carry adsorbate molecules through the structure to the micropores used for storage. They require very high pressures to fill, and contribute very little towards the surface area of an adsorbate. Macroporosity is usually characterised using mercury intrusion porosimetry, which is a destructive measurement <sup>19</sup>.

## 3.5 INTERPRETING ADSORPTION

### 3.5.1 IUPAC ISOTHERM CLASSIFICATION

In 1940, Brunauer *et al.*<sup>20</sup> predicted that all isotherms could be classified by five idealised models. In 1985, the International Union of Pure and Applied Chemistry (IUPAC) published a set of recommendations for reporting physisorption data, which included a Type VI isotherm<sup>6</sup>. Recent updates to the IUPAC classification scheme have been published and are shown in Figure 3.5, a description of the process that produces each isotherm is given below<sup>1</sup>, and all isotherms that are described in the literature should be comparable to one, or a combination, of these models.

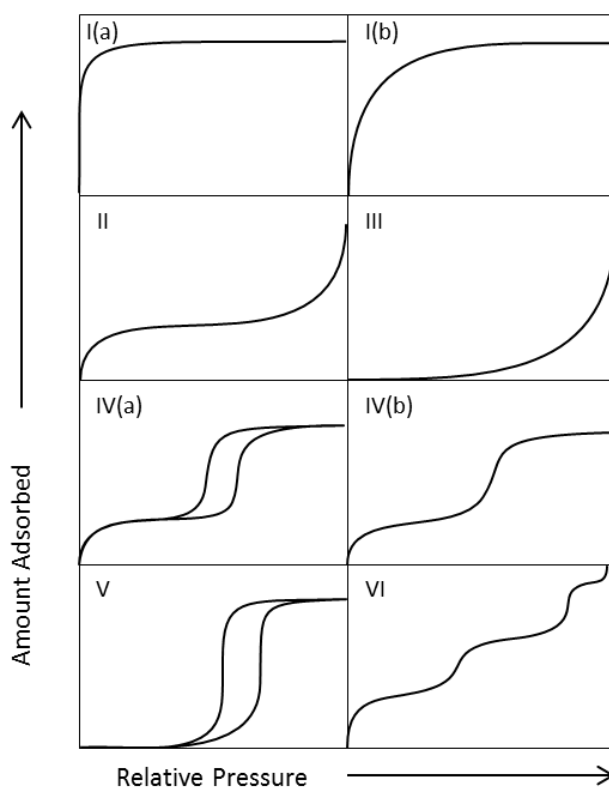


**Figure 3.5: IUPAC Classification for adsorption isotherms plotted as amount adsorbed against relative pressure ( $P/P_0$ )<sup>1</sup>.**

*Type I(a) Isotherm* – This characteristic isotherm, which is concave to the  $P/P_0$  axis, is common for microporous materials that have low external surface areas. A

sharp increase in the amount adsorbed at low pressures, followed by a limiting plateau as  $P/P_0$  approaches 1, is the result of strong adsorbate-adsorbent interactions from overlapping potentials of the pore walls that are in close proximity, producing energy minima; consequently, the smaller the micropore width ( $< 1$  nm) the lower the relative pressure at which maximum adsorption occurs. Therefore, any limitation in uptake is a consequence of the accessibility of the micropore volume and not the surface area; as the micropore diameter approaches the molecular dimensions of the adsorbate it enhances micropore filling (Section 3.6.6 ). The isotherm is reversible, however this curve is also seen for chemisorptive processes, with hysteretic desorption as adsorbate molecules are tightly held by strong surface interactions.

*Type I(b) Isotherm* – Type I(b) differs from Type I(a) only by a broadening of the pore size distribution of the adsorbent material, including larger micropores and narrow mesopores ( $< 2.5$  nm).

*Type II Isotherm* – Plot shows concave curve at low  $P/P_0$ , followed by a linear region, before convex curve at high  $P/P_0$ . Typically measured for isotherms of nonporous or macroporous adsorbents, the shape is characteristic of monolayer formation at low pressure, followed by unrestricted multilayer formation (exponential increase in uptake as  $P/P_0$  approaches 1), the behaviour is due to the space above the external surface area being infinite, or the pore size being much larger than the molecular dimension of the adsorptive ( $> 50$  nm). The point at which monolayer formation occurs is indicated by a sharp knee at the concave curve of the isotherm; if the curvature is more gradual there is overlap between the monolayer coverage and multilayer formation, making characterisation more difficult.

*Type III Isotherm* – A convex curve over the full  $P/P_0$  range is observed for Type III isotherms, showing that there is no distinct monolayer coverage. The strength of interactions between adsorptive and adsorbent is weak, leading to low uptake at low pressure; adsorbate-adsorbate interactions dominate at high pressure forming clusters of adsorbate molecules at the most favoured surface sites, leading to a sharp increase in uptake. With no limiting adsorption capacity at  $P/P_0 = 1$ , this type of adsorption is characteristic of nonporous or macroporous adsorbents and has been witnessed with water adsorption where there are strong adsorptive/adsorbate intermolecular forces.

*Type IV(a) Isotherm* – Type IV has similarity to Type II, as it exhibits the same shape where monolayer coverage occurs; it differs by the inclusion of a plateau at high pressure, indicating a limit to adsorption uptake. This form of adsorption is common for mesoporous materials, where pore size restricts multilayer formation, and a phenomenon known as capillary condensation occurs, where gas condenses to a liquid-like state below the saturation pressure,  $P_0$ . The most characteristic section of the Type IV(a) isotherm is the hysteresis loop, attributed to the occurrence of capillary condensation in mesopores, which are larger than a critical width ( $> 4$  nm).

*Type IV(b) Isotherm* – Type IV(b) shows reversible adsorption, occurring when mesopores are present that have dimensions smaller than the critical width.

*Type V Isotherm* – This type of isotherm is observed when weak adsorbate-adsorbent interactions occur, similar to Type III. The presence of a limiting uptake at high pressures suggests a pore filling mechanism, so it may possibly be exhibited by microporous and mesoporous materials.

*Type VI Isotherm* – A special case, where formation of distinct layers occurs in steps, with full coverage occurring before the next multilayer begins. Type VI isotherms are seen for highly uniform nonporous adsorbents.

### 3.5.2 HYSTERESIS LOOPS

As shown in Types IV(a) and V, a deviation from the adsorption branch, resulting in a different mechanism for desorption, is known as a hysteresis loop. In the standard isotherms, hysteresis is a consequence of multilayer formation and the presence of capillary condensation within mesoporosity<sup>1</sup> (Section 3.7.1). The classification of hysteresis loops is given in the IUPAC Technical report, and are described below (Figure 3.6):

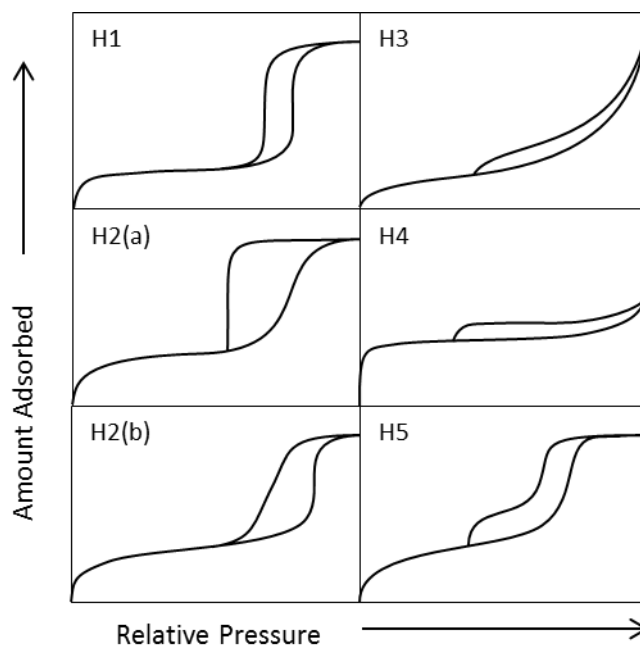


**Figure 3.6: IUPAC Classification for adsorption hysteresis loops, plotted as amount adsorbed against relative pressure ( $P/P_0$ )<sup>1</sup>.**

*Type H1* – Adsorption/desorption branches are steep and narrow and is exhibited by materials with narrow range of uniform mesopores. The effect of network connectivity between pores is minimal and effects are solely from condensation of adsorbate within pores and metastability of the condensed pseudo-liquid and surface tension effects of the meniscus.

*Type H2(a)* – Adsorption branch is a gradual increase to a maximum, whereas the desorption is a steep and abrupt drop at a specific pressure related to the pore structure of the material. The porosity is evidently more complex, having network connectivity. The steep descent of the desorption curve is related to pore-blocking in a narrow pore neck, or cavitation of the liquid adsorbed layer within the pore.

*Type H2(b)* – 2(b) has similar effects related to pore-blocking, however the range of pore necks over which this occurs is now wider, resulting in a more gradual gradient of the desorption branch.

*Type H3* – H3 loops do not show a plateau at high relative pressure, and are often associated with Type II isotherms. The closing of the desorption branch occurs at a specific range determined by the choice of adsorbate, this corresponds to the cavitation point of the adsorbate ( $P/P_0$  0.4 – 0.5 for nitrogen ( $N_2$ ) at 77 K).

*Type H4* – Again, similar to H3 where no plateau is reached and desorption closes at the cavitation point of the adsorbate. These hysteresis loops are commonly seen in Type I and Type II composite materials, with the high uptake at low  $P/P_0$  associated with micropore filling.

*Type H5* – H5 is associated with mesoporous materials that have both open and partially blocked pores.

Recent studies have noted the presence of low pressure hysteresis loops in some porous materials, which has been reported to be an artefact of experimental practices through low equilibration times, or ineffective outgassing procedures, during measurements<sup>21</sup>. However, structural transformations can be induced through adsorption of gases and vapours, especially in the case of flexible MOFs<sup>22</sup>; these can induce non-reversible phase transitions during adsorption/desorption, with it only being possible to return to the initial state once complete desorption of the adsorbate has occurred.

## 3.6 ADSORPTION THEORIES

### 3.6.1 HENRY'S LAW

Adsorption at low surface coverage can be suggested to follow a linear relationship, which is a result of the adsorbed molecules interacting with the adsorbent surface, and having no interaction with other adsorbate molecules, analogous to Henry's proposition for infinitely dilute solutions<sup>23</sup>. This is defined by Henry's Law<sup>24</sup>:

$$n = K_H P \quad (3-3)$$

Where:

$n$	=	specific surface excess amount (mol g <sup>-1</sup> )
$K_H$	=	Henry's Law Constant (mol g <sup>-1</sup> Pa <sup>-1</sup> )
$P$	=	Pressure (Pa)

### 3.6.2 VIRIAL EQUATION

The virial equation has the form<sup>25</sup>:

$$\ln\left(\frac{n}{p}\right) = A_0 + A_1 n + A_2 n^2 \dots \quad (3-4)$$

Where:

$n$	=	amount adsorbed (mol g <sup>-1</sup> )
$p$	=	pressure (Pa)
$A_0$	=	parameter indicative of adsorbate-adsorbent interaction
$A_1$	=	parameter indicative of adsorbate-adsorbate interaction

The equation can be used to analyse the low surface coverage region as it relates to Henry's law through  $A_0$ ; the Henry's Law constant can be expressed by  $K_H = \exp(A_0)$ , and gives a measure of the interaction of the adsorbate with the adsorbent surface.  $A_1$  can be used to determine the strength of adsorbate-adsorbate interactions, however does

not have a physical meaning in terms of the quantity. Using Equation (3-4) for adsorption at low surface coverage, the higher terms  $A_2$  and above can be neglected as they have little physical meaning<sup>10</sup>.

### 3.6.3 LANGMUIR ISOTHERM EQUATION

The theory developed by Langmuir was the first theoretical model for adsorption, with previous models being based on empirical methods, having been determined via experimental data. Langmuir's theory<sup>26</sup> provides a number of mechanisms through which adsorption can occur; in all cases, the underlying principle is that an adsorbent surface has a limited number of adsorption sites. From van der Waals' theory that the boundary between two phases exists as a continuous transition, Langmuir was able to postulate a theory for the adsorption of gases and vapours on a solid surface. In an adsorption system, the adsorbate molecules will accumulate close to the adsorbent surface due to the attractive forces generated by the surface atoms; the surface atoms are chemically bound to the bulk solid, however, they are not fully coordinated due to the asymmetry of the surface structure. This leads to unsaturated bonding at the interface, hence, the interfacial atoms have a higher energy potential than the bulk atoms.

Adsorptive molecules experience a series of collisions as they travel through their constituent phase; when a molecule from the gas phase strikes a surface, it is held there as a consequence of losing kinetic energy from the collision and it experiences a more stable state as a result of close proximity to the surface atoms. Molecules 'condense' onto the surface and escape through 'evaporation', when evaporation is slow the molecules accumulate and form a layer, which achieves chemical saturation of the surface. This means that the mechanisms of 'condensation' (adsorption) and

‘evaporation’ (desorption) occur as dynamic processes and the rate of each can significantly alter the uptake, and the time for equilibrium to occur. The equation that Langmuir devised is based on these rates of ‘condensation’ and ‘evaporation’ from the surface; however a number of assumptions were made to simplify the solution:

1. Only monolayer coverage of adsorbed molecules occurs, and additional layers are prevented from forming
2. The solid surface is homogeneous and adsorption sites are energetically equal
3. An equilibrium exists between the adsorbed phase and the bulk gas phase
4. Successful collisions with a vacant adsorption site result in adsorption
5. Adsorbed molecules do not interact, and are localised to an adsorption site

The rate of collisions with the surface ( $\mu$ ) is determined from the kinetic theory of gases, namely the rate is proportional to the bulk gas pressure:

$$\mu = \frac{P}{\sqrt{2\pi MRT}} \quad (3-5)$$

Where:

$P$	=	bulk pressure (Pa)
$M$	=	molar mass of the adsorbate ( $\text{g mol}^{-1}$ )
$R$	=	universal gas constant ( $8.314 \text{ J mol}^{-1} \text{ K}^{-1}$ )
$T$	=	temperature (K)

The rate of condensation is related to the collision rate by  $\alpha\mu(1-\theta)$ , where  $\alpha$  is the fraction of molecules condensing on the surface, and  $\theta$  is the fraction of adsorbed molecules, therefore, the rate is proportional to the fraction of vacant sites  $(1-\theta)$ , where condensation can occur. The rate of evaporation is given as  $\nu\theta$ , where  $\nu$  is the rate of evaporation at full coverage. When the surface is in dynamic equilibrium with the bulk phase the rates will be equal, giving the following equation:

$$\alpha\mu(1 - \theta) = \nu\theta \quad (3-6)$$

Rearranging gives:

$$\theta = \frac{\alpha\mu}{\nu + \alpha\mu} \quad (3-7)$$

By taking the ratio of the rates,  $\sigma = \alpha/\nu$ , and applying a number of simplifications, Equation (3-8) is written in a format that is more common within the literature, and more accessible to the researcher using the equation for fitting to adsorption data:

$$q = \frac{abP}{1 + aP} \quad (3-8)$$

Where  $q$  is a measure of the quantity of uptake at a set pressure  $P$ , and  $a$  and  $b$  are constants related to the rates of adsorption and desorption and the maximum coverage of the monolayer, respectively:

$$a = \frac{\sigma}{\sqrt{2\pi MRT}} \quad \text{and} \quad b \propto N_0 \quad (3-9)$$

Where  $N_0$  is the total number of adsorption sites on the surface, giving the maximum possible monolayer coverage of the adsorbent. Langmuir's isotherm model shows that, for low pressures or high temperatures,  $aP$  tends towards 0 therefore making the denominator equal to unity by assuming  $1 \gg aP$ , the formula then follows Henry's Law where uptake is proportional to pressure. At high pressure and low temperature the reverse is true and  $aP \gg 1$ , therefore the formula tends towards the constant  $b$ , which is related to the monolayer coverage of the surface and the asymptote towards the monolayer plateau is observed.

Equation (3-10) is often written in the linear form when analysing isothermal data:

$$\frac{P}{q} = \frac{P}{b} + \frac{1}{ab} \quad (3-10)$$

By plotting  $P/q$  against  $P$ , the constants  $a$  and  $b$  can be found from the intercept and gradient, respectively.

The model provided by Langmuir is often applied to microporous adsorbents, which display a Type I isotherm; when the pore size approaches that of the kinetic diameter of the adsorbate, the adsorbed layer can only, by virtue of the physical constraints, be one molecule thick, therefore, preventing multilayer formation, which is seen in mesopores. However, this application of the theory is inaccurate as Langmuir's assumptions were intended for monolayer coverage on a plane surface and not the process of micropore filling seen in porous adsorbents<sup>24</sup>.

#### 3.6.4 BRUNAUER-EMMETT-TELLER (BET) THEORY

Langmuir theory was further developed to include the formation of multilayers, first by Langmuir in his original paper<sup>26</sup>, then by Brunauer, Emmett and Teller<sup>27</sup> who produced a simplified equation using additional assumptions:

1. Multiple layer formation is unrestricted
2. Only adsorbed molecules in direct contact with the bulk gas are in dynamic equilibrium
3. The enthalpy of adsorption of the second and higher layers is equal to the enthalpy of condensation
4. The number of adsorption sites is fixed and adsorption is localised to these sites
5. Surface adsorption sites are equivalent and have a constant enthalpy of adsorption in the monolayer

6. Molecules in the same plane do not interact

The BET equation is widely used by researchers to model adsorption isotherms for pore characterisation and the calculation of BET surface area. As stated above, the equation was derived from Langmuir's theory of adsorption kinetics, wherein the authors applied the condition that the rate of adsorption from the first layer was equal to the rate of desorption at equilibrium, the same holds true for all subsequent layers, so that for each layer on the adsorbed surface:

$$a_i P \theta_{i-1} = b_i \theta_i e^{-E_i/RT} \quad (3-11)$$

Where, for  $i > 1$ , the enthalpy of adsorption is equal to the enthalpy of condensation. Further manipulations bring about the BET equation in its linear form:

$$\frac{P}{n(P_o - P)} = \frac{1}{n_m C} + \frac{C-1}{n_m C} \cdot \frac{P}{P_o} \quad (3-12)$$

Where,  $n_m$  is the monolayer coverage, and  $C$  is a constant related to the adsorption enthalpy by:

$$C = \exp\left(\frac{E_o - E_L}{RT}\right) \quad (3-13)$$

Where  $E_o$  and  $E_L$ , are the enthalpy of adsorption and liquefaction, respectively.

As seen from Figure 3.7, the equation easily predicts Type II isotherms, and varying the value of  $C$  can produce Type II and Type III isotherms. As  $C$  approaches 1 the value of  $E_o$  becomes smaller, and the adsorbate-adsorbent interaction is correspondingly weaker than the adsorbate-adsorbate strength. When  $C$  is large, the enthalpy of interaction with the surface is greater and the model can initially fit a Type I isotherm. The authors determined that it was possible to determine the point at which monolayer coverage is complete, i.e. when the isotherm produces a clear 'knee', as seen for values of  $C \sim 100$  (Figure 3.7). When  $C$  becomes larger still, the surface interaction

is considered to be more specific (higher energy adsorption sites dominate, leading to a heterogeneous surface), therefore, prediction of the monolayer capacity is limited. It is possible to plot the values of  $P/n(P_o - P)$  vs  $P/P_o$  to obtain a straight line, where  $C$  and  $n_m$  can be determined from the gradient and intercept. The linear region, for such plots, was determined empirically to exist within the  $P/P_o$  region of 0.05 to 0.35, as the equation often deviates from experimental data above and below this region, due to failings of the assumptions made by Brunauer *et al.* <sup>27</sup>. New advice on selecting an appropriate relative pressure range dependent on the specific system has recently been published <sup>28</sup>. The BET model is widely applied in determining the accessible surface area of porous materials, with standards also published by IUPAC on how to perform measurements for pore characterisation <sup>1</sup>.

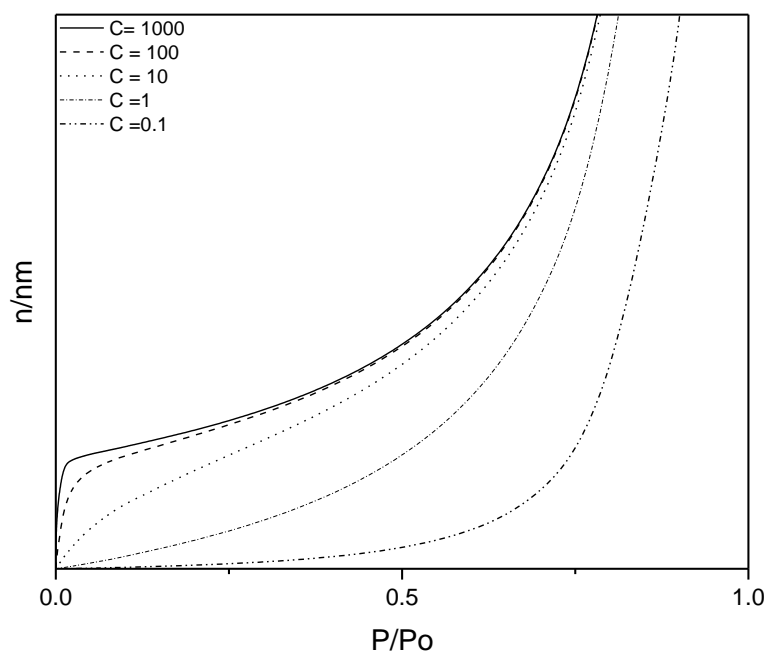


**Figure 3.7: BET isotherm model, showing a range of  $C$  values and the subsequent impact on the isothermal curve obtained**

### 3.6.5 POLANYI POTENTIAL THEORY

It is of great importance to understand the mechanism of filling for micropores in porous materials (width  $< 2$  nm), as these govern the adsorptive capabilities of a given material by acting as storage sites<sup>29</sup>. Early attempts by Polanyi, in 1914, to develop a theory of adsorption potential was largely rejected and overshadowed by Langmuir's theory<sup>30</sup>. Polanyi described the adsorbent surface as having a cohesive potential that interacts with adsorbate molecules, with the strength of interaction determined by the distance of the adsorbate molecule from the surface<sup>30</sup>; the strong attractive force is not shielded when a monolayer is adsorbed on the surface, which contrasts starkly with Langmuir's theory. The dispersion forces applied by the surface on the adsorbate creates a compression on the layers, producing a density gradient (Figure 3.8), which leads to the formation of a liquid film on the surface and extends until the adsorbate is in the bulk gas phase.

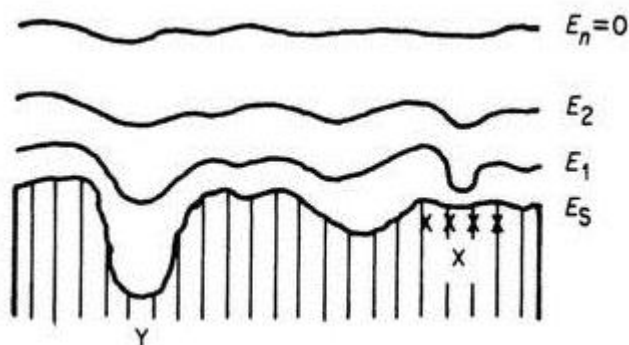


**Figure 3.8: Representation of Polanyi's theory. Cross-section of the adsorbed phase showing energy levels increasing with a decrease in the distance to the surface<sup>18</sup>**

This led Polanyi to suggest an equation based on the ‘adsorption potential’ where energy of the adsorbed layer is related to the density of the adsorbate at a set pressure.

$$A = \int_{\rho_x}^{\rho_i} V dP \quad (3-14)$$

Where:

$A$	=	adsorption potential (J)
$V$	=	adsorbate molar volume ( $\text{m}^3 \text{mol}^{-1}$ )
$\rho_x$	=	gas phase density ( $\text{kg m}^{-3}$ )
$\rho_i$	=	adsorbed phase density ( $\text{kg m}^{-3}$ )

This equation defines the characteristic curve of a material, which is fixed for any adsorption system and is independent of temperature. Assuming the adsorbate behaves as an ideal gas, the key equation is given as:

$$A = RT \ln \frac{P_o}{P} \quad (3-15)$$

Where:

$A$	=	adsorption potential (J)
$R$	=	universal gas constant ( $8.314 \text{ J mol}^{-1} \text{ K}^{-1}$ )
$T$	=	temperature (K)
$P$	=	pressure (Pa)
$P_o$	=	saturation pressure (Pa)

### 3.6.6 DUBININ-RADUSHKEVICH MODEL – THEORY OF VOLUME FILLING OF MICROPORES

Dubinin was the first to establish that Polanyi's theory, although flawed in certain aspects, could be applied to the concept of micropore volume filling<sup>13</sup>. By suggesting that the adsorption potential,  $A$ , could be interpreted as the thermodynamic free energy change of a mole of adsorbate molecules ( $-\Delta G$ ), transferring from the bulk gas phase to a bulk liquid phase adsorbed on the solid surface, the system could be simplified as a liquid in equilibrium with its saturated vapour at pressure  $P_0$ . Due to the dimensions of micropores being close to the kinetic size of adsorbate molecules, the successive formation of adsorbed layers is impossible and the idea of surface area loses significance<sup>14</sup>. Dubinin suggested that the process of volume filling of the adsorption space was important, and introduced the degree of pore filling,  $\theta$ :

$$\theta = \frac{w}{w_0} \quad (3-16)$$

Where,  $w$  and  $w_0$  are the filled volume and total micropore volume ( $\text{cm}^3 \text{g}^{-1}$ ), respectively.

Assuming a Gaussian distribution of pore size <sup>29</sup>, the degree of filling was related to the molar work of adsorption:

$$\theta = \exp \left[ -k \left( \frac{A}{\beta} \right)^2 \right] \quad (3-17)$$

Where:

- $k$  = constant relating to breadth of Gaussian distribution  
 $A$  = Polanyi adsorption potential (J)  
 $\beta$  = adsorbate affinity coefficient

Using Polanyi's theory, the molar work of adsorption 'A' can be replaced with (3-15), and the well-known Dubinin-Radushkevich (D-R) equation is obtained (3-18), followed by its linear simplification (3-19):

$$w = w_o \exp \left[ -B \frac{T^2}{\beta^2} \left( \log \frac{P_o}{P} \right)^2 \right] \quad (3-18)$$

$$\log w = \log w_o - D \log^2 \left( \frac{P_o}{P} \right) \quad (3-19)$$

Where:

- $D = B \frac{T^2}{\beta^2}$ , a measure of the pore size distribution of the adsorbent  
 $B = (2.3026R)^2 k$  and  $R$  is the universal gas constant (8.314 J mol<sup>-1</sup> K<sup>-1</sup>)

Plotting the log of amount adsorbed ( $\log(w)$ ) against  $\log^2(P_o/P)$  produces a linear plot whereupon the micropore volume can be obtained from the intercept. The equation is applicable to homogeneous microporous adsorbents with narrow pore size distributions, and is frequently used to characterise microporous carbons. Dubinin showed that Polanyi's theory holds true for microporous adsorbents by demonstrating temperature invariance on several adsorbent-adsorbate systems <sup>4,14</sup>.

Various modifications have been made to the D-R equation <sup>29</sup>; for example the Dubinin-Astakhov (D-A) equation gives a generalised form of the D-R equation <sup>31</sup>:

$$\log W = \log W_o - D \log^n \left( \frac{P_o}{P} \right) \quad (3-20)$$

The D-A equation included the term ‘ $n$ ’, deemed the ‘heterogeneity factor’ <sup>29</sup>, in place of the squared term, and was reported to have values between  $n = 1 - 3$  <sup>32</sup> for porous carbons, and suggested to have values of  $n = 4 - 6$  for zeolite materials <sup>29</sup>. Further improvements were made for situations where  $n$  is not an integer, and the system could be described as having a broad range of pore sizes, spanning the different micropore regions (ultra-, super-) <sup>33</sup>. For such heterogeneous solids with a broad range of micropores, the D-R equation can be expressed as a sum of pore size contributions; for a continuous distribution, the sum is approximated to an integral equation:

$$W = \int_0^{\infty} f(B) \exp[-B \cdot y] dB \quad (3-21)$$

Where  $f(B)$  is the distribution function (Gaussian for the standard D-R equation), and  $y$  is the variable:

$$y = \left( \frac{T}{\beta} \right)^2 \log^2(P_o/P) \quad (3-22)$$

The distribution function was suggested to provide better fitting to heterogeneous and highly activated carbons, which would have a large distribution of micropore sizes <sup>33</sup>. The authors suggest that the three parameters contained within the expression (3-21) have more physical meaning ascribed to them than the heterogeneity term  $n$  in the D-A equation (3-20).

Difficulty arises in using either of the generalised forms of the D-R equation, as they require computational methods to minimise and find meaningful values for the terms in the equations, and apply distribution functions to the data. A useful derivation of the D-R equation is from simple visual analysis of the graph obtained from Equation (3-19). Figure 3.9 shows the linear plots of the D-R function and possible deviations from linearity that may be observed in the data. These deviations have been ascribed to differences in the Gaussian distribution of micropores within the material <sup>34</sup>.

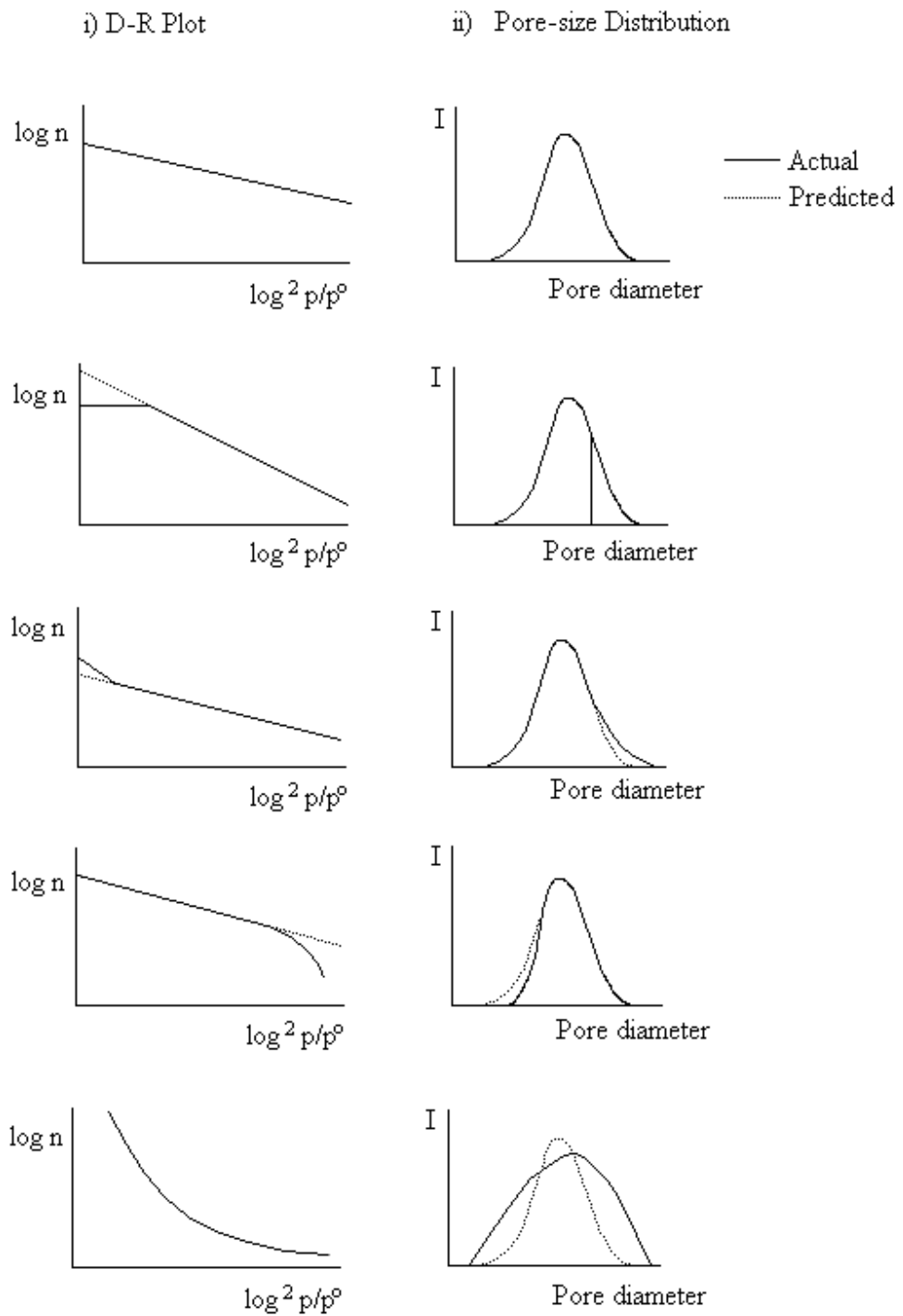


**Figure 3.9: Diagrammatic representation of the deviations from linearity seen in the D-R Equation, and how this relates to pore-size distribution<sup>34</sup>. (Image courtesy of Dr. Ashleigh J. Fletcher<sup>35</sup>)**

### 3.6.7 DETERMINATION OF SURFACE AREA

Although not always relevant for microporous materials <sup>14</sup>, the surface area is still used as a good comparison between adsorbents, giving a ‘fingerprint’ that represents the accessible surface area, which is dependent on the adsorbate chosen <sup>1</sup>. Having determined the monolayer capacity ( $n_m$ ) from either the Langmuir or BET equations, the specific surface area can be obtained from the calculation:

$$a_s = n_m \cdot N_A \cdot \sigma_m \quad (3-23)$$

Where,

$$\begin{aligned} a_s &= \text{surface area (m}^2 \text{g}^{-1}\text{)} \\ \sigma_m &= \text{cross-sectional area of adsorbate molecule (16.2 \AA}^2 \text{ for N}_2\text{)}^{36} \\ N_A &= \text{Avogadro's number (mol}^{-1}\text{)} \end{aligned}$$

In both cases, the method used to obtain the surface area has weaknesses due to the assumptions made by previous theories <sup>1</sup>. Each theory assumes adsorption occurs on a plane surface, and also either assumes only one adsorbed layer can form, or there is unlimited free space above the surface for multilayer formation, making this only practicable for macro- or non-porous materials; only under strict circumstances does the BET equation produce a relevant result for the area, regarded as the ‘probe accessible area’ when concerning materials that produce well-defined Type II or IVa isotherms <sup>1</sup>.

As described in Dubinin’s theory <sup>14</sup>, adsorption in micropores can occur via a volume filling mechanism, making determination of the exact point of monolayer adsorption challenging. The application of the Langmuir model to a Type I isotherm is not always applicable as this assumes that micropores have specific sites for adsorption, and does not account for volume filling where specific sites are unimportant. Additionally, many adsorbents exhibit uptakes most appropriately ascribed to

combinations of isotherms (Type I and II, or I and IV), due to different pore sizes present, and even applying the BET to these isotherms in the classical linear region (0.05 to 0.35  $P/P_0$ ) can lead to erroneous values of  $n_m$ . A method for determination of the most appropriate location of the linear BET region on an isotherm has been outlined recently<sup>28</sup>, and requires that a set of criteria be met:

1. A plot of  $n(P_0 - P)$  vs.  $P/P_0$  should continuously increase with  $P/P_0$  for the chosen range
2. The BET plot should be linear for the chosen range, and the intersection with the vertical axis should be positive, producing a meaningful value of the constant  $C$
3. The corresponding value of  $P/P_0$  for  $n_m$  should lie within the chosen pressure range
4. Alternatively, it should be possible to recalculate the point of monolayer formation,  $P/P_0$ , to within 10% by using the value of  $C$  in  $1/(\sqrt{C} + 1)$ , by stating  $n = n_m$  in the BET equation.

## 3.7 ADSORPTION PHENOMENA

### 3.7.1 CAPILLARY CONDENSATION

The phenomenon of Capillary Condensation causes the occurrence of hysteresis within mesoporous materials, due to a difference in mechanism of the adsorption and desorption of adsorbate molecules <sup>1</sup>. Figure 3.10 is used to describe the process of capillary condensation.

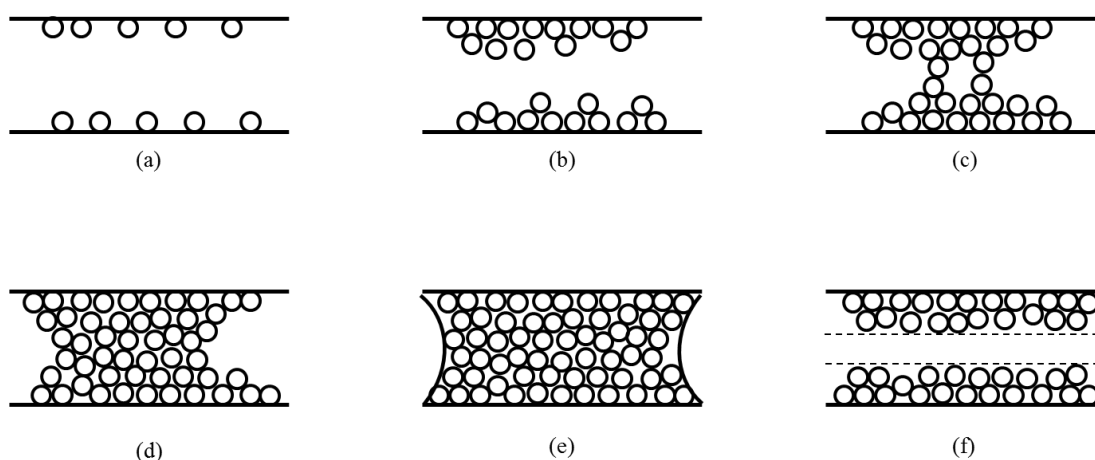


**Figure 3.10: Capillary condensation mechanism, (a) monolayer adsorption, (b) multilayer formation, (c) stabilised adsorbate molecules within the central core of the pore, (d) condensation of liquid-like adsorbate, (e) complete pore filling at  $P/P_0 = \sim 1$ , (f) altered desorption mechanism with core adsorbed liquid desorbing from pore first**

During adsorption, monolayer coverage is initially completed at low pressure (a). As pressure is increased, multilayer formation begins for pores which are larger than the molecular dimensions of the adsorbate (b). At a critical relative pressure (initiation of the hysteresis loop) the multilayers in the pore experience stronger van der Waals interactions between the two opposite walls, and adsorbate molecules are stabilised between the two adsorbed layers (c), from which point condensation of the gas phase into a liquid adsorbed in the pores occurs; this process occurs below the vapour pressure of the adsorbate, but only within pores of sufficient size. The condensing liquid forms a meniscus at the interface with the gas phase, and continues to

fill the pores as the relative pressure is increased (d); at the saturation pressure, the pore is completely filled with adsorbate (e). The closing of the hysteresis loop through desorption occurs as the condensate within the pore is now stabilised, and desorption of the adsorbate occurs through an evaporation process. Once the pressure has been lowered enough to overcome the surface tension of the meniscus, the internal volume of the pore liquid desorbs (f), and after this, the desorption process again proceeds via the same process as adsorption through desorption of the multilayers.

### 3.7.2 ACTIVATED DIFFUSION

As mentioned in Section 3.2, the process of physisorption on a surface is always exothermic; therefore the amount of material adsorbed at any given pressure will decrease with increasing temperature. It has been observed many times that this does not hold with porous materials that have pore sizes similar to the kinetic diameters of adsorbate molecules<sup>37,38</sup>. The deviation from this law is defined by the presence of energy barriers to diffusion, which require thermal energy in order to overcome the barrier to allow adsorption. Using the Arrhenius equation<sup>39</sup>, it is possible to define the energy required to overcome an adsorption barrier at a pore opening:

$$k = Ae^{-\frac{E_A}{RT}} \quad (3-24)$$

Where:

$k$	=	rate of adsorption ( $s^{-1}$ )
$E_A$	=	activation energy of the diffusion barrier ( $J mol^{-1}$ )
$A$	=	pre-exponential factor ( $s^{-1}$ )
$R$	=	universal gas constant ( $8.314 J mol^{-1} K^{-1}$ )
$T$	=	temperature (K)

It is clear that the rate of reaction is dependent upon the activation energy and is inversely related to the temperature of the system. Assuming a pore has a fixed activation energy, which a molecule must have to enter the pore, a decrease in temperature will decrease the rate at which molecules can diffuse into the material. Characteristically, this results in low adsorption capacities, which are not true equilibrium values, at low temperatures. The adsorption will increase with increasing temperature, up to a maximum, where the activation energy into the constricted pores is equal to the energy provided to the adsorbing molecules.

MOFs can have very fixed pore widths dependent upon the nature of packing of their framework constituents in space, forming 3-dimensional structures with porosity. When pore widths are within the range of  $< 0.7$  nm, the effects of activated diffusion can become dominant in the rate of diffusion of gas molecules. This has been characterised in zeolites and carbons, when assessment of the microporosity is performed using  $N_2$  adsorption at 77 K; at pore widths less than 0.7 nm, this corresponds to a bilayer thickness of  $N_2$  molecules, and the possibility of pre-adsorbed  $N_2$  at the pore opening can result in blocking further adsorbate molecules from entering the pore volume. As the filling of ultramicropores occurs at very low relative pressures ( $10^{-7}$  to  $10^{-5}$ ), the driving force of adsorption is low, and diffusion and equilibration times are high, as to be detrimental to experimental time<sup>18</sup>. Within this work, results of standard  $N_2$  adsorption isotherms were impacted by activated diffusion effects, and could have resulted in their rejection as possible materials for further study.

Suggestions to overcome these issues with  $N_2$  are the use of argon (Ar) at 87 K (boiling point) or  $CO_2$  at 273 K<sup>1,38,40</sup>. Ar is found to fill micropores of 0.4 – 0.7 nm width, at relative pressures that are  $\sim 1.5$  times higher than those for  $N_2$ . The spherical shape of Ar and its single atomic structure is more suited to use as a probe adsorbate

compared with N<sub>2</sub>, which is a diatomic molecule and has a more elongated form and larger diameter. As a single atomic noble gas, Ar has only dispersive interactions with the adsorbent surface, compared to N<sub>2</sub>, which has a weak quadrupole moment. Overall, the use of Ar for micropore analysis of materials would be more beneficial and should reduce the analysis time through faster diffusion kinetics and equilibration times; its adoption as a standard has been limited by the high cost of its liquid form required for immersion of the sample to reach temperatures of 87 K, and the wide availability of commercial equipment for N<sub>2</sub> adsorption.

## 3.8 ADSORPTION KINETICS

The models above are used exclusively to describe adsorption isotherms that are at thermodynamic equilibrium. However, the process of adsorption is one that involves the diffusion of gas molecules towards a surface, and so the kinetics of adsorption must be considered when looking at industrial processes that cannot be performed on a thermodynamic timescale. From the models discussed here, it is possible to directly measure the rates of adsorption, and determine the effects of the porous structure that limit the rate of diffusion and ultimately impact on the adsorption capabilities.

### 3.8.1 DIFFUSION MECHANISMS

*“True adsorption is nearly instantaneous. Any lag at present can be accounted for by the time required for the dissipation of the heat evolved or the comparative inaccessibility of a portion of the surface of a porous adsorbing agent.”* McBain, 1919 <sup>41</sup>

The statement above explains that a gas phase in contact with an adsorbing surface will adsorb onto the surface at a rate that is immeasurable; in the case of porous adsorbents, a second process of diffusion of the gas phase to the adsorbent surface is required in order for adsorption to take place and this can be assessed. Diffusion is the process by which atoms or molecules are transported from one position to another through random molecular motion, along a concentration (or chemical potential) gradient <sup>42</sup>. The rate at which diffusion through the porous structure occurs is the rate-limiting step for adsorption <sup>43</sup>.

Evaluation of the diffusion kinetics of an adsorption system can provide information regarding the pore filling process. The diffusion of a gas or vapour is dependent upon the pore width, and the relative ratio of pore width to adsorbate size. The mean free path of a molecule is the average distance that a molecule travels between collisions <sup>39</sup>. It is defined by the equation:

$$\lambda = \frac{RT}{\sqrt{2}\pi d^2 N_A P} \quad (3-25)$$

Where,

- $\lambda$  = mean free path (m)
- $R$  = universal gas constant (8.314 J mol<sup>-1</sup> K<sup>-1</sup>)
- $d$  = collision diameter (m)
- $N_A$  = Avogadro's number (mol<sup>-1</sup>)
- $P$  = pressure (Pa)

Depending upon the pore size, the adsorbing molecule will experience a difference in the path it takes for diffusion, and induces one of four diffusional processes; 1) gas diffusion, 2) Knudsen diffusion, 3) surface diffusion, and 4) activated diffusion (Figure 3.11).

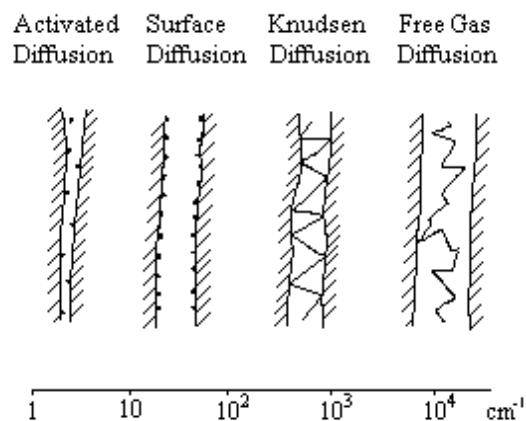


**Figure 3.11: Mechanisms of diffusion based upon the mean free path of the molecule.**

When the pore diameter is larger than the mean free path, the adsorbate acts as a freely diffusing gas, and collisions between other gas molecules occur more frequently than with the pore surface; this is usual for macropores. As pore size decreases, collisions with the surface occur more frequently as the mean free path becomes similar to the pore size, and Knudsen diffusion becomes the dominant mechanism. Surface diffusion becomes important when the mean free path is greater than the pore size, and results in the adsorbate being in close contact with the surface and diffusion occurs through movement of the molecule along the pore walls. Finally the pore size reaches a critical point when the pore opening is similar in size to the kinetic diameter of the adsorbing gas, here activated diffusion effects dominate, where an energy barrier at the pore opening prevents fast penetration, and the gas molecules must overcome the energy barrier to diffuse, similar to the activation energy of a chemical reaction pathway. This type of diffusion occurs often in micropores whose pore sizes are similar to adsorbate diameters (Section 3.7.2).

Diffusion of a substance was first proposed by Fick, who compared the movement of molecules to the conduction of heat, also due to molecular motions, creating an analogous equation to Fourier's theory <sup>42</sup>:

$$F = -D \left( \frac{\partial C}{\partial x} \right) \quad (3-26)$$

Where:

- $F$  = rate of transfer per cross-sectional unit area ( $\text{mol m}^{-2} \text{s}^{-1}$ )
- $C$  = concentration gradient of diffusing substance ( $\text{mol m}^{-3}$ )
- $x$  = direction of motion measured normal to cross-sectional area (m)
- $D$  = diffusion coefficient ( $\text{m}^2 \text{s}^{-1}$ )

Fickian diffusion is therefore concentration dependent and depends on the bulk movement of gases within pores. This is true for the movement of gas molecules in

transport pores, but fails when micropores are involved, as surface diffusion effects are prominent. The process of surface diffusion is therefore better described as a relaxation process, as the adsorbate moves from one adsorption site to another, moving further into the porosity until it reaches a thermodynamic equilibrium.

Rates of diffusion for any process can be defined empirically by the equation <sup>42</sup>

$$\frac{M_t}{M_e} = kt^n \quad (3-27)$$

Where

- $M_t$  = amount adsorbed (g) at time  $t$  (s)
- $M_e$  = adsorbate uptake at equilibrium (g)
- $k$  = constant dependent upon the structural characteristics of the material and on the adsorbent/adsorbate interaction ( $s^{-1}$ )
- $n$  = diffusional exponent, which indicates the transport mechanism.

The equation above can describe the mechanism of diffusion through a plot of  $\ln(M_t/M_e)$  against  $\ln(t)$ , where the gradient of the line gives the exponent,  $n$ . As stated previously, Fickian diffusion is a concentration dependent process. For the empirical relation, this is found when  $n = 0.5$ , therefore  $M_t/M_e$  is not directly proportional to  $t$ , giving a rate process that is not first order. Where  $n = 1$ , the mass change is directly proportional to  $t$ , and, therefore, concentration independent. This is defined as Case II diffusion <sup>42</sup>.

The variation between Case I (Fickian) and Case II (Linear Driving Force model) is in terms of diffusion and relaxation times. In Case I, diffusion times are dominant and slower than surface relaxation, while in Case II relaxation is dominant as described below.

### 3.8.2 LINEAR DRIVING FORCE MODEL (CASE II)

If concentration independent, the diffusion process follows a Linear Driving Force (LDF) model, and is controlled by an advancing front with constant velocity. The equation is defined as:

$$\frac{M_t}{M_e} = \left(1 - e^{-kt}\right) \quad (3-28)$$

A plot of  $\ln(1 - M_t/M_e)$  against time,  $t$ , will provide a linear plot where the gradient is equal to the rate constant.

The equation has many variations from which it can be derived, namely a simplistic view of Fickian diffusion where the process is concentration independent, and also from a derivation of the rate of adsorption given by Langmuir<sup>26,43</sup>:

$$\frac{d\theta}{dt} = k_1(1 - \theta) - k_2\theta \quad (3-29)$$

Integrating,

$$\theta = \frac{k_1}{k_1 + k_2} \left[1 - e^{-(k_1+k_2)t}\right] \quad (3-30)$$

Substitution of  $t = \infty$ ,  $\theta = \theta_e$  where  $\theta_e$  is the surface fraction covers at equilibrium,

$$\theta_e = \frac{k_1}{k_1 + k_2} \quad (3-31)$$

We arrive at the comparable result

$$\theta = \theta_e \left[ 1 - e^{-kt} \right] \quad (3-32)$$

Where,

- $\theta$  = surface coverage fraction
- $k_1$  = constant relating to pressure
- $k_2$  = constant relating to the rate of evaporation
- $t$  = time (s)
- $k$  =  $k_1 + k_2$

Changing the fraction of surface sites to the mass uptake relative to the monolayer coverage, we can arrive at the same expression as in (3-28). The Linear Driving Force (LDF) mass transfer model has been used as an appropriate function to describe the kinetics by phenomenological description<sup>44</sup>, and has been effectively used in the evaluation of kinetic processes in a number of porous materials<sup>10,11,35,44,45</sup>.

### 3.8.3 NON-FICKIAN / ANOMALOUS DIFFUSION MODELS

In cases where  $0.5 < n < 1$ , for the empirical formula, anomalous or non-Fickian diffusion processes occur<sup>42</sup>. Crank described that the concentration dependence of Fickian diffusion is important in rubbery polymers, but is often inadequate to describe the adsorption of a penetrant molecule into a glassy polymer structure, and as such anomalous diffusion processes can be associated with the changes in structure in response to the adsorption and desorption of molecules<sup>42</sup>. By applying this idea to porous media, the rigidity of carbons, zeolites and MOFs (even in flexible structures of MOFs, which often do not respond until external stimuli are presented) can impact on the diffusion process as they are slow to respond and change their structures in the presence of adsorbate molecules, thus they are more likely to experience non-Fickian behaviour. These intermediate mechanisms are defined as having similar relaxation and diffusion rates.

### 3.8.4 STRETCHED EXPONENTIAL

Klafter *et al.*<sup>46</sup> suggested that the stretched exponential equation could be used to describe complex systems that undergo a relaxation process. For adsorption systems, the equation takes the form:

$$\frac{M_t}{M_e} = A(1 - e^{(-kt)^\beta}) \quad (3-33)$$

Where,

$A$	=	constant, $A = 1$ when $M_t = M_e$
$K$	=	rate constant ( $s^{-1}$ )
$t$	=	time (s)
$\beta$	=	exponential parameter

Using the stretched exponential model, the diffusion of both gases and vapours into porous materials has been described<sup>47,48</sup>. The diffusion of the gas into the porous material is a relaxation process and  $k$  is a measure of the rate by which this process occurs. The exponent  $\beta$  can take values of 0.5 – 1, where 0.5 gives a process that is controlled by a distribution of relaxation times and is a one-dimensional process, and 1 gives a single relaxation time, which is equivalent in all three dimensions. The latter function is equivalent to the LDF model, and  $\beta$  can take on any value between 1 and 0.5, indicating an intermediate process.

### 3.8.5 AVRAMI MODEL

The model developed by Avrami *et al.*<sup>49</sup>, is included here due to its use within the Intelligent Gravimetric Analyser for real-time kinetics modelling of adsorption systems, which was first developed by Benham *et al.*<sup>50,51</sup>. Avrami's model, which has a similar form to the SE model, was first used to describe solid state phase transformations<sup>49</sup>; however it has been used in the fields of materials science, thermal analysis and the formation of metal hydrides by hydrogen adsorption<sup>52</sup>. The model used in the context of adsorption, relates the adsorption of gas molecules on a surface to that of nucleation; the model also assumes random spatial nucleation, which relates to the random interaction of adsorbates with surface sites on a plane surface. The Avrami model assumes a form identical to that in Equation (3-33), the difference arises from the value to which  $\beta$  takes, as it is now dependent upon the geometry, and takes values between 1 and 4<sup>51</sup>. This reduces the model to a LDF model when  $\beta = 1$ , and when  $1 < \beta \leq 4$ , the function takes on a sigmoidal form which describes the nucleation and growth of a phase within a host matrix<sup>51</sup>. Avrami suggests that the equation takes integer values of 1 – 4, with 4 representing a 3-dimensional growth rate, and 1 indicating a constant rate<sup>49</sup>.

### 3.8.6 NESTED KINETIC MODELS

Bagley and Long<sup>53</sup> performed experiments looking at the adsorption of acetone vapour on cellulose acetate polymer, and experienced non-Fickian behaviour of the adsorption kinetics. They observed that adsorption of the vapour at a fixed pressure occurred in a two-step process, where an initial fast rate of adsorption over small timescales was followed by a ‘Quasi-equilibrium’ state, before a slow rate process attained the adsorption maximum.

It has been suggested that adsorption kinetics should be modelled as a complete set of nested equations, which can better capture the diffusional processes by reduction of an overall parent equation, to the previously outlined LDF and SE models, and processes incorporating two rate limiting processes<sup>54</sup>.

#### 3.8.6.1 DOUBLE EXPONENTIAL

Recent investigations into adsorption kinetics in a MOF material have also found a kinetic process that can be better described by two linear driving force models combined<sup>55</sup>, and other investigations have confirmed this phenomenon<sup>56,57</sup>. The Double Exponential (DE) model, can determine two rate limiting processes, each with their own distinct rate constants by the following equation:

$$\frac{M_t}{M_e} = A(1 - e^{(-k_1 t)}) + (1 - A)(1 - e^{(-k_2 t)}) \quad (3-34)$$

Where:

$M_t$	=	amount adsorbed (g) at time $t$ (s)
$M_e$	=	equilibrium uptake (g)
$k_1$	=	rate constants ( $s^{-1}$ )
$k_2$	=	rate constants ( $s^{-1}$ )
$A$	=	contribution of rate constant $k_1$ to the overall rate of adsorption; also written as $A_1$ and $A_2$ , where $A_1 + A_2 = 1$

The processes governing diffusion are determined based upon the chemistry and structural properties of the material being studied. In the previous studies where DE kinetics were observed, these two processes were suggested to be controlled by i) slow diffusion through the pore windows with a high activation energy, and ii) fast diffusion through the pores with low activation energy. This is similar to the description by Rao *et al.*<sup>58</sup>, who suggested that diffusion of gases into microporous carbons would have energy barriers for the pore entry and pore diffusion.

### 3.8.6.2 DOUBLE STRETCHED EXPONENTIAL

The parent model, which can be used to describe the adsorption process above, is the Double Stretched Exponential (DSE) model. The model takes the form:

$$\frac{M_t}{M_e} = A \left( 1 - e^{(-k_1 t)^{\beta_1}} \right) + (1 - A) \left( 1 - e^{(-k_2 t)^{\beta_2}} \right) \quad (3-35)$$

It differs from the DE model only by the inclusion of two exponent parameters,  $\beta_1$  and  $\beta_2$ . Reduction of the equation to the DE model requires only that the exponent terms are equal to 1. The SE model is obtained by setting  $A$  equal to 1 or 0, thereby reducing the model to one rate process. Finally the LDF model is obtained by setting  $A = 1$  and  $\beta = 1$ .

## 3.9 ADSORPTION THERMODYNAMICS

### 3.9.1 CLAUSIUS-CLAPEYRON EQUATION

It is possible to determine Heats of adsorption using Van't Hoff isochores, which are found from the Clausius-Clapeyron equation:

$$\frac{dp}{dT} = \frac{\Delta H_{vap}}{T\Delta V_{vap}} \quad (3-36)$$

together with the fact that  $V(g) \gg V(l)$  at standard temperature and pressure (STP), then if the adsorbate follows gas ideality, then  $\Delta V_{vap} \approx V_m$  can be replaced by the ideal gas law,  $RT/p$ . Rearrangement of the equation, assuming that  $\Delta H$  is temperature independent it follows that:

$$\frac{dp}{dT} = \frac{\Delta H_{vap}}{RT^2} p \quad (3-37)$$

$$\frac{d \ln p}{dT} = \frac{\Delta H_{vap}}{RT^2} \quad (3-38)$$

$$\ln p = \frac{-\Delta H_{vap}}{RT} + C \quad (3-39)$$

A plot of  $\ln(p)$  against  $1/T$  at fixed surface coverage (isosteric) should provide a straight line with a gradient that yields the isosteric enthalpy of adsorption ( $-\Delta H_{vap}/R$ ). By making the assumption that the adsorption process is at equilibrium between the gas phase and adsorbed phase, it follows that the Van't Hoff Equation can be applied:

$$\frac{d \ln K_{eq}}{dT} = \frac{\Delta H}{RT^2} \quad (3-40)$$

In a gas phase system, the equilibrium constant can be related to the partial pressure of the components; in a pure component system, this reduces to the total pressure of the

gas phase. Using the definition of Gibbs Free Energy from Equation (3-2), and applying Equation (3-41):

$$\Delta G = -RT \ln K_{eq} \quad (3-41)$$

We obtain the expression:

$$\ln p = \frac{-\Delta H}{RT} + \frac{\Delta S}{R} \quad (3-42)$$

Therefore, taking the intercept from the plot of  $\ln p$  vs.  $1/T$  we can obtain the entropy of adsorption ( $\Delta S/R$ ).

### 3.9.2 ARRHENIUS EQUATION FOR ACTIVATION ENERGY OF REACTION RATE

Van't Hoff provided an equation for the temperature dependence of chemical equilibrium in the form <sup>59</sup>:

$$\left(\frac{\partial \ln K_c}{\partial T}\right)_p = \frac{\Delta U^o}{RT^2} \quad (3-43)$$

Where:

- $K_c$  = concentration equilibrium constant
- $\Delta U^o$  = internal energy of the system ( $\text{kJ mol}^{-1}$ )
- $R$  = universal gas constant ( $8.314 \text{ J mol}^{-1} \text{ K}^{-1}$ )
- $T$  = temperature (K)

Van't Hoff derived that the equilibrium constant was a ratio of the forward and reverse reactions of a system, and that the equation could be written in the form:

$$\left(\frac{d \ln k}{dT}\right)_p = \frac{E}{RT^2} \quad (3-44)$$

Where  $E$  is the energy change between the two reversible reactions

Arrhenius used this as a basis for his theory, in which a reaction progresses along a pathway which takes the reactants through an activated complex <sup>39</sup>, and that equilibrium is established between these two states through a temperature independent function <sup>59</sup>, derived from Van't Hoff's theory:

$$k = Ae^{-\frac{E_a}{RT}} \quad (3-45)$$

Where

- $A$  = pre-exponential or frequency factor ( $\text{s}^{-1}$ )
- $E_a$  = activation energy ( $\text{kJ mol}^{-1}$ )

Arrhenius used Equation (3-45) as the starting point of his general concept on the way in which reactions proceed. The equation has been empirically observed to fit a large amount of experimental data. A plot of  $\ln(k)$  against  $1/T$  should provide a straight line with gradient  $-E_a/R$  and an intercept equal to  $\ln(A)$ . The activation energy is the minimum kinetic energy that molecules in a reaction system must have before they are able to overcome the maximum potential energy related to the transition state of the reaction (the point where the activated complex is formed) and begin the formation of products.

The number of molecules within a system which have the required energy to overcome the activation energy is given by Maxwell's law, which states that the fraction of molecules having energy greater than  $E_a$  is given by a Boltzmann distribution<sup>39</sup>:

$$\frac{N_i}{N_j} = e^{\left[ -(E_i - E_j) / kT \right]} \quad (3-46)$$

Which takes the form of the exponential term in Equation (3-45).

In systems of adsorption, the rate of adsorption onto a surface can be determined using the methods described in Section 3.8. From this the linear plots of  $\ln k$  vs.  $1/T$  provide the activation energies at isosteric conditions, and the zero coverage activation energy can be found from the intercept of the  $E_a$  vs.  $n$  curve at  $n = 0$ .

### 3.10 REFERENCES

1. Thommes, M., Kaneko, K., Neimark, A. V., Olivier, J. P., Rodriguez-Reinoso, F., Rouquerol, J. & Sing, K. S. W. Physisorption of gases, with special reference to the evaluation of surface area and pore size distribution (IUPAC Technical Report). *Pure and Applied Chemistry* **87**, 1051-69 (2015).
2. Rouquerol, F., Rouquerol, J., Sing, K. S. W., Maurin, G. & Llewellyn, P. in *Adsorption by Powders and Porous Solids (Second Edition)* pp. 1-24 (Academic Press, 2014).
3. Maurin, G. in *Adsorption by Powders and Porous Solids (Second Edition)* pp. 191-235 (Academic Press, 2014).
4. Dubinin, M. M. The Potential Theory of Adsorption of Gases and Vapors for Adsorbents with Energetically Non-uniform Surfaces. *Chemical Reviews* **60**, 235-41 (1960).
5. Horike, S. & Kitagawa, S. in *Metal-Organic Frameworks* pp. 1-21 (Wiley-VCH Verlag GmbH & Co. KGaA, 2011).
6. Sing, K. S. W., Everett, D. H., Haul, R. A. W., Moscou, L., Pierotti, R. A., Rouquerol, J. & Siemieniewska, T. Reporting Physisorption Data for Gas Solid Systems with Special Reference to the Determination of Surface-Area and Porosity (Recommendations 1984). *Pure and Applied Chemistry* **57**, 603-19 (1985).
7. Gurvitsch, L. *Journal of Physical Chemistry Soc Russ* **47**, 805 (1915).
8. Everett, D. H. Manual of Symbol and Terminology for Physicochemical Quantities and Units: Appendix -Definitions, Terminology and Symbols in Colloid and Surface Chemistry. *Pure and Applied Chemistry* **31**, 579-638 (1972).
9. Fletcher, A. J., Thomas, K. M. & Rosseinsky, M. J. Flexibility in metal-organic framework materials: Impact on sorption properties. *Journal of Solid State Chemistry* **178**, 2491-510 (2005).
10. Reid, C., O'koye, I. & Thomas, K. Adsorption of gases on carbon molecular sieves used for air separation. Spherical adsorptives as probes for kinetic selectivity. *Langmuir* **14**, 2415-25 (1998).
11. Reid, C. & Thomas, K. Adsorption of gases on a carbon molecular sieve used for air separation: Linear adsorptives as probes for kinetic selectivity. *Langmuir* **15**, 3206-18 (1999).
12. Reid, C. R. & Thomas, K. M. Adsorption kinetics and size exclusion properties of probe molecules for the selective porosity in a carbon molecular sieve used for air separation. *Journal of Physical Chemistry B* **105**, 10619-29 (2001).
13. Bering, B. P., Dubinin, M. M. & Serpinsky, V. V. Theory of Volume Filling for Vapor Adsorption. *Journal of Colloid and Interface Science* **21**, 378+ (1966).

14. Dubinin, M. M. Adsorption in Micropores. *Journal of Colloid and Interface Science* **23**, 487-& (1967).
15. Dubinin, M. M. Fundamentals of the Theory of Adsorption in Micropores of Carbon Adsorbents - Characteristics of Their Adsorption Properties and Microporous Structures. *Carbon* **27**, 457-67 (1989).
16. Sing, K. S. W., Rouquerol, F., Llewellyn, P. & Rouquerol, J. in *Adsorption by Powders and Porous Solids (Second Edition)* pp. 303-20 (Academic Press, 2014).
17. Gregg, S. J., Sing, K. S. W. *Adsorption, Surface Area and Porosity*. 2 edn, (Academic Press, 1982).
18. Lowell, S., Shields, J. E., Thomas, M. A. & Thommes, M. *Characterization of Porous Solids and Powders: Surface Area, Pore Size and Density*. 1 edn, (Springer, 2004).
19. Rouquerol, J., Avnir, D., Fairbridge, C. W., Everett, D. H., Haynes, J. H., Pernicone, N., Ramsay, J. D. F., Sing, K. S. W. & Unger, K. K. Recommendations for the Characterization of Porous Solids. *Pure and Applied Chemistry* **66**, 1739-58 (1994).
20. Brunauer, S., Deming, L. S., Deming, W. E. & Teller, E. On a Theory of the van der Waals Adsorption of Gases. *Journal of the American Chemical Society* **62**, 1723-32 (1940).
21. Silvestre-Albero, A. M., Juárez-Galán, J. M., Silvestre-Albero, J. & Rodríguez-Reinoso, F. Low-Pressure Hysteresis in Adsorption: An Artifact? *The Journal of Physical Chemistry C* **116**, 16652-5 (2012).
22. Llewellyn, P., Maurin, G. & Rouquerol, J. in *Adsorption by Powders and Porous Solids (Second Edition)* pp. 565-610 (Academic Press, 2014).
23. Rouquerol, F., Rouquerol, J. & Sing, K. S. W. in *Adsorption by Powders and Porous Solids (Second Edition)* pp. 25-56 (Academic Press, 2014).
24. Sing, K. S. W., Rouquerol, F. & Rouquerol, J. in *Adsorption by Powders and Porous Solids (Second Edition)* pp. 159-89 (Academic Press, 2014).
25. Cole, J. H., Everett, D. H., Marshall, C. T., Paniego, A. R., Powl, J. C. & Rodríguez-Reinoso, F. Thermodynamics of the high temperature adsorption of some permanent gases by porous carbons. *Journal of the Chemical Society, Faraday Transactions 1: Physical Chemistry in Condensed Phases* **70**, 2154-69 (1974).
26. Langmuir, I. The Adsorption of Gases on Plane Surfaces of Glass, Mica and Platinum. *Journal of the American Chemical Society* **40**, 1361-403 (1918).
27. Brunauer, S., Emmett, P. H. & Teller, E. Adsorption of gases in multimolecular layers. *Journal of the American Chemical Society* **60**, 309-19 (1938).
28. Rouquerol, J., Llewellyn, P. & Rouquerol, F. Is the BET Equation Applicable to Microporous Adsorbents? *Characterization of Porous Solids Vii - Proceedings of the 7th International Symposium on the Characterization of Porous Solids (Cops-Vii), Aix-En-Provence, France, 26-28 May 2005* **160**, 49-56 (2006).

29. Hutson, N. D. & Yang, R. T. Theoretical basis for the Dubinin-Radushkevitch (D-R) adsorption isotherm equation. *Adsorption* **3**, 189-95 (1997).
30. Polanyi, M. The Potential Theory of Adsorption. *Science* **141**, 1010-3 (1963).
31. Dubinin, M. & Astakhov, V. Development of the concepts of volume filling of micropores in the adsorption of gases and vapors by microporous adsorbents. *Russian Chemical Bulletin* **20**, 3-7 (1971).
32. Dubinin, M. M. & Stoeckli, H. F. Homogeneous and Heterogeneous Micropore Structures in Carbonaceous Adsorbents. *Journal of Colloid and Interface Science* **75**, 34-42 (1980).
33. Huber, U., Stoeckli, F. & Houriet, J.-P. A generalization of the Dubinin-Radushkevich equation for the filling of heterogeneous micropore systems in strongly activated carbons. *Journal of Colloid and Interface Science* **67**, 195-203 (1978).
34. Marsh, H. Adsorption methods to study microporosity in coals and carbons--a critique. *Carbon* **25**, 49-58 (1987).
35. Fletcher, A. J. & Thomas, K. M. Compensation Effect for the Kinetics of Adsorption/Desorption of Gases/Vapors on Microporous Carbon Materials. *Langmuir* **16**, 6253-66 (2000).
36. McClella, A. L. & Harnsber, H. F. Cross-Sectional Areas of Molecules Adsorbed on Solid Surfaces. *Journal of Colloid and Interface Science* **23**, 577-& (1967).
37. Marsh, H. & WynneJones, W. F. K. The Surface Properties of Carbon .1. The Effect of Activated Diffusion in the Determination of Surface Area. *Carbon* **1**, 269-79 (1964).
38. Garrido, J., Linaressolano, A., Martinmartinez, J. M., Molinasabio, M., Rodriguezreinoso, F. & Torregrosa, R. Use of N<sub>2</sub> vs CO<sub>2</sub> in the Characterization of Activated Carbons. *Langmuir* **3**, 76-81 (1987).
39. Atkins, P. W. *Atkins' physical chemistry*. 8th edn, (Oxford, New York : Oxford University Press, 2006).
40. Lozano-Castello, D., Cazorla-Amoros, D. & Linares-Solano, A. Usefulness of CO<sub>2</sub> adsorption at 273 K for the characterization of porous carbons. *Carbon* **42**, 1233-42 (2004).
41. McBain, J. W. Theories of Occlusion; and the Sorption of Iodine by Carbon. *Transactions of the Faraday Society* **14**, 202-12 (1919).
42. Crank, J. *The mathematics of diffusion*. 2d ed.. edn, (Oxford, Eng : Clarendon Press, 1979).
43. Brunauer, S. *Adsorption of gases and vapours. v.1. physical adsorption*. (1943, 1943).

44. Foley, N. J., Thomas, K. M., Forshaw, P. L., Stanton, D. & Norman, P. R. Kinetics of water vapor adsorption on activated carbon. *Langmuir* **13**, 2083-9 (1997).
45. Harding, A. W., Foley, N. J., Norman, P. R., Francis, D. C. & Thomas, K. M. Diffusion barriers in the kinetics of water vapor adsorption/desorption on activated carbons. *Langmuir* **14**, 3858-64 (1998).
46. Klafter, J. & Shlesinger, M. F. On the Relationship Among Three Theories of Relaxation in Disordered Systems. *Proceedings of the National Academy of Sciences of the United States of America* **83**, 848-51 (1986).
47. Stylianou, K. C., Rabone, J., Chong, S. Y., Heck, R., Armstrong, J., Wiper, P. V., Jelfs, K. E., Zlotogorsky, S., Bacsa, J., McLennan, A. G., Ireland, C. P., Khimyak, Y. Z., Thomas, K. M., Bradshaw, D. & Rosseinsky, M. J. Dimensionality Transformation through Paddlewheel Reconfiguration in a Flexible and Porous Zn-Based Metal-Organic Framework. *Journal of the American Chemical Society* **134**, 20466-78 (2012).
48. Zhao, X., Villar-Rodil, S., Fletcher, A. J. & Thomas, K. M. Kinetic Isotope Effect for H<sub>2</sub> and D<sub>2</sub> Quantum Molecular Sieving in Adsorption/Desorption on Porous Carbon Materials. *The Journal of Physical Chemistry B* **110**, 9947-55 (2006).
49. Avrami, M. Kinetics of Phase Change. II Transformation-Time Relations for Random Distribution of Nuclei. *The Journal of Chemical Physics* **8**, 212-24 (1940).
50. Benham, M. J. & Ross, D. K. Experimental Determination of Adsorption-Desorption Isotherms by Computer-Controlled Gravimetric Analysis. *Zeitschrift Fur Physikalische Chemie Neue Folge* **163**, 25-32 (1989).
51. Broom, D. P. in *Hydrogen Storage Materials: The Characterisation of Their Storage Properties* Ch. 4 - Gas Sorption Measurement Techniques, pp. 117-39 (Springer London, 2011).
52. Broom, D. P. in *Hydrogen Storage Materials: The Characterisation of Their Storage Properties* Ch. 3 - Hydrogen Sorption Properties of Materials, pp. 61-115 (Springer London, 2011).
53. Bagley, E. & Long, F. A. Two-stage Sorption and Desorption of Organic Vapors in Cellulose Acetate. *Journal of the American Chemical Society* **77**, 2172-8 (1955).
54. Fletcher, A. J., Uygur, Y. & Thomas, K. M. Role of surface functional groups in the adsorption kinetics of water vapor on microporous activated carbons. *Journal of Physical Chemistry C* **111**, 8349-59 (2007).
55. Fletcher, A. J., Cussen, E. J., Bradshaw, D., Rosseinsky, M. J. & Thomas, K. M. Adsorption of gases and vapors on nanoporous Ni<sub>2</sub>(4,4'-bipyridine)<sub>3</sub>(NO<sub>3</sub>)<sub>4</sub> metal-organic framework materials templated with methanol and ethanol: Structural effects in adsorption kinetics. *Journal of the American Chemical Society* **126**, 9750-9 (2004).
56. Kondo, A., Kojima, N., Kajiro, H., Noguchi, H., Hattori, Y., Okino, F., Maeda, K., Ohba, T., Kaneko, K. & Kanoh, H. Gas Adsorption Mechanism and Kinetics of an

Elastic Layer-Structured Metal-Organic Framework. *Journal of Physical Chemistry C* **116**, 4157-62 (2012).

57. Chen, B., Zhao, X., Putkham, A., Hong, K., Lobkovsky, E. B., Hurtado, E. J., Fletcher, A. J. & Thomas, K. M. Surface Interactions and Quantum Kinetic Molecular Sieving for H<sub>2</sub> and D<sub>2</sub> Adsorption on a Mixed Metal–Organic Framework Material. *Journal of the American Chemical Society* **130**, 6411-23 (2008).
58. Rao, M. B., Jenkins, R. G. & Steele, W. A. Potential functions for diffusive motion in carbon molecular sieves. *Langmuir* **1**, 137-41 (1985).
59. Laidler, K. J. The development of the Arrhenius equation. *Journal of Chemical Education* **61**, 494 (1984).

# Chapter IV

# 4 CRYSTALLOGRAPHY

---

## 4.1 DIFFRACTION BY CRYSTALLINE SOLIDS

The discovery in 1895 of the electromagnetic radiation known as X-rays by Wilhelm Röntgen was the first step in the development of techniques for the characterisation of crystalline materials. In 1912, Max von Laue discovered the ability of crystalline materials to diffract X-rays when exposed to a beam of said radiation. The observations were similar to those of Thomas Young in the ‘double slit experiment’, where visible light produces interference patterns when passed through slits of millimetre width <sup>1</sup>.

Diffraction is a phenomenon whereby converging waves produce constructive and destructive interference patterns due to the waves being in-phase or out-of-phase, respectively. This process occurs when the wave front encounters an obstacle or slit which is of similar width to the wavelength of the wave. In electromagnetic radiation, the wave is elastically scattered retaining its kinetic energy and only experiences a change in direction. It is now known that X-rays have a wavelength range between 0.1 – 100 Å, a length scale similar to the distances between atoms in a crystal of 0.5 – 2.5 Å. The well-developed macro prismatic structures of crystals led researchers to believe that their internal structures were formed from periodic units which regularly repeat in 3-dimensional space. These repeating units can be formed from atoms (inorganic structures such as perovskites), small organic molecules, or in the case of porous materials, repeating units of a polymeric structure; due to their long range periodic order, the contents of the crystal can act as a 3-dimensional diffraction grating which scatters X-rays <sup>2</sup>.

Von Laue developed his hypothesis on these now well-known facts, and in his experiments in 1912, he was able to observe spots on a photographic film which proved the incident radiation on the crystal was deviated from its initial trajectory. The findings formed a strong basis for the discovery of diffraction by crystals; however it was the work of W. L. Bragg and W. H. Bragg around the same time as Laue's experiments that was crucial for the development of crystallography as a technique in determining the structures of crystals <sup>1</sup>.

#### 4.1.1 BRAGG'S LAW

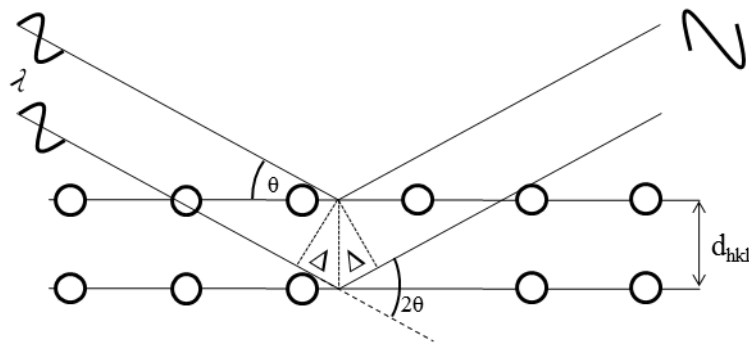


**Figure 4.1: Simplified diagrammatic representation of Bragg's Law. Incident radiation of wavelength,  $\lambda$ , interacts with a set of parallel planes at an angle of incidence,  $\theta$ , which are separated by a distance,  $d_{hkl}$ . X-rays are scattered and if the path length difference between two waves is a positive integer, then constructive interference occurs. Adadpted from Stout *et al.* <sup>2</sup>**

W. L. Bragg was able to deduce that crystals could be regarded as having atoms arranged in a series of planes, and diffraction of X-rays could be simplified to a simple equation by considering the waves as being reflected by these planes. During a diffraction experiment, radiation of wavelength,  $\lambda$ , is incident on a set of parallel planes which are at an angle of incidence,  $\theta$ , from the wave. Due to the interaction of X-rays with the electrons in atoms, the X-rays are scattered elastically at an angle of reflection,  $\theta$ ; X-rays which are not scattered by atoms in the first plane will transmit through the crystal until they contact with a lower plane which is separated by a distance,  $d$ , below

the first plane. The second scattered wave has a path length longer than the first wave; therefore if the path length difference is a positive integer, then constructive interference of the waves will occur. This physical phenomenon, shown diagrammatically in Figure 4.1 <sup>2</sup>, is mathematically derived as Bragg's Law;

$$n\lambda = 2d \sin \theta \quad (4-1)$$

Where;

- $n$  = positive integer
- $\lambda$  = wavelength of radiation (Å)
- $d$  = spacing between planes of atoms (Å)
- $\theta$  = angle of incidence of the x-ray on the plane (°)

#### 4.1.2 MILLER INDICES

Owing to its periodic arrangement, the array of atoms/molecules within a crystal structure can be defined as a series of repeating points in space, which form a lattice or grid of equally spaced parallel planes, known as Miller planes. Each set of planes is defined by a set of indices, h, k and l, which define the number of planes which intersect the a, b and c axes of a unit cell, respectively; each set of planes is separated by a d-spacing,  $d_{hkl}$ . Figure 4.2 <sup>2</sup> shows a set of 2-dimensional planes and their indices (all planes are parallel to the c-axis and do not intersect, making  $l = 0$ ).

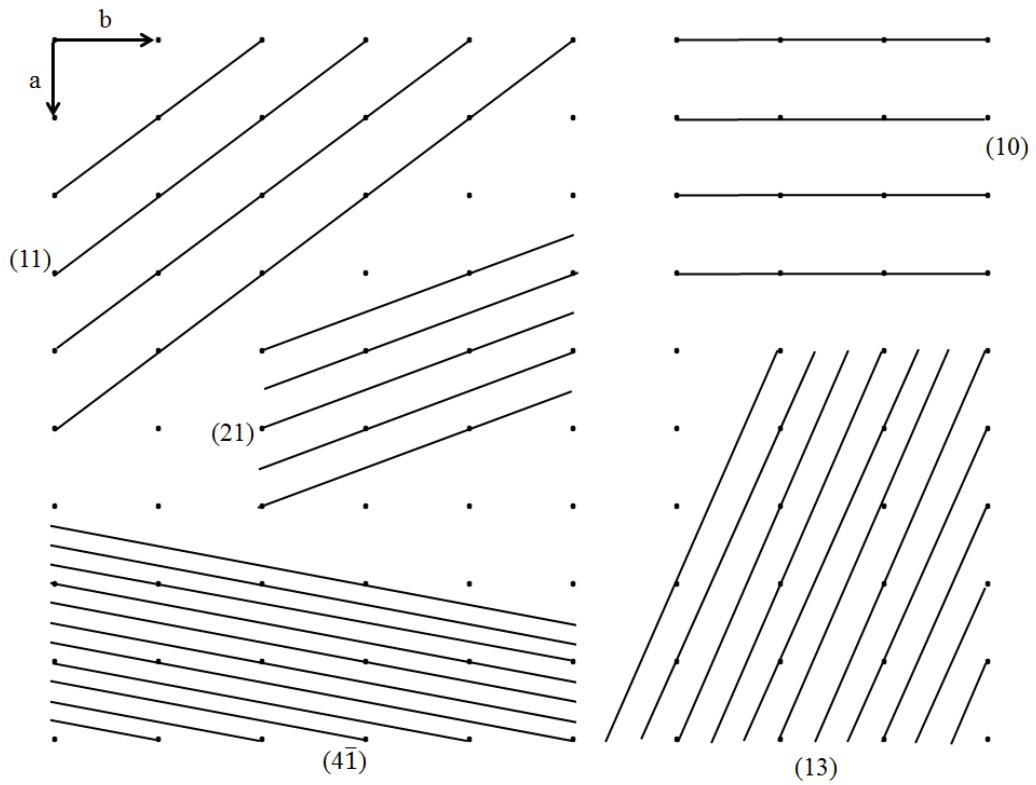
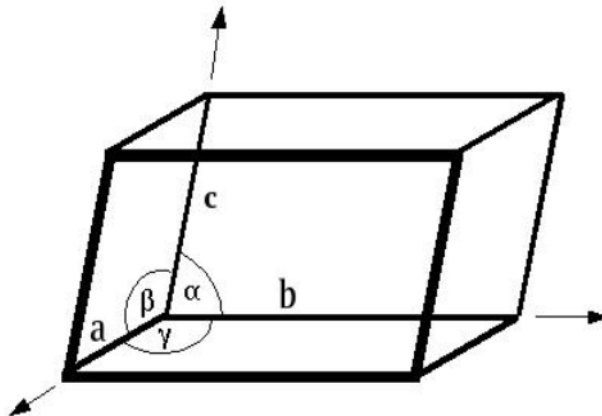


**Figure 4.2: Series of 2-dimensional lattice planes, showing the corresponding miller indices (hkl), c-axis is perpendicular to the ab plane, therefore  $l = 0$ . Adapted from Stout *et al.* <sup>2</sup>**

These imaginary planes define the possible positions where X-rays can be scattered by atoms within the crystal structure and produce constructive interference patterns. Using Bragg's Law, it is possible to scan a range of  $\theta$  values to find points where constructive interference between Miller planes occurs. These locations are seen as peaks of intensity on a detector, which can be measured and collectively interpreted to provide information on the atomic positions and structure of the crystalline material.

### 4.1.3 CRYSTAL SYSTEMS

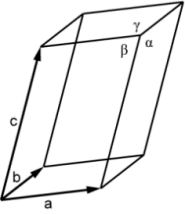
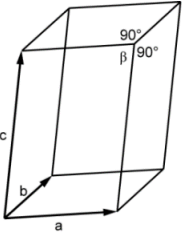
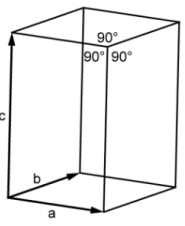
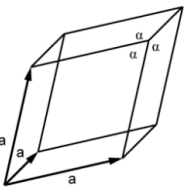
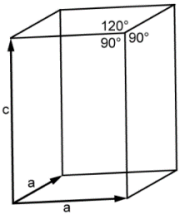
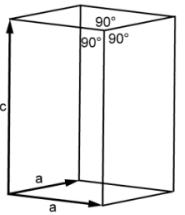
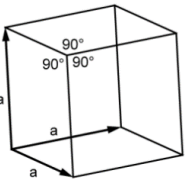
The periodic structure of crystalline materials can be described by a set of symmetry elements which are applied to atoms or groups of atoms. The smallest 3-dimensional array that can describe the entire periodic structure and all its symmetry elements is known as a unit cell. The cell is described using six parameters which are shown in Figure 4.3;  $a$ ,  $b$  and  $c$ , the lengths in the  $x$ ,  $y$  and  $z$  coordinates and  $\alpha$ ,  $\beta$  and  $\gamma$  define the angles between these axes.



**Figure 4.3: Definition of Unit Cell, showing lengths  $a$ ,  $b$  and  $c$ , with corresponding angles  $\alpha$ ,  $\beta$  and  $\gamma$**

The different combinations of lengths and angles can give rise to seven possible crystal systems; cubic, tetragonal, orthorhombic, hexagonal, rhombohedral, monoclinic and triclinic. The distinct positioning of lattice points within the seven cells can also define the lattice type. A cell where lattice points are found only at the corners of the cell is Primitive (P); additional lattice points can be placed on the faces of the cell which gives face-centred (F) and side-centred (A, B, or C) lattices, or a cell with a lattice point within its centre is a body-centred (I) lattice. The combination of crystal system and lattice type provides the 14 Bravais lattices. Table 4.1 gives the various crystal systems, the constraints placed on the cell lengths and angles, and the possible lattice types which give the 14 Bravais lattices.

**Table 4.1: Unit cell configurations, unique cell dimensions and possible Bravais lattices**

Unit cell		Unit Cell Constraints	14 Bravais Lattices
	Triclinic	$a \neq b \neq c$ $\alpha \neq \beta \neq \gamma$	P
	Monoclinic	$a \neq b \neq c$ $\alpha = \gamma = 90^\circ \neq \beta \neq 90^\circ$	P, C
	Orthorhombic	$a \neq b \neq c$ $\alpha = \beta = \gamma = 90^\circ$	P, C, I, F
	Rhombohedral	$a = b = c$ $\alpha = \beta = \gamma \neq 90^\circ$	P
	Hexagonal	$a = b \neq c$ $\alpha = \beta = 90^\circ \neq \gamma = 120^\circ$	P
	Tetragonal	$a = b \neq c$ $\alpha = \beta = \gamma = 90^\circ$	P, I
	Cubic	$a = b = c$ $\alpha = \beta = \gamma = 90^\circ$	P, I, F

The internal symmetry of a unit cell can be defined by point symmetry elements, such as mirror planes, rotational axes, and inversion axes. The stacking of unit cells in a grid-like fashion can describe the macro structure of the crystal, however to relate the cells to each other additional space symmetry elements are required, screw axes and glide planes. These two special symmetry operations are necessary to describe 3D periodic patterns, of which crystalline materials are an example, and involve either a rotational axis or mirror plane, along with a translational component along one of the defined axes of the cell, allowing the periodic structure to be continuous between unit cells. A description of the different symmetry elements and their Hermann-Mauguin symbols often used by crystallographers are given in Table 4.2.

**Table 4.2: Examples of possible symmetry elements within unit cells**

Symmetry Element	Description	Example
m	Mirror plane	Reflection across a plane
1	Inversion point	Reflection through a central point
2, 3, 4 or 6	Inversion axis	Rotational axis of the order $360/n$ , with inversion through axis. 2 is equivalent to a mirror plane
n (2,3,4 or 6)	Rotational axis	Rotational axis of the order $360/n$
$n_m$	Screw axis	Rotation about an axis in the order of $360/n$ , followed by a translation parallel to the axis of rotation equal to $m/n$ of the axis length. $4_1$ is a $90^\circ$ rotation, with a $1/4$ translation along the axis
a, b, c, d, n	Glide plane	Reflection through a plane which is parallel to the axis a, b or c (respectively), followed by a $1/2$ translation along the plane. n is a reflection along the diagonal of a face followed by a $1/2$ translation of the diagonal length. d is the reflection along a face or space diagonal of the unit cell followed by a $1/4$ translation

The final defining classification of the crystal system is the space group. By taking a combination of the lattice type and the major symmetry elements of the three highest symmetry directions of the unit cell, a 'code' describing the full structure and symmetry of the crystal can be obtained. The overall atomic structure of the crystal can therefore be defined from an asymmetric unit including the minimum number of atoms

required to describe the entire structure, and applying the symmetry elements from the space group, it is possible to find the positions of every atom within the unit cell. An example is the face-centred cubic structure of sodium chloride (NaCl) shown in Figure 4.4. The unit cell of NaCl shows ions of  $\text{Na}^+$  and  $\text{Cl}^-$  alternating in three dimensions, giving the cell a face-centred lattice. The major symmetry elements of the cubic cell are the mirror planes along  $ab$  and  $ac$  or  $bc$  planes, and a three-fold inversion axis along the body diagonal between two opposite corners of the lattice; this provides a combined space group notation of  $\text{Fm}\bar{3}\text{m}$ . It is possible to define only the positions  $\text{Na}^+$  (0, 0, 0) and  $\text{Cl}^-$  (0.5, 0.5, 0.5), and applying the symmetry operations to each atom gives all the corresponding positions within the cell.

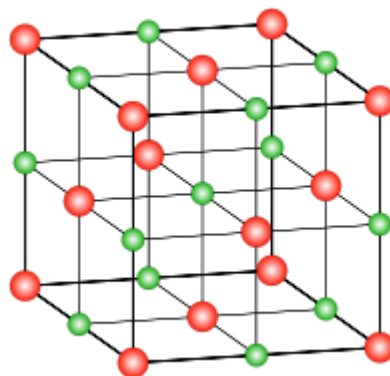


**Figure 4.4: Crystal structure of Sodium Chloride (NaCl).  $\text{Na}^+$  (green),  $\text{Cl}^-$  (red) <sup>4</sup>**

The various combinations of the symmetry elements and lattice centring P, F, I, and C (or A or B), can provide 230 possible space groups all of which are characterised in the International Tables for Crystallography <sup>5</sup>.

#### 4.1.4 X-RAY GENERATION

X-ray radiation is generated using a specially devised instrument in order to obtain a monochromatic wavelength suitable for structural determination. X-rays are produced from the emission spectrum of an electron falling from a high energy level to a low energy level. The radiation is produced in a diffractometer by accelerating electrons emitted from a tungsten filament to an anode by placing a high potential of 30-40 kV between the cathode and anode. The anode material is a metal such as copper, molybdenum or iron and the electrons incident on the metal ionise a core electron in the low energy s orbitals, allowing a high energy electron in the p or d orbitals to fall to a more stable energy level, emitting an x-ray photon in the process. This creates an emission spectrum where the major emission peak for copper is the 2p to 1s transition of wavelength 1.5418 Å for copper known as  $k\alpha$ . A second transition between the 3p and 1s orbitals is the  $k\beta$  wavelength of 1.3922 Å, this is often filtered out by using a nickel film which has an absorption edge at a wavelength of 1.488 Å which lies between the two wavelengths of copper; this leaves a monochromatic source suitable for X-ray characterisation techniques. Additionally,  $k\alpha$  radiation is also split into two peaks,  $\alpha_1$  and  $\alpha_2$ , due to the relative electron spins of the 2p and 1s orbitals. Often diffractometer software will average out the wavelengths, or filtering of the  $\alpha_2$  radiation is possible with a monochromator.

#### 4.1.5 X-RAY DIFFRACTION TECHNIQUES

A crystal of any particular molecule will have an almost unique arrangement of atoms in the Miller planes. These are governed by the close packing arrangement of the molecules/atoms, which are organised in order to maximise intermolecular interactions, therefore this will produce different intensities and angles at which a peak

is observed; this makes X-ray diffraction patterns of a crystal structure a ‘fingerprint’ of the unique configuration of atomic positions within the lattice. The principle of X-ray diffraction techniques is the measurement of the intensity of radiation striking a detector at angles where Bragg’s law is satisfied. The angle of  $2\theta$  between the radiation source and the detector is varied, and the sample is positioned within the incident beam.

During single crystal measurements, a single crystal is mounted on a goniometer, and rotated within the X-ray beam. This allows for the collection of diffraction patterns from each of the various lattice planes found within the cell, and produces a series of 2-dimensional images of the diffraction peaks, shown as intense ‘spots’, which lie at fixed distances from the central origin of the image. Indexing and measurement of the distances between successive layers of spots on each of the images is used to determine the unit cell dimensions with the unique cell constraints being useful in determining the type of unit cell, and examination of the systematic absence of intensity spots from planes (due to translational symmetry), and the appearance of mirror and rotation axes within the images is used to determine the symmetry elements, and therefore the space group of the lattice.

Single crystal diffraction patterns can be further interpreted to determine the atomic positions within the unit cell. Here the intensities of the diffraction spots become important, as these are related to the amplitude of the diffracted waves from a particular set of planes within the cell. The electrons within the structure each diffract a small fraction of the incident X-ray radiation, and the sum of the amplitudes from each of the electrons gives the resultant atomic scattering factor,  $f_n$ ; therefore, atoms with a larger electron density will generate a larger intensity. Taking into account all the atoms within a set of parallel planes (hkl), the overall ‘structure factor’,  $F_{hkl}$  can be determined from the equation;

$$F_{hkl} = \sum_n f_n e^{2\pi i(hx+ky+lz)} \quad (4-2)$$

Where  $f_n$  is the scattering factor of atom  $n$ , which varies as a function of  $(\sin\theta)/\lambda$ .

The structure factor is a combination of the amplitude of the waves being scattered, and the phase,  $\delta$ , which is expressed by the exponential term in Equation (4-2). The major difficulty in structural analysis of crystals lies in ‘the phase problem’, which arises from the fact that the intensity of a diffraction spot is proportional to the square of the structure factor magnitude;

$$I_{hkl} = |F_{hkl}|^2 \quad (4-3)$$

Therefore the phase of a structure factor, being a vector quantity, cannot be directly determined, and the information is lost within the diffraction experiment. Several methods have been developed in order to overcome the phase problem, which is required to refine the structure of a crystal. The most commonly used methods are the “Direct Methods” which require some prior knowledge of the structure, such as an understanding of ‘reasonable’ interatomic distances, and assumes the electron density of the unit cell is composed of discrete spherical regions to which the atoms are located. The software used within this research, SHELXS <sup>6</sup> and SIR92 <sup>7</sup> applies Direct Methods to determine the atomic positions of the single crystal structure. Initial estimates are determined based on the chemical nature, and these are refined against the experimental results until the calculated intensities come within a reasonable degree of fit.

Further parameters are included within the structure factor calculation through the thermal vibrations of the atoms within the unit cell. Atoms will have a degree of thermal motion related to the temperature at which the experiment is carried out; the

consequence of thermal motion is to spread the electron density of the atom over a larger volume, as a result the scattering ability of the atom is reduced and is related by the function

$$e^{-8\pi^2 \langle u^2 \rangle (\sin^2 \theta) / \lambda^2} \quad (4-4)$$

Where  $\langle u^2 \rangle$  is the mean-square amplitude of the atomic vibration, usually denoted as the temperature factor, and is a measure of the displacement of the atom around the point x,y,z.

For initial refinement of structure factors, the thermal vibrations of all atoms can be assumed to be isotropic (spherical) to reduce computation time when determining atomic positions. However, atoms within the structure will most certainly vibrate to different extents dependent upon their bonding and molecular weight, therefore a more comprehensive refinement of anisotropic (ellipsoidal) temperature factors is done for each individual atom, which requires six independent temperature factors to describe the ellipsoidal distribution of electron density of each atom. Therefore, to reduce the amount of thermal vibration to a minimum and improve the 'sharpness' of the intensities, it is common for single crystal measurements to be carried out at temperatures well below room temperature, and crystals are often cooled using a stream of cold nitrogen gas.

The final result of the refinement is to obtain the electron density map of the cell, and determine the atomic positions based on high density regions containing ‘heavier’ atoms, and low density regions containing smaller atoms. The electron density at a specific location in the cell (x,y,z) can be found from Equation (4-5);

$$\rho_{xyz} = \frac{1}{V} \sum_{hkl} |F_{hkl}| e^{-2\pi i(hx+ky+lz)} \quad (4-5)$$

Where  $\rho_{xyz}$  is the electron density and  $V$  is the cell volume.

This defines that the electron density of a point in space is the Fourier Transform of the structure factors. This allows the calculation of an overall electron density map for the crystal from the observed structure factors ( $F_o$ ) from the intensities, and the initial guess of the phase; in turn the electron density can be used to calculate the calculated structure factors ( $F_c$ ) to determine if the assumed phases were correct. A least-squares refinement of the data is performed, with iterations of the parameters made until the calculated structure factors closely matches the observed values; the overall property which is often output by refinement software for the closeness of a fit to observed data is the Goodness of Fit (GOF), defined in Equation (4-6):

$$GOF = \left[ \frac{\sum w(|F_o|^2 - |F_c|^2)^2}{n - m} \right]^{1/2} \quad (4-6)$$

Where  $w$  is a weighting factor calculated during the refinement,  $n$  is the number of reflections used in the refinement, and  $m$  is the number of least squares parameters used for the refinement of the model.

Powder diffraction uses a bulk sample of the crystalline material, which is ground into a fine polycrystalline sample. The polycrystalline sample is irradiated with

X-rays which produces the diffracted beams from all possible orientations of the crystal, and averages out the diffraction ‘spots’ from the single crystal measurement into diffraction cones. The reflections in single crystal X-ray diffraction that are related by point group symmetry are superimposed onto one another within the diffraction cones, which has the effect of reducing the amount of structural information that can be obtained from the collected data, but is still sufficient to perform a structural refinement; providing there is a known single crystal structure which closely matches the material being studied, the atomic positions can be refined to determine if the polycrystalline structure is closely related to the known structure. The collected information from a single crystal gives 3-dimensional diffraction data, during the data collection of a powder diffraction experiment this is compressed into 1-dimension; the observed data from a powder diffraction experiment is the cross-section of the diffraction cones, showing intense peaks which occur at fixed positions of  $2\theta$  related to the symmetry and structure of the molecules within the unit cell, and the low intensity troughs in between is background radiation. While single crystal measurements are essential for fully characterising the atomic structure of the molecules within the crystal, powder diffraction is an effective method for screening samples for identification of the bulk purity of a sample.

#### 4.1.6 RIETVELD REFINEMENT AND LE BAIL METHOD

Methods for structural analysis of crystals using powder X-ray diffraction data differ from those of single crystal X-ray diffraction. The two main methods used for the analysis of powder diffraction data are Le Bail refinement and the Rietveld refinement. Le Bail refinement is used to refine the unit cell parameters of the analysed material and determine the best estimations for the peak intensities from a complete diffraction pattern<sup>8</sup>. The Le Bail refinement is independent of the contents of the unit

cell, and the only parameters used for refinement of the data are the unit cell dimensions, and parameters associated with peak shape that are related to the instrument setup.

Like single crystal diffraction, the intensities of the peaks are related to the square of the structure factors for a particular set of hkl planes. Initially, estimations of the intensities of peaks and unit cell parameters are chosen as guess values, which are then used to calculate the observed intensities and are compared using a least-squares refinement technique to obtain the new parameters. The process is repeated, taking the newly refined parameters each time, until the least-squares residuals,  $S$ , is minimised using Equation (4-7) <sup>9</sup>:

$$S = \sum_i w_i (y_{obs} - y_{calc})^2 \quad (4-7)$$

Where:

- $w_i$  = weighting factor
- $y_{obs}$  = observed intensities
- $y_{calc}$  = calculated intensities

To give a measureable quantity of how good the model fits to the data, the values of  $R_{wp}$  and  $\chi^2$  are calculated:

$$R_{wp} = \sqrt{\frac{\sum_i w_i (y_{obs} - y_{calc})^2}{\sum_i w_i y_{obs}}} \quad (4-8)$$

$$\chi^2 = \frac{\sum_i w_i (y_{obs} - y_{calc})^2}{(N - P)} \quad (4-9)$$

Where:

- $N$  = number of observations
- $P$  = number of variables used for fit

Therefore, a well fitted model to a set of data will have values of  $R_{wp}$  and  $\chi^2$  which minimise towards 0 and 1, respectively.

The Le Bail refinement method can give a good indication of the best possible fit of a model that can be achieved using the Rietveld refinement method, however the Le Bail fitting cannot define atomic positions from the analysis. The Rietveld method uses the same basis for the equations of refinement, but also includes information pertaining to the atomic positions within the unit cell <sup>9</sup>.

## 4.2 REFERENCES

1. Glazer, A. M. The first paper by W.L. Bragg – what and when? *Crystallography Reviews* **19**, 117-24 (2013).
2. Stout, G. H. *X-ray structure determination : a practical guide*. 2nd ed.. edn, (New York : Wiley, 1989).
3. Jeffrey, P. *X-ray Data Collection Course*, <<http://xray0.princeton.edu/~phil/Facility/Guides/XrayDataCollection.html>> (2006), Accessed on: 25/05/2017
4. Prolineserver. (Wikimedia Commons, 2007) <<https://commons.wikimedia.org/wiki/File:Ionlattice-fcc.svg>>, Accessed on: 30/05/2017
5. Hahn, T. *International Tables for Crystallography*. Vol. A (Wiley, 2005).
6. Sheldrick, G. M. A short history of SHELX. *Acta Crystallographica Section A: Foundations of Crystallography* **64**, 112-22 (2007).
7. Altomare, A., Cascarano, G., Giacovazzo, G., Guagliardi, A., Burla, M. C., Polidori, G. & Camalli, M. SIR92 - a program for automatic solution of crystal structures by direct methods. *Journal of Applied Crystallography* **27**, 435 (1994).
8. Le Bail, A. Whole powder pattern decomposition methods and applications: A retrospection. *Powder Diffraction* **20**, 316-26 (2005).
9. Young, R. A. *The Rietveld method*. (Chester, England : International Union of Crystallography, 1993).

# Chapter V

# 5 EXPERIMENTAL METHODS

---

## 5.1 MATERIALS USED

### 5.1.1 SYNTHESIS COMPONENTS

The components used in the synthesis of Metal-Organic Framework (MOF) products were used as received from the stated suppliers; 1,2-bis(4-pyridyl)ethane 99% (bpetha) (Sigma Aldrich), ammonium hexafluorosilicate 98% ((NH<sub>4</sub>)<sub>2</sub>SiF<sub>6</sub>) (Alfa Aesar), copper(II)nitrate hemipentahydrate 98% (Cu(NO<sub>3</sub>)<sub>2</sub>·2.5H<sub>2</sub>O) (Sigma Aldrich), copper(II)tetrafluoroborate hexahydrate (Cu(BF<sub>4</sub>)<sub>2</sub>·6H<sub>2</sub>O), potassium chloride (KCl) (Sigma Aldrich). The ligand 2,4,6-tris(4-pyridyl)-1,3,5-triazine (TPT), was synthesised in the laboratory using the components as received; 4-cyanopyridine 98% (Acros Organics), 1,4,7,10,13,16-hexaoxacyclooctadecane (18-Crown-6) (Fluorochem), potassium hydroxide (KOH) (Sigma Aldrich). Solvents were purchased and used as supplied by Sigma Aldrich, which included; chloroform (CHCl<sub>3</sub>), ethanol (EtOH), methanol (MeOH), and tetrachloroethylene 99.5%.

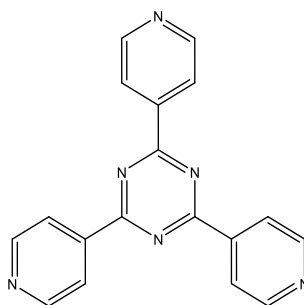


**Figure 5.1: Chemical Structure of 2,4,6-tris(4-pyridyl)-1,3,5-triazine**

The tridentate ligand 2,4,6-tris(4-pyridyl)-1,3,5-triazine, shown in Figure 5.1, was synthesised from a procedure detailed by Li *et al.*<sup>1</sup>. A mixture of 18-crown-6 (1 g) and KOH (0.225 g) was dissolved in 5 ml methanol under stirring for 15 min. The mixture was left to evaporate in a fume cupboard for approx. 30 min, until an oil residue remained. 4-cyanopyridine (10 g) was ground into a fine powder, before mixing together with the previously prepared oil, and was transferred to a 23 ml Teflon liner. The liner was placed in a stainless steel autoclave, sealed following the manufacturer's guidelines, and placed in an oven at room temperature and heated to 473 K for 7 h, before cooling at a rate of 0.1 K min<sup>-1</sup>. Table 5.1 shows the heating regime used for the reaction process.

<b>Table 5.1: Solvothermal synthesis conditions of 1,3,5-tris(4-pyridyl)-2,4,6-triazine</b>		
<b>Temperature (K)</b>	<b>Heating Rate (K/min)</b>	<b>Hold Time (h)</b>
<b>353*</b>	1	1
<b>393</b>	0.5	-
<b>473</b>	0.25	7
<b>373</b>	0.25	1
<b>293</b>	0.1	-

\*Approximately heated to the melting point of 4-cyanopyridine (349 K – 352 K)

The resulting solid material was removed from the Teflon liner using an excess of distilled water. The remaining solid was vacuum filtered through a Buchner funnel, using distilled water and EtOH to wash. The dried solid was placed in a 1:1 mixture of H<sub>2</sub>O/EtOH and heated at the boiling temperature for 1 h, before further filtration and drying in air.

## 5.1.2 ADSORPTIVE GASES USED

Carbon dioxide (CO<sub>2</sub>), oxygen-free nitrogen (N<sub>2</sub>), and methane (CH<sub>4</sub>) were supplied by BOC, UK. CO<sub>2</sub> and N<sub>2</sub> were used as supplied; CH<sub>4</sub> was cleaned to remove moisture and oxygen prior to adsorption studies by passing the gas through a Combo oxygen/moisture trap (AG0-4779) supplied by Phenomenex Ltd. Gas properties are detailed in Table 5.2.

**Table 5.2: Physical Properties of Gases**

Physical Properties	N <sub>2</sub>	CO <sub>2</sub>	CH <sub>4</sub>
Molecular Weight / g mol <sup>-1</sup>	28.01	44.01	16.0425
Melting Point / K	63.14	216.59 <sup>‡</sup>	91
Liquid Density / kg m <sup>-3</sup>	806.08 <sup>*</sup>	1178.5 <sup>†</sup>	422.36 <sup>*</sup>
Boiling Point / K	77.355	194.75 <sup>‡</sup>	111.667
Critical Temperature / K	126.192	304.1282	190.564
Critical Pressure / bar	33.958	73.773	45.992
Critical Density / kg m <sup>-3</sup>	313.3	467.6	162.33
Gas Density / kg m <sup>-3</sup>	4.6121 <sup>*</sup>	2.814 <sup>†</sup>	1.8164 <sup>*</sup>

<sup>\*</sup> at atmospheric pressure (1.01325 bar) and T = T<sub>b</sub>

<sup>†</sup> at the triple point (CO<sub>2</sub>: 216.59 K, 5.1796 bar)

<sup>‡</sup> CO<sub>2</sub> undergoes sublimation at atmospheric pressure

As defined in Chapter II, the adsorptive gas is thought to form a pseudo-liquid layer on the internal surface of the adsorbent; therefore, the adsorbate no longer follows the defined properties of the gas or vapour phase, and a separate adsorbed liquid density is required for each gas used. The adsorbed liquid density was determined via a linear approximation from liquid density data, obtained from NIST Thermophysical properties of Fluid Systems<sup>2</sup>. As stated by Dubinin<sup>3</sup>, the liquid density of a fluid below its boiling point follows an approximately linear relationship with increasing temperature. Above its boiling point, the density falls off rapidly, reaching a minimum value at the critical temperature. During adsorption, the adsorptive is acted upon by the adsorption force field generated by the potential energy of the pore walls (Section 3.6.5), which places it in a highly compressed state. The reduction in degrees of freedom from interaction with the pore walls, and a constant volume maintained by the restricted pore

volume, reduces the impact of temperature on the liquid density, to which Dubinin formulated the linear relationship to define the adsorbate phase density:

$$\rho^* = \rho_b - n(T - T_b) \quad (5-1)$$

Where  $\rho^*$  is the adsorbate density at temperature,  $T$ , and  $\rho_b$  and  $T_b$  are the density and temperature at the normal boiling point. ‘ $n$ ’ is determined from the limiting conditions of the liquid density curve, the normal boiling point and the critical point, and is essentially the gradient of a straight line between the two points;

$$n = \frac{(\rho_b - \rho_{cr})}{(T_{cr} - T_b)} \quad (5-2)$$

Where the critical density is calculated from the inverse of the van der Waals constant,  $b$ .

Such calculations have been questioned and Ozawa *et al.* determined that the use of the van der Waals  $b$  constant, to determine  $\rho_{cr}$ , produced inconsistencies<sup>4</sup>, and a temperature-dependent term was required to more accurately describe the adsorbed phase as a superheated liquid. The linear form of the equation follows, including the term  $\alpha_e$ , which is the mean value for the thermal expansion of liquefied gases ( $2.5 \times 10^{-3} \text{ K}^{-1}$ ), and is independent of the adsorbed species:

$$\ln \rho^* = \ln \rho_b - \alpha_e (t - t_b) \quad (5-3)$$

Camacho *et al.*<sup>5</sup>, provided the linear extrapolation to the liquid density curves of  $\text{CO}_2$ ,  $\text{N}_2$  and  $\text{CH}_4$  shown in Figure 5.2. In studying the MOF MIL-53(Al), Camacho *et al.* estimated values for the thermal expansion coefficient,  $\alpha_e$ , to obtain the characteristic curve of each adsorbate for this particular MOF. The equations, shown in Figure 5.2(b) give the thermal expansion coefficients of all three adsorbates, as the

gradient of each line; the linear equations were used to determine the adsorbate density of the gas at the specified isotherm temperature used in each measurement.

For those measurements performed at temperatures above the critical point, conditions are such that the gas is above the critical temperature, but below the critical pressure, and is, therefore, still compressible. It is stated by Ozawa *et al.* that the pressure dependencies of the terms within the equation will be negligible; therefore the density was assumed to follow the same linear trend above the critical temperature.

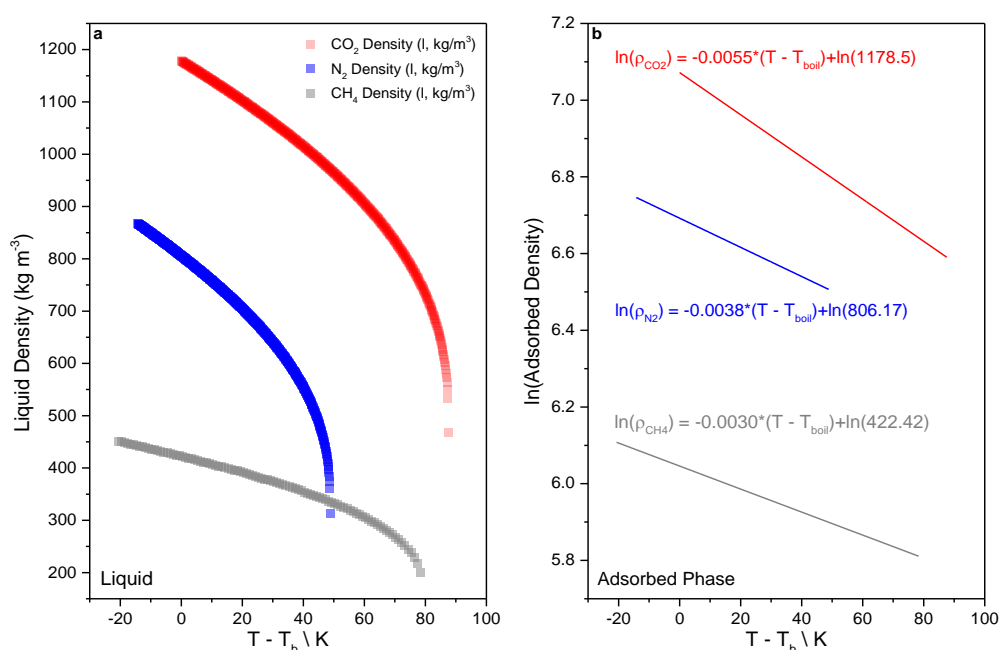


**Figure 5.2: (a) plot of liquid density vs. temperature for gases CO<sub>2</sub> (red), CH<sub>4</sub> (grey), and N<sub>2</sub> (blue). (b) linear extrapolation from Equation (5-3) determined by Camacho *et al.* <sup>5</sup>, density plotted on natural log scale. It should be noted, that due to CO<sub>2</sub> subliming at low temperatures, liquid data was unavailable below the triple point; therefore values used for the boiling point in the calculation were taken from the triple point of CO<sub>2</sub>.**

## 5.2 SYNTHESIS TECHNIQUES

The methods described here are general outlines of the synthetic procedures used to develop the new materials being analysed for their adsorption properties. Although several methods were attempted to synthesise crystals suitable for the range of analysis techniques used in this study, only those which were successful will be discussed in Chapter 6.

Several methods are employed by experimentalists to synthesise crystals for various laboratory analysis techniques. The importance of obtaining crystals of sufficient quality is dictated by the need for structural determination via X-ray diffraction techniques, which relies heavily on single crystals of sufficient size and quality<sup>6</sup>. The process of crystallisation is dependent upon the properties of the compounds involved and, in some cases more difficult to control, the environmental conditions of the surroundings.

### 5.2.1 SOLVENT DIFFUSION

Spingler *et al.*<sup>6</sup> provide a concise review of the techniques for crystallisation where a minimum of two solvents are allowed to diffuse into one another to crystallise a range of small molecules. Of note are the techniques of vapour diffusion, solvent evaporation, and solvent layering. Vapour diffusion provides an easy method where a solute molecule to be crystallised is dissolved in a solvent. This is placed in a small vial, which is then placed in a larger vial containing an anti-solvent, and subsequently sealed. The anti-solvent vaporises and diffuses into the solvent contained within the smaller vial, promoting crystallisation of the solute. The process can be carried out at room temperature, and a large number of solvent combinations can be chosen to obtain

the desired crystal quality; however, there are no set rules as to which combination works best for the system of choice, and a trial-and-error approach is likely the only option.

The difficulty with using vapour diffusion to obtain single crystals of MOFs is the need for several components in the synthesis (metal salt + organic ligand), therefore vapour diffusion may not necessarily provide the easiest option for obtaining crystals, since movement of components between two phases could prove difficult. Therefore, solvent diffusion via a layering technique can be more advantageous; by allowing the two solvents being used to directly mix, the reactants are also in direct contact and crystallisation of the MOF is more likely.

In the simplest case, a container, such as a sample vial with narrow diameter, is chosen. Two solutions are prepared, the first being an aqueous solution of the metal salt, the second an organic solvent containing the coordinating ligand molecule. Additional components, such as a base needed to ionise a carboxylic acid ligand, are added to one of the solutions. The two solutions are carefully layered on top of each other, and the vial sealed to await crystallisation of the product material.

A similar technique is layering by using “H-cells”. The simple design of the cell forming an ‘H’ allows for the two reactant solutions to be contacted through a slow diffusion process. Approximately 2 ml of the aqueous and organic phases of the synthesis mixture are placed in individual legs of the cell, however more or less solution can be added depending on the concentration available. A third layer of solvent is carefully layered on top of the solutions, filling the cross-bar of the cell, before the openings are sealed with rubber septums.

Using the right conditions, both methods can prove effective for the growth of single crystals, however extra care must be taken to ensure the system is left undisturbed, as shocks, vibrations, or extreme changes in temperature could result in the formation of unwanted products through a kinetic process rather than the thermodynamic process. In each method, the choice of solvents is crucial; the components must fully dissolve in solution, which may dictate a narrow selection as the metal salts may only dissolve in aqueous solution. Additionally, the densities of the solvents should be different, in order to prevent mixing when layering, and in the case of sample vial layering, a 'buffer zone' can be added between the two reactant layers to prevent instant precipitation <sup>6</sup>.

These crystallisation techniques are often slow (ranging from a few days to several weeks), with sample vial layering having shorter timescales than H-cells, as diffusion is aided by gravity and involves smaller volumes (~10 ml vs. 50 ml),

### 5.2.2 SOLVOTHERMAL

Hydro/solvothermal synthesis techniques were developed from procedures used for extraction of elements from minerals, and have been used extensively for the formation of zeolite materials <sup>7</sup>. Hydrothermal and solvothermal syntheses are terms for the formation of crystalline substances through chemical reactions, which are performed at temperatures above the boiling point of water (hydro) and organic solvents (solvo), within a sealed environment which generates autogenous pressures. Reactions of MOFs are commonly performed in the temperature range 353 – 533 K <sup>7</sup>.

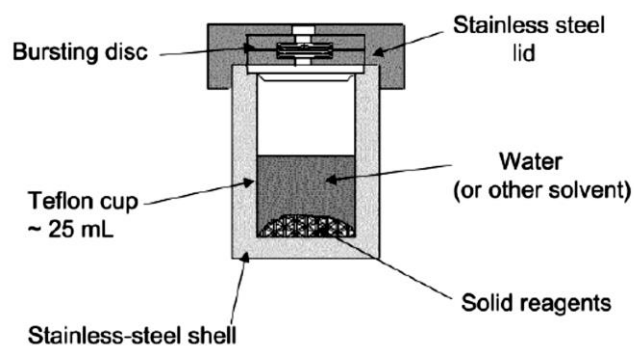


**Figure 5.3: Schematic of a Parr® Autoclave <sup>8</sup>**

Reaction vessels are commonly stainless steel autoclaves, a representative schematic of which is shown in Figure 5.3 <sup>8</sup>; these vessels can vary in terms of their volume. Reactions are contained within a Teflon® liner, which sits within the stainless steel body of the outer vessel. The liner is secured within the vessel using a spring loaded lid, which is screwed down onto the liner to seal it in place. Due to the generation of pressure within the vessel by the heating of any solvents present to produce a vapour pressure, a bursting disc is placed between the liner and lid, to allow safe release of excessive pressure during reaction; however this may result in some reaction mixture losses.

### 5.2.3 DIRECT ADDITION (BATCH CRYSTALLISATION)

When single crystals are available from the other synthesis methods described above, it is often useful for the purposes of adsorption measurements to be able to produce materials on a larger bulk scale, as often measurements require much larger quantities than those possible through single crystal formation. Batch crystallisation is the non-solvothermal synthesis of a MOF product at ambient pressure, through direct mixing of two or more solutions containing the precursors. The use of non-solvothermal temperatures is beneficial for the cost and simplicity of synthesis <sup>9</sup>. Concentrations of precursors are made up in solutions which can be equivalent to those used in the solvent diffusion methods; however, higher concentrations would be more

appropriate as crystallisation will occur through reduction of the supersaturation of the solution. Reactions are monitored through formation of a precipitate of the solid MOF product, and it is commonly noted to have a colour change through change in coordination of the metal centre.

The resultant material is usually in a polycrystalline form, due to the fast reaction that occurs between the components; therefore, the product is amenable to powder X-ray diffraction analysis, and comparison of the purity of the sample can be made directly with the knowledge gained from single crystal diffraction results.

### 5.3 ANALYTICAL TECHNIQUES

X-ray diffraction analysis was used to determine structural information about the materials synthesised. Single-crystal X-ray diffraction (SCXRD) and Powder X-ray diffraction (PXRD) experiments were performed on their respective crystalline forms. Further chemical analysis was performed using thermogravimetric analysis, Fourier transform infrared spectroscopy, and elemental analysis.

#### 5.3.1 SINGLE CRYSTAL X-RAY DIFFRACTION

In order to determine the atomic structure of a crystalline material, a Single Crystal X-Ray Diffractometer (SCXRD) was used. A standard diffractometer consists of an X-ray generator, sample mount, detector, a cooling system for the generator, and a cryostat for the cooling of the single crystal, typically a jet of cold N<sub>2</sub> gas generated from a liquid N<sub>2</sub> Dewar. Experimental data were measured at low temperature (123 K) using Oxford Diffraction Gemini S or Xcalibur E instruments equipped with Cryojet systems, using monochromated Cu or Mo radiation.

The benefit of SCXRD is its ability to provide a complete analysis of the crystal in terms of its atomic parameters and lattice parameters. Additional refinement of the model is required to obtain such information; therefore, knowledge of its components (metal ions, organic ligands, etc.) is required before analysis can be performed. However, as described in the previous section (Section 5.2), high-quality single crystals are required to produce meaningful data, and on occasion this can prove difficult due to a number of factors.

### 5.3.2 POWDER X-RAY DIFFRACTION

Powdered samples of crystalline materials were analysed using a Powder X-Ray Diffractometer (PXRD). A basic diffractometer will consist of an X-ray generator, a sample mount, which is either a flat-plate geometry or capillary, a detector collecting the reflected X-rays from the sample, and a number of optics which can be used to alter the path of the beam, such as filtering wavelengths, or altering the beam to be divergent or collimated. The sample can be rotated to reduce the effects of preferred orientation

All PXRD measurements were carried out using a Bruker D8 ADVANCE diffractometer, with Bragg-Brentano geometry. The instrument set-up was a sealed X-ray tube with a Cu target radiation source (1.5418 Å), which used a Göbel mirror to select  $k_{\alpha}$  radiation and produce a parallel beam. Soller slits were used on the incident and diffracted beam to reduce angular divergence of the beam, and a knife-edge collimator was used to reduce background radiation at low angles from air scattering.

Samples for analysis were ground using a mortar and pestle to produce a fine powder. Each sample was packed in a sample holder, which was a flat-plate for reflection geometry; the sample was open to the atmosphere and at ambient

temperature. The sample stage had multiple positions, so several samples could be run simultaneously, and the stage allowed for rotation of the sample. Measurements were performed between  $3 - 90^\circ 2\theta$ , a step size of  $\sim 0.02^\circ 2\theta$ , and detector count time was between 0.5 – 1 s. The ‘DIFFRAC.SUITE measurement centre’ software provided by Bruker was used for data collection.

PXRD data can be an easy method for analysis of polycrystalline samples, for phase identification and purity analysis, prior to adsorption studies. Due to the nature of the data collected, much of the structural information obtained through SCXRD is lost in PXRD, analysis of the peak positions can determine unit cell dimensions and the space group of the crystal, but information about the atomic positions within the cell is limited, and therefore knowledge of the chemical structure (usually from collected single crystal data, or data from an analogous material) is required to complete a full refinement of the crystal structure. On the other hand, PXRD measurements have faster collection times compared to SCXRD, making them more suitable for routine analyses, and bulk sample purity can be tested instead of individual crystals.

### 5.3.3 THERMOGRAVIMETRIC ANALYSIS

Prior to analysis by adsorption studies, it was necessary to understand the thermal properties of the material. Thermogravimetric Analysis (TGA) can be used to determine physical and chemical properties of a material through analysis of the mass loss response as a function of temperature. It can be used in conjunction with Differential Scanning Calorimetry (DSC) to determine phase transitions (such as melting and boiling points), and the exothermic or endothermic energy from a transition or reaction. For the analysis of MOFs and other porous materials, the prime consideration of these measurements is the thermal stability of the material over a range

of temperatures, and the determination of the quantity of adsorbed species within the porosity, which can give an approximate value of the pore volume to compare with more accurate measurements using adsorption techniques.

Analyses of materials were performed using a Netzsch STA 449 F3 Jupiter model; A Simultaneous Thermal Analyser (STA) is a combined TGA/DSC instrument. The instrument is composed of an upright balance head, a Silicon-Carbide furnace capable of achieving temperatures in the range room temperature to 1773 K, which is lowered over the balance head; a water bath for thermostating the balance at 298 K was also provided. Sample weights of approximately 10 mg were added to a ceramic crucible which was placed on top of the balance head, along with a reference crucible of the same material. The furnace was lowered into position over the balance and a constant flow of  $70 \text{ cm}^3 \text{ min}^{-1} \text{ N}_2$  ( $20 \text{ cm}^3 \text{ min}^{-1}$  to protect the balance and  $50 \text{ cm}^3 \text{ min}^{-1}$  over the sample) was applied. Once the mass was stable, under these conditions, the temperature was ramped at a rate of  $5 \text{ K min}^{-1}$  to a maximum temperature of 1273 K. The change in mass was recorded using the Proteus software and output data recorded as a percentage loss. Due to the nature of solvent molecules contained within porous materials, the initial mass loss observed is usually attributable to desorption, as weak intermolecular forces will most commonly be involved in the interaction with the solid adsorbent, allowing the separation of weakly interacting species early in the temperature program, and well below the temperature, hence, the energy, required to formally break a covalent, ionic or dipolar bonding found within the framework structure.

### 5.3.4 FOURIER TRANSFORM INFRARED SPECTROSCOPY

To gain further insight into the chemical bonding within the MOFs synthesised, infrared (IR) spectroscopy was performed. IR spectroscopy uses infrared radiation to probe the bonding energies of atoms within a molecule, to determine the type of bonding present. It is well established that the vibrational energy of a bond is equivalent to the energy of the IR wavelength range, and a detailed description of the theory behind IR spectroscopy can be found in any standard physical chemistry textbook<sup>10</sup>. In summary, in order for a bond to be infrared active, it must undergo a change in dipole moment, which requires that the molecule vibrate asymmetrically; therefore a diatomic molecule of N<sub>2</sub> will not undergo a vibration that changes its dipole moment, but a molecule of CO<sub>2</sub> can vibrate asymmetrically along the axis of the C=O bonds, or through bending vibrations, resulting in an infrared active stretch which can be observed when the molecule is irradiated and the bond absorbs a photon of energy corresponding to the energy needed for the vibrational mode. Fourier Transform Infrared (FT-IR) Spectroscopy uses radiation covering a range of wavelengths to irradiate the sample for analysis; the transmitted light passing through the sample is split into two paths which differ in their path length. When the beams are recombined, they create interference patterns, where constructive interference occurs when the path difference is an integer. A computer algorithm is used to perform a Fourier transform on the collected interference pattern, and this generates an absorbance or transmittance curve as a function of wavenumber (cm<sup>-1</sup>).

Spectra were collected using an ABB MB3000 ATR-FTIR spectrometer; spectra were recorded within the range of 550 – 4000 cm<sup>-1</sup>. Samples were analysed by placing approximately 2 mg into a small trough and pressing into place with a clamp. Measurements were taken at resolutions of 1 cm<sup>-1</sup> and averages were taken from 32 consecutive scans.

## 5.4 GAS ADSORPTION ANALYSIS

Adsorption analysis was carried out using both volumetric and gravimetric techniques, each has benefits for the particular samples analysed and both are described here.

### 5.4.1 VOLUMETRIC ADSORPTION APPARATUS

Volumetric measurements were performed using a Mircomeritics ASAP 2420. The volumetric system is commonly used for simple adsorption isotherm measurements using  $N_2$  as adsorptive at 77 K, and is easy to operate, with the possibility of a commercial instrument offering multiple measuring ports for simultaneous sample characterisation. A simplified diagram of the measurement setup is shown in Figure 5.4<sup>11</sup>.

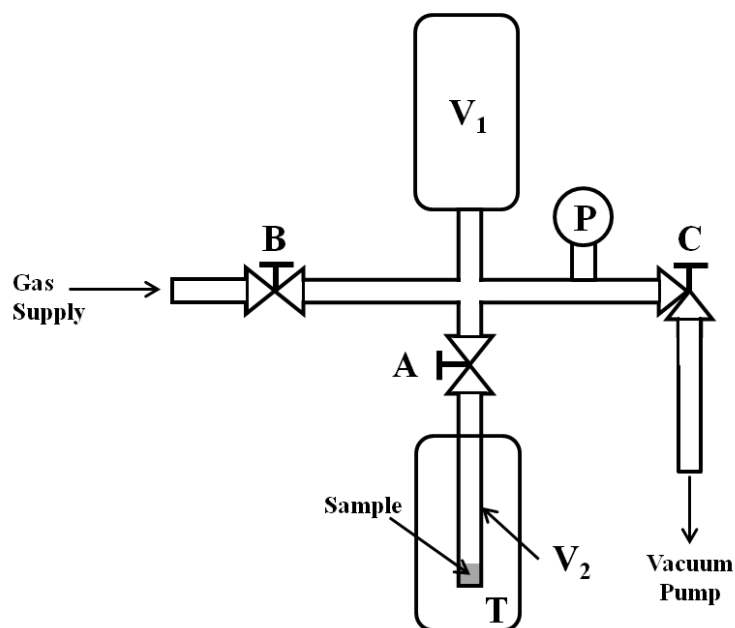


**Figure 5.4: Schematic of Volumetric measurement setup. Two volume chambers  $V_1+V_2$  connected by valve A, connection to gas supply through valve B and vacuum through valve C. Sample is contained in chamber  $V_2$  which is temperature controlled using a thermostat (T)<sup>11</sup>**

The setup involves two chambers,  $V_1$  and  $V_2$ , of known volumes, connected by a valve, A. The chamber  $V_2$  is filled with the porous media to be analysed; the entire system is degassed using a vacuum by opening valve C. Once the sample has been sufficiently 'cleaned', valves A and C are closed before valve B is opened (connection to the gas supply), allowing  $V_1$  to be filled to a set pressure. Subsequently, valve B is closed and valve A is opened, exposing  $V_2$  to the gas. The drop in pressure can be attributed to the volume difference between  $V_1$  and  $V_1+V_2$ , and any further reductions must therefore be the adsorption of gas into the porous media, as it moves from the gas phase into the adsorbate phase on the solid's surface <sup>11</sup>.  $V_2$  is maintained at 77 K using liquid  $N_2$ ; therefore an isotherm collected for  $N_2$  as the adsorptive will have a maximum pressure of ~1 bar, with a relative pressure range ( $P/P_0$ ) from 0 - 1. The amount of adsorbed gas at a set pressure  $P_i$  is given by Equation (5-4) <sup>11</sup>:

$$\Delta n = \frac{P_i V_1}{Z_{i,T} RT} - \frac{P_f (V_1 + V_2)}{Z_{f,T} RT} \quad (5-4)$$

Where:

$\Delta n$	=	adsorbed amount (mol)
$P_i$	=	initial pressure (Pa)
$P_f$	=	final pressure (Pa)
$V_1$	=	volume of dosing chamber ( $m^3$ )
$V_2$	=	volume of sample chamber ( $m^3$ )
$R$	=	universal gas constant ( $8.314 \text{ J mol}^{-1} \text{ K}^{-1}$ )
$T$	=	Temperature (K)
$Z_{i,T}$	=	gas compressibility at $P_i$
$Z_{f,T}$	=	gas compressibility at $P_f$

Measurements which are performed on commercial instruments will use both  $N_2$  for analysis, and He to measure the 'dead volume' <sup>12</sup>. Due to its inert properties compared to  $N_2$ , helium (He) can be used to measure the volume that will not be filled with adsorbed gas, therefore removing the volume of gas phase  $N_2$  from the calculation

of the adsorbed gas (effectively providing  $V_2$  from the equation above which is complicated by the presence of the solid adsorbent). However, recent investigations within the literature have confirmed that 'He entrapment' is possible in very narrow micropore samples (due to the overlapping of pore wall potentials generating a highly stable environment)<sup>13</sup>. Therefore, measurements can be 'reversed', by performing analysis with  $N_2$  and correcting using He after.

$N_2$  is historically chosen as the standard adsorptive due to its availability as a liquid, and classical adsorbents were found to exhibit a well-defined monolayer when analysed using  $N_2$ <sup>12</sup>. For determination of surface area (common analysis used with volumetric systems), the adsorptive of choice should have a low physisorptive energy, which is defined by the C constant in the BET equation, to prevent localised adsorption on heterogeneous surfaces<sup>14</sup>. Although  $N_2$  is suited to analysis of the mesoporous character of some adsorbents, more recently it has been found that it presents unsatisfactory results for microporous adsorbents, and adsorbents that have specific surface interactions, such as functional groups and charge balancing ions, due to the quadrupole moment of the adsorptive<sup>12</sup>. Argon (Ar) adsorption at 87 K is the recommended method for characterisation of micropore size. Having no quadrupole, it does not interact strongly with specific surface sites, and its monolayer structure is more well-defined than the diatomic molecule of  $N_2$  as it packs as single atoms. Therefore, more information about the adsorption isotherm can be determined at lower relative pressures, and the adsorption in micropores is better analysed<sup>12</sup>.

The method of using volumetric measurements can be quick and reliable; however, certain errors are unavoidable when carrying out such techniques. As with any adsorption measurement, the largest source of error is generated from maintaining the pressure and temperature at a constant value<sup>14</sup>. Due to the nature of the volumetric

measurement as seen in (5-4), any errors associated with a previous pressure step will affect the following steps in the isotherm, generating a cumulative error. To obtain a measureable uptake, it is suggested that the quantity of sample used for the measurement should be enough to provide a surface area between 40 – 120 m<sup>2</sup> (i.e. if a sample has surface area of 40 m<sup>2</sup>g<sup>-1</sup>, a sample mass of 1 g is required) <sup>15</sup>. Additionally, the level of liquid N<sub>2</sub> used as coolant must be kept constant to maintain the warm and cold zones of the sample tube (the measured gas volumes within the sample tube which lie above and below the level of liquid N<sub>2</sub> in the dewar, respectively). It is suggested, for the ASAP 2420 system used in this study, that the level be kept at a maximum height of ¼ in. below the top of the isothermal jacket, which is placed around the sample tube <sup>16</sup>.

#### *5.4.1.1 INSTRUMENT METHOD*

The following is a description of the standard method used for measuring N<sub>2</sub> adsorption isotherms. Initially, a dried sample tube was collected and the empty mass recorded. The sample was added to the tube and the mass recorded. The sample tube was attached to one of the degas ports, and a heating jacket placed around the bulb at the bottom of the tube. Degassing was performed by reducing the pressure to 5 mmHg and heating to 323 K, followed by reducing the pressure to 10 µmHg. Once these conditions have been met, the temperature was increased to 483 K for 2 h. The sample tube was subsequently backfilled with N<sub>2</sub>, and the degassed sample was weighed to give the mass of dry sample. The sample tube was placed onto an analysis port, with an isothermal jacket. The instrument automatically dosed the sample tube with He from the manifold to measure the dead volume, before finally evacuating the tube to commence analysis with N<sub>2</sub>. Typically, collected datasets consisted of approx. 40 adsorption points and 30 desorption points.

## 5.4.2 INTELLIGENT GRAVIMETRIC ANALYSER

Gravimetric measurements were performed using an Intelligent Gravimetric Analyser (IGA) (models 001 and 003 were available) supplied by Hiden Isochema Ltd. Measurements were conducted using CO<sub>2</sub>, CH<sub>4</sub> and N<sub>2</sub>, at temperatures close to ambient, with either static or dynamic (flowing) set-ups available. The instrument is composed of a highly sensitive vacuum microbalance, an automated gas handling system, a computer module for monitoring the outputs from the various control components, and a PC running a dedicated software package (IGASwin) for user interfacing with the IGA unit. Figure 5.5 shows the IGA unit with key components labelled and Figure 5.6 shows a close up of the internal components which are housed within the casing.

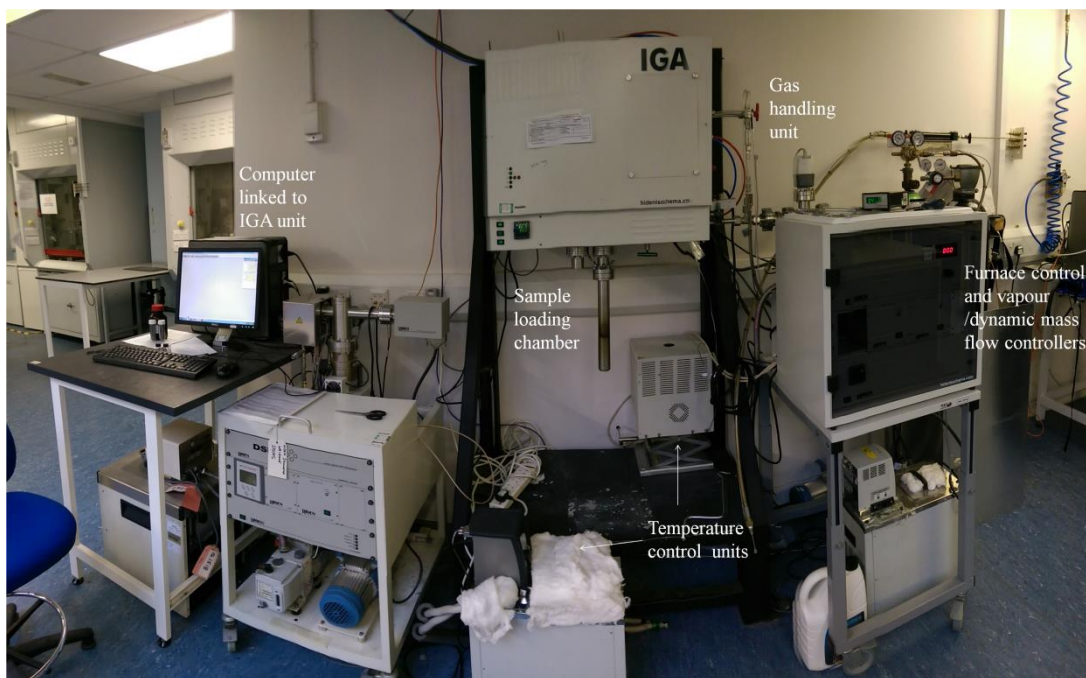


**Figure 5.5: IGA unit within Chemical and Process Engineering Department. From left to right; Computer user interface with IGA unit hosting IGASwin software, sample chamber, temperature controlling units, gas cylinders and external valves, Mass flow controllers and furnace controller**



**Figure 5.6: Internal components of IGA system. From left to right; computer module, stainless steel microbalance chamber, gas dosing pipework**

The IGA is capable of studying the adsorption/desorption isotherms of a single sorbent at any one time, therefore making it less suitable for performing routine measurements. However, the various gauges and controllers within the instrument provide accurate readings of the parameters influencing adsorption, and automated control ensures stability is maintained, minimising errors. This allows for precise measurements of the kinetics associated with adsorption, through measurement of the mass change profile at constant values of temperature and pressure.

#### *5.4.2.1 MICROBALANCE*

The IGA unit contains a microbalance capable of measuring the minute changes in mass that accompany adsorption/absorption of gas species onto a sorbent (Figure 5.7). The sample being studied is suspended in a Pyrex or quartz bulb from a compensating beam balance, with a counterweight suspended from the opposite arm of the balance to stabilise. The position of the balance head is monitored by displacement of an infrared sensor, and the beam is maintained in a zero position by applying a current through a coil. Therefore when a load is applied to the sample through gas adsorption, the current required to hold the balance head level is proportional to the force, hence the mass of adsorbed species <sup>11</sup>.

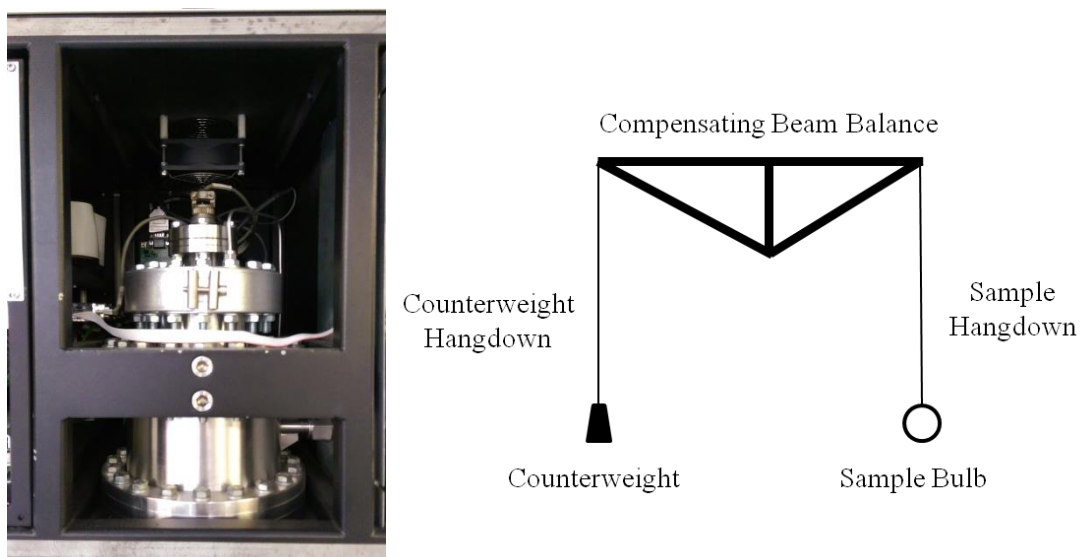


**Figure 5.7: IGA microbalance chamber, and simplified diagram of the compensating beam balance**

The overall capacity of the balance (the sum weight of all the hanging components) is either 1 g or 5 g. This allows for a weighing range of either 100 mg or 200 mg, respectively. Assuming the system is properly thermostatted, the balance will detect mass changes on a scale of 0.1  $\mu\text{g}$ , or 0.2  $\mu\text{g}$  for the 5 g capacity balance <sup>17</sup>.

The sample and counterweight are suspended using tungsten hooks fixed to the balance head and gold chain hangdowns (with an additional tungsten hook connected to the bottom of the sample hangdown chain to support the sample bulb). In order to prevent damage to the balance head by exceeding temperatures greater than 373 K, these low thermal conductivity metals are used to prevent heat transfer from the sample bulb, which can be heated to maximum temperatures of 773 K.

#### 5.4.2.2 PRESSURE REGULATION

Gas is supplied via a direct line from a cylinder when performing static measurements (additionally passing through a mass flow controller (MFC) when dynamic runs are performed), and the system has a maximum design pressure of 20 bar. The pressure within the reactor chamber is controlled via admit and exhaust valves, and monitored by three pressure transducers, 0 – 100 mbar, 0 – 1000 mbar and 0 – 20 bar (only one 0 – 20 bar transducer was available when using the IGA-001 model). The accuracy of all the transducers to regulate the set-point is 0.02% of the total range <sup>17</sup>. Figure 5.8 shows the system used to control the pressure and flow of the gas into the sample chamber.



**Figure 5.8: Pressure dosing system containing pressure transducers, automated admit and exhaust valves, and pipework for delivery of gas/vapours to IGA chamber**

Active control of pressure inside the chamber is achieved by regulation of the valve position using stepper motors attached to the shaft of each valve, and is controlled via the IGA software. During pressure set, the motors are adjusted in small increments

until the transducer detects a change in pressure (*crack rotation*); the valve is subsequently closed past the crack point to avoid overshoot and the motor adjusted slowly to allow slow ingress of pressure towards the set-point.

A number of variables can be set within the software, which controls the approach to the set-point. The motors are controlled via a Proportional-Integral-Derivative (PID) controller, allowing fine tuning of the pressure control to minimise ‘overshoot’ of the set-point. Precise control is necessary as a number of conditions must be considered to obtain meaningful results about the adsorption kinetics. Minimising overshoot avoids the system being exposed to large pressure fluctuations (i.e. during adsorption, the sample should only be exposed to increasing pressure), which may impact on the adsorption/desorption interactions, thereby avoiding the introduction of additional diffusional processes which could influence and complicate the adsorption kinetics. Pressure increases are usually carried out over a short period of time, so as to avoid interfering with the kinetics, but should be slow enough to avoid disruption of the sample.

#### *5.4.2.3 TEMPERATURE CONTROL*

The IGA is able to effectively control the temperature at a constant value to allow isothermal studies of materials, or heating to a specified temperature for outgassing of samples to a dried state before measurement. A variety of devices can be used, such as furnaces, thermo-stirrers, or cryostats. The temperature inside the reactor chamber was measured via a Type K thermocouple with resolution of  $\pm 1$  K.

Thermo-stirrers are used to regulate temperature by recirculating a heating/cooling fluid around the reactor chamber using an environmental jacket <sup>17</sup>. Typically, water is used for temperatures from 288 – 353 K (in this study, isotherms

were collected using temperatures up to a maximum of 333 K), and for temperatures below this, a mixture of 1:1 ethylene glycol-water was used, which should allow for temperatures as low as 243 K; however, the minimum temperature studied was 263 K. The system was controlled using a Grant Optima water bath, connected to the dedicated PC for automated control of the temperature set-point, allowing an accuracy of  $\pm 0.1$  K.

All sample guest species were removed prior to analysis using pre-determined outgas conditions; often requiring high temperatures. A standard 773 K furnace, supplied by Hiden Isochema Ltd. was used for this purpose. The furnace was capable of setting a range of temperatures between 373 – 773 K, at a maximum ramp rate of  $3 \text{ K min}^{-1}$ . Control of the furnace temperature was achieved using regulation of the power.

Cryostats are used for isothermal analysis requiring liquid gas temperatures. These are glass lined, insulated vessels with, in this study, a 5 L capacity. Typical cryogens used are liquid  $\text{N}_2$  (77 K), or a mixture of dry ice (solid  $\text{CO}_2$ ) and acetone (195 K), and allow for the measurement of  $\text{N}_2$  or  $\text{CO}_2$  at their boiling points, respectively. Once the dewars are filled, the sample temperature can be maintained for approximately 12 h; however, this is highly dependent on environmental conditions within the laboratory.

#### 5.4.2.4 *TEMPERATURE CONTROL OF INTERNAL BALANCE*

The internal components of the IGA unit must be kept at a constant temperature of 328 K to ensure reliable measurement of both weight and pressure. A thermoregulator within the casing circulates air around the microbalance and gas handling system. A platinum resistance thermometer is used to accurately measure the temperature to within  $\pm 0.01$  K, and small adjustments are made using a small fan heater.

#### 5.4.2.5 *REAL-TIME ANALYSIS*

The measurement of uptake within a pressure set-point is monitored by the IGASwin software in real-time to predict the asymptotic value. During each relaxation of the mass profile for each pressure step, the approach to equilibrium uptake is monitored using a non-linear least squares regression analysis against a mathematical model; in this case the Avrami model<sup>18</sup> (as discussed in Section 3.8.5) was used in the first instance, as provided by the IGASwin software. The use of the model allows for determination of the equilibration timescale, and when timescales are longer than would be appropriate for good use of instrument time, it allows a best approximation of the fitting parameters by extrapolation of the model curve. Data collected from the mass-time profiles can be used to determine kinetic parameters for the diffusion of adsorptive into the sample material. During measurements, the calculation of the model is initiated after a fixed percentage of the pressure ramp is complete; values between 50 % and 99 % are possible as the mathematical model is only used to fit the relaxation of the mass profile, and should not include sections of the pressure ramp.

#### 5.4.2.6 *TYPICAL EXPERIMENTAL PROCEDURE*

Initially, the IGA was prepared for measurement, ensuring the unit was properly thermostatted and gas supplies were connected. Having checked the sample chamber was at atmospheric pressure (either backfilled with inert gas or air from the laboratory through the air admit valve) and room temperature, the chamber was unsealed by loosening the six hexagonally arranged bolts that seal the flange fitting, and the chamber lowered slowly away from the hanging sample container. The sample bulb was carefully removed from the tungsten wire hangdown attached to the balance, by using the supplied container carrier. The bulb was cleaned and replaced onto the

balance, before the reactor chamber was replaced to act as a draught shield. Once the bulb was stable on the balance (weight had stabilised and any sway of the bulb had slowed to a minimum), the 'empty pan reading' was recorded which 'zeros' the mass reading ready for sample loading. The bulb was removed from the balance and approximately 40 mg of sample was added. Once the bulb was replaced and stability of the balance was achieved, the chamber was sealed by replacing the copper gasket which forms a seal by virtue of two opposing stainless steel knife edges biting into the copper metal; hence, this requires that a new gasket is used after every measurement to ensure a proper seal.

A first-stage rotary vacuum pump was started, lowering the pressure to below 15 mbar, after which a turbomolecular pump started, which brought the vacuum down to  $10^{-6} - 10^{-8}$  mbar; subsequent to reaching this level of vacuum, the pressure isolation valve 1 (PIV1) was opened to expose the chamber to the full force of the vacuum. It should be noted that opening PIV1 before achieving a low vacuum would result in damage to the turbomolecular pump and possible loss of fine powdered samples. During this time, an appropriate thermoregulator was chosen to heat the sample to its outgassing temperature (specified by the robustness of the sample to temperature, and data collected from the thermo-gravimetric analysis (TGA)). Outgassing was commonly carried out overnight (~16 h), but was deemed to be complete once the mass loss profile had stabilised at a value lower than the initial 'wet' weight of sample. At this time, the dry mass and zero pressure were input into the IGASwin software to initialise the data, and appropriate pressure steps were chosen for the isothermal experiment. Finally, the temperature for analysis was set (which would, in some cases, require changing the thermoregulator from the furnace to thermo-stirrer), and PIV1 was closed. Once at equilibrium, the experiment was commenced.

#### 5.4.2.7 DATA COLLECTION

Once the measurement was complete, after the specified adsorption/desorption points had been collected, data were extracted from the IGASwin software, collecting both the isothermal data (weight, pressure, temperature, and concentration for each step in the isotherm) and kinetic data (time, weight, pressure, and temperature recorded continuously over the course of the measurement). As stated above, the asymptotic values of the equilibrium points were not always achieved within the maximum time chosen for equilibration, due to time constraints set for each measurement. Therefore, manual analysis, which was performed on the kinetic data to determine kinetic parameters, was additionally used to obtain a 'corrected' equilibrium value for the mass at each pressure step. This was possible, due to the data points being independent of the prior measured steps, as initialisation of each step is performed against the calculated dry mass (mass of sample with no adsorbed species), which is measured after the outgassing procedure. A further correction is required, in order to account for the buoyancy effects on the sample due to the ingress of pressure at the beginning of each step. The mathematics required to perform this buoyancy correction is given in the Hiden manual<sup>17</sup>, however its interpretation for use in the manual correction of isotherms in this work is detailed in Appendix 10.6. In cases where equilibrium was not reached within the allotted time, the chosen kinetic model was used to determine the final uptake. However, errors in the final value will result from using a fraction of the complete equilibrium curve; therefore, an estimation of the percentage error was determined and is detailed in Section 10.6.1.

## 5.5 REFERENCES

1. Li, M.-X., Miao, Z.-X., Shao, M., Liang, S.-W. & Zhu, S.-R. Metal-organic frameworks constructed from 2,4,6-tris(4-pyridyl)-1,3,5-triazine. *Inorganic Chemistry* **47**, 4481-9 (2008).
2. Lemmon, E. W., McLinden, M. O. & Friend, D. G. *Thermophysical Properties of Fluid Systems in NIST Chemistry WebBook, NIST Standard Reference Database Number 69*. (National Institute of Standards and Technology).
3. Dubinin, M. M. The Potential Theory of Adsorption of Gases and Vapors for Adsorbents with Energetically Non-uniform Surfaces. *Chemical Reviews* **60**, 235-41 (1960).
4. Ozawa, S., Kusumi, S. & Ogino, Y. Physical Adsorption of Gases at High-Pressure .4. Improvement of Dubinin-Astakhov Adsorption Equation. *Journal of Colloid and Interface Science* **56**, 83-91 (1976).
5. Camacho, B. C. R., Ribeiro, R. P. P. L., Esteves, I. A. A. C. & Mota, J. P. B. Adsorption equilibrium of carbon dioxide and nitrogen on the MIL-53(Al) metal organic framework. *Separation and Purification Technology* **141**, 150-9 (2015).
6. Spingler, B., Schnidrig, S., Todorova, T. & Wild, F. Some thoughts about the single crystal growth of small molecules. *CrystEngComm* **14**, 751-7 (2012).
7. Feng, S. & Guanhua, L. in *Modern Inorganic Synthetic Chemistry* pp. 63-95 (Elsevier, 2011).
8. Walton, R. I. Subcritical solvothermal synthesis of condensed inorganic materials. *Chemical Society Reviews* **31**, 230-8 (2002).
9. Stock, N. & Biswas, S. Synthesis of metal-organic frameworks (MOFs): routes to various MOF topologies, morphologies, and composites. *Chemical Reviews* **112**, 933-69 (2012).
10. Atkins, P. W. *Atkins' physical chemistry*. 8th edn, (Oxford, New York : Oxford University Press, 2006).
11. Broom, D. P. in *Hydrogen Storage Materials: The Characterisation of Their Storage Properties* Ch. 4 - Gas Sorption Measurement Techniques, pp. 117-39 (Springer London, 2011).
12. Thommes, M., Kaneko, K., Neimark, A. V., Olivier, J. P., Rodriguez-Reinoso, F., Rouquerol, J. & Sing, K. S. W. Physisorption of gases, with special reference to the evaluation of surface area and pore size distribution (IUPAC Technical Report). *Pure and Applied Chemistry* **87**, 1051-69 (2015).
13. Silvestre-Albero, J., Silvestre-Albero, A. M., Llewellyn, P. L. & Rodriguez-Reinoso, F. High-Resolution N<sub>2</sub> Adsorption Isotherms at 77.4 K: Critical Effect of the He Used During Calibration. *Journal of Physical Chemistry C* **117**, 16885-9 (2013).

14. Lowell, S., Shields, J. E., Thomas, M. A. & Thommes, M. *Characterization of Porous Solids and Powders: Surface Area, Pore Size and Density*. 1 edn, (Springer, 2004).
15. Corp, M. I. *ASAP 2020 Accelerated Surface Area and Porosimetry System Operator's Manual V4.01*. (2011).
16. Corp., M. I. *Application Note 84 Liquid Nitrogen Level When Using Isothermal Jackets*. (1998).
17. Hiden Analytical Ltd. *IGA Systems User Manual*. (2002).
18. Avrami, M. Kinetics of Phase Change. II Transformation-Time Relations for Random Distribution of Nuclei. *The Journal of Chemical Physics* **8**, 212-24 (1940).

# Chapter VI

# 6 CHARACTERISATION OF MOF STRUCTURES

---

## 6.1 SYNTHESIS & CHARACTERISATION OF $\text{Cu}(\text{BPETHA})_2\text{SiF}_6$

The Metal-Organic Framework (MOF),  $[\text{Cu}(\text{bpetha})_2(\text{SiF}_6)]_n$ , was synthesised using a method adapted from the Noro *et al.*<sup>1</sup> synthesis of  $\text{Cu}(\text{bpetha})_2(\text{PF}_6)$ , via a batch diffusion of two solutions. Initially, a  $20 \text{ cm}^3$  aqueous solution was prepared containing a 1:1.5 molar ratio of inorganic reactants,  $\text{Cu}(\text{BF}_4)_2 \cdot 6\text{H}_2\text{O}$  (1 mmol, 345 mg) and  $(\text{NH}_4)_2(\text{SiF}_6)$  (1.5 mmol, 267 mg). The aqueous solution was heated to  $\sim 353 \text{ K}$  to aid dissolution of  $(\text{NH}_4)_2\text{SiF}_6$ . Additionally, a  $20 \text{ cm}^3$  acetone or methanol solution containing 2 equivalents (w.r.t. Cu) of 1,2-bis(4-pyridyl)ethane (bpetha) (2 mmol, 368 mg) was prepared. After sufficient time, when the clarity of the aqueous solution suggested maximum dissolution of the inorganic components had been achieved, the solution was allowed to cool below the boiling point of the organic solvent used in the second solution, before mixing both solutions together and stirring for 15 min, during which a purple powder was formed. Powders were filtered and washed in excess of fresh mother liquor, before drying in air. Prior to adsorption analysis, the powder was solvent exchanged for 3 d in methanol, with the solution being changed twice daily. The final sample gave a yield of 78.4 %.

### 6.1.1 PREPARATION OF SINGLE CRYSTALS OF $\text{Cu}(\text{BPETHA})_2\text{SiF}_6$

In addition to the batch diffusion method, solvent diffusion experiments were set up to obtain single crystals for X-ray diffraction to determine the crystal structure of the produced material. The same solutions were prepared as above; a  $2 \text{ cm}^3$  volume of

each solution was extracted and layered in a glass vial, with the addition of a buffer solution of water, used to separate the two layers. After two weeks, purple crystals formed, which were subsequently analysed by single crystal X-ray diffraction.

A variety of metal salt components and different solvents were used in an attempt to synthesise crystals of sufficient quality, dictated by the quality of the diffraction pattern obtained by single crystal X-ray diffraction; **Table 6.1** shows the different conditions that were used to grow crystals based on the methods employed by Zaworotko *et al.*<sup>2</sup> for the production of SIFSIX-2-Cu and SIFSIX-2-Cu-I, the non-interpenetrated and interpenetrated versions of Cu(dpa)<sub>2</sub>SiF<sub>6</sub> (dpa = 1,2-bis(4-pyridyl)ethyne MOF, and Noro *et al.* synthesis of Cu(bpetha)<sub>2</sub>(PF<sub>6</sub>)<sub>2</sub><sup>1</sup>.

**Table 6.1: Conditions used for the synthesis of Cu(bpetha)<sub>2</sub>SiF<sub>6</sub>, as adapted from Zaworotko *et al.*<sup>2</sup>**

Reaction No.	Reactant	Inorganic concentration (M)	Solvent	Organic concentration (M)	Solvent
1	Cu(NO <sub>3</sub> ) <sub>2</sub> .2.5H <sub>2</sub> O	0.05	Water	0.1	Acetone
2	Cu(NO <sub>3</sub> ) <sub>2</sub> .2.5H <sub>2</sub> O	0.0745	Ethylene glycol	0.0575	Ethanol
3	Cu(BF <sub>4</sub> ) <sub>2</sub> .6H <sub>2</sub> O	0.0745	Ethylene glycol	0.0575	Ethanol
4	Cu(SO <sub>4</sub> ).6H <sub>2</sub> O	0.0745	Ethylene glycol	0.0575	Ethanol
5	Cu(NO <sub>3</sub> ) <sub>2</sub> .2.5H <sub>2</sub> O	0.0745	Methanol	0.0575	Dimethyl sulfoxide
6	Cu(BF <sub>4</sub> ) <sub>2</sub> .6H <sub>2</sub> O	0.0745	Methanol	0.0575	Dimethyl sulfoxide
7	Cu(SO <sub>4</sub> ).6H <sub>2</sub> O	0.0745	Methanol	0.0575	Dimethyl sulfoxide

### 6.1.2 NON-POROUS $[\text{Cu}(\text{BPETHA})(\text{OH}_2)_3(\text{NO}_3)]\text{SiF}_6 \cdot (\text{H}_2\text{O}) \cdot 0.5(\text{CH}_3\text{OH})$

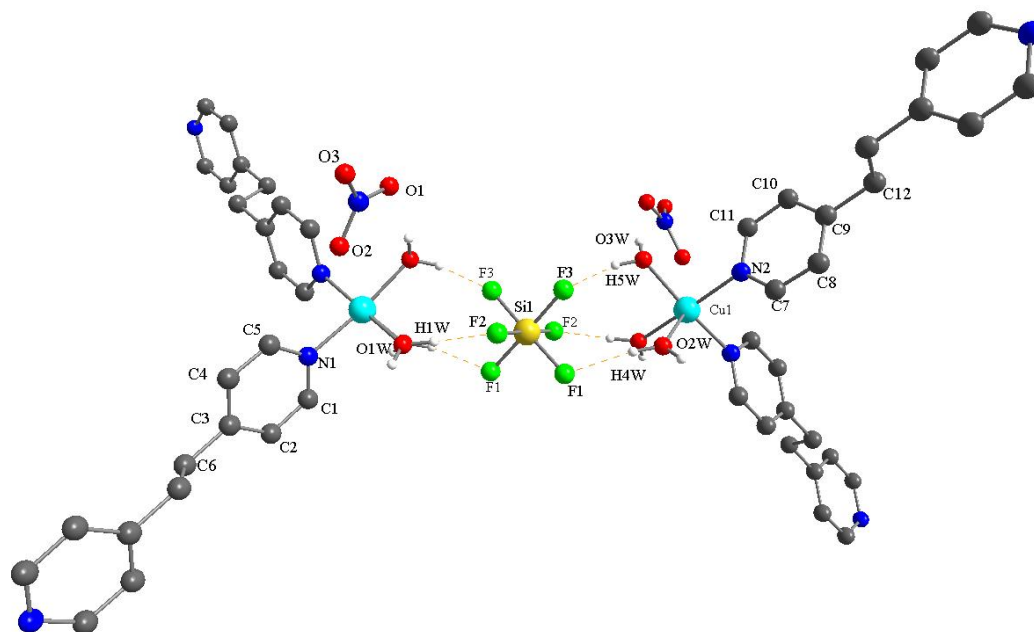


**Figure 6.1:** Structure of  $[\text{Cu}(\text{bpetha})(\text{OH}_2)_3(\text{NO}_3)]\text{SiF}_6 \cdot (\text{H}_2\text{O}) \cdot 0.5(\text{CH}_3\text{OH})$ . Cu (light blue), Si (yellow), F (green) O (red), N (blue), C (grey). Uncoordinated solvents and H's on ligands omitted for clarity. Depicts polymeric chains of Cu-bpetha, Cu coordinated to water molecules which interact with  $\text{SiF}_6^{2-}$  through hydrogen bonding to link chains.

Reaction 1 was found to produce two distinct crystal morphologies, which were visually distinguishable by their purple and blue colours. The purple crystals were unidentifiable through use of single crystal X-ray diffraction, with no structural solution possible, due to a broad diffraction pattern, and a highly disordered structure. The blue crystals were identified as a dense structure with the formula  $[\text{Cu}(\text{bpetha})(\text{OH}_2)_3(\text{NO}_3)]\text{SiF}_6 \cdot (\text{H}_2\text{O}) \cdot 0.5(\text{CH}_3\text{OH})$ , as shown in Figure 6.1. The structure has a monoclinic space group  $C2/c$ , with lattice parameters  $a = 17.5309(10) \text{ \AA}$ ,  $b = 15.8396(9) \text{ \AA}$ ,  $c = 12.9996(8) \text{ \AA}$ , and  $\beta = 90.1559(31)^\circ$ , and a cell volume of  $3609.75(37) \text{ \AA}^3$ . The extended structure of the unit cell consists of a  $\text{Cu}^{2+}$  metal centre coordinated to two bpetha units, which are positioned in a cis conformation around  $\text{Cu}^{2+}$ . The coordination around the metal centre is square pyramidal; it is linked via a dipolar bond to the N atoms of the bpetha ligands and coordinated to three water

molecules. A monodentate nitrate group is positioned axially to the bpetha ligands and has a longer range interaction with the  $\text{Cu}^{2+}$  atom, completing a distorted octahedral geometry. This conformation produces 1D polymer chains of  $\text{Cu}^{2+}$  atoms bonded to bpetha ligands. A 3-dimensional lattice is formed via hydrogen bonding interactions between the  $[\text{SiF}_6]^{2-}$  units and the coordinated water molecules on the  $\text{Cu}^{2+}$  atoms as shown in Figure 6.1. The coordinated water molecules are connected to  $\text{Cu}^{2+}$ , at distances of 1.9565(1) Å, 1.9928(1) Å, and 2.2491(1) Å for Cu1 - O1W, Cu1 - O3W, and Cu1 - O2W, respectively. It follows that the H-F distances between the coordinated water molecules and fluorine atoms of the  $[\text{SiF}_6]^{2-}$  unit are 1.7228(222) Å, 1.7314(326) Å, and 2.1627(321) Å for bonds H1W - F2, H5W - F3, and H4W - F1, respectively. However, the interaction is maximised by distortion of the octahedral position of the coordinated water molecule (O2W), so that the angle between O2W - Cu1 - O2, the coordinated oxygen atom of the nitrate group, is 158.287(2) °.

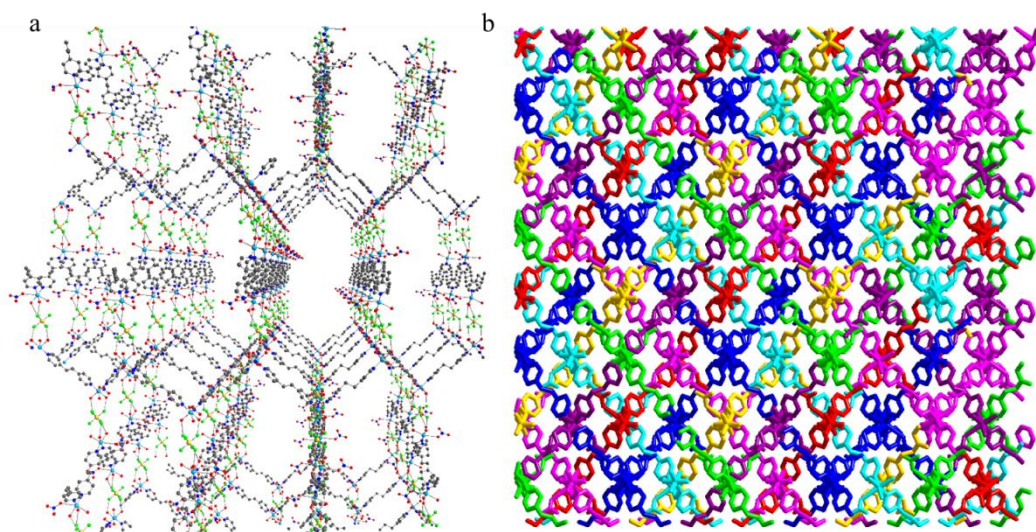


**Figure 6.2:** (a) One network formed by coordination of  $[\text{SiF}_6]^{2-}$  units to chains of Cu(bpetha). (b) Structure is 8-fold interpenetrated shown by intertwined chains of different colours.

The extended structure links orthogonal chains of Cu-bpetha through hydrogen bonded  $[\text{SiF}_6]^{2-}$  units, forming a ‘honeycomb’ network as seen in Figure 6.2(a). The identical interpenetrating networks create an 8-fold interpenetrated structure (Figure

6.2(b)), which is found to have zero solvent accessible volume from PLATON<sup>3</sup>, giving a non-porous, densely packed crystal structure. Within the framework structure are two non-coordinating water molecules, and one non-coordinating methanol molecule. Hydrogen bonding between the solvent molecules and the framework structure is represented in Figure 6.3. Free water molecules exhibit hydrogen bond lengths between H3W – O4W (1.852 Å) and H7W – O2W (2.689 Å), and between the nitrate groups and solvent water molecules, H8W – O3 (2.021 Å). The oxygen atom of the methanol molecule, O1S, sits at distances from N1 and N2 of the bpetha molecules of 2.447 Å and 2.765 Å, respectively. The methanol molecule lies between two interpenetrating frameworks, and is disordered across two sites with fractional occupancy of 0.5.

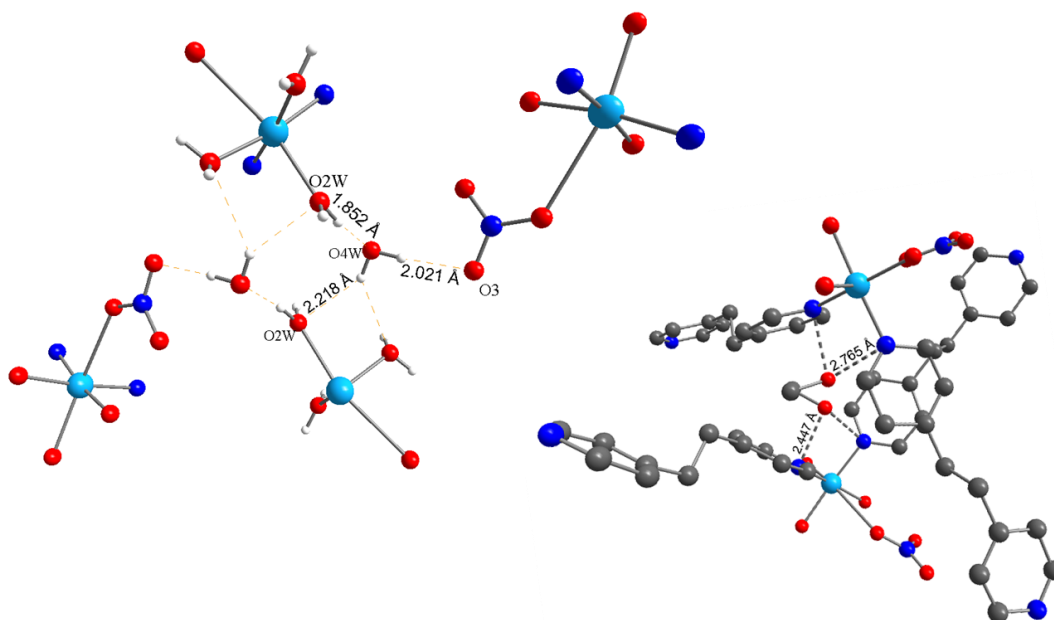


**Figure 6.3: Hydrogen bonding present between coordinated water molecules and nitrate groups, and methanol molecule to nitrogen atoms on bpetha ligands.**

### 6.1.3 STRUCTURAL DETERMINATION OF POROUS $\text{Cu}(\text{BPETHA})_2(\text{SiF}_6)$

The second phase produced from the synthesis method described above was unsuitable for X-ray diffraction, due to disorder, and therefore could not be used to obtain a structure solution. At the time of writing, no method attempted was able to provide crystals that were suitable for single crystal X-ray diffraction. Measurement using powder X-ray diffraction (PXRD) showed that the material formed from batch solution reactions, using  $\text{Cu}(\text{BF}_4)_2 \cdot 6\text{H}_2\text{O}$  as a starting material, formed a single phase structure, while reactions using similar salts,  $\text{Cu}(\text{NO}_3)_2 \cdot 2.5\text{H}_2\text{O}$  (or  $3\text{H}_2\text{O}$ ) and  $\text{Cu}(\text{SO}_4) \cdot 6\text{H}_2\text{O}$ , formed a different phase or mixed phases. Figure 6.4 shows a comparison between the collected PXRD patterns of the materials obtained from syntheses using the three aforementioned metal salts. It was not possible to match any of the diffraction patterns to the predicted pattern of  $[\text{Cu}(\text{bpetha})(\text{OH}_2)_3(\text{NO}_3)]\text{SiF}_6 \cdot (\text{H}_2\text{O}) \cdot 0.5(\text{CH}_3\text{OH})$ .

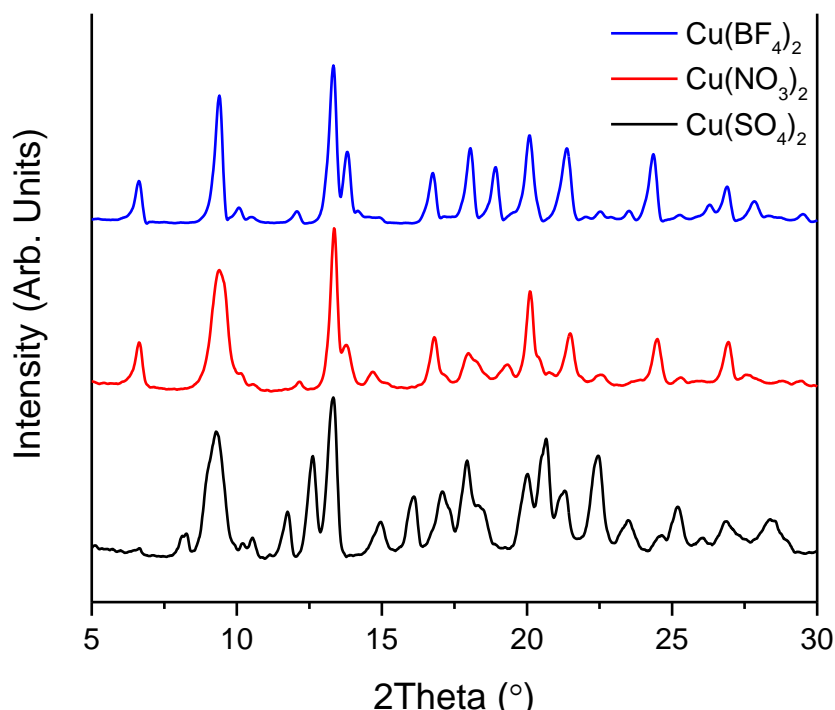


**Figure 6.4:** Powder X-ray diffraction data collected for samples of  $\text{Cu}(\text{bpetha})_2\text{SiF}_6$  using different Cu metal salts.

A search of the literature revealed a number of isostructural structures based on the  $[\text{SiF}_6]^{2-}$  unit, using copper centres and a variety of ligands, as detailed in Table 6.2. A number of other structures have been synthesised using different transition metal centres and hexafluoro- ( $\text{MF}_6$ ) anions<sup>2,4-8</sup>, which tend to have the general formula of  $[\text{Cu}(\text{bipyridyl ligand})_2(\text{SiF}_6)]_n$ ; it is currently proposed that by synthesising the materials in this study using methods similar to those used to produce the materials identified from the open literature, that the formula for the reported material will likely be of the form  $[\text{Cu}(\text{bpetha})_2(\text{SiF}_6)]$ . Comparison of the ligand structures, shown in Figure 6.5, indicates that ligands with terminal nitrogen atoms in the para- position to the interconnecting bond between the pyridyl rings, produce tetragonal structures. Hence, it was postulated that the structure obtained via batch synthesis was most likely a tetragonal cell, as this is also known to be a common crystal system for this type of MOF. In the case where the ligand is flexible, such as UTSA-48, the structure maintains a tetragonal cell with the ligand no longer lying in-plane between the copper centres<sup>6</sup>. This provides strength to the argument that the structure of bpetha will likely form a tetragonal cell, which has a copper centre coordinated via nitrogen to four bpetha units in the equatorial plane, and coordinated to two  $[\text{SiF}_6]^{2-}$  units via the fluorine atoms in the axial position.

**Table 6.2: Collection of Crystal structures of similar  $\text{Cu}(\text{ligand})_2\text{SiF}_6$  containing structures**<sup>2,5-8</sup>

MOF	$\text{Cu}(\text{SiF}_6)$ (Bipy) <sub>2</sub> · 4H <sub>2</sub> O	$\text{Cu}(\text{bpy}-2)_2$ ( $\text{SiF}_6$ )	$\text{Cu}(\text{SiF}_6)(\text{dpm})_2$ · 2H <sub>2</sub> O	$\text{Cu}(\text{SiF}_6)$ (4-PINA) <sub>2</sub> UTSA-48	$\text{Cu}(\text{dpa})_2(\text{SiF}_6)$ SIFSIX-2-Cu	$\text{Cu}(\text{dpa})_2(\text{SiF}_6)$ · 2.5CH <sub>3</sub> OH SIFSIX-2-Cu-i
Chemical Formula	C <sub>20</sub> H <sub>32</sub> CuF <sub>6</sub> N <sub>4</sub> O <sub>8</sub> Si	C <sub>24</sub> H <sub>20</sub> CuF <sub>6</sub> N <sub>4</sub> Si	C <sub>22</sub> H <sub>20</sub> CuF <sub>6</sub> N <sub>4</sub> O <sub>4</sub> Si	C <sub>24</sub> H <sub>18</sub> CuF <sub>6</sub> N <sub>4</sub> O <sub>4</sub> Si	C <sub>24</sub> H <sub>16</sub> CuF <sub>6</sub> N <sub>4</sub> Si	C <sub>26.5</sub> H <sub>26</sub> CuF <sub>6</sub> N <sub>4</sub> O <sub>2.5</sub> Si
Formula Mass	662.14	570.7	610.05	632.06	566.04	646.14
Crystal System	Tetragonal	Tetragonal	Monoclinic	Tetragonal	Tetragonal	Tetragonal
Space Group	P4/mmm	P4/nmm	C2/c	P4/ncc	P4/mmm	I4/mmm
a (Å)	11.108(1)	18.8471(11)	22.276(3)	18.2679(3)	13.6316(14)	13.6490(11)
b (Å)	11.108(1)	18.8471(11)	8.0625(11)	18.2679(3)	13.6316(14)	13.6490(11)
c (Å)	8.1107(9)	7.9975(5)	15.773(2)	15.9522(5)	7.968(1)	8.0920(6)
β (°)	-	-	123.757(2)	-	-	-
Vol (Å <sup>3</sup> )	1000.8(1)	2840.8	2355.2(5)	5323.5(2)	1480.6(3)	1507.5(2)
Density (g cm <sup>-3</sup> )	1.098	0.666	1.720	0.789	0.635	1.423

dpm = di(3-pyridyl)methanone

4-PINA = (4-Pyridyl)isonicotinamide

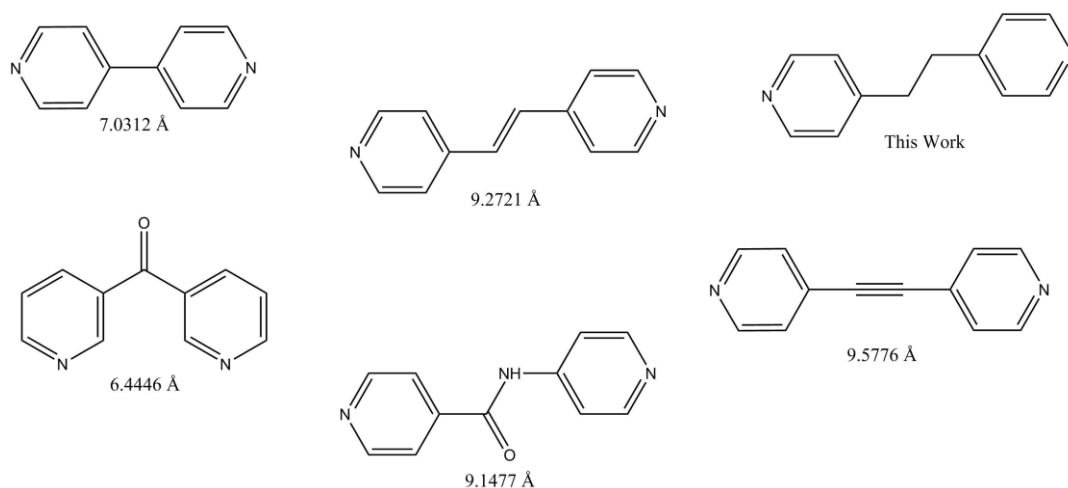


**Figure 6.5: Organic ligand structures and the associated distances between the terminal nitrogen atoms of the ligand<sup>2,5-8</sup>. Used for comparison with bpetha ligand used in this work.**

Diffraction data collected on the batch synthesis product from the metal salt  $\text{Cu}(\text{BF}_4)_2 \cdot 6\text{H}_2\text{O}$ , was analysed using the GSAS software<sup>9</sup>, where a Le Bail refinement was performed, allowing fitting of the diffraction data to a set of unit cell parameters and instrumental corrections, such as zero point, peak width and peak shape parameters. In such refinements, a space group is chosen to define the symmetry within the cell, however, the structural (atomistic) parameters are not defined and the unit cell is essentially a ‘black box’. Using lattice parameters similar to those found from the materials reported in the literature, and assuming an initial space group of  $P4$ , the lowest symmetry allowed for a tetragonal cell, a model was refined to fit the data which produced the fit shown in Figure 6.6. The red dots show the experimental data, which is overlaid by the calculated pattern in green. The difference curve (magenta) and black tick marks of the  $P4$  space group show the good agreement between the predicted model and the experimentally obtained diffraction data, as only small deviations are seen between the collected and calculated peaks, determined by atomic positions within the cell, which, therefore, cannot be corrected using a Le Bail refinement model.

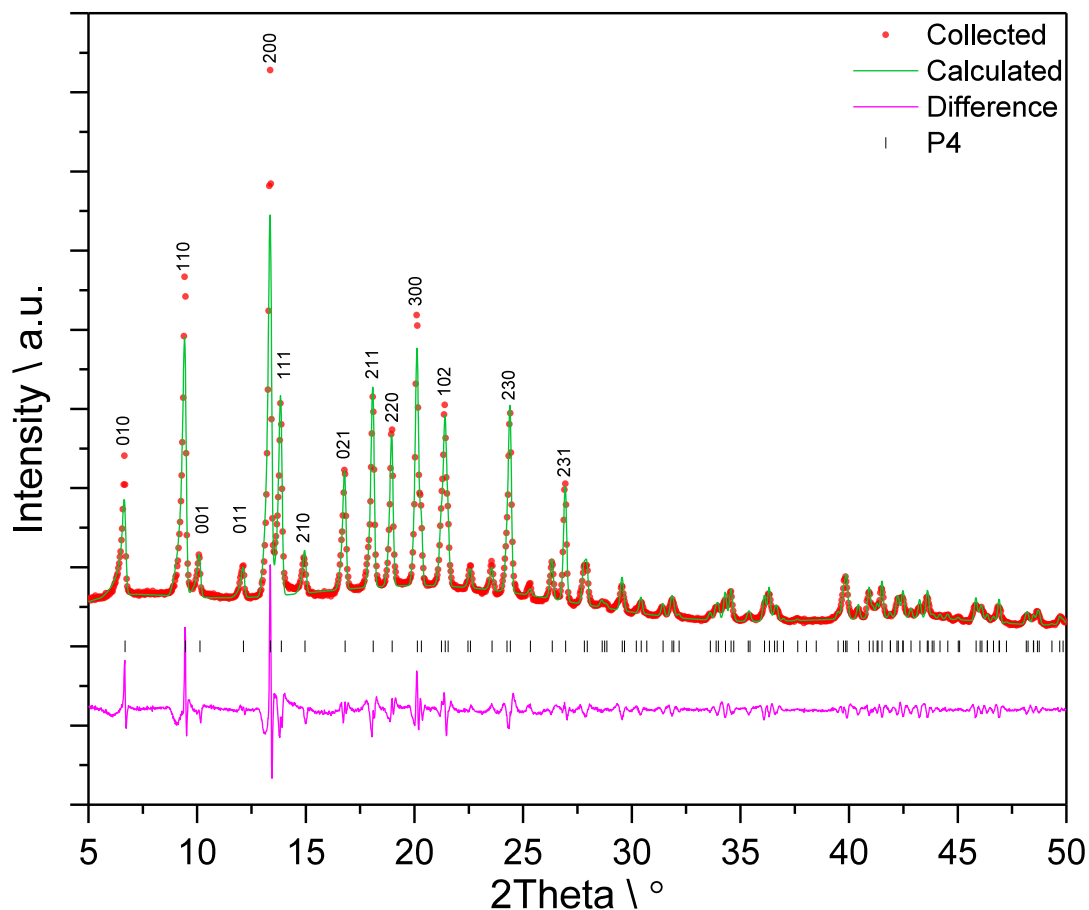


**Figure 6.6: GSAS Le Bail refinement of powder diffraction data collected on  $\text{Cu}(\text{bpetha})_2\text{SiF}_6$ . Pattern was fit to the P4 space group. Collected data (red), Calculated peaks (green), Difference curve (pink), allowed reflections of the P4 space group (|)**

Additionally, there are no tick marks present that do not have an associated intensity peak from the material, suggesting that there are no obvious impurities within the sample, and the symmetry is appropriate for the pattern. Higher symmetry will be possible, with the structure likely to possess systematic absences dependent upon the atom positions within the cell, however, due to the lack of information which powder X-ray diffraction provides on peaks with similar d-spacings, it is difficult to fully determine the crystal structure for such a complex metal-organic framework, with additional issues arising from the weaker diffracting atoms that are more abundant in the structure than the stronger diffracting species (copper and silicon).

The predicted lattice parameters were calculated to be  $a = b = 13.2157(6)$  Å and  $c = 8.7321(4)$  Å; with an  $R_{wp} = 0.0659$ . Comparison of the crystal structure of  $\text{Cu}(\text{bpy}-2)_2(\text{SiF}_6)$  in Table 6.2 with  $\text{Cu}(\text{bpetha})_2(\text{SiF}_6)$ , which is chemically similar bar the mass difference of two hydrogen atoms, shows that the new cell is predicted to be slightly elongated in the c-axis and the a and b-axes are a factor of  $\sqrt{2}$  smaller.

#### 6.1.4 THERMAL STUDIES OF $\text{Cu}(\text{BPETHA})_2(\text{SiF}_6)$

A Powder X-ray diffraction experiment was performed by Dr Elliot J. Carrington (University of Sheffield), which followed the structural changes associated with the heating of a sample of  $\text{Cu}(\text{bpetha})_2(\text{SiF}_6)$ . The experiment consisted of a series of 30 min scans over the  $2\theta$  range  $5 - 60^\circ$ , at temperatures from 353 K to 453 K, in 20 K increments. Figure 6.7 shows a stacked plot of the scans, with an initial measurement at 298 K, followed by the scans at increasing temperature, and the final result again showing the diffraction pattern after cooling to 298 K.

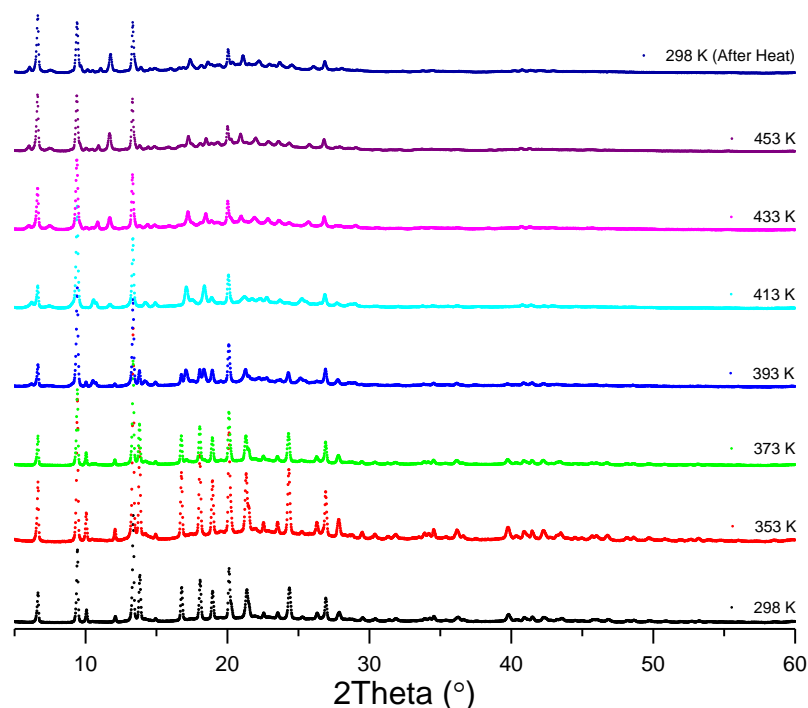


**Figure 6.7: Powder diffraction data collected during heating of the sample  $\text{Cu}(\text{bpetha})_2\text{SiF}_6$ . The sample diffraction pattern was measured at 20 K intervals from 353 K to 453 K.**

It can be seen, from the results presented, that the initial heating to 353 K produced higher intensity peaks over the entire temperature range, with the same number and position of reflections as the initial measurement. The most obvious changes in the pattern occur at 393 K when additional low intensity reflections begin to appear. After heating, the material is irreversibly changed with a number of new reflections appearing, for example at  $6.05^\circ$  and  $7.51^\circ$ , and peaks associated with the original phase, for example the 001 and 111 reflections, having been lost.

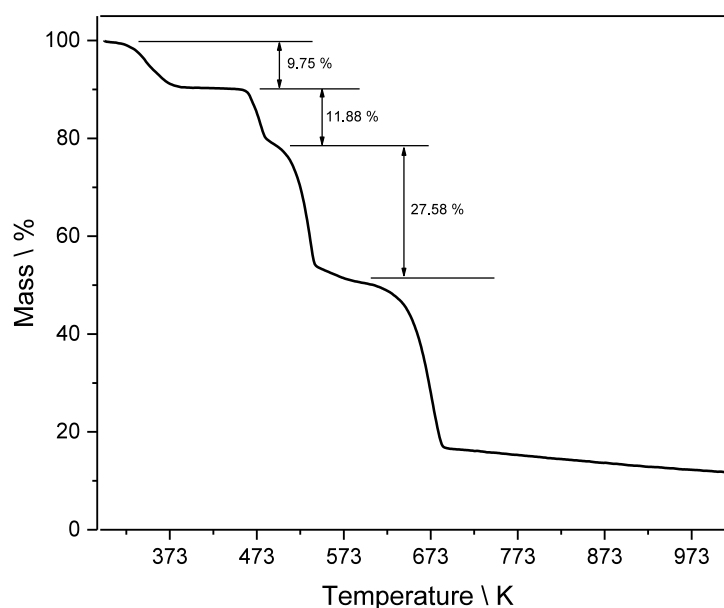


**Figure 6.8: Thermogravimetric analysis of  $\text{Cu}(\text{bpetha})_2\text{SiF}_6$ . Initial mass loss shows 9.75 % solvent content up to 473 K. Structure begins to degrade after 473 K**

Thermogravimetric analysis of the as-synthesised structure was performed to determine solvent content of the structure and the temperature at which degradation of the structure occurs. Figure 6.8 shows the mass loss profile, from room temperature to 1023 K, for the as-synthesised structure which is dried in air after methanol exchange for 3 d. The profile shows four distinct mass losses up to a temperature of 693 K, at which point complete degradation of the sample has occurred. The first mass loss of 9.64 % is associated with loss of solvent from the porosity; complete desolvation of the material, with heating at atmospheric pressure, occurs at  $\sim 393$  K. The further mass

losses are associated with loss of components from the coordinated structure. The structural integrity of the material is maintained from room temperature up to 453 K.

### 6.1.5 ELEMENTAL ANALYSIS OF $\text{Cu}(\text{BPETHA})_2\text{SiF}_6$

Analysis of the bonding within the synthesised structure was performed using Fourier Transform Infrared (FT-IR) Spectroscopy. The comparison between the three materials synthesised using the components,  $\text{Cu}(\text{BF}_4)_2 \cdot 6\text{H}_2\text{O}$ ,  $\text{Cu}(\text{NO}_3)_2 \cdot 2.5\text{H}_2\text{O}$ , and  $\text{Cu}(\text{SO}_4)_2 \cdot 6\text{H}_2\text{O}$ , is shown in Figure 6.9. Table 6.3 gives the wavenumbers of the prominent peaks, which samples exhibited each peak, and the peak assignments which could be identified.

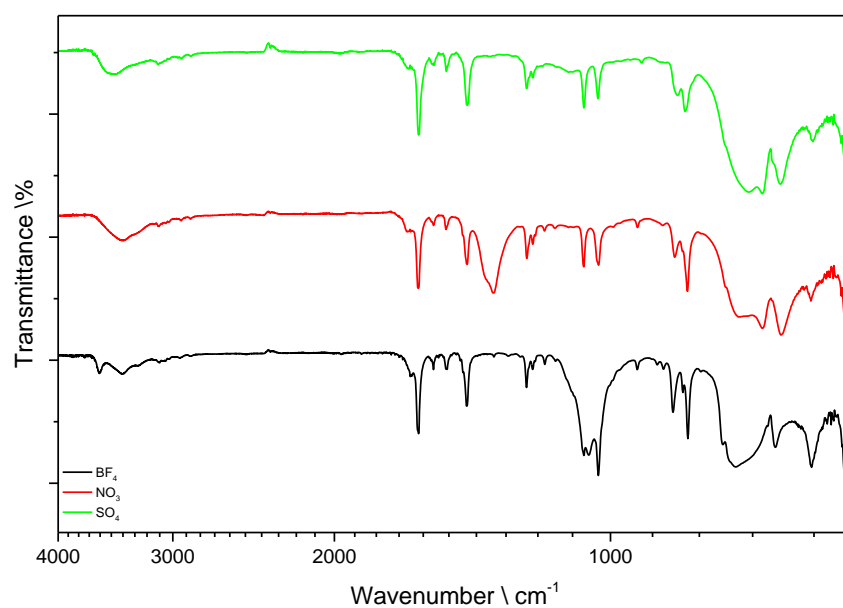


**Figure 6.9: FT-IR Spectra for  $\text{Cu}(\text{bpetha})_2\text{SiF}_6$ . Measurements of three synthesised materials using metal salts,  $\text{Cu}(\text{SO}_4)$  (green),  $\text{Cu}(\text{NO}_3)_2$  (red), and  $\text{Cu}(\text{BF}_4)_2$  (black).**

**Table 6.3: Key Infrared peaks for samples of Cu(bpetha)<sub>2</sub>SiF<sub>6</sub>, and associated bond vibrations**

Wavenumber (cm <sup>-1</sup> )	Sample	Vibration
554	All	-
604	All	Pyridine (Py)
652, (662)	NO <sub>3</sub> , SO <sub>4</sub> , (BF <sub>4</sub> )	-
669- 761 (broad)	All	C-H
824, (829)	BF <sub>4</sub> , NO <sub>3</sub> (SO <sub>4</sub> )	-
854, 851, 845	BF <sub>4</sub> , NO <sub>3</sub> , SO <sub>4</sub>	-
934, (924)	BF <sub>4</sub> , NO <sub>3</sub> , (SO <sub>4</sub> )	-
1030	All	C-C stretch, bend
1056	BF <sub>4</sub>	-
1068	All	C-C stretch, bend
1179	BF <sub>4</sub> , NO <sub>3</sub>	-
1215	All	C-C stretch, bend
1234	All	C-C stretch, bend
1342	NO <sub>3</sub> (broad)	NO <sub>3</sub> <sup>-</sup> stretch
1434	All	C-H bend
1508	All	C=C, Aromatic
1559	All	C=C, Aromatic
1619	All	C=N, Aromatic
2349	All (negative peak)	(CO <sub>2</sub> ) stretch, captured by material
2872	All	C-H stretch
2940	All	C-H stretch
3100	All	C-H stretch, Aromatic
3408, (3481)	All, broad peaks (SO <sub>4</sub> )	H bonds
3605	BF <sub>4</sub> <sup>*</sup>	O-H stretch,

<sup>\*</sup>possibly hidden in NO<sub>3</sub> and SO<sub>4</sub>

CHN analysis was performed on the samples which showed similar results from the powder diffraction data. Table 6.4 shows the percentages of carbon, hydrogen and nitrogen within the materials analysed. Expected percentages were assumed based on a double interpenetrated structure of Cu(bpetha)<sub>2</sub>SiF<sub>6</sub>.

**Table 6.4: CHN analysis of Cu(bpetha)<sub>2</sub>SiF<sub>6</sub> for structures synthesised from Cu(NO<sub>3</sub>)<sub>2</sub> and Cu(BF<sub>4</sub>)<sub>2</sub>**

Material	C	H	N
Expected Structure	50.21	4.18	9.76
Cu(bpetha) <sub>2</sub> SiF <sub>6</sub> (BF <sub>4</sub> )	43.80	4.57	8.6
Cu(bpetha) <sub>2</sub> SiF <sub>6</sub> (NO <sub>3</sub> )	42.75	4.74	10.05

## 6.2 SYNTHESIS & CHARACTERISATION OF [Cu(TPT)]BF<sub>4</sub>.0.75H<sub>2</sub>O

The MOF material, [Cu(TPT)]BF<sub>4</sub>.0.75H<sub>2</sub>O, was synthesised using a solvothermal method, using initially determined conditions of 423 K with Cu(BF<sub>4</sub>)<sub>2</sub>.6H<sub>2</sub>O (2 mmol, 690 mg) and 2,4,6-tri(4-pyridyl)-1,3,5-triazine (TPT) (1 mmol, 312.3 mg) in 10 cm<sup>3</sup> of methanol. After heating in a stainless steel autoclave with inner Teflon<sup>®</sup> liner for 48 h, the mixture produced small red crystals of the product. The resulting solution was further washed and filtered with excess methanol to remove impurities. Yield from synthesis method was determined to be 14.3 %

Insoluble impurities of TPT were found to persist after washing of the reaction mixture, due to the low solubility of TPT in methanol at room temperature. A further separation technique was required to purify the MOF product for characterisation and study of adsorption properties. Solutions of TPT which have been used in the synthesis of MOFs have often been solvent mixtures allowing low concentrations to be dissolved. A 2:3 solution of ethanol/chloroform was used to dissolve TPT at a concentration of 12.8 mM with refluxing at 353 K; this method was initially used to dissolve impurities of TPT from the reaction mixture, however this resulted in the dissolution/degradation of the MOF material. A density separation technique was used to collect pure crystals of [Cu(TPT)]BF<sub>4</sub>.0.75H<sub>2</sub>O; the density of the ligand TPT was found from the literature to be 1.42 g cm<sup>-3</sup><sup>10</sup>, whereas the expected crystal density of the MOF product from X-ray diffraction experiments was calculated to be 1.62 g cm<sup>-3</sup>. The difference in densities allowed for their separation by using a solvent which has a density between 1.42 and 1.62; the chosen solvent was tetrachloroethylene (density 1.623 g cm<sup>-3</sup>, at 293 K), which has a higher density than the range required and no other suitable solvents could be found which were within the density range and posed a lower risk than tetrachloroethylene. The impure product was added to the solvent at room temperature

in a measuring cylinder, the temperature of the solution was increased under the control of a water bath until separation of the MOF crystals from the TPT solids was sufficient. The floating TPT solids were collected from the top of the solvent, leaving the MOF product at the bottom of the measuring cylinder. The MOF crystals were collected and separated from tetrachloroethylene, washed and stored in methanol prior to drying for adsorption measurements.

Single crystal diffraction data were collected by Dr. Alan R. Kennedy, giving space group *Cc* with lattice parameters  $a = 19.6546(8) \text{ \AA}$ ,  $b = 17.9133(6) \text{ \AA}$ ,  $c = 24.0581(11) \text{ \AA}$ , and  $\beta = 112.816(5)^\circ$ , with cell volume  $7807.6(5) \text{ \AA}^3$ . The coordination geometry around copper within the MOF crystal is shown in Figure 6.10; The  $\text{Cu}^+$  metal centres are coordinated via N atoms to three TPT ligands in a trigonal planar arrangement with bond distances between  $1.9613 - 1.9970 \text{ \AA}$ . A charge balancing  $[\text{BF}_4]^-$  anion is present within the coordination sphere of the metal atom, with Cu2-F distance of  $2.6784(1) \text{ \AA}$ . One TPT ligand in each bonding triplet is rotated by  $84.171 - 86.599^\circ$  from the horizontal plane, which allows the structure to extend in 3-dimensions. The overall unit cell is formed by the interpenetration of four nets; each has a distinct copper centre.

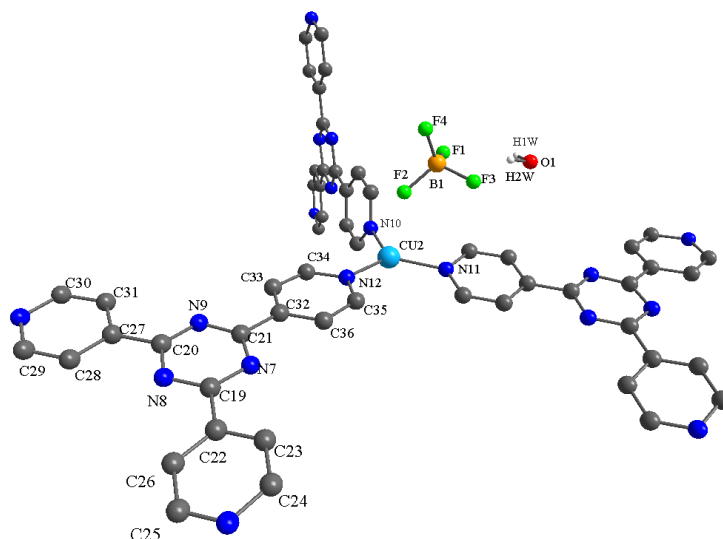


**Figure 6.10:** Structure of  $[\text{Cu}(\text{TPT})]\text{BF}_4 \cdot 0.75\text{H}_2\text{O}$ . Cu (light blue), F (green), O (red), N (blue), C (grey), B (orange), H (white). Framework H's were omitted for clarity.

The asymmetric unit of the structure is shown in Figure 6.11. This shows the four copper centres, bonded to a TPT ligand, and the anions, which charge balance the positive framework. Four  $[\text{BF}_4]^-$  units are observed, with one unit being disordered over two positions (Fractional Occupancy  $\frac{3}{4}\text{B4}$ :  $\frac{1}{4}\text{B5}$ ). Guest molecules of water are found within the structure, with 3 molecules per 4 Cu atoms of the asymmetric unit. These molecules are hydrogen bonded to the F atoms of the  $[\text{BF}_4]^-$  anions, with bond lengths ranging from 1.7154 – 2.8052 Å. The position of the anion and guest species are within a pore channel located along the a axis of the framework. The anions are centralised within the pore channel, with only F2 having a bond distance to Cu2, which closely resembles an interaction with the metal centre of 2.6784 Å. The space filling model of the  $\text{BF}_4$  units in Figure 6.12 shows that most of the pore volume is filled by the anions, and analysis using PLATON<sup>3</sup> found the accessible void volume to be 356.5 Å<sup>3</sup> which represents 4.6 % of the unit cell volume.

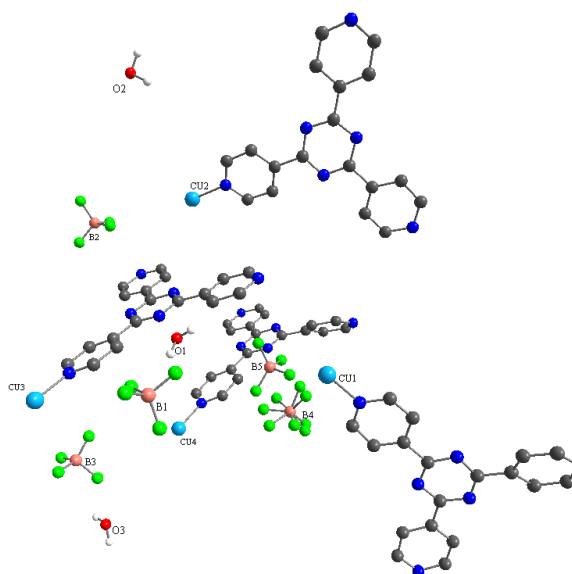


**Figure 6.11:** asymmetric unit of  $[\text{Cu}(\text{TPT})]\text{BF}_4 \cdot 0.75\text{H}_2\text{O}$ . Cu (light blue), F (green), O (red), N (blue), C (grey), B (orange), H (white). Framework H's were omitted for clarity.

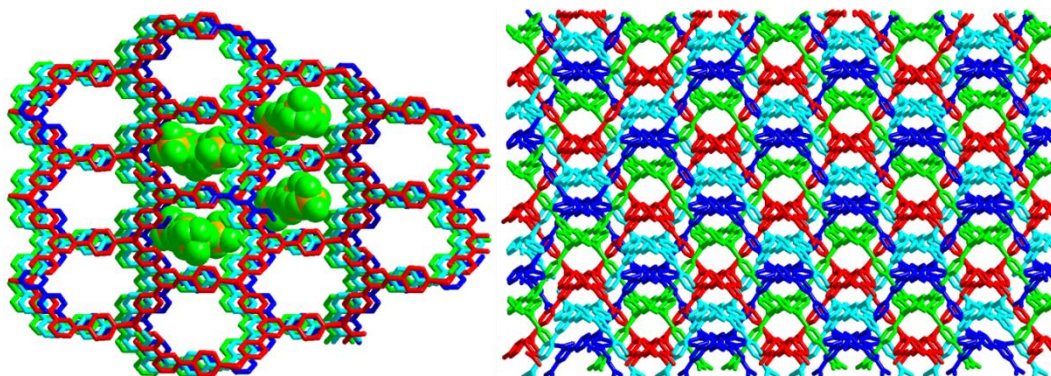


**Figure 6.12:** Extended framework of structure  $[\text{Cu}(\text{TPT})]\text{BF}_4 \cdot 0.75\text{H}_2\text{O}$ , with space filling model of included  $[\text{BF}_4]^-$  anions within the pores. Interpenetrated networks shown by different colours.

The final structure of the MOF product generates an interesting coordination of the copper centre. As stated previously, the metal centre exhibits a trigonal planar arrangement of N atoms, and the long Cu-F distances suggest there is no formal bond between the metal and  $[\text{BF}_4]^-$ . The 1:1 ratio of Cu atoms to  $[\text{BF}_4]^-$  suggests that the metal has undergone a reduction from  $\text{Cu}^{2+}$  to  $\text{Cu}^+$  during the reaction.  $\text{Cu}^+$  is found to exist as a trigonal planar metal complex with cyanide ( $[\text{Cu}(\text{CN})_3]^{2-}$ )<sup>11</sup>, however very few MOFs have been reported where copper exists in this arrangement and oxidation state<sup>1</sup>. To confirm this, a bond valence sum was performed to determine the oxidation state of the copper centre. The bond valence sum is given as:

$$\text{Bond Valence} = \exp\left(\frac{R_o - R}{B}\right) \quad (6-1)$$

where  $R_o$  is the bond length between two ions which have a bond of unit valence, and  $R$  is the experimental bond length.  $B$  is an empirical parameter determined for a particular cation-anion interaction from a number of structures within the literature<sup>12</sup>. Calculations for both the 3 and 4 coordinate N atoms have been considered, due to the delocalised nature of the pyridine ring. A full list of the valence sums and constants for the bonds of interest are given in Appendix 10.1. From the valence sums, it is evident that all four Cu centres are +1

<sup>1</sup> Literature search of the Cambridge Structural Database (CSD) for 3-coordinate  $\text{Cu}^+$  with charge balancing anion which does not form one of the coordination bonds

oxidation state, with values approximately equal to 0.85 for 3-coordinate N, and 1.15 for 4-coordinate N. The values of Cu-F bond valences are negligible, except for Cu2-F2 which has a value of 0.0542 for +1 oxidation state of Cu, however this affects the valence sum little for this atom.

Powder X-ray diffraction data were collected on bulk samples of  $[\text{Cu}(\text{TPT})]\text{BF}_4 \cdot 0.75\text{H}_2\text{O}$  to analyse the purity of the material. Results from Figure 6.13 show variation in the intensities of peaks and possible impurities present from the unreacted TPT from the synthesis (diffraction pattern in black). The presence of an intense peak at low angle is indicative of a MOF product, due to the long range order of the pore structure.

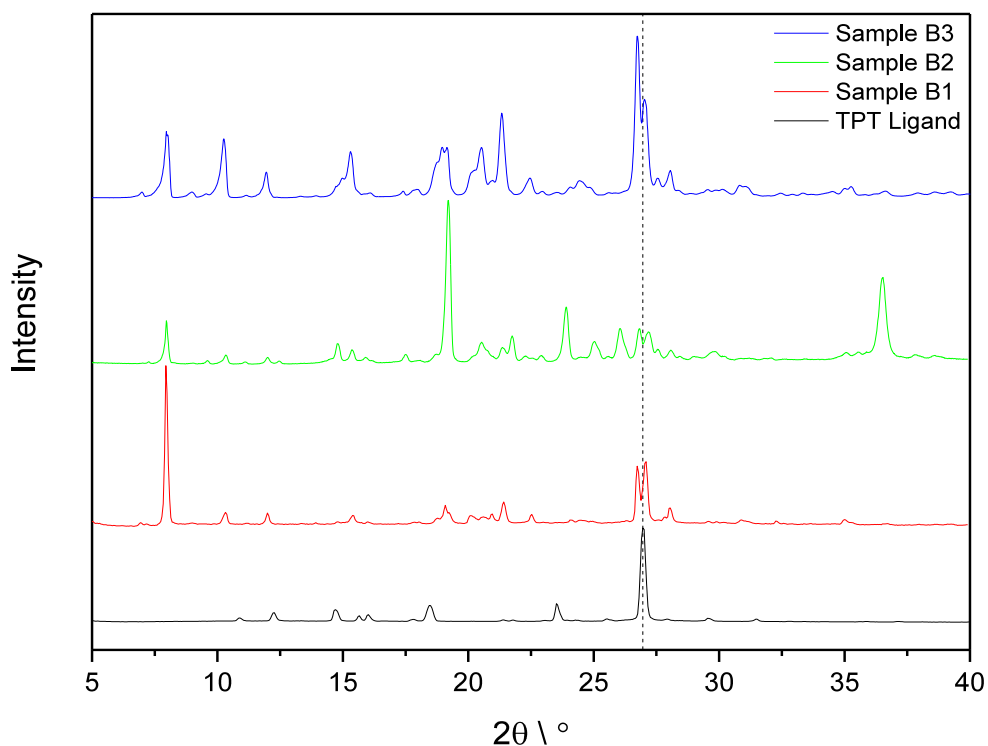


**Figure 6.13: Powder diffraction data of synthesised  $[\text{Cu}(\text{TPT})]\text{BF}_4 \cdot 0.75\text{H}_2\text{O}$  samples, additional pattern (black) shows diffraction data from synthesised TPT ligand.**

## 6.2.1 THERMAL STUDIES OF $[\text{Cu}(\text{TPT})]\text{BF}_4 \cdot 0.75\text{H}_2\text{O}$

Thermogravimetric analysis of the as-synthesised structure was performed to compare solvent content, determined from single crystal data, and determine the temperature at which degradation of the structure occurs. Figure 6.14 shows the mass loss profile, from room temperature to 873 K, for the as-synthesised structure which is dried in air after methanol exchange for 3 d. The profile shows a small mass loss of 4.55 %, up to a temperature of ~503 K; this corresponds well with the calculated solvent volume from crystallographic data of 4.6 %. After desolvation of the material, further heating to a temperature of 623 K results in degradation of the material. The loss of 63.73 % is expected to be the complete loss of ligand TPT (%mass of unit cell is 65.58 %), the final loss is ~20 %, corresponding to the  $[\text{BF}_4]^-$  units, with a leftover mass of ~11 %, which is likely the mass of Cu (13.34 % of unit cell).

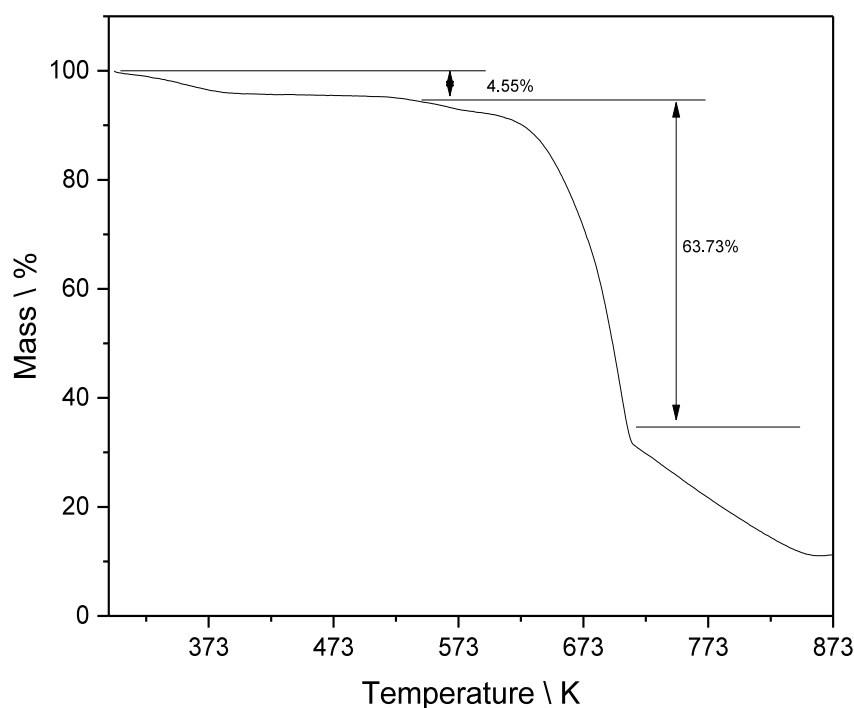


**Figure 6.14:** Thermogravimetric analysis of  $[\text{Cu}(\text{TPT})]\text{BF}_4 \cdot 0.75\text{H}_2\text{O}$ . Shows small solvent loss of 4.55 % upto 473 K, with degradation of the material at 573 K

## 6.2.2 ELEMENTAL ANALYSIS OF $[\text{Cu}(\text{TPT})]\text{BF}_4 \cdot 0.75\text{H}_2\text{O}$

Analysis of the bonding within the synthesised structure was performed using Fourier Transform Infrared (FT-IR) Spectroscopy. Figure 6.15 shows the transmittance plots of  $[\text{Cu}(\text{TPT})]\text{BF}_4 \cdot 0.75\text{H}_2\text{O}$ , the synthesised ligand TPT, and the reactant used in the synthesis, 4-cyanopyridine. Table 6.5 gives the wavenumbers of the prominent peaks and the assignments which could be identified. The peaks worth mentioning are the  $2237\text{ cm}^{-1}$  peak associated with the  $\text{C}\equiv\text{N}$  stretch, and the  $1366\text{ cm}^{-1}$  and  $1504\text{ cm}^{-1}$  from TPT,  $1370\text{ cm}^{-1}$  and  $1511\text{ cm}^{-1}$  from  $[\text{Cu}(\text{TPT})]\text{BF}_4 \cdot 0.75\text{H}_2\text{O}$ , which both signify the triazine ring stretches.

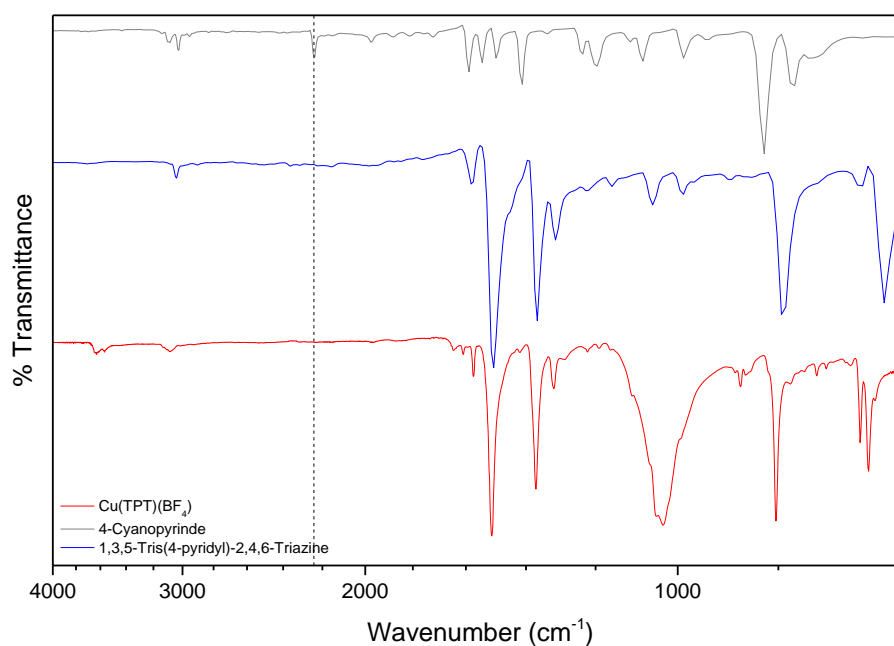


**Figure 6.15: FT-IR spectra for  $[\text{Cu}(\text{TPT})]\text{BF}_4 \cdot 0.75\text{H}_2\text{O}$ , TPT ligand, and starting material for organic ligand synthesis, 4-cyanopyridine.**

**Table 6.5: Key Infrared peaks for [Cu(TPT)]BF<sub>4</sub>·0.75H<sub>2</sub>O, and their associated bond vibrations**

		Wavenumber(cm <sup>-1</sup> )			
	4-PyCN	TPT		[Cu(TPT)]BF <sub>4</sub> ·0.75H <sub>2</sub> O	
771	C-H	-	-	-	-
825					
987	Ring	987	Ring	*	
1080	Breathing	1056	Breathing		
-	-	-	-	1034	BF <sub>4</sub> <sup>-</sup>
1411	C-C C-N Stretching	1366 1504	C-C C-N Stretching	1370	C-C
1496				C-N	
1543				Stretching	
1589					
2237	C≡N	-	-	-	-
3024	C-H	3040	C-H	3091	C-H
3086					
-	-	-	-	3567	H <sub>2</sub> O
				3629	H <sub>2</sub> O

\* Broad stretch of [BF<sub>4</sub>]<sup>-</sup> masks ring stretching of Py

CHN analysis was performed on [Cu(TPT)]BF<sub>4</sub>·0.75H<sub>2</sub>O, data is given in **Table 6.6** shows the percentages of carbon, hydrogen and nitrogen within the material analysed. Expected percentages were assumed based on the formula unit from single crystal data. Results showed variation in the calculated values of C, H, and N, but an average of the data gives a good approximation of the expected result. Differences are possibly due to solvent content within the porous structure.

**Table 6.6: CHN analysis of [Cu(TPT)]BF<sub>4</sub>·0.75H<sub>2</sub>O**

Material	C	H	N
<b>Expected (%)</b>	45.4	2.84	17.65
<b>Found 1 (%)</b>	51.53	3.33	19.63
<b>Found 2 (%)</b>	38.43	2.49	14.76
<b>Average (%)</b>	44.98	2.91	17.195

### 6.3 SYNTHESIS AND CHARACTERISATION OF [Cu(TPT)]NO<sub>3</sub>.MeOH

The MOF material, [Cu(TPT)]NO<sub>3</sub>.MeOH, was synthesised via the method described by Feng *et al.*<sup>13</sup>, using a solvothermal method at conditions of 413 K with Cu(NO<sub>3</sub>)<sub>2</sub>.2.5H<sub>2</sub>O (1 mmol, 232.6 mg) and 2,4,6-tri(4-pyridyl)-1,3,5-triazine (TPT) (1 mmol, 312.3 mg) in 11.5 cm<sup>3</sup> of methanol. After heating in a stainless steel autoclave with inner Teflon<sup>®</sup> liner for 72 h, the mixture produced small red crystals of the product. The resulting solution was further washed and filtered with excess methanol. In contrast to the previously studied material, insoluble impurities of TPT which were present in the reaction mixture were able to be dissolved in a large volume of 10:15 ethanol/chloroform mixture with heating to the boiling point of the mixture, without loss of crystalline MOF phase.

Single crystal diffraction data were collected by Dr. Alan R. Kennedy, giving space group P2<sub>1</sub>/n with lattice parameters  $a = 9.8511(2) \text{ \AA}$ ,  $b = 8.9191(2) \text{ \AA}$ ,  $c = 21.7793(3) \text{ \AA}$ , and  $\beta = 97.564(2)^\circ$ , with cell volume  $1896.94(6) \text{ \AA}^3$ . The structure previously reported in the literature<sup>13</sup> shows the space group in the alternative setting P2<sub>1</sub>/c, and slight differences in the lattice parameters. The R(F) values of the fits are 0.0926 (This Work) and 0.125<sup>13</sup>, suggesting a slight improvement in the model of the structure.

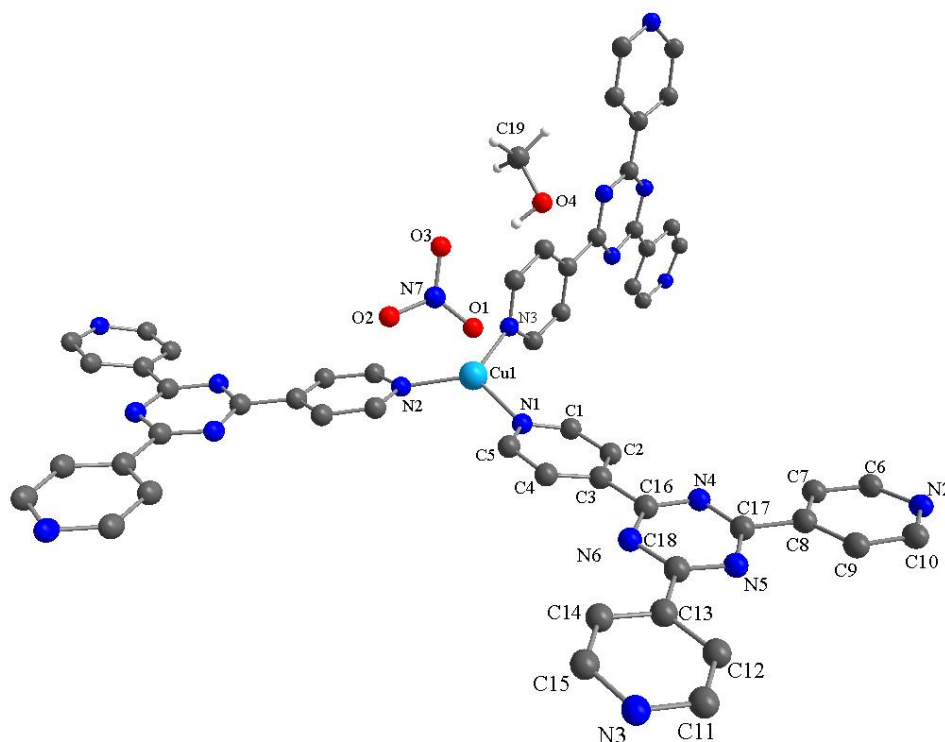


**Figure 6.16: Structure of [Cu(TPT)]NO<sub>3</sub>.MeOH. Cu (light blue), O (red), N (blue), C (grey), H (white). Framework H's were omitted for clarity.**

Additionally, the structure shown here contains a molecule of methanol per Cu atom, whereas the structure of Feng *et al.* is a monohydrate. The coordination geometry around Cu within the MOF crystal is shown in Figure 6.16; similar to the BF<sub>4</sub> analogue of the structure, the Cu<sup>+</sup> metal centres are coordinated via N atoms to three TPT ligands with bond distances between 1.9643 – 2.0202 Å. Each ligand bonds to three Cu<sup>+</sup> metal centres, which creates a cationic polymeric structure. The nitrate anion (NO<sub>3</sub><sup>-</sup>) is within the coordination sphere of the Cu<sup>+</sup> centre, and the bond distance between Cu1-O1 is 2.5438 Å. The close proximity of the NO<sub>3</sub><sup>-</sup> unit distorts the trigonal planar arrangement of the N atoms, with the angles between N-Cu-N not all equal to 120 °. One TPT ligand is rotated ~88.3 ° relative to the other coordinated ligands. The ligands are distorted from being completely planar, with each pyridine ring rotated around the C-C bond connecting it to the triazine central ring by an angle of 4.782 °, 8.402 °, or 11.477 °. The unit cell is comprised of four interpenetrating nets which are equivalent by symmetry,

shown in Figure 6.17. Voids extend within the network along the crystallographic b axis, with methanol solvent molecules as guests (Figure 6.17).

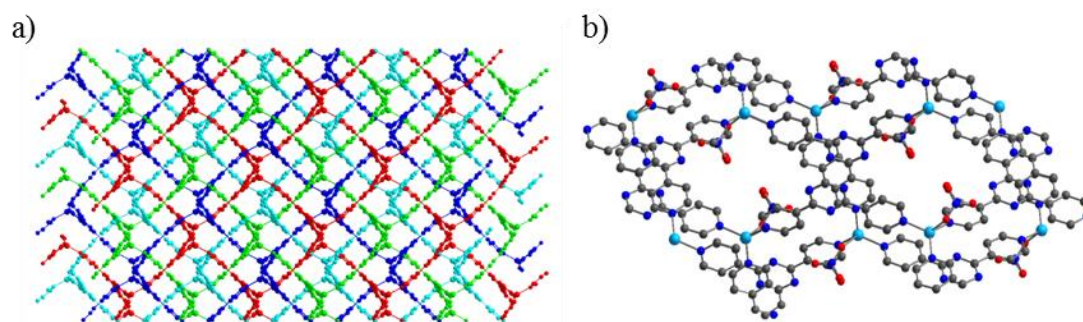


**Figure 6.17: 4-fold interpenetrated framework of [Cu(TPT)]NO<sub>3</sub>.MeOH. View down b-axis of the porous structure, H atoms and methanol molecules removed for clarity.**

Each copper centre within the structure is charge balanced by a NO<sub>3</sub><sup>-</sup> anion, which is disordered in the N7 and O3 positions. The disorder maximises the hydrogen bonding interactions with the methanol molecules, with O3-H1S distance being 1.9545 Å, and O3A-H19A and O3A-H19C being 2.1404 Å and 1.8676 Å, respectively. Figure 6.18 shows the hydrogen bonding which propagates along the pore in the b-axis by interaction of the H atoms of the -OH and -CH<sub>3</sub> of the methanol molecules. The available pore volume was calculated using PLATON<sup>3</sup>, and found the volume to be 134.6 Å<sup>3</sup> which represents 7.1 % of the unit cell volume.

A bond valence calculation was performed to ensure the correct oxidation state was determined. Again calculation for the 3 and 4 coordinate N atoms was considered due to the delocalised nature of the pyridine ring. The full list of valence sums is given in Appendix 10.1. The calculation is simplified in the case of [Cu(TPT)]NO<sub>3</sub>.MeOH, due to the equivalent symmetry of the four Cu atoms of each interpenetrating net. It is obvious from the calculations that the oxidation state of Cu is +1, having obtained values of 0.9061 and 1.1989 for 3- and 4-coordinate N atoms. These include the bond valence of the Cu1-O1 bond, which does not contribute strongly to the valence sum.

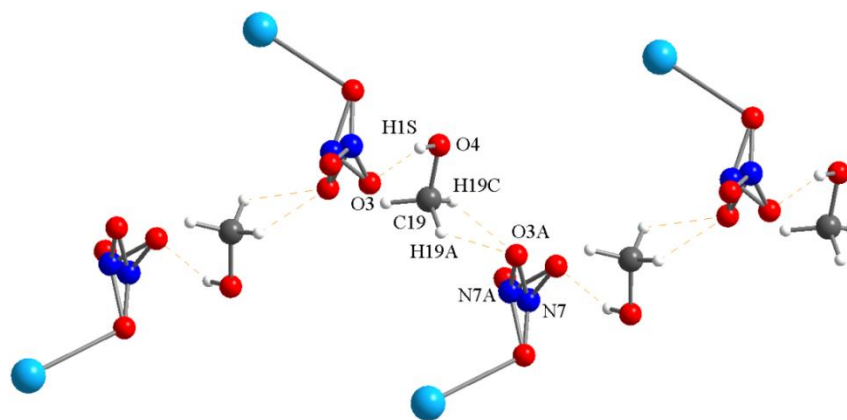


**Figure 6.18: Hydrogen bonding present between methanol solvent molecules and coordinated nitrate groups.**

Powder X-ray diffraction data were collected on bulk samples of  $[\text{Cu}(\text{TPT})]\text{NO}_3 \cdot \text{MeOH}$  to analyse the purity of the material. Results from Figure 6.19 show samples N1, N2, and N3 which were three samples synthesised using the method outlined for synthesis, Samples LN1 and LN2 used a  $45 \text{ cm}^3$  autoclave, and quantities of the reagents were increased to have the same concentration of MOF solids as those in the synthesis using the  $23 \text{ cm}^3$  autoclaves. Variation in the intensities of peaks and possible impurities is observed. Patterns show that some peaks match to the allowed reflections of the space group and unit cell parameters.

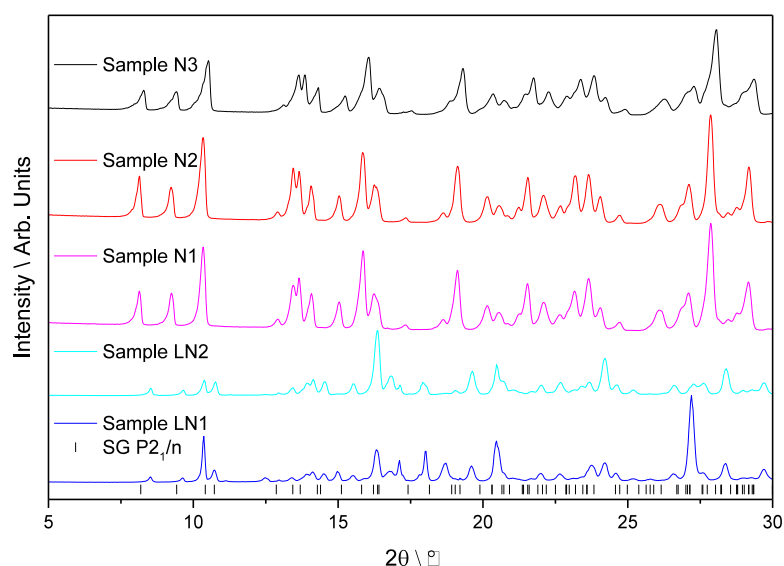


**Figure 6.19: Powder diffraction data of synthesised samples of  $[\text{Cu}(\text{TPT})]\text{NO}_3$ . Tick marks shown for space group  $P2_1/n$ .**

### 6.3.1 THERMAL STUDIES OF [Cu(TPT)]NO<sub>3</sub>.MeOH

Thermogravimetric analysis of the as-synthesised structure was performed to compare solvent content, determined from single crystal data, and determine the temperature at which degradation of the structure occurs. Figure 6.20 shows the mass loss profile, from room temperature to 873 K, for the as-synthesised structure, which was dried in air after methanol exchange for 3 d. The profile shows a small mass loss of 4.32 %, up to a temperature of ~453 K; taking into account the density of methanol as 0.792 g cm<sup>-3</sup>, the corresponding volume of solvent lost is 0.595 mm<sup>3</sup> (8.98 %), which is larger than the crystallographic solvent loss, but could be accounted for by entrained solvent in the interstitial space between particles due to the low quantity (~2 % volume). After desolvation of the material, further heating to a temperature of 513 K results in degradation of the material; resulting in three consecutive mass losses before a final % mass of ~25 % is left, which corresponds to 4 units of CuNO<sub>3</sub>. The three losses upon degradation are expected to be fragments of the TPT ligand, with the first two losses associated with the pyridine rings, and the third loss being the triazine ring (~16.6% of unit cell weight) (Appendix 10.2.3).

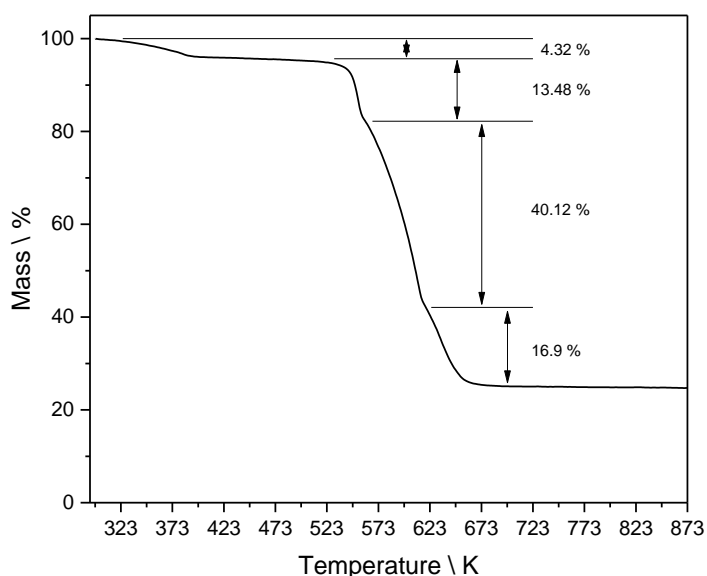


**Figure 6.20: Thermogravimetric analysis of [Cu(TPT)]NO<sub>3</sub>.MeOH. Shows solvent loss of 4.32 % up to 453 K. Degradation of the material begins at 513 K**

### 6.3.2 ELEMENTAL ANALYSIS OF [Cu(TPT)]NO<sub>3</sub>.MeOH

Analysis of infrared spectroscopy was performed on [Cu(TPT)]NO<sub>3</sub>.MeOH, as shown in Figure 6.21. Results show no impurities from 4-cyanopyridine present in either TPT or [Cu(TPT)]NO<sub>3</sub>.MeOH. [Cu(TPT)]NO<sub>3</sub>.MeOH shows peaks which are related to the presence of TPT within the structure, and shows a broad peak at approximately 1230 – 1400 cm<sup>-1</sup>, related to the presence of [NO<sub>3</sub>]<sup>-</sup> (1390 cm<sup>-1</sup>), and two smaller peaks which are marked at 735 and 826 cm<sup>-1</sup> which are not present in the starting material spectra.

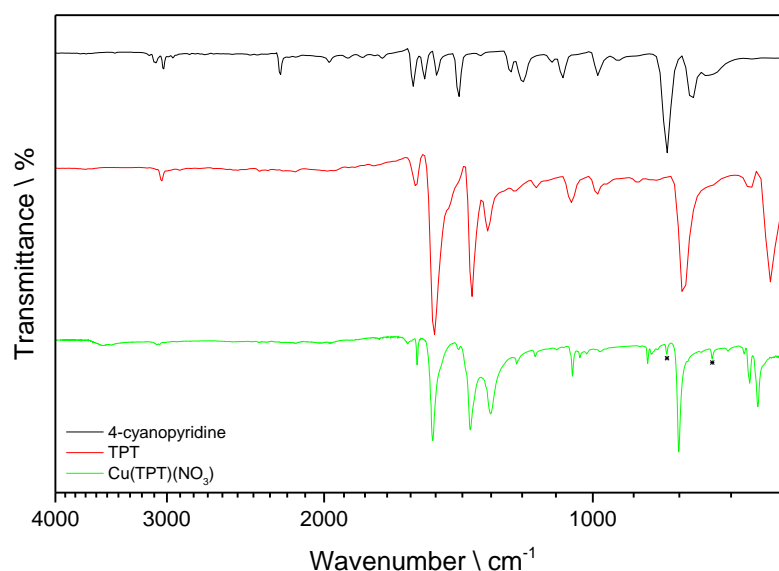


Figure 6.21: FT-IR spectra of [Cu(TPT)]NO<sub>3</sub>.MeOH, TPT, and 4-cyanopyridine.

CHN analysis was performed on [Cu(TPT)]NO<sub>3</sub>.MeOH, data is given in **Table 6.7** shows the percentages of carbon, hydrogen and nitrogen within the materials analysed. Expected percentages were assumed based on the formula unit from single crystal data.

**Table 6.7: CHN analysis of [Cu(TPT)]NO<sub>3</sub>.MeOH**

Material	C	H	N
Expected (%)	48.56	3.41	20.87
Found (%)	42.23	2.755	18.715

## 6.4 POROUS CHARACTERISATION

### 6.4.1 ADSORPTION ANALYSIS OF $\text{Cu}(\text{bpetha})_2\text{SiF}_6$

Results for  $\text{Cu}(\text{bpetha})_2(\text{SiF}_6)$  from  $\text{N}_2$  adsorption at 77 K are shown in Figure 6.22. The adsorption isotherm matches a Type II IUPAC standard isotherm, with very low uptake at low pressure, and a large increase to  $17.6 \text{ cm}^3\text{g}^{-1}$  at  $P/P_0 = 0.992$ . Although there is no asymptote to adsorption, a simple calculation of the pore volume from the maximum  $\text{N}_2$  uptake yields a value of  $0.027 \text{ cm}^3\text{g}^{-1}$  ( $\text{N}_2$  density  $0.8081 \text{ g cm}^{-3}$ ). The plots of  $Q(1 - P/P_0)$  vs  $P/P_0$  and the linear BET plot used in the Rouquerol transformation, which is used to define an appropriate linear range for the BET calculation are shown in Figure 6.23. The linear region of the BET equation was found as  $P/P_0$  0.01 – 0.12, this gave a monolayer coverage of  $2.388 \pm 0.009 \text{ cm}^3 \text{ g}^{-1}$  and C constant  $367 \pm 37$ . An estimate of the BET surface area provides a value of  $10.39 \pm 0.04 \text{ m}^2\text{g}^{-1}$ . The combined results from the  $\text{N}_2$  analysis at 77 K reveal in isolation that the material is non-porous.

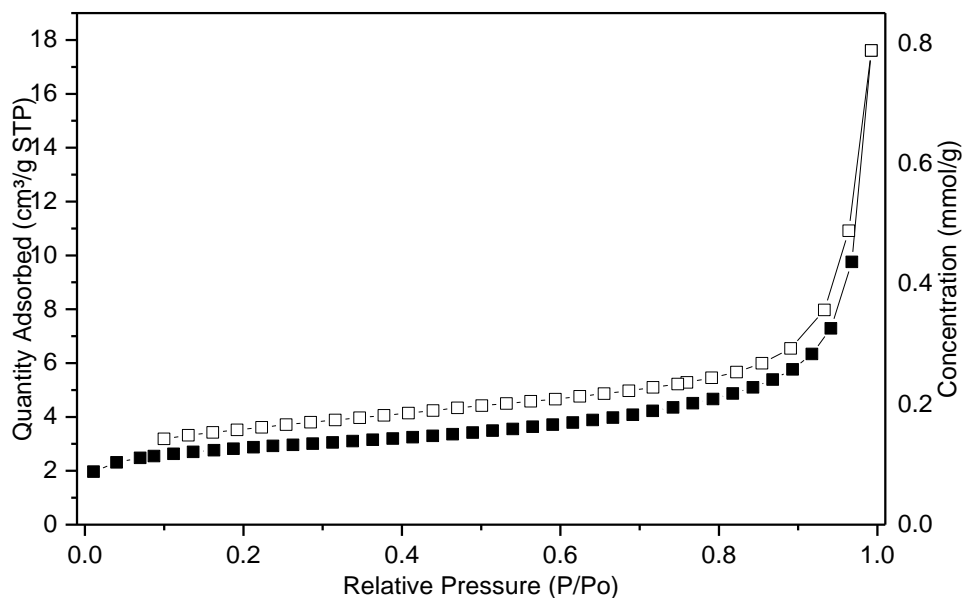
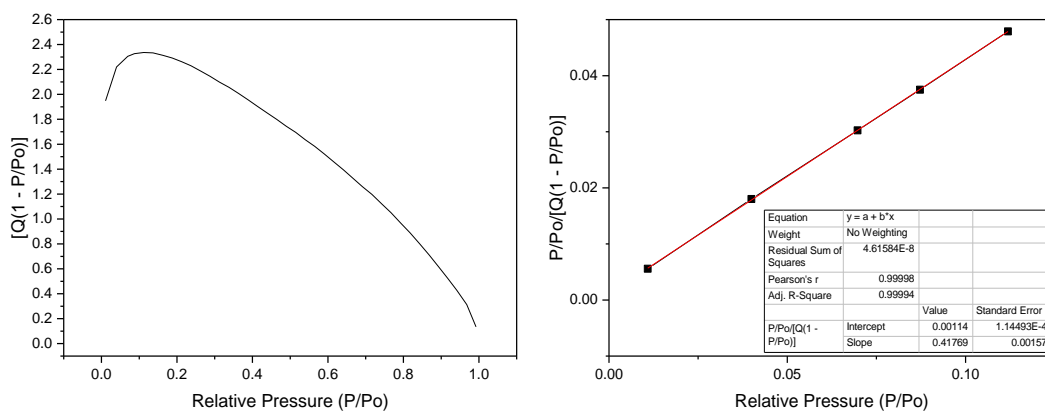
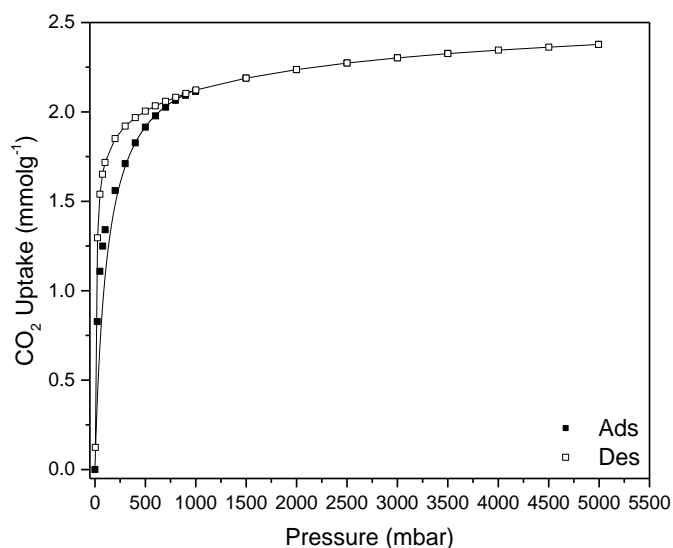


Figure 6.22:  $\text{N}_2$  adsorption isotherm at 77 K on  $\text{Cu}(\text{bpetha})_2\text{SiF}_6$



**Figure 6.23: Analysis of BET linear equation to determine surface area of Cu(bpetha)<sub>2</sub>SiF<sub>6</sub>.**

Further analysis was performed on Cu(bpetha)<sub>2</sub>(SiF<sub>6</sub>) using CO<sub>2</sub> at 273 K in the pressure range 0 – 5000 mbar, which is shown in Figure 6.24. Here a Type I IUPAC classified isotherm is obtained, showing high uptake at low pressure. A Langmuir fit was chosen to obtain an estimate of the total pore volume, shown in Figure 6.25. Analysis of the linear regression shows experimental data fits with an R<sup>2</sup> value of 99.988%. Monolayer coverage was calculated to be 2.423 ± 0.009 mmol g<sup>-1</sup>, giving a pore volume of 0.1234 ± 0.0004 cm<sup>3</sup> g<sup>-1</sup> (CO<sub>2</sub> density 0.864 g cm<sup>-3</sup>). The CO<sub>2</sub> accessible surface area was calculated from the monolayer coverage and found to be 306.3 ± 1.1 m<sup>2</sup> g<sup>-1</sup>.



**Figure 6.24: CO<sub>2</sub> adsorption isotherm at 273 K on Cu(bpetha)<sub>2</sub>SiF<sub>6</sub>, Ads (■) and Des (□). Shows Type I isotherm classification. Presence of hysteresis, however mild conditions for outgassing removes guest species.**

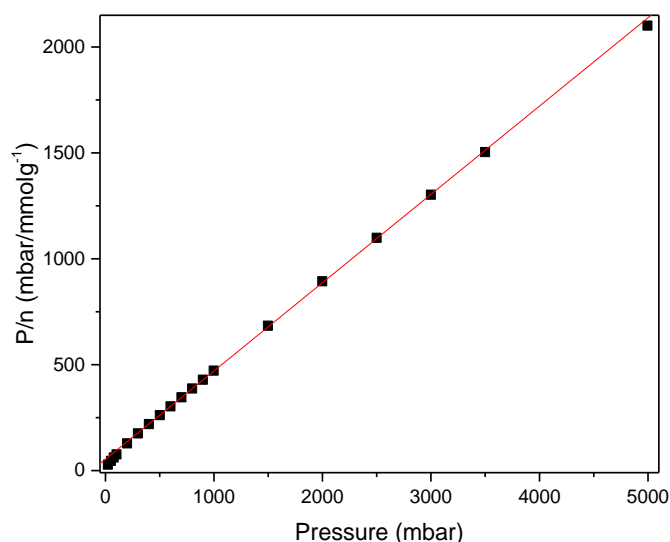


**Figure 6.25: Langmuir linear plot of CO<sub>2</sub> isotherm at 273 K for the determination of monolayer capacity of Cu(bpetha)<sub>2</sub>SiF<sub>6</sub>**

The Dubinin-Radushkevich (D-R) equation was used to provide an estimate of the micropore volume. Figure 6.26 shows the D-R plot for Cu(bpetha)<sub>2</sub>(SiF<sub>6</sub>); results show linearity in the region of 500 – 5000 mbar with a R<sup>2</sup> value of 99.88 %. The final micropore volume obtained from the D-R equation was found to be  $0.1298 \pm 0.0004 \text{ cm}^3 \text{ g}^{-1}$  (CO<sub>2</sub> density  $0.864 \text{ g cm}^{-3}$ ).

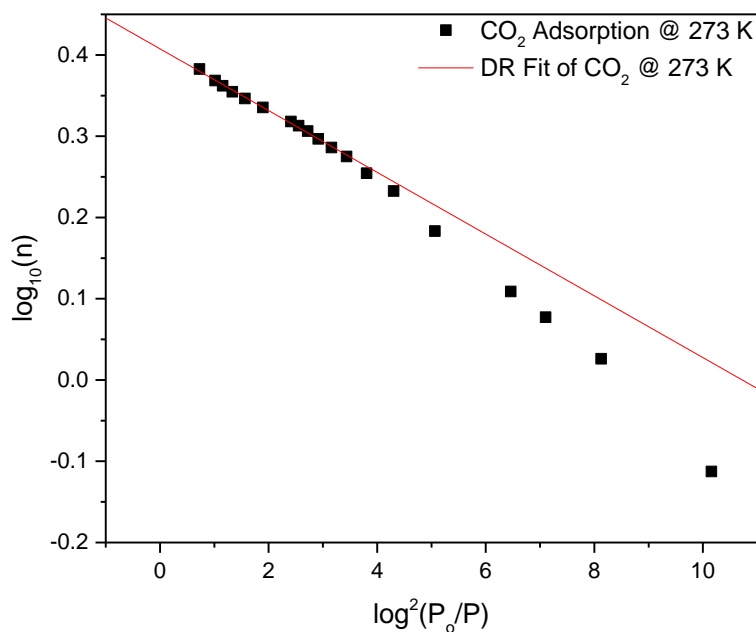


**Figure 6.26: D-R linear equation of CO<sub>2</sub> isotherm at 273 K to determine the micropore volume of Cu(bpetha)<sub>2</sub>SiF<sub>6</sub>**

## 6.4.2 ADSORPTION ANALYSIS OF [Cu(TPT)]BF<sub>4</sub>·0.75H<sub>2</sub>O

Results of N<sub>2</sub> adsorption for [Cu(TPT)]BF<sub>4</sub>·0.75H<sub>2</sub>O at 77 K are shown in Figure 6.27. The adsorption isotherm does not appear to match any of the IUPAC standard isotherms. The isotherm shows a linear trend with very low uptake across the entire relative pressure range, with a deviation away from linearity at high pressure, typical of condensation of N<sub>2</sub> near 1 bar at its boiling point, leading to a final uptake of ~5.05 cm<sup>3</sup>g<sup>-1</sup> at P/P<sub>0</sub> = 0.99. Further analysis of the BET surface area was deemed irrelevant due to the poor adsorption profile which resulted from N<sub>2</sub> adsorption.

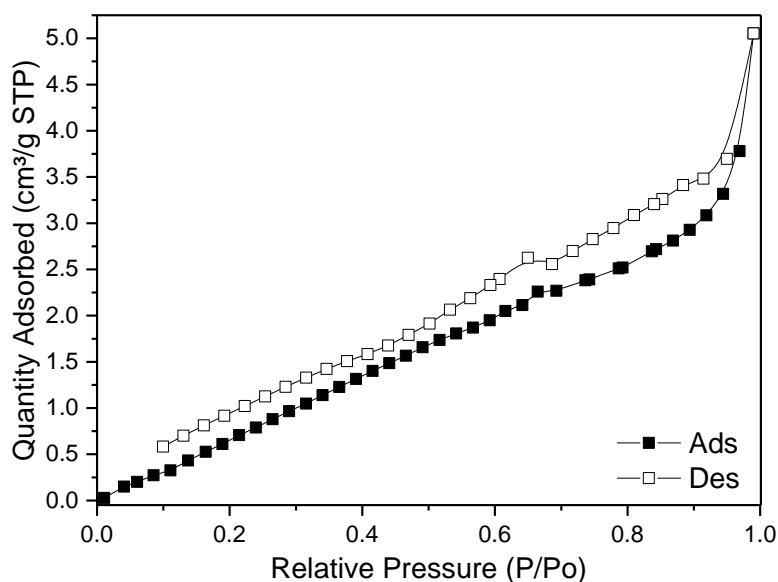


**Figure 6.27:** N<sub>2</sub> adsorption isotherm at 77 K on [Cu(TPT)]BF<sub>4</sub>·0.75H<sub>2</sub>O. Linear trend in isotherm does not correspond to classical isotherm type, suggested to be the result of activated diffusion occurring in very narrow micropores.

Further analysis using CO<sub>2</sub> at 273 K was performed on [Cu(TPT)]BF<sub>4</sub>·0.75H<sub>2</sub>O, which is shown in Figure 6.28. Here, a Type I IUPAC classified isotherm is obtained showing relatively high uptake at low pressure. A Langmuir fit was performed, shown in Figure 6.29. Analysis of the linear regression shows experimental data fits with an R<sup>2</sup> value of 99.778%. Monolayer coverage was calculated to be 1.780 ± 0.022 mmol g<sup>-1</sup>, giving a pore volume of 0.091 ± 0.001 cm<sup>3</sup>g<sup>-1</sup>. The CO<sub>2</sub> accessible surface area was found to be 225.1 ± 2.8 m<sup>2</sup>g<sup>-1</sup>.

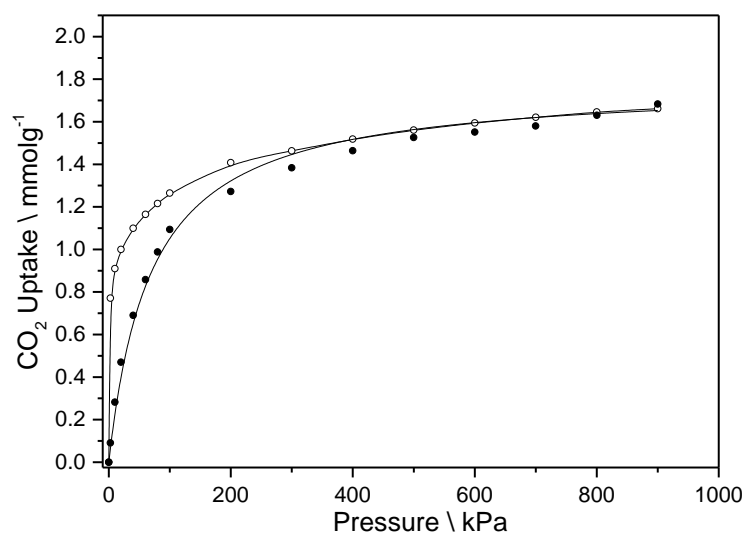


**Figure 6.28:** CO<sub>2</sub> adsorption at 273 K on [Cu(TPT)]BF<sub>4</sub>·0.75H<sub>2</sub>O. Shows Type I isotherm classification. Presence of hysteresis, use of mild conditions for outgassing removes guest species.

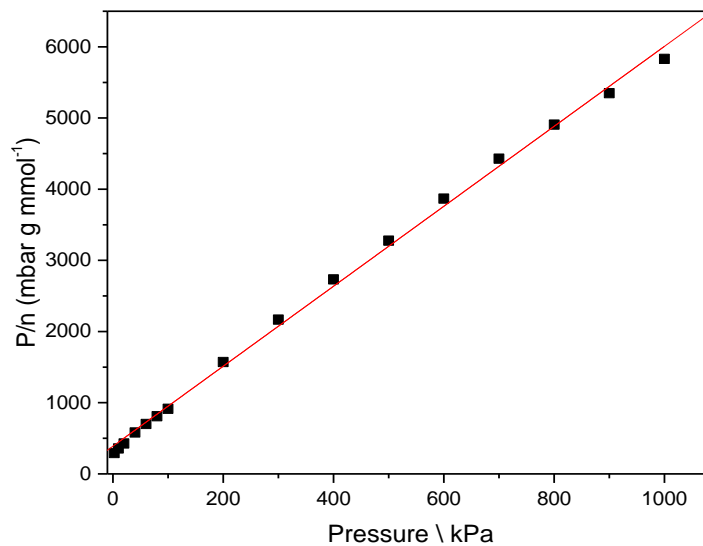


**Figure 6.29:** Langmuir linear plot of CO<sub>2</sub> isotherm at 273 K for the determination of monolayer capacity of [Cu(TPT)]BF<sub>4</sub>·0.75H<sub>2</sub>O

The data was also fit to the D-R equation shown in Figure 6.30; results show linearity in the region of 800 – 10000 mbar with a  $R^2$  value of 99.249 %. The final micropore volume obtained from the D-R equation was found to be  $0.0908 \pm 0.0008 \text{ cm}^3\text{g}^{-1}$  which agrees well with the total pore volume obtained from the Langmuir analysis.

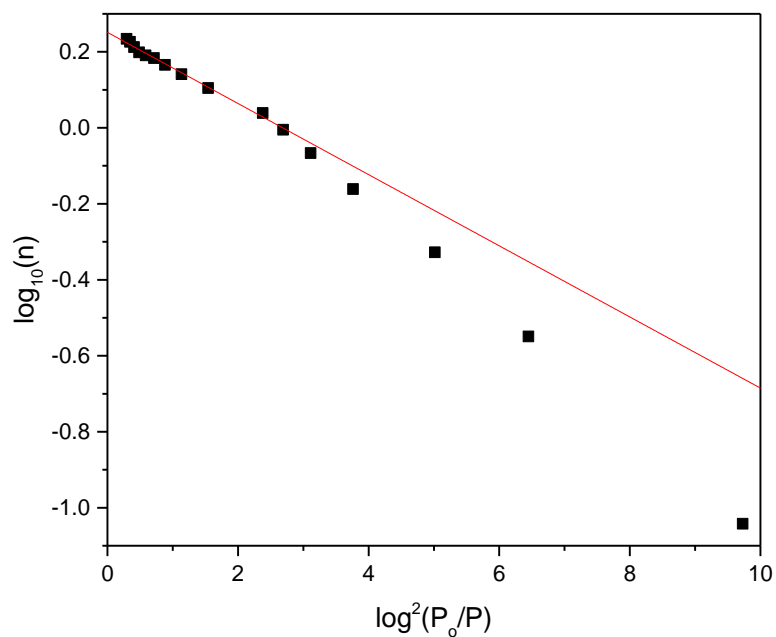


**Figure 6.30: D-R linear equation of  $\text{CO}_2$  isotherm at 273 K to determine the micropore volume of  $[\text{Cu}(\text{TPT})]\text{BF}_4 \cdot 0.75\text{H}_2\text{O}$**

### 6.4.3 ADSORPTION ANALYSIS OF [Cu(TPT)]NO<sub>3</sub>.MeOH

Porous characterisation of [Cu(TPT)]NO<sub>3</sub>.MeOH was initiated by analysis of the N<sub>2</sub> adsorption at 77 K to obtain the BET surface area. Figure 6.31 shows the results of adsorption analysis under N<sub>2</sub>, which shows a possible Type II/ Type III isotherm. The initial increase at low pressure is indicative of the Type II standard isotherm, however its maximum amount relative to the high pressure region of the isotherm makes it difficult to determine if the result is within experimental errors. The decreasing uptake observed above P/P<sub>0</sub> = 0.5 is typical of a measurement where the adsorbent mass does not provide at least 50 m<sup>2</sup> of surface area within the measurement tube. During this experiment, 253.1 mg of dry sample was used for analysis, this would suggest that the accessible surface area of the material is low and the decrease in uptake is an erroneous result.

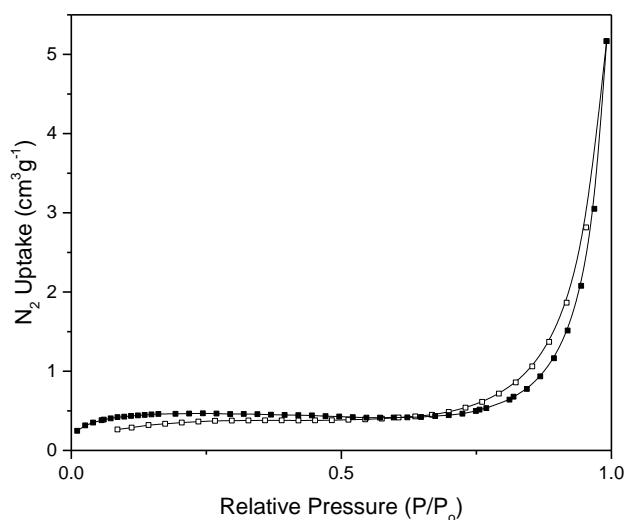


**Figure 6.31:** N<sub>2</sub> adsorption isotherm (cm<sup>3</sup> g<sup>-1</sup>) over relative pressure range (P/P<sub>0</sub>) at 77 K on [Cu(TPT)]NO<sub>3</sub>.MeOH.

The BET surface area was calculated using the Rouquerol transform which was used to define the appropriate linear range from a plot of Q(1-P/P<sub>0</sub>) vs. P/P<sub>0</sub>. Figure 6.32(a) shows the transform plot which shows the chosen region lies between

$P/P_0 = 0 - 0.17$ ; the graph in (b) shows the linear regression for the BET plot, which gives an  $R^2$  fit of 99.936 %. The results of the analysis give a monolayer coverage of  $0.405 \pm 0.003 \text{ cm}^3 \text{ g}^{-1}$ , and a C constant of  $141 \pm 14$ . The BET surface area calculated was  $1.76 \pm 0.01 \text{ m}^2 \text{ g}^{-1}$ .

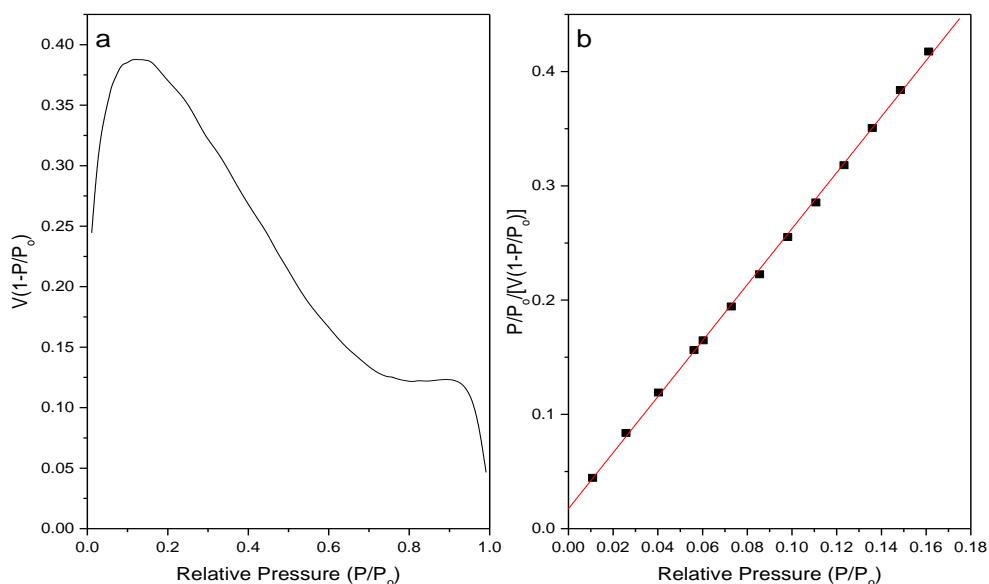


**Figure 6.32: Analysis of BET linear equation to determine surface area of  $[\text{Cu}(\text{TPT})]\text{NO}_3 \cdot \text{MeOH}$ . (a) shows plot of  $V(1-P/P_0)$  vs.  $P/P_0$  used to determine the appropriate linear region for the BET equation. (b) shows the plot of  $P/P_0/[V(1-P/P_0)]$  vs.  $P/P_0$  to obtain the linear plot of the BET equation. Monolayer capacity and C constant are determined from the gradient and intercept of the line and used to determine the surface area**

Analysis of the  $\text{CO}_2$  uptake was performed at 273 K. Figure 6.33 shows the  $\text{CO}_2$  adsorption isotherm within the region 0 – 1000 kPa. Initially, this does not follow a standard IUPAC adsorption isotherm; a suppression of the uptake is observed at low pressure, before a sharp increase in adsorbed amount between 10 – 20 kPa, resulting in a Langmuir Type I isotherm with a maximum uptake of  $1.956 \text{ mmol g}^{-1}$  at 1000 kPa, which appears to have reached monolayer capacity.

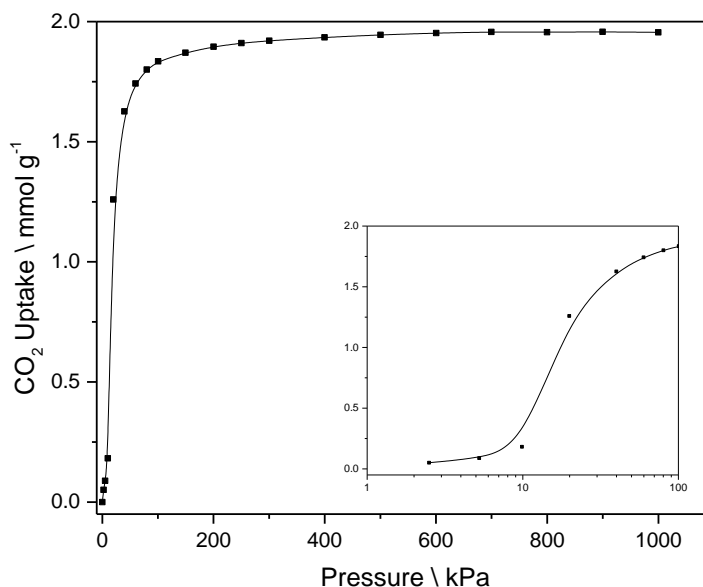


**Figure 6.33:** CO<sub>2</sub> adsorption at 273 K on [Cu(TPT)]NO<sub>3</sub>.MeOH. Shows Type I isotherm classification. Inset: log(P) plot showing sharp increase in adsorption amount at 20 kPa

Langmuir analysis was performed (Figure 6.34), and the plot shows a deviation from linearity at low pressure (inset). The linear fit of the data from 20 – 1000 kPa was calculated, and a monolayer coverage was calculated as  $1.976 \pm 0.002 \text{ mmol g}^{-1}$ ; the CO<sub>2</sub> accessible surface area was calculated to be  $249.8 \pm 0.2 \text{ m}^2 \text{ g}^{-1}$ .

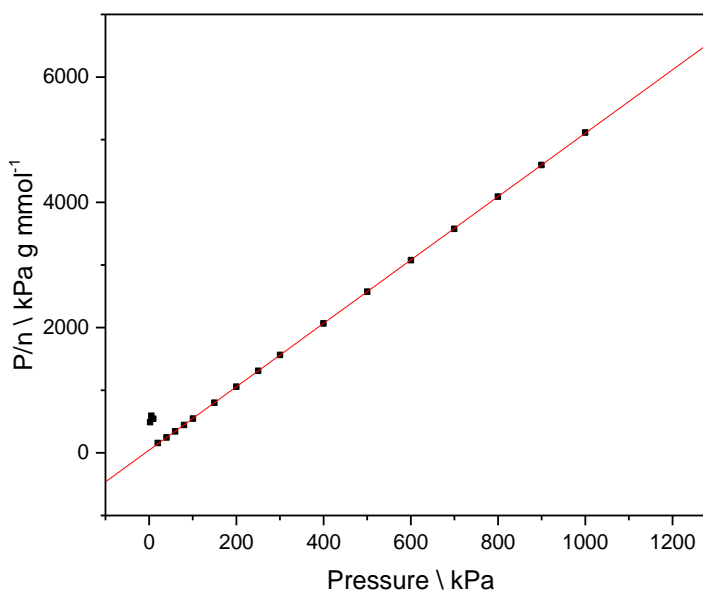


**Figure 6.34:** Langmuir plot of  $P/n$  ( $\text{kPa g mmol}^{-1}$ ) vs. pressure (kPa) to obtain linear plot of CO<sub>2</sub> adsorption isotherm at 273 K for the determination of monolayer capacity of [Cu(TPT)]NO<sub>3</sub>.MeOH. Monolayer capacity calculated from gradient as  $1.976 \text{ mmol g}^{-1}$

Analysis of the D-R equation from the data at 273 K is given in Figure 6.35. Again, deviation from linearity was observed within the low pressure region, with the linear range for the data gathered within the pressure range 100 – 700 kPa. The calculated micropore volume from the D-R analysis was  $0.1015 \pm 0.0001 \text{ cm}^3 \text{ g}^{-1}$ . This compares well with the pore volume calculated from Langmuir analysis ( $0.1007 \pm 0.0001 \text{ cm}^3 \text{ g}^{-1}$ ).

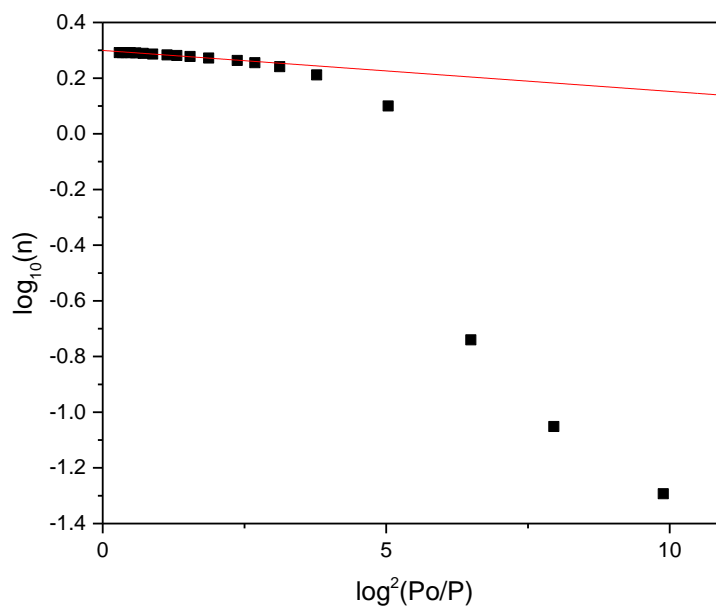


**Figure 6.35: Plot of  $\log(n)$  vs  $\log^2(P_o/P)$  to obtain linear function of D-R equation for  $\text{CO}_2$  adsorption isotherm at 273 K to determine the micropore volume of  $[\text{Cu}(\text{TPT})]\text{NO}_3 \cdot \text{MeOH}$ . Micropore volume was determined from intercept of line to obtain a value of  $0.1015 \text{ cm}^3 \text{ g}^{-1}$ .**

## 6.5 DISCUSSION

### 6.5.1 STRUCTURAL ANALYSIS OF $\text{Cu}(\text{BPETHA})_2\text{SiF}_6$

The synthesis of  $\text{Cu}(\text{bpetha})_2\text{SiF}_6$  was performed via a simple batch crystallisation method to form a polycrystalline material, which was amenable to analysis by PXRD. The use of solvent diffusion methods to obtain single crystals of the porous MOF has been shown to produce sufficient crystals for SCXRD in other analogous materials<sup>14</sup>. By utilising the same solvent systems used in the synthesis of these literature materials, as described in **Table 6.1**, to obtain crystals of  $\text{Cu}(\text{bpetha})_2\text{SiF}_6$ , it was postulated that the material could be easily produced, owing to their similar structures.

The formation of the secondary non-porous product,  $[\text{Cu}(\text{bpetha})(\text{OH}_2)_3(\text{NO}_3)]\text{SiF}_6 \cdot (\text{H}_2\text{O}) \cdot 0.5(\text{CH}_3\text{OH})$ , is likely to be the result of the formation of a thermodynamic product of crystallisation. Similar to Kawano *et al.*<sup>15</sup>, a porous structure of  $[(\text{ZnBr}_2)_3(\text{TPT})_2(\text{Tr})]$  (Tr = Triphenylene), was synthesised via batch crystallisation methods, and a non-porous 1-dimensional structure with the same stoichiometry was obtained through solvent diffusion methods. It is possible that the porous structure is initially formed during the first few days of crystallisation and that, over time, the formation of the thermodynamic product then occurs. This is seen from the formation of two distinct different crystal forms of purple and blue colour, indicating a difference in metal coordination. Higgins<sup>16</sup> noted that, once crystallisation of the product had occurred on the walls of the vessel, after some time the crystals would eventually sink to the bottom of the solution, suggesting that a more dense structure was forming. Despite the various synthesis conditions attempted, the quality

of the purple crystals was insufficient for SCXRD, even if a secondary product was not formed.

The non-porous crystals proved interesting to study, as they provided evidence that the  $[\text{SiF}_6]^{2-}$  unit was contained within the solution, and could be present as a ligand within the porous material. It was observed that, in the aqueous solution of metal salt and ammonium hexafluorosilicate, the solution took on a translucent appearance, even when it was heated to aid dissolution, suggesting the components were not fully dissolved. With the  $[\text{SiF}_6]^{2-}$  anion present as a coordinating species with the non-porous crystal, it was assumed that if  $[\text{Cu}(\text{bpetha})(\text{OH}_2)_3(\text{NO}_3)]\text{SiF}_6 \cdot \text{H}_2\text{O} \cdot 0.5\text{CH}_3\text{OH}$  was a thermodynamic product of the attempted synthesis of  $\text{Cu}(\text{bpetha})_2\text{SiF}_6$ , it would contain fragments of the components within the kinetic product, and these ligands would, therefore, be present in the porous material.

Characterisation of the product formed from batch crystallisation was performed, as analysis of its adsorption properties made it an interesting sample to study in more detail (discussed later). The instantaneous formation of solid product from solution, which was purple in colour, suggested fast crystallisation of a product that was of different coordination around the  $\text{Cu}^{2+}$  centre than the starting materials. Powder formation was possible from all metal starting materials used; however, examination of the PXRD patterns in Figure 6.4 suggests that different products are generated. Similarities between the products formed from  $\text{Cu}(\text{BF}_4)_2$  and  $\text{Cu}(\text{NO}_3)_2$  indicate that the same porous product may have been formed, however, the sharper peaks within the material synthesised from  $\text{Cu}(\text{BF}_4)_2$  could be due to better diffracting ability of the crystalline material through differences in particle size. It has been shown in MOF-5 that differences in peak broadening and intensities can be related to the presence of Zn-species and solvent molecules causing pore blockage<sup>17</sup>. The presence

of a peak at  $\sim 7^\circ$  provides evidence of a porous framework, due to large d-spacing; however, the low intensity of the peak in  $\text{Cu}(\text{SO}_4)$  shows that this is not the product of highest yield within this synthesis.

A comparison of the two similar ligands used in the synthesised product  $\text{Cu}(\text{bpetha})_2\text{SiF}_6$  and  $\text{Cu}(\text{dpa})_2\text{SiF}_6$ , as reported by Zaworotko *et al*<sup>8</sup>, shows that the difference between the two ligands is the change in hybridisation of the C atoms of the central bond, from  $\text{sp}^2$  to  $\text{sp}^3$  hybridisation, as expected from comparison of their skeletal structures. This would create a more flexible ligand, due to the loss of the  $\pi$ -bonding/double bond character, thus allowing rotation around the central bond.  $\text{Cu}(\text{bpetha})_2\text{SiF}_6$  was compared with other known structures of the same coordination, but that contain different organic ligands, to see if trends in the crystal structures could be found. **Table 6.2** showed that, in the majority of cases, the structures formed were of the tetragonal crystal system, and similarities in their unit cell sizes were found between ligands of similar length. In UTSA-48<sup>6</sup>, where the ligand (N-(4-pyridyl)isonicotinamide) was also flexible due to the central C-N bond, the structure was still found to be tetragonal, and had a similar set of unit cell parameters to  $\text{Cu}(\text{bpy}-2)_2(\text{SiF}_6)$  (bpy-2 = 1,2-Bis(4-pyridyl)ethene)<sup>8</sup>; differences in its symmetry result from the bending of the ligand and distortion out of plane with the Cu centres. Using this knowledge of previously reported materials, a Le Bail refinement was performed on PXRD data collected from the  $\text{Cu}(\text{BF}_4)_2$  synthesised product, and fit to a lower symmetry tetragonal cell, P4, using the cell parameters of  $\text{Cu}(\text{bpy}-2)_2(\text{SiF}_6)$  as an initial starting point for the calculation to refine. The analysis (Figure 6.6) shows a good fit to the diffraction data, with all peaks matched to a symmetry allowed reflection. The low value of  $R_{\text{wp}}$  is expected from Le Bail refinements, since no atomic data is used in the calculation of the peaks, however, an incorrect choice of symmetry would result in a higher  $R_{\text{wp}}$  value. The cell parameters are similar to those of other SIFSIX structures.

The c-axis is slightly elongated compared to  $\text{Cu}(\text{bpy-2})_2(\text{SiF}_6)$ , but shorter than that determined for UTSA-48, while the a and b axes are shorter than  $\text{Cu}(\text{bpy-2})_2(\text{SiF}_6)$  and UTSA-48, but of similar sizes to SIFSIX-2-Cu (and Cu-i). The elongation of the c-axis could be the result of a longer Cu-F bond. Within  $\text{Cu}(\text{bpy-2})_2(\text{SiF}_6)$  the ligand is fully conjugated by electron delocalisation from the pyridine rings through the double bond. This results in 1,2-bis(4-pyridyl)ethene being a stronger electron withdrawing group than 1,2-bis(4-pyridyl)ethane; the ligand of the studied material has a C-C single bond which no longer provides full conjugation of the molecule. Consequently, the  $\text{Cu}^{2+}$  in  $\text{Cu}(\text{bpy-2})_2(\text{SiF}_6)$  is surrounded by strong electron withdrawing groups, (ligand and  $\text{F}^-$  in axial positions), and the bonds to all coordinated atoms experience similar lengthening; in  $\text{Cu}(\text{bpetha})_2(\text{SiF}_6)$ , the  $\text{F}^-$  units would likely be more electron withdrawing than the organic ligands, and therefore would experience a longer lengthening than the equatorial coordinated atoms. The reduction in size of the a, b unit cell axes of  $\text{Cu}(\text{bpetha})_2(\text{SiF}_6)$  is possibly due to a change in the position of the unit cell with respect to the structure; a rotation of  $45^\circ$  of the  $\text{Cu}(\text{bpy-2})_2(\text{SiF}_6)$  unit cell but retaining the same symmetry, would reduce the cell size by  $\sqrt{2}$ , thus the cell of  $\text{Cu}(\text{bpetha})_2(\text{SiF}_6)$  is likely related by this transformation. The length of ligands 1,2-bis(4-pyridyl)ethane and 1,2-bis(4-pyridyl)ethene are similar, therefore, Cu-Cu distances should be similar between structures, assuming the same coordination. In order to perform a Rietveld refinement of the diffraction data, the atomic positions of the structure would need to be assumed and be within close approximation of the final structure. The differences in the cell orientation make comparison of the atomic positions difficult between  $\text{Cu}(\text{bpy-2})_2(\text{SiF}_6)$  and  $\text{Cu}(\text{bpetha})_2(\text{SiF}_6)$ .

To further elucidate the structure of the porous material, PXRD heating studies were performed, which analyse the structural changes related to desolvation of the void space, structural transformations related to the loss of guest or increase in

energy of the framework to allow movement of flexible ligands, and degradation of the structure, which would result in an amorphous material. All changes result in alteration of the peak positions within the diffraction pattern as changes in the structure cause differences in the d-spacing. Figure 6.7 shows the heating of  $\text{Cu}(\text{bpetha})_2(\text{SiF}_6)$  from room temperature to 453 K, with diffraction data recorded every 20 K between 353 K and 453 K. As stated previously, the most obvious changes occur at a temperature of 393 K, showing various new peaks appearing in the diffraction pattern between  $15 - 25^\circ$ . This is coupled with the loss in intensity of some of the peaks of the as-synthesised material, and overall the final structure after heating gives a pattern that appears to have a mix of phases; the as-synthesised product, and a 'closed' pore material. The alteration of the structure at 393 K occurs around the same temperature as full desolvation of the material from TGA data, as shown in Figure 6.8. Thus the appearance of new peaks can be explained by a collapsing of the pore structure of the material, without loss of framework integrity. A flexing of the organic ligand around the  $\text{sp}^3$  hybridised bond would reduce the Cu-Cu distance resulting in a closed form of the pore. To avoid the presence of a vacuum within the framework, solvent molecules are situated within the pore space and act as a template for the framework; their removal from the pore would leave the framework empty and prone to collapse of the ligand into a more stable arrangement. Complete loss of the structure has not occurred as peaks from the initial diffraction pattern are present within the final pattern. However, within the low angle region, which suggests long range order, new peaks form on either side of the original  $7^\circ$  peak; a splitting of the peak to higher and lower angle values is likely the impact of a shortening and lengthening of the a and b axes, changing the symmetry of the unit cell, which is supported by the inability to fit the new pattern to the original cell with altered parameters. Thus, it is suggested that this material has a thermally stable range between 298 – 453 K; the desolvation of the structure within this temperature range results in a closure of some of the porosity,

evidenced by the alteration of the PXRD data at 393 K, however, the structure remains intact by this collapse, which is likely due to the flexibility of the ligand bpetha.

Analysis of the IR spectra and CHN analysis shows some differences between the different metal salt synthesised products, from  $\text{Cu}(\text{BF}_4)_2$ ,  $\text{Cu}(\text{NO}_3)_2$  and  $\text{Cu}(\text{SO}_4)$ . The presence of peaks associated with 1,2-bis(4-pyridyl)ethane are found within each of the spectra in Figure 6.9. The broad bands at wavenumbers below  $800\text{ cm}^{-1}$  make characterisation within this region difficult. The identification of the anionic species  $[\text{SiF}_6]^{2-}$  also proved difficult; IR active stretches of  $[\text{SiF}_6]^{2-}$  are suggested to be found at  $741$  and  $483\text{ cm}^{-1}$ <sup>18</sup>. All samples exhibit a broad stretch across the range  $\sim 670 - 760$ , it is possible that the  $[\text{SiF}_6]^{2-}$  stretch is hidden within the wagging peak of the H atoms of the pyridine rings, which, due to their abundance, may mask a weaker stretch. IR Stretching due to the anions, which were part of the reactant metal salt, are suggested to be present at the following positions:  $[\text{BF}_4]^-$  ( $1070, 533$ ),  $[\text{NO}_3]^-$  ( $1390, 830, 720\text{ cm}^{-1}$ ),  $[\text{SO}_4]^{2-}$  ( $1130, 620\text{ cm}^{-1}$ )<sup>18,19</sup>. The most notable peak for  $\text{NO}_3$  at  $1339\text{ cm}^{-1}$  is possibly due to the nitrate anion being present within the MOF; the likely side product of  $(\text{NH}_4)_2(\text{NO}_3)$  may be present within the porous structure, and correlation with the CHN analysis data (Table 6.4) shows that more nitrogen content than predicted is found within this sample. Within the sample synthesised from  $\text{Cu}(\text{BF}_4)_2$ , an IR active stretch is seen at  $1056\text{ cm}^{-1}$ , which is not seen in the other two samples; again it could be that this is the product of the anion still present within the sample, possibly as a side product from the change in metal coordination. Cu-N frequencies have been seen to occur within the region  $260 - 300\text{ cm}^{-1}$ <sup>18</sup>. Unfortunately due to constraints set by the instruments capabilities, it was not possible to record the IR spectra within this region, therefore it could not be confirmed using this method whether all synthesised materials were Cu-bpetha coordinated complexes. It was assumed that the colour change during reaction would be a result of the coordination

around the Cu atom being altered, and since colour changes of this nature have been seen by similar structures to correspond to coordination of the bpetha units around the metal atom, it can still be deduced that the geometry around the metal centre will be similar in all variations of the Cu(bpetha) structures synthesised, and the differences in their IR spectra are due to other coordinating groups, or impurities. An additional peak in all recorded data is seen for CO<sub>2</sub> at 2349 cm<sup>-1</sup>. Although reference spectra were recorded, this peak was seen to increase in intensity over the course of the measurements. This may be due to issues with the instrument, or exchange of adsorbed CO<sub>2</sub> with atmospheric moisture (more intense O-H stretch in NO<sub>3</sub> and SO<sub>4</sub>, relative to a more negative CO<sub>2</sub> peak).

The results of the CHN analyses performed on BF<sub>4</sub> and NO<sub>3</sub> synthesised products were inconclusive as to the exact content of the measured species. The process of elemental analysis is complicated by the presence of larger elemental species, such as metals, and Si atoms, as side products (such as silicon carbide SiC) can take place, which is not measured by the instrument, resulting in differences between the expected and experimental results.

Porous characterisation of Cu(bpetha)<sub>2</sub>SiF<sub>6</sub> was initially performed using N<sub>2</sub> adsorption at 77 K to determine the porous structure and BET surface area. Figure 6.22 shows the N<sub>2</sub> adsorption profile over the full relative pressure range, which can be used to determine the type of pores within the material being studied. Similar materials have been analysed using this standard technique and have shown microporous materials due to their Type I classification<sup>2,8,20</sup>. Cu(bpetha)<sub>2</sub>SiF<sub>6</sub> can be classified as Type II, which is generally obtained for non-porous materials. The low surface area calculated from the analysis of the isotherm using the Rouquerol transform (Figure 6.23)<sup>21</sup>, and low maximum uptake at P/P<sub>0</sub> = 1, corroborates the result that this material is non-porous.

Due to the unexpected result compared to other materials of similar structure, further analysis of the adsorption capabilities were performed. Adsorption of CO<sub>2</sub> at 273 K (Figure 6.24) showed that the material had strong microporous character. The Langmuir (Figure 6.25) and D-R (Figure 6.26) analyses can be used for determination of the microporous nature of adsorbents. The results of the total pore volume and micropore volume for each analysis show that the porosity of Cu(bpetha)<sub>2</sub>SiF<sub>6</sub> is all microporous, and the precision to which both analyses determined the value is a good indication of the accuracy of the pore volume. There are limitations associated with using D-R analysis for low P/P<sub>0</sub> range data, which reduces the available information that can be obtained from the plot. Measurements were performed using an Intelligent Gravimetric Analyser, Hiden Isochema Ltd. (Warrington), which has a maximum working pressure of 20 bar. Measurements performed at the standard D-R analysis temperature of 273 K, provide a saturated vapour pressure for CO<sub>2</sub> of 34.762 bar, therefore, a maximum relative pressure of 0.67 can be achieved at this temperature. As described in Section 3.6.6, the deviation from linearity at high log<sup>2</sup>(P<sub>0</sub>/P) suggests the Gaussian pore size distribution is reduced at lower micropore sizes; due to the ordered structure of MOFs, it is expected that their pore size distribution would have a narrower range as the void space within the framework has a fixed size. Furthermore, had measurements been performed over the maximum range possible it is likely that the pore distribution would deviate at low log<sup>2</sup>(P<sub>0</sub>/P) to show a larger pore distribution; this is likely as defects in the formation of the crystalline material will result in large cavities and dislocations of the crystal faces which would appear as larger pores within the structure.

The pore volume determined from Langmuir and D-R analyses suggests that Cu(bpetha)<sub>2</sub>SiF<sub>6</sub> is an interpenetrated structure. The results of experimental and theoretical micropore volumes of the interpenetrated and non-interpenetrated versions

of SIFSIX-2-Cu, showed a 4x decrease in pore volume on generating an interpenetrated structure of the material <sup>2</sup>. The micropore volume obtained from our D-R analysis shows that it lays within the range of the interpenetrated structure, and simulations of the pore volume of a proposed structure show similar results <sup>22</sup>. Coupled with the results from N<sub>2</sub> analysis, an interpenetrated structure will have a much reduced pore size; as a result the effects of activated diffusion will prevent the adsorption of N<sub>2</sub> at 77 K into the porous structure <sup>23</sup>. The alteration of the structure due to the ligand's flexibility will reduce the pore size further than expected. It is therefore suggested that CO<sub>2</sub> at 273 K should be performed as a routine measurement to probe the adsorbent structure, as the strong attraction of CO<sub>2</sub> due to its quadrupole moment will enhance adsorption in very narrow micropores, and the higher temperatures limit the diffusion problems <sup>24</sup> (See Section 3.7.1).

## 6.5.2 STRUCTURAL ANALYSIS OF [Cu(TPT)]BF<sub>4</sub>·0.75H<sub>2</sub>O

The synthesis of MOF material [Cu(TPT)]BF<sub>4</sub>·0.75H<sub>2</sub>O was performed using a similar method to Feng *et al.*<sup>13</sup>. The method requires heating temperatures of up to 433 K to produce sufficient quantities of the MOF product, with respect to impurities of unreacted TPT<sup>25,26</sup>. The impact of this method of synthesis was seen in the reduction of Cu<sup>2+</sup> to Cu<sup>+</sup> metal centres. The colour of the crystals changing from blue Cu<sup>2+</sup> starting material to red crystal of the product was an indication that changes in the electronic configuration of Cu had occurred. The bond valence calculations proved the Cu atom was in the +1 oxidation state, and the Cu-F bond distances are longer than typical bond distances of this type, so [BF<sub>4</sub>]<sup>-</sup> is not within the main coordination sphere of the Cu<sup>+</sup> atom and does not formally bond with the metal centre, nor impact the coordination geometry. It is, however, a direct charge balancing ion for the metal centres, and the framework could not exist without it. Its location within the central cavity of the MOF structure was considered to impede adsorption capacity, due to the large size of the anion. Influence of the anion group had not been studied in the literature for this material (similar materials have been synthesised incorporating different anions and metal centres<sup>13,27-30</sup>), and interest in its effect on the adsorption properties and structural morphology were considered in this work. [BF<sub>4</sub>]<sup>-</sup> is a weakly coordinating anion compared with [NO<sub>3</sub>]<sup>-</sup><sup>31</sup>, this may allow for interesting adsorption properties.

The incorporation of triazine moieties to the MOF structure was expected to help enhance the CO<sub>2</sub> selectivity of the adsorbent material, through interaction of the quadrupole moment with the basic nitrogen donor sites<sup>32</sup>. Structures containing N sites incorporated within the organic ligand (3,6-bis(4-pyridyl)-1,2,4,5-tetrazine) have been previously studied<sup>33</sup>, which generated 2-dimensional ladder-like structures; it was proposed that the trivalent coordination of TPT, and the larger size of the [BF<sub>4</sub>]<sup>-</sup> anion

would help extend the structure in 3-dimensions, possibly enhancing the dimensionality of the porous structure through templating effects of the anion. The formation of the MOF material in this study was highly interpenetrated, resulting in one-dimensional pores along the a axis of the unit cell. The four interpenetrated nets stabilise the MOF structure, and as was seen in the TGA data collected up to 873 K (Figure 6.14), the structure did not collapse until a temperature of 623 K, making it a very stable material for a Cu-N coordinated structure.

The use of primary amines has been extensive within the literature to enhance interactions with CO<sub>2</sub>. One such case was the post-synthetic modification of Mg<sub>2</sub>(dobpdc) with an alkyldiamine onto the open metal site<sup>34</sup>. The amine functionality showed impressive CO<sub>2</sub> capture and selectivity, however, its strong basic character can lead to heats of adsorption of  $-71 \text{ kJ mol}^{-1}$ <sup>34</sup>, which is higher than expected for a physisorptive adsorption process, and is close to that of a chemisorptive interaction (Section 3.2). This requires high temperatures for regeneration, which reduces its effectiveness in carbon capture processes, as lowering energy requirements is one of the conditions which new adsorbent materials is trying to improve, relative to amine scrubbing reactions<sup>35</sup>. The interaction of secondary and tertiary amine moieties with CO<sub>2</sub> is said to be weaker than primary amines<sup>36</sup>. The reduced basicity of heterocyclic nitrogen sites is said to be the cause of the reduced interaction strength with CO<sub>2</sub><sup>32</sup>. In order to reduce the chemisorptive potential of the amine interaction, the choice of using triazine nitrogen sites was to potentially reduce the adsorption enthalpy of the material, and in doing so, reduce the regeneration costs. The physisorptive interaction was postulated to still have an enhancement of the selectivity of the material for CO<sub>2</sub>.

Studies of the PXRD data in Figure 6.13 showed a number of variations between diffraction patterns collected. Tick marks shown depict the allowed reflections

from the Cc space group, and in all patterns some of the possible reflections are seen. It is likely that preferred orientation of the crystalline material occurred during measurement; in some cases crystals were left unground to avoid mixing and breaking down larger crystals of the unreacted TPT ligand impurities to allow easy removal from bulk. In addition, desolvation of the material could have led to changes in the crystalline structure. This was ruled out by analysis of the structure by SCXRD after CO<sub>2</sub> adsorption had been performed on the material (Data from single crystal X-ray diffraction given in Appendix 10.5). The analysis was performed to determine whether retained CO<sub>2</sub> molecules could be located within the crystal structure, after it was found that a large hysteresis loop was observed (Section 3.5.2); although CO<sub>2</sub> molecules could not be seen, suggesting loss of gas molecules on exposure to atmosphere, the structure was marginally altered, however, this change could not have resulted in the differences seen in the powder diffraction patterns.

The collected pattern of the TPT ligand is shown in Figure 6.13 (black line), and the largest peak marked (~27 °) by a vertical dashed line for comparison with the other diffraction data. The large number of tick marks that are allowed within the region of this peak makes determination of the impurity within analysed samples difficult. All samples used for adsorption analysis were characterised using SCXRD methods to ensure that the synthesised crystals were the same.

The loss of 2237 cm<sup>-1</sup>, the peak responsible for the nitrile group (C≡N), in the TPT IR spectrum suggests no impurities of 4-cyanopyridine were left from synthesis. The large broad peak with maximum at 1034 cm<sup>-1</sup> in the MOF spectrum is likely that of the [BF<sub>4</sub>]<sup>-</sup> anion<sup>18</sup>. The presence of H<sub>2</sub>O, which was shown to be the solvent within the crystalline structure is also characterised the IR spectrum of the MOF. The spectrum recorded from the synthesised product, [Cu(TPT)]BF<sub>4</sub>.0.75H<sub>2</sub>O, suggests the structure

contains coordinated ligands of TPT, and the presence of  $[\text{BF}_4]^-$  anions. The results of the CHN analysis again show issues in resolving their structure. The presence of metals and other non-organic constituents can lead to unwanted side reactions, which can lead to spurious results.

Porous characterisation proved difficult for  $[\text{Cu}(\text{TPT})]\text{BF}_4 \cdot 0.75\text{H}_2\text{O}$ , as data collected using  $\text{N}_2$  at 77 K (Figure 6.27) showed a linear trend over 95 % of the relative pressure range, and only minimal uptake ( $\sim 5 \text{ cm}^3 \text{ g}^{-1}$ ). This does not fit one of the standard isotherm classifications<sup>20</sup>, and is the result of poor equilibration of the material, probably due to the pore blocking effects of the  $[\text{BF}_4]^-$  anions. It was possible however to perform  $\text{CO}_2$  measurements at 273 K for Langmuir and D-R analysis. The result of both analyses agree to a high degree of accuracy that the pore volume from  $\text{CO}_2$  analysis is  $0.091 \text{ cm}^3 \text{ g}^{-1}$  ( $\text{CO}_2$  density  $0.864 \text{ g cm}^{-3}$ ); this is a low pore volume attributable to the small pore size found from crystallographic data. Interestingly, the calculated pore volume from PLATON<sup>3</sup> suggests a pore volume of  $0.029 \text{ cm}^3 \text{ g}^{-1}$ , this suggests that a structural change may have occurred during adsorption which has expanded the pore volume by  $\sim 3\text{x}$ . The reduced adsorption of  $\text{N}_2$  is again the impact of activated diffusion within the structure, due to the small pore size and low temperature for analysis.

### 6.5.3 STRUCTURAL ANALYSIS OF [Cu(TPT)]NO<sub>3</sub>.MeOH

To further study the adsorption capabilities of adding nitrogen donor groups into the structure of the organic ligand, [Cu(TPT)]NO<sub>3</sub>.MeOH was synthesised according to the synthesis of Feng *et al.*<sup>13</sup>. The conditions for synthesis were unaltered, except the lower hydrated form of Cu(NO<sub>3</sub>)<sub>2</sub>.2.5H<sub>2</sub>O was used instead of Cu(NO<sub>3</sub>)<sub>2</sub>.6H<sub>2</sub>O. The resultant crystal was characterised in an alternative space group setting, P2<sub>1</sub>/n, to that used by Feng *et al.*, P2<sub>1</sub>/c; the lattice parameters were also slightly altered compared to the previously characterised material<sup>13</sup>. The improvements in the refined model can be attributed to the lower temperature use for data collection; previously X-ray data were collected at 293 K, the data collected here was at 123 K. This would reduce the amount of thermal motion of the atoms, making it easier to determine their positions. The larger electron density contributing from the C and O atoms of the methanol molecules will improve the accuracy of determining the solvent positions, compared with the H<sub>2</sub>O molecules of the original structure, owing to the slight improvement of the refinement fit performed in this work. The inclusion of methanol molecules, as opposed to H<sub>2</sub>O, within the porous structure could have resulted in the increased unit cell volume, as templating of the structure around the larger molecules alters the arrangement of atoms within the framework. The [NO<sub>3</sub>]<sup>-</sup> anion is weakly coordinated, as is seen from the bond valence calculation, showing a low contribution to the overall sum (Appendix 10.1). However, it is more closely coordinated than [BF<sub>4</sub>]<sup>-</sup> to the Cu<sup>+</sup> centres, consistent with it being a poorer leaving group than [BF<sub>4</sub>]<sup>-</sup><sup>37</sup>, which results in distortion of the trigonal planar arrangement of the nitrogen atoms of the TPT molecules coordinated to Cu<sup>+</sup>. The anions are not directly situated within the centre of the pore, however, an O atom protrudes into the central space from either side, as can be seen in Figure 6.17(b).

Studies of PXRD for several synthesised samples are shown in Figure 6.19; a number of variations were found between diffraction patterns. The samples N1, N2, and N3, marked as black, red, and pink lines, are three batches synthesised concurrently within three separate autoclaves; the samples LN1 and LN2 (blue and light blue lines) were synthesised together, but in two separate 45 cm<sup>3</sup> autoclave vessels. The former three have very similar patterns, mainly with variations in intensity. Similarly the 45 cm<sup>3</sup> samples have similar patterns, except for the blue pattern which shows a large peak at ~27°; it is likely that this peak is due to the impurities of unreacted TPT, as the largest peak is found at this position (Figure 6.19). The tick marks shown are for the allowed reflections from the P2<sub>1</sub>/n space group. The reflection at ~10.5° is consistent for all patterns, and the three largest peaks at low angle are seen in all patterns, with slight offsets from the calculated positions of the space group. Desolvation of the material has likely led to changes in the crystalline structure, as will be discussed in Chapter VII, the results from adsorption studies indicate a structural change in the framework resulting in interesting adsorption properties.

The thermal studies performed on [Cu(TPT)]NO<sub>3</sub>.MeOH show that only 4.32 % of mass loss is associated with solvent loss from the structure, and occurs up to 423 K. The thermal stability of this material appears to be lower than its counterpart [Cu(TPT)]BF<sub>4</sub>.0.75H<sub>2</sub>O, with thermal degradation occurring at 548 K; the structure is completely degraded by 673 K.

FT-IR analysis of the synthesised product shows similarities to the spectra of TPT (Figure 6.21). Previously, peaks from [NO<sub>3</sub>]<sup>-</sup> were suggested as appearing at positions 1390, 830, and 720 cm<sup>-1</sup> <sup>18,19</sup>. Two peaks that are not present in either of the starting materials have been marked on Figure 6.21 (corresponding to 735 and 826 cm<sup>-1</sup>); it is suggested that these peaks represent the stretching of the [NO<sub>3</sub>]<sup>-</sup> group. The additional peak at 1390 cm<sup>-1</sup> is hidden by the two peaks 1302 and 1372 cm<sup>-1</sup>; the

broadness of the peak is similar to that experienced in the  $\text{Cu}(\text{bpetha})_2\text{SiF}_6$  sample synthesised from  $\text{Cu}(\text{NO}_3)_2$ , suggesting that this could indicate a peak for  $[\text{NO}_3]^-$  at this position.

The results from porous characterisation of  $[\text{Cu}(\text{TPT})]\text{NO}_3 \cdot \text{MeOH}$  show that the material appears non-porous from  $\text{N}_2$  adsorption at 77 K. The low surface area was calculated to a high degree of accuracy, and the value of the C constant suggests a Type II classification. Issues resulting from a lower desorption branch than adsorption are likely due to a lower surface area than the minimum required to be present during the measurement; a relatively large sample mass was used to collect the data shown in Figure 6.31, therefore it was considered unnecessary to increase the amount used as the result would not produce any more meaningful results than had already been obtained.

Figure 6.33 shows the  $\text{CO}_2$  measurement performed at 273 K; Langmuir and D-R analysis were performed and shown in Figure 6.34 and Figure 6.35. The adsorption isotherm for  $\text{CO}_2$  shows that initially uptake is low, indicating weak interactions of the adsorbate with the adsorbent surface. This is possibly due to the initial structure upon desolvation being in a closed form, restricting access to the pore volume. The results of Langmuir and D-R analyses agree well that the pore volume from  $\text{CO}_2$  analysis is  $0.1015 \text{ cm}^3 \text{ g}^{-1}$  ( $\text{CO}_2$  density  $0.864 \text{ g cm}^{-3}$ ); this is higher than was obtained from the analogous material  $[\text{Cu}(\text{TPT})]\text{BF}_4 \cdot 0.75\text{H}_2\text{O}$ , as was expected from the reduced pore blocking by the anion. Analyses of the results from PLATON<sup>3</sup> suggests a pore volume of  $0.046 \text{ cm}^3 \text{ g}^{-1}$ ; this suggests that a structural change occurred during adsorption which expanded the pore volume by  $\sim 2\text{x}$ . As shown from  $\text{N}_2$  adsorption, activated diffusion is still a limiting factor, as uptake of  $\text{CO}_2$  at a temperature of 273 K is much higher than  $\text{N}_2$  adsorption at 77 K, . The quadrupole moment of  $\text{CO}_2$  may have an electrostatic effect on the structure which allows the gas to access the pore volume after a specific gating pressure is reached.

## 6.6 REFERENCES

1. Noro, S.-i., Horike, S., Tanaka, D., Kitagawa, S., Akutagawa, T. & Nakamura, T. Flexible and Shape-Selective Guest Binding at Cu-II Axial Sites in 1-Dimensional Cu<sup>II</sup>-1,2-Bis(4-pyridyl)ethane Coordination Polymers. *Inorganic Chemistry* **45**, 9290-300 (2006).
2. Nugent, P., Belmabkhout, Y., Burd, S. D., Cairns, A. J., Luebke, R., Forrest, K., Pham, T., Ma, S., Space, B., Wojtas, L., Eddaoudi, M. & Zaworotko, M. J. Porous materials with optimal adsorption thermodynamics and kinetics for CO<sub>2</sub> separation. *Nature* **495**, 80-4 (2013).
3. Spek, A. L. Structure validation in chemical crystallography. *Acta Crystallographica Section D-Biological Crystallography* **65**, 148-55 (2009).
4. Nugent, P., Rhodus, V., Pham, T., Tudor, B., Forrest, K., Wojtas, L., Space, B. & Zaworotko, M. Enhancement of CO<sub>2</sub> selectivity in a pillared pcu MOM platform through pillar substitution. *Chemical Communications* **49**, 1606-8 (2013).
5. Noro, S., Kitagawa, S., Kondo, M. & Seki, K. A new, methane adsorbent, porous coordination polymer {CuSiF<sub>6</sub>(4,4'-bipyridine)<sub>2</sub>}(n). *Angewandte Chemie-International Edition* **39**, 2082-4 (2000).
6. Xiong, S., He, Y., Krishna, R., Chen, B. & Wang, Z. Metal-Organic Framework with Functional Amide Groups for Highly Selective Gas Separation. *Crystal Growth & Design* **13**, 2670-4 (2013).
7. Yang, Y.-L. Poly[[ $(\mu_2$ -di-3-pyridylmethanone- $\kappa^2$ N:N')(\mu\_2-hexafluorosilicato- $\kappa^2$ F:F')-copper(II)] dihydrate]. *Acta Crystallographica Section E* **68**, m209 (2012).
8. Burd, S. D., Ma, S., Perman, J. A., Sikora, B. J., Snurr, R. Q., Thallapally, P. K., Tian, J., Wojtas, L. & Zaworotko, M. J. Highly Selective Carbon Dioxide Uptake by Cu(bpy-n)<sub>2</sub>(SiF<sub>6</sub>) (bpy-1=4,4'-Bipyridine; bpy-2=1,2-Bis(4-pyridyl)ethene). *Journal of the American Chemical Society* **134**, 3663-6 (2012).
9. Larson, A. C. & Von Dreele, R. B. General Structure Analysis System (GSAS). *Los Alamos National Laboratory Report*, 86-748 (2004).
10. Janczak, J., Sledz, M. & Kubiak, R. Catalytic trimerization of 2-and 4-cyanopyridine isomers to the triazine derivatives in presence of magnesium phthalocyanine. *Journal of Molecular Structure* **659**, 71-9 (2003).
11. Greenwood, N. N. & Earnshaw, A. *28 - Copper, Silver and Gold*. (Butterworth-Heinemann, 1997).
12. Brown, I. D. *The chemical bond in inorganic chemistry : the bond valence model*. (Oxford ; New York : Oxford University Press, 2002).
13. Feng, M., Tian, H.-J., Mi, H.-F. & Hu, T.-L. Poly[[ $(\mu_3$ -2,4,6-tri-4-pyridyl-1,3,5-triazine)copper(I)] nitrate monohydrate]. *Acta Crystallographica Section E-Structure Reports Online* **67**, M515-U1143 (2011).

14. Shekhah, O., Belmabkhout, Y., Adil, K., Bhatt, P. M., Cairns, A. J. & Eddaoudi, M. A facile solvent-free synthesis route for the assembly of a highly CO<sub>2</sub> selective and H<sub>2</sub>S tolerant NiSIFSIX metal-organic framework. *Chemical Communications* **51**, 13595-8 (2015).
15. Marti-Rujas, J. & Kawano, M. Kinetic Products in Coordination Networks: Ab Initio X-ray Powder Diffraction Analysis. *Accounts of Chemical Research* **46**, 493-505 (2013).
16. Higgins, C. *New Materials for Gas Storage and Separation* Master of Science thesis, University of Strathclyde, (2010).
17. Hafizovic, J., Bjorgen, M., Olsbye, U., Dietzel, P. D. C., Bordiga, S., Prestipino, C., Lamberti, C. & Lillerud, K. P. The inconsistency in adsorption properties and powder XRD data of MOF-5 is rationalized by framework interpenetration and the presence of organic and inorganic species in the nanocavities. *Journal of the American Chemical Society* **129**, 3612-20 (2007).
18. Nakamoto, K. *Infrared and Raman spectra of inorganic and coordination compounds Part A : theory and applications in inorganic chemistry*. 6th ed.. edn, (Wiley Oxford, 2009).
19. Larkin, P. *Infrared and raman spectroscopy principles and spectral interpretation*. (Elsevier, 2011).
20. Thommes, M., Kaneko, K., Neimark, A. V., Olivier, J. P., Rodriguez-Reinoso, F., Rouquerol, J. & Sing, K. S. W. Physisorption of gases, with special reference to the evaluation of surface area and pore size distribution (IUPAC Technical Report). *Pure and Applied Chemistry* **87**, 1051-69 (2015).
21. Rouquerol, J., Llewellyn, P. & Rouquerol, F. Is the BET Equation Applicable to Microporous Adsorbents? *Characterization of Porous Solids Vii - Proceedings of the 7th International Symposium on the Characterization of Porous Solids (Cops-Vii), Aix-En-Provence, France, 26-28 May 2005* **160**, 49-56 (2006).
22. Campbell, C., *Personal Communication*, 2016
23. Fletcher, A. J., Thomas, K. M. & Rosseinsky, M. J. Flexibility in metal-organic framework materials: Impact on sorption properties. *Journal of Solid State Chemistry* **178**, 2491-510 (2005).
24. Garrido, J., Linaressolano, A., Martinmartinez, J. M., Molinasabio, M., Rodriguezreinoso, F. & Torregrosa, R. Use of N<sub>2</sub> vs CO<sub>2</sub> in the Characterization of Activated Carbons. *Langmuir* **3**, 76-81 (1987).
25. Beveridge, S. *New Materials for Gas Storage and Separation* Master of Science thesis, University of Strathclyde, (2015).
26. Devlin, J. *New Materials for Gas Storage and Separation: The Synthesis and Characterization of Metal-Organic Frameworks for Carbon Capture* Master of Science thesis, University of Strathclyde, (2016).

27. Abrahams, B. F., Batten, S. R., Hamit, H., Hoskins, B. F. & Robson, R. A cubic (3,4)-connected net with large cavities in solvated  $\text{Cu}_3(\text{tpt})_4(\text{ClO}_4)_3$  (tpt=2,4,6-tri(4-pyridyl)-1,3,5-triazine). *Angewandte Chemie-International Edition in English* **35**, 1690-2 (1996).
28. Feng, M., Tian, H.-J., Mi, H.-F. & Hu, T.-L. catena-Poly [[diaquabis(formato- $\kappa\text{O}$ )nickel(II)]- $\mu$ -2,4,6-tris(4-pyridyl)-1,3,5-triazine- $\kappa^2\text{N}^2:\text{N}^4$ ]. *Acta Crystallographica Section E-Structure Reports Online* **67**, M563-U77 (2011).
29. Lo, K. M. & Ng, S. W. Diaqua(trifluoroacetato- $\kappa^2\text{O},\text{O}'$ )[2,4,6-tri-2-pyridyl-1,3,5-triazine- $\kappa^3\text{N}^2,\text{N}^1,\text{N}^6$ ]manganese(II) trifluoroacetate. *Acta Crystallographica Section E* **65**, m591-m2 (2009).
30. Wang, Y.-P., Zhang, N., He, X., Shao, M. & Li, M.-X. Poly[dinitrato[ $\mu_3$ -2,4,6-tris(4-pyridyl)-1,3,5-triazine]cobalt(II)]. *Acta Crystallographica Section E* **67**, m751 (2011).
31. Khlobystov, A. N., Blake, A. J., Champness, N. R., Lemenovskii, D. A., Majouga, A. G., Zyk, N. V. & Schroder, M. Supramolecular design of one-dimensional coordination polymers based on silver(I) complexes of aromatic nitrogen-donor ligands. *Coordination Chemistry Reviews* **222**, 155-92 (2001).
32. Sumida, K., Rogow, D. L., Mason, J. A., McDonald, T. M., Bloch, E. D., Herm, Z. R., Bae, T.-H. & Long, J. R. Carbon Dioxide Capture in Metal-Organic Frameworks. *Chemical Reviews* **112**, 724-81 (2012).
33. Dooris, E., McAnally, C., Cussen, E., Kennedy, A. & Fletcher, A. A Family of Nitrogen-Enriched Metal Organic Frameworks with CCS Potential. *Crystals* **6**, 14 (2016).
34. McDonald, T. M., Lee, W. R., Mason, J. A., Wiers, B. M., Hong, C. S. & Long, J. R. Capture of Carbon Dioxide from Air and Flue Gas in the Alkylamine-Appended Metal-Organic Framework mmen- $\text{Mg}_2(\text{dobpdc})$ . *Journal of the American Chemical Society* **134**, 7056-65 (2012).
35. Li, J.-R., Ma, Y., McCarthy, M. C., Sculley, J., Yu, J., Jeong, H.-K., Balbuena, P. B. & Zhou, H.-C. Carbon dioxide capture-related gas adsorption and separation in metal-organic frameworks. *Coordination Chemistry Reviews* **255**, 1791-823 (2011).
36. Choi, S., Drese, J. H. & Jones, C. W. Adsorbent Materials for Carbon Dioxide Capture from Large Anthropogenic Point Sources. *ChemSusChem* **2**, 796-854 (2009).
37. Brammer, L., Rodger, C. S., Blake, A. J., Brooks, N. R., Champness, N. R., Cunningham, J. W., Hubberstey, P., Teat, S. J., Wilson, C. & Schroder, M. Bridging mode flexibility of 1,3-dithiacyclohexane in silver(I) co-ordination polymers. *Journal of the Chemical Society-Dalton Transactions*, 4134-42 (2002).

# Chapter VII

# 7 ADSORPTION ANALYSIS OF MOF STRUCTURES

---

## 7.1 ADSORPTION ON $\text{Cu}(\text{BPETHA})_2\text{SiF}_6$

### 7.1.1 $\text{CO}_2$ ADSORPTION ISOTHERMS

Initial analysis of the adsorption capabilities of  $\text{Cu}(\text{bpetha})_2\text{SiF}_6$  was performed using  $\text{CO}_2$  as adsorbate at standard isotherm temperatures of 273 K and 298 K. This analysis gives an understanding of the factors affecting the adsorption mechanism and provides comparisons between other studied materials within the literature. Figure 7.1 shows the  $\text{CO}_2$  adsorption isotherms for 273 K and 298 K. Both isotherms follow the expected trends for physisorptive processes, with total adsorption having a lower uptake value with an increase in temperature. Although each shows hysteresis when approaching the low pressure region, it was observed that with mild heat ( $\sim 333$  K) the full desorption of  $\text{CO}_2$  could be achieved. Maximum capacities were calculated from the Langmuir adsorption isotherm model; at 273 K this was found in Section 6.4.1 to be  $2.398 \pm 0.007 \text{ mmol g}^{-1}$  and at 298 K it was calculated to be  $1.957 \pm 0.009 \text{ mmol g}^{-1}$ . The classification for the isotherms at 273 K and 298 K are Type I, however at 298 K it appears to show a plateau over this region and at 273 K it does not. It is suggested that they are distinguished as types I(a) and I(b), respectively, as at 273 K the isotherm does not show a completely horizontal plateau at the pressure range studied.

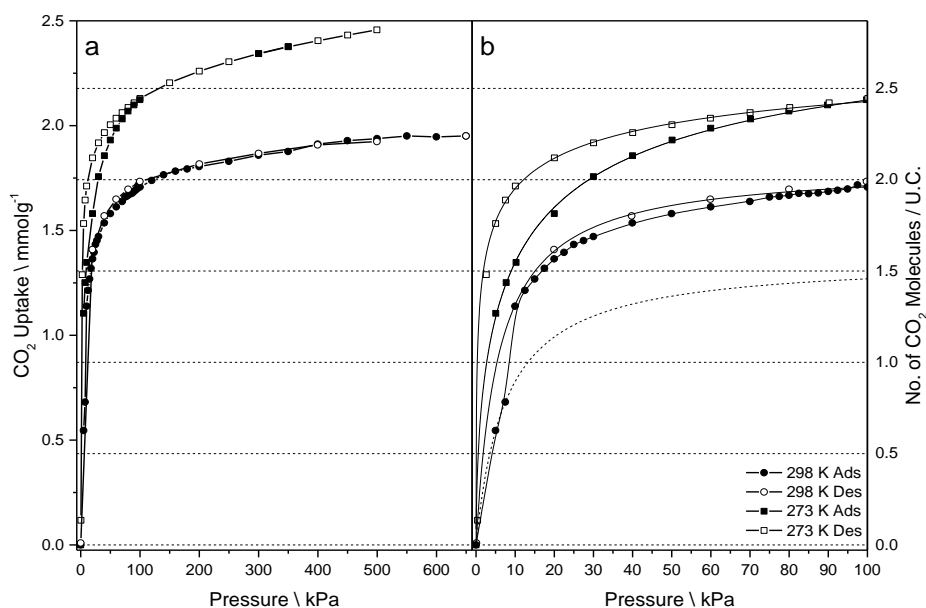


**Figure 7.1: CO<sub>2</sub> adsorption analysis on Cu(bpetha)<sub>2</sub>SiF<sub>6</sub> at 273 K and 298 K. (a) Pressure range 0 – 700 kPa, (b) Pressure range 0 – 100 kPa. ‘step’ in 298 K isotherm observed at 7.5 – 10 kPa**

Of special note within the isotherm at 298 K is the large increase in uptake (step) seen at the pressure increase from 7.5 – 10 kPa, accounting for ~23 % of the maximum capacity, as determined from Langmuir analysis; this is shown more clearly in Figure 7.1(b). Figure 7.1 also gives the uptake of CO<sub>2</sub> in terms of the number of molecules adsorbed (right-hand axis) within the expected unit cell of the material. In the case of Cu(bpetha)<sub>2</sub>SiF<sub>6</sub> this is determined from the formula weight of the expected unit cell structure; a doubly interpenetrated version of the Cu(bpethene)<sub>2</sub>SiF<sub>6</sub> material, which provides a unit cell molar weight of 1148.2 g mol<sup>-1</sup>. This shows that the ‘step’ occurs at an integer value of one CO<sub>2</sub> molecule, suggesting that the framework is required to open to permit further adsorption. The uptake of the initial pressure step of 273 K is above the point at which the step should occur, and therefore could not be probed at this temperature.

Additional measurements were performed for CO<sub>2</sub> at higher temperatures up to 100 kPa, in order to probe the adsorption performance at temperatures within the region 313 – 333 K; conditions which simulate flue gas streams during a post-combustion carbon capture processes<sup>1</sup>. Figure 7.2 shows the comparison of the two previous isotherms against isothermal temperatures of 318, 328, and 333 K. Adsorption continues to follow a physisorptive process, having lower uptakes at higher temperatures. In each isotherm, there is no significant hysteresis, and none of the higher temperature isotherms shows a significant increase in uptake at one CO<sub>2</sub> molecule per unit cell. To determine if this phenomenon was present at all temperatures the kinetics of adsorption was studied for the five isotherms (Section 7.1.4), which should give a better understanding of the adsorption process.

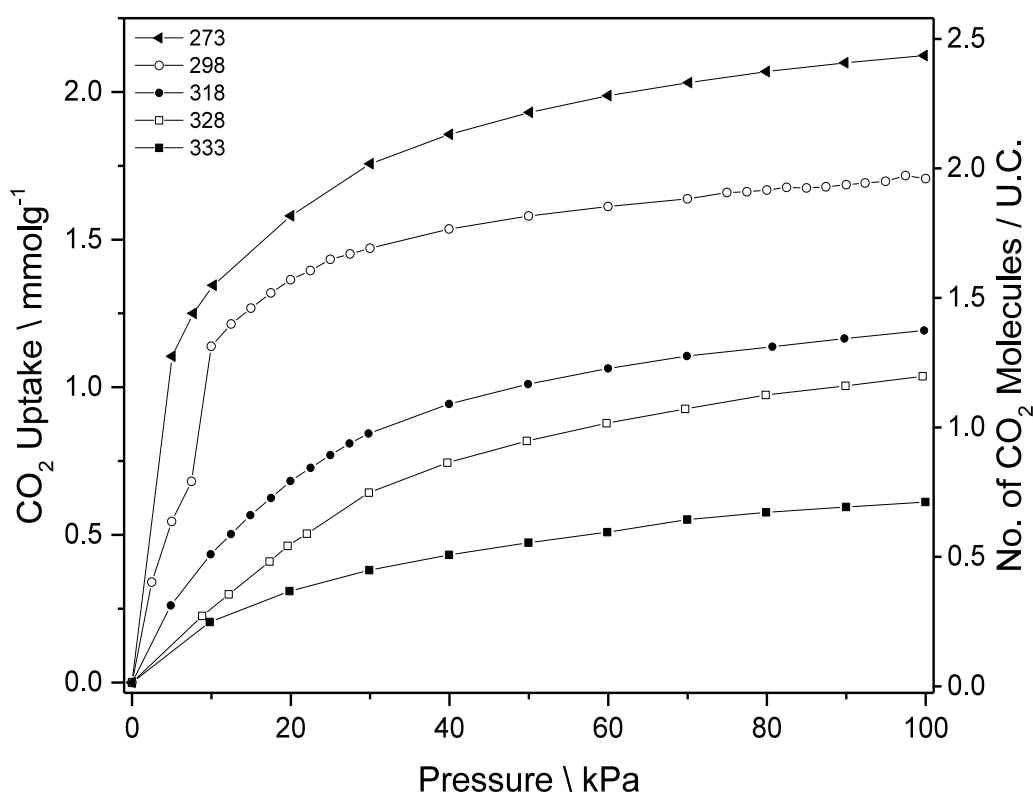
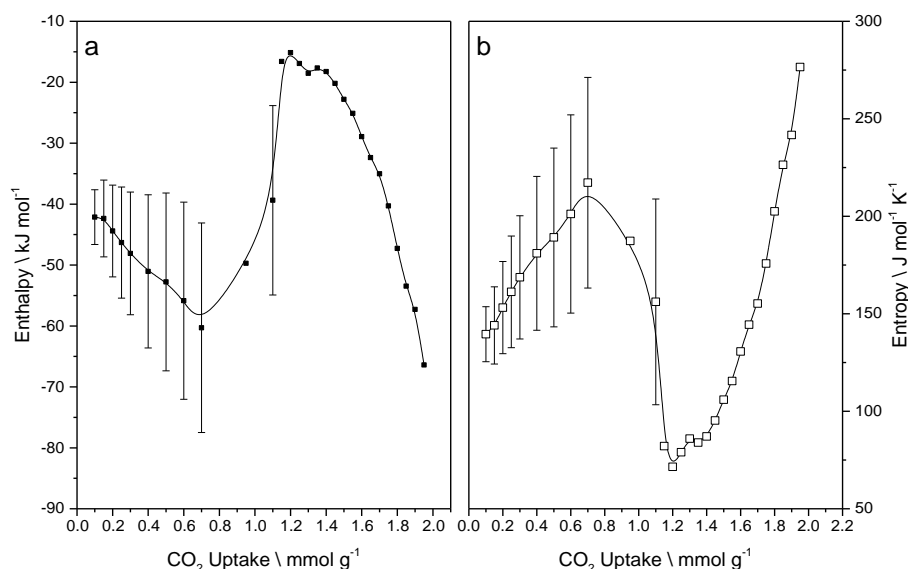


Figure 7.2: CO<sub>2</sub> adsorption isotherms in temperature range 273 K – 333 K for Cu(bpe)<sub>2</sub>SiF<sub>6</sub> over pressure range 0 – 100 kPa.

## 7.1.2 THERMODYNAMICS OF ADSORPTION



**Figure 7.3:** (a) Plot of isosteric enthalpy of adsorption ( $\text{kJ mol}^{-1}$ ) and (b) plot of isosteric entropy of adsorption ( $\text{J mol}^{-1}\text{K}^{-1}$ ) against  $\text{CO}_2$  molar uptake ( $\text{mmol g}^{-1}$ ) for  $\text{Cu}(\text{bpetha})_2\text{SiF}_6$ . Isosteres taken from isotherms to obtain pressures, which were plotted as the  $\ln(P)$  against  $1/T$ . Linear regression of the points for each isostere gave values for the gradient and intercept which could be used to obtain the enthalpy and entropy values, respectively. Errors were obtained from the least squares regression analysis.

Isosteric heats of adsorption could be determined from the series of temperatures recorded for  $\text{CO}_2$ , using the Clausius-Clapeyron equation. Analysis was performed by taking isochores through the adsorption data in Figure 7.2, and recording the pressure for each temperature measured. The resulting plots of  $\ln(P)$  vs.  $1/T$  gave enthalpy values from the gradient, and entropy values from the intercept. Figure 7.3 shows the values of Enthalpy (a) and Entropy (b) against the molar uptake. Linear plots below a molar uptake of  $1.1 \text{ mmol g}^{-1}$  were taken for a minimum of three temperatures; to obtain a rough estimate of the enthalpy and entropy values above  $1.1 \text{ mmol g}^{-1}$ , isochosres were taken through data collected at the temperatures 273 K and 298 K, therefore error values could not be determined for these results. The enthalpy of adsorption has values in the range  $-15 - -70 \text{ kJ mol}^{-1}$ . Zero coverage isotheric heat of adsorption was estimated to be  $\sim 40 \text{ kJ mol}^{-1}$ , with the zero coverage entropy being  $\sim 125 \text{ J mol}^{-1} \text{ K}^{-1}$ . The plot shows that there are distinct regions before and after the

'step' in the isotherms, considered to be the 'closed' and 'open' pore forms of the MOF, and a region between  $0.8 - 1.2 \text{ mmol g}^{-1}$  where there is a transition between the regions which cannot be well defined. The results from the plots above  $1.2 \text{ mmol g}^{-1}$  ('open' pore) must be considered with some degree of caution, as these data points are obtained from a straight line between two points. Even with the errors taken into consideration from the 'closed' pore data, the two regions are distinct. The enthalpy of the 'closed' pore form is higher than the value obtained for the 'open' pore ( $-40 \text{ kJ mol}^{-1}$  vs.  $-15 \text{ kJ mol}^{-1}$ ).

### 7.1.3 PURE COMPONENT ADSORBATE ISOTHERMS

Having studied the thermodynamic properties of CO<sub>2</sub> in Cu(bpe<sub>th</sub>)<sub>2</sub>SiF<sub>6</sub>, measurements of isotherms of methane (CH<sub>4</sub>) and nitrogen (N<sub>2</sub>) were performed at temperatures above and below the critical point of CO<sub>2</sub>, to compare with standard isotherms at 298 K, and determine the capacity of CH<sub>4</sub> and N<sub>2</sub> at the carbon capture conditions. Figure 7.4 shows the isotherms for 298 K and 333 K for the three competitive gases. The equilibrium CO<sub>2</sub> adsorption is higher for both 298 K and 333 K than CH<sub>4</sub> and N<sub>2</sub> at low pressures; Table 7.1 provides uptake capacities at 15 kPa, 100 kPa, and 500 kPa for each of the adsorbates used. At 298 K, CO<sub>2</sub> and N<sub>2</sub> follow a Langmuir plot, whereas CH<sub>4</sub> appears to be within the Henry's region over the whole pressure range studied; this results in an overlap in adsorption capacity with CO<sub>2</sub> at 300 kPa, and produces a larger equilibrium uptake for CH<sub>4</sub> at pressures above 300 kPa.

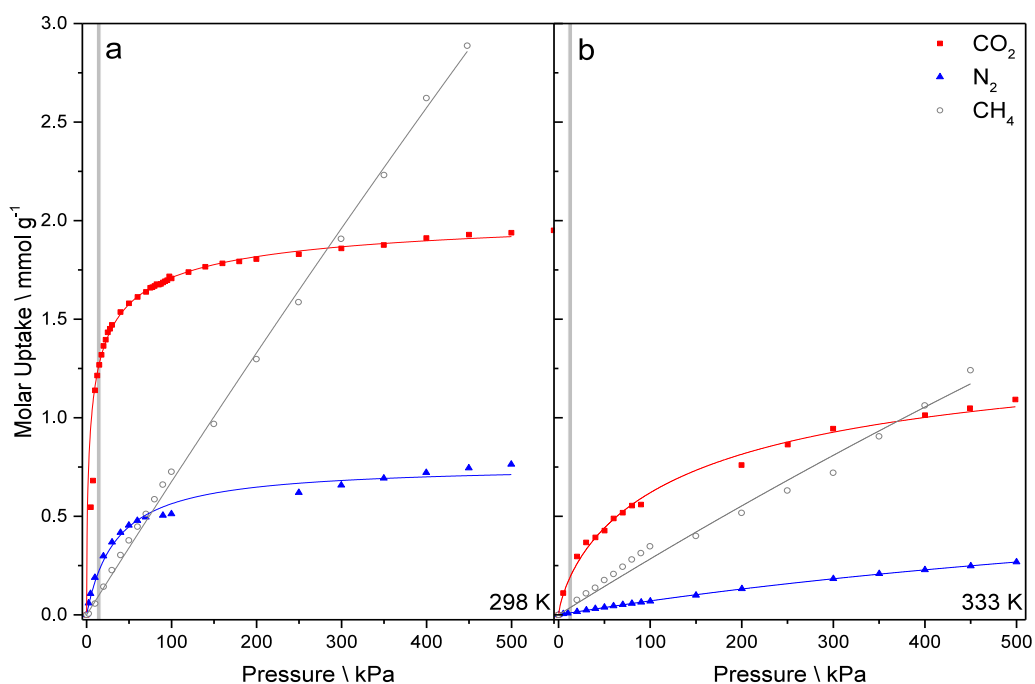


**Figure 7.4:** Adsorption isotherms for CO<sub>2</sub> (red ■), CH<sub>4</sub> (grey ○), and N<sub>2</sub> (blue ▲), at temperatures 298 K (a), and 333 K (b). Pressure range 10 – 15 kPa is highlighted (grey) to show the adsorption capacities for each gas at typical CO<sub>2</sub> concentrations.

The trend for CH<sub>4</sub> continues at 333 K, with an overlap in equilibrium adsorption capacity at 400 kPa with CO<sub>2</sub>, and the uptake for N<sub>2</sub> follows a similar linear plot, showing a maximum uptake at 500 kPa of 0.27 mmol g<sup>-1</sup>. The results were compared at the simulated conditions of flue gas streams, and for CO<sub>2</sub>/CH<sub>4</sub> compositions found in natural gas streams of between 10 – 15 % CO<sub>2</sub>. The grey band in Figure 7.4 shows the uptake in this region for both 298 K and 333 K, and shows that Cu(bpetha)<sub>2</sub>SiF<sub>6</sub> is selective for CO<sub>2</sub> at 298 K, and still has a higher uptake for CO<sub>2</sub> at 333 K, but at a much reduced equilibrium capacity; as shown in Table 7.1, the uptake capacities for the three gases are 0.21 mmol g<sup>-1</sup>, 0.04 mmol g<sup>-1</sup>, and 0.01 mmol g<sup>-1</sup>, which gives selectivity values based on molar ratios of 5.25 for CO<sub>2</sub>/CH<sub>4</sub> and 21 for CO<sub>2</sub>/N<sub>2</sub>.

**Table 7.1: Results of CO<sub>2</sub>, CH<sub>4</sub>, and N<sub>2</sub> adsorption at specified pressure intervals**

Pressure	Temperature (K)	Molar Uptakes (mmol g <sup>-1</sup> )		
		CO <sub>2</sub>	CH <sub>4</sub>	N <sub>2</sub>
15 kPa	298	1.27	0.1	0.23
	333	0.21	0.04	0.01
100 kPa	298	1.71	0.68	0.56
	333	0.62	0.28	0.07
500 kPa *	298	1.92	2.86	0.71
	333	1.06	1.17	0.27

\*CH<sub>4</sub> max. pressure was limited to 450 kPa for safety reasons

#### 7.1.4 ADSORPTION KINETICS

The kinetic data of the measured isotherms were fitted using the nested model of equations using the Double Stretched Exponential (DSE) as the basis for all analyses.

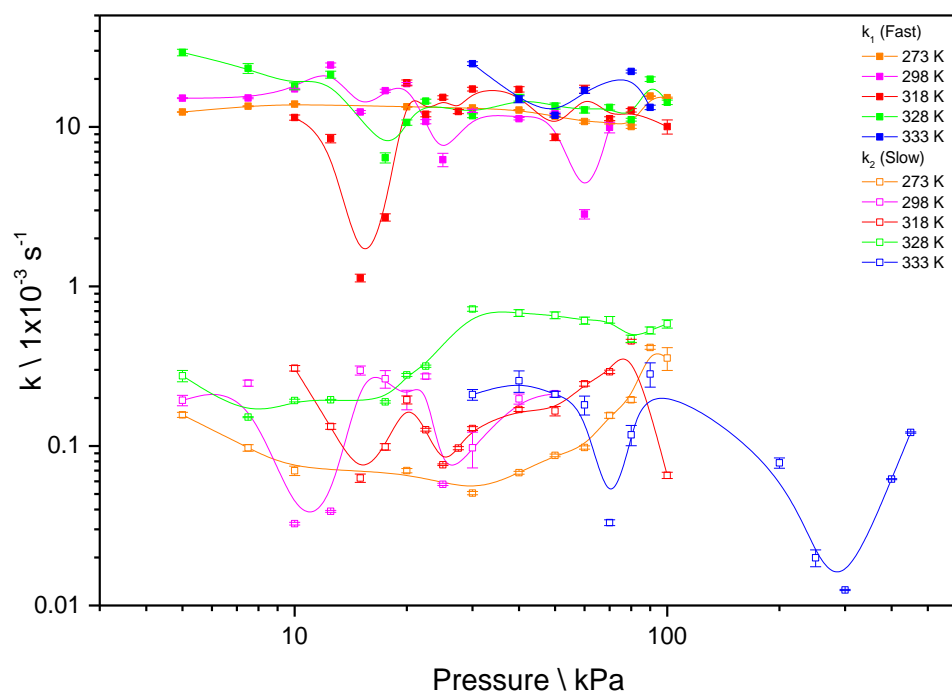
The equation shown in Chapter II for this model is defined as:

$$\frac{M_t}{M_e} = A_1 \left( 1 - e^{-(k_1 t)^{\beta_1}} \right) + A_2 \left( 1 - e^{-(k_2 t)^{\beta_2}} \right) \quad (7-1)$$

Where:

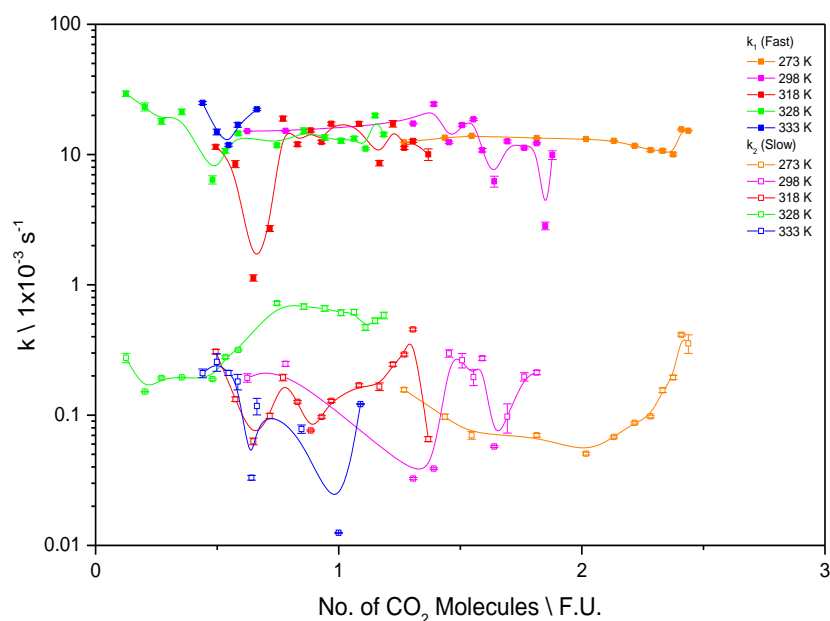
$M_t$	=	amount adsorbed (g) at time $t$ (s)
$M_e$	=	equilibrium uptake (g)
$k_1$	=	rate constants for process 1 ( $s^{-1}$ )
$k_2$	=	rate constants for process 2 ( $s^{-1}$ )
$t$	=	time (s)
$\beta_1$	=	exponential parameter for process 1
$\beta_2$	=	exponential parameter for process 2

All kinetic points were fitted to the most appropriate model with the minimum number of variables within the equation, and all kinetic models could be derived from the DSE model through reducing  $A_2$  to zero (Stretched Exponential SE), setting  $\beta$  values to one (Double Exponential DE), and reducing  $A_2$  to zero and setting  $\beta_1$  to one (Linear Driving Force LDF). Results were fit to a linear regression model and acceptable fits were considered when residuals were within  $\pm 0.02 - 0.04$  of the normalised kinetic profiles. The correction detailed in Section 10.6, is used for estimating the equilibrium uptake mass.



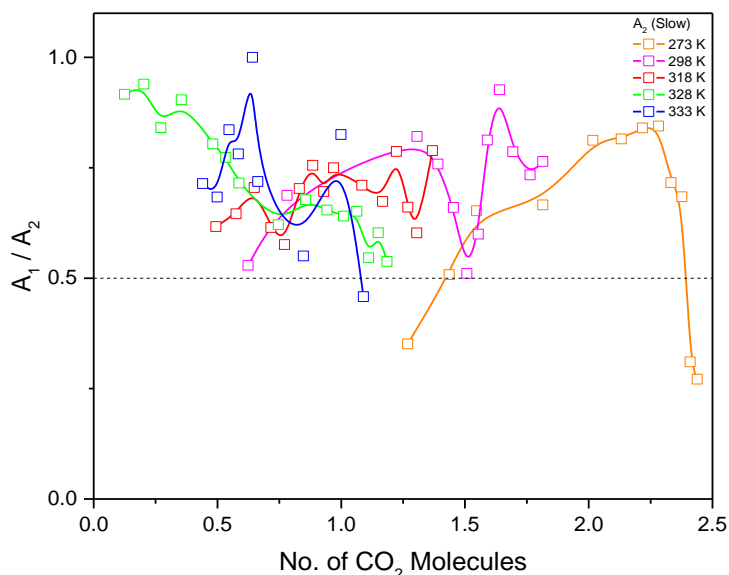
**Figure 7.5: Adsorption kinetic rate constants,  $k$  ( $s^{-1}$ ), for  $CO_2$  adsorption against pressure (kPa).  $CO_2$  is modelled to a Double Exponential, giving two rate constants,  $k_1$  having values of  $10^{-2} s^{-1}$ ,  $k_2$  having values of  $10^{-4} s^{-1}$ .**

The adsorption of  $CO_2$  at temperatures ranging from 273 – 333 K was studied for adsorption kinetics. The model fit to the data was DE, showing that the diffusion of  $CO_2$  into the pores was limited by two processes. The fast process  $k_1$ , had rates which were approximately between  $0.01 - 0.04 s^{-1}$ , whereas the slow process  $k_2$  was between  $1 \times 10^{-5} - 1 \times 10^{-3} s^{-1}$ . Figure 7.5 shows the plot of rate constants against pressure on a log scale. The plot shows that the rate constants follow similar trends at all temperatures. Additionally, the results are shown against the No. of  $CO_2$  molecules per unit cell (Figure 7.6), which shows that the rate constants show approximately a 10-fold decrease in the value of  $k_2$ , at values of one  $CO_2$  molecule per unit cell. This is not seen in the data for 273 K, as the molar uptake of the first pressure step is higher than the transition point of one  $CO_2$  molecule.



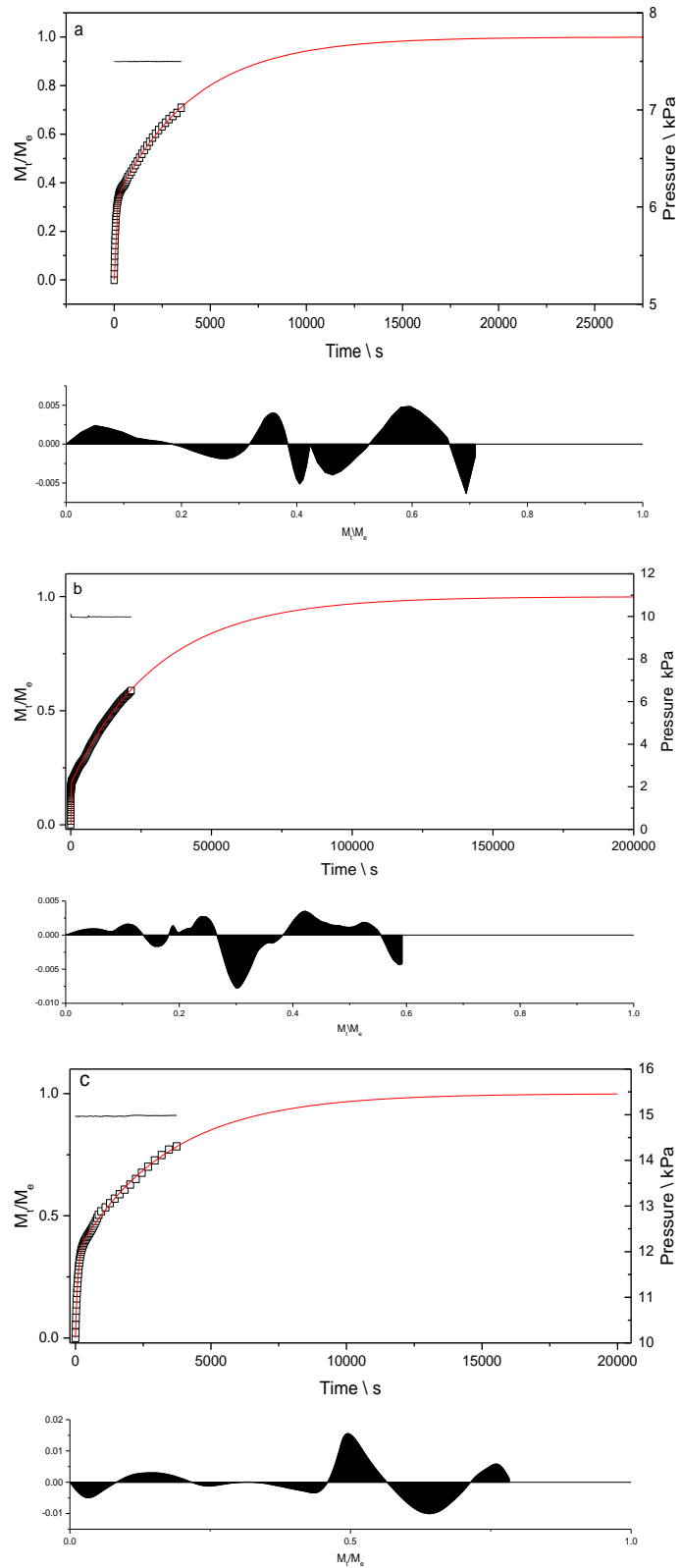
**Figure 7.6: Adsorption kinetic rate constants,  $k$  ( $s^{-1}$ ), for  $CO_2$  adsorption against No. of  $CO_2$  molecules per unit cell.  $CO_2$  is modelled to a Double Exponential, giving two rate constants,  $k_1$  having values of  $10^{-2} s^{-1}$ ,  $k_2$  having values of  $10^{-4} s^{-1}$ .**

A plot of the pre-exponential factor for the slow process from the DE equation,  $A_2$ , against the molar uptake for each of the temperatures measured (Figure 7.7) shows that the slow process is dominant at all temperatures. The trend shows the contributions converge towards 0.5.



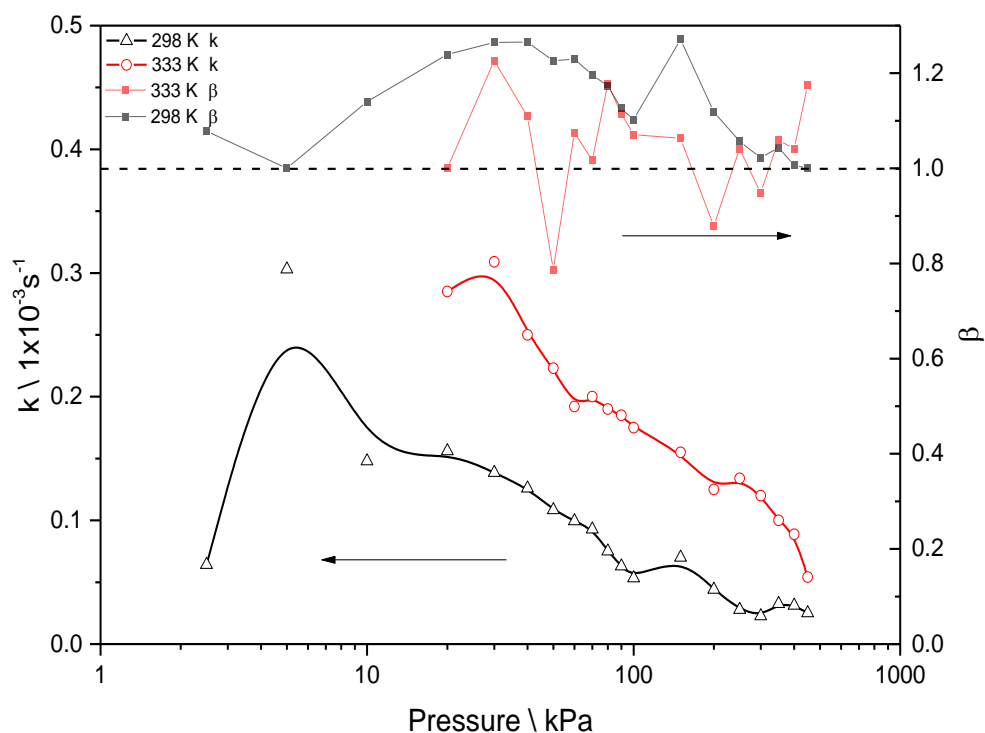
**Figure 7.7: Pre-exponential factor,  $A_2$ , for  $CO_2$  adsorption kinetics from DE model for temperatures from range 273 – 333 K. Only  $A_2$  is shown for clarity, the combination of  $A_1 + A_2 = 1$**

The plots of the kinetic profile data for 298 K (Figure 7.8) show the large increase in equilibrium time which occurs at the pressure increment 75 – 100 kPa, when compared with 5 – 7.5 kPa and 12.5 – 15 kPa.



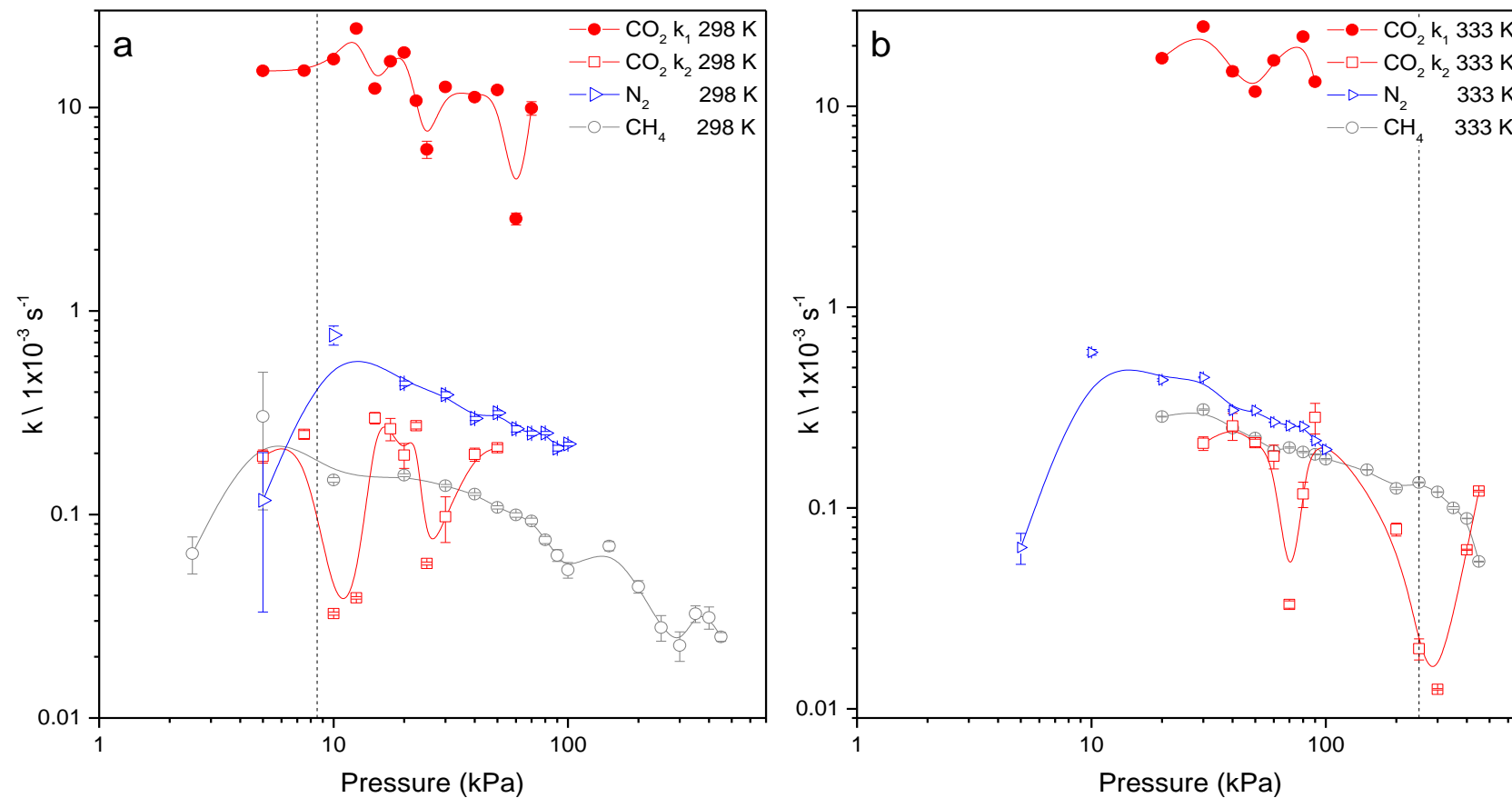
**Figure 7.8: Kinetic mass profiles vs time (s) of CO<sub>2</sub> adsorption pressure steps 5 – 7.5 kPa (a), 7.5 – 10 kPa (b), and 12.5 – 15 kPa (c). Plot (b) corresponds to the point at which the ‘step’ in the 298 K isotherm occurs, and shows an increase from 20000 s to 200000 s equilibration time. Plots are shown with their residuals for the fits, showing good agreement to the DE model.**

Having analysed the CO<sub>2</sub> kinetic rates, the kinetics of CH<sub>4</sub> and N<sub>2</sub> adsorption were analysed at temperatures of 298 K and 333 K. Figure 7.9 shows the kinetic parameters CH<sub>4</sub> for the rate constant  $k$  and the exponent, at temperatures of 298 K and 333 K. The rate constants show an increase in value with increase in temperature, and the exponent shows that the process follows typically an LDF model, with slight variations in the exponent.



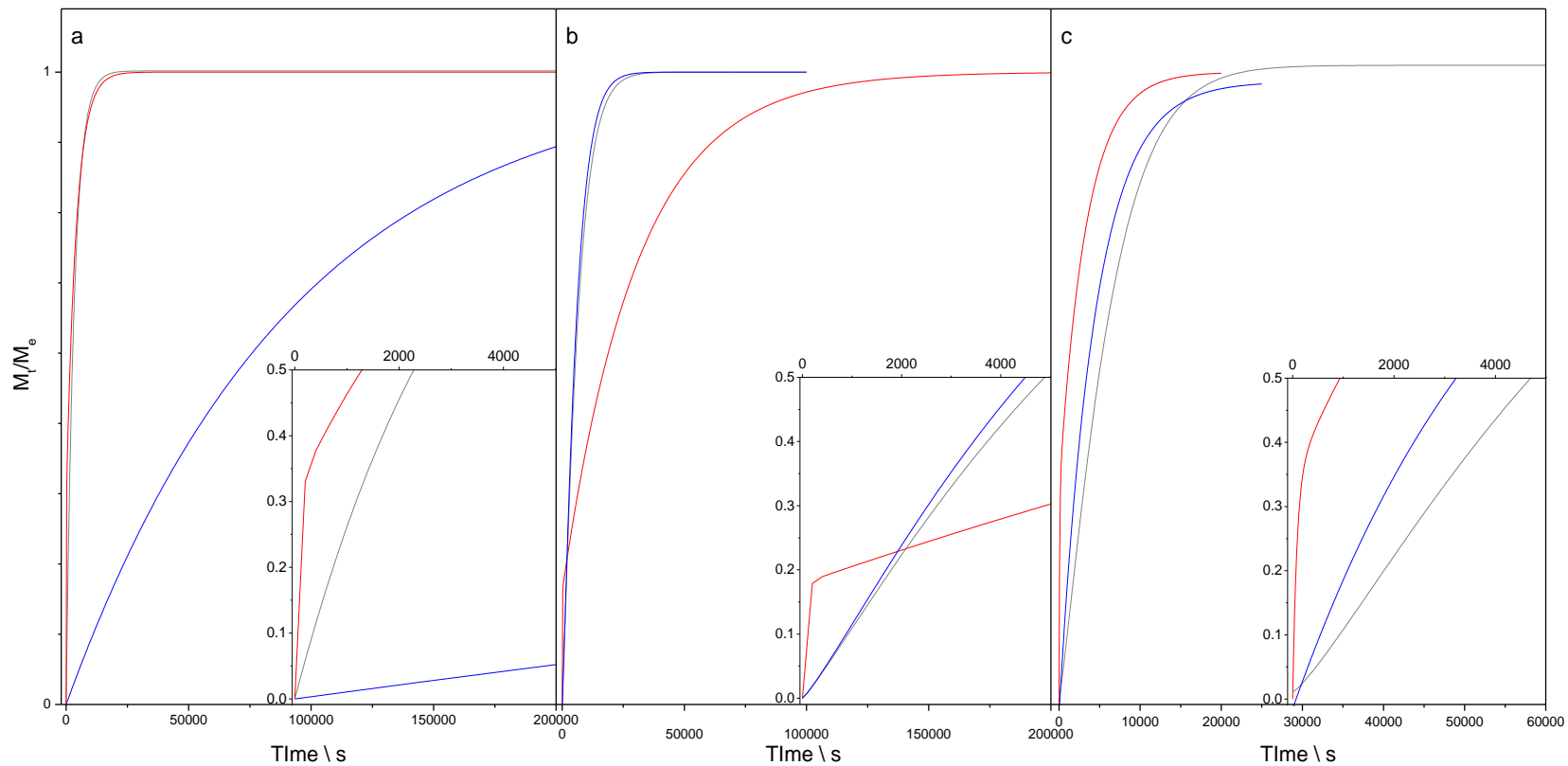
**Figure 7.9: Plot of CH<sub>4</sub> adsorption kinetics at 298 K and 333 K. Data for  $k$  (left-axis) and  $\beta$  (right axis) for the SE model used to fit the data. Data fits closely to a LDF model with exponent values ranging between 0.8 – 1.2.**

Figure 7.10 shows the rate constants of CO<sub>2</sub>, CH<sub>4</sub>, and N<sub>2</sub> at temperatures of 298 K (a) and 333 K (b). Both CH<sub>4</sub> and N<sub>2</sub> followed a stretched exponential (SE) rate process, with both being of similar magnitude to carbon dioxide's  $k_2$  constant. It can be seen from the graph that only CO<sub>2</sub> experiences a 10-fold change in the slow rate constant. Nitrogen has rate constants which are higher than CO<sub>2</sub> and CH<sub>4</sub>, however carbon dioxide's  $k_1$  rate constant ensures the diffusion process is always much quicker than either gas.



**Figure 7.10: Comparison of adsorption kinetic rate constants,  $k$  ( $\text{s}^{-1}$ ), against pressure (kPa) for  $\text{CO}_2$  (red),  $k_1$  (●) and  $k_2$  (□),  $\text{CH}_4$  (grey ○), and  $\text{N}_2$  (blue ▽) at (a) 298 K and (b) 333 K.  $\text{CO}_2$  fits to a DE model, whereas  $\text{CH}_4$  and  $\text{N}_2$  fit to a SE model. Dashed lines signify the pressure at which the volume filling reaches one molecule of  $\text{CO}_2$  per unit cell.**

The kinetic profiles of CO<sub>2</sub>, CH<sub>4</sub>, and N<sub>2</sub> were compared at the ‘step’ in the isotherm performed at 298 K, to see how the rate of CO<sub>2</sub> adsorption was impacted by the structural change of the MOF (Section 6.5.1). Figure 7.11(b) shows the pressure increment for the step in the CO<sub>2</sub> isotherm. As seen from Figure 7.4(a), the equilibrium uptake of CO<sub>2</sub> is much higher than those of N<sub>2</sub> and CH<sub>4</sub>; the plot shown in Figure 7.11(b) shows that CO<sub>2</sub> requires longer timescales to reach full capacity at 10 kPa and temperature. The initial rate of CO<sub>2</sub> due to  $k_1$  causes the uptake value to always be higher than the competing gases in the first few minutes of adsorption (inset figures in Figure 7.11).



**Figure 7.11: Mass-time profiles for CO<sub>2</sub> (red), CH<sub>4</sub> (grey), and N<sub>2</sub> (blue) at pressures before (a), during (b), and after (c) the 'step' in the CO<sub>2</sub> isotherm at 298 K. Inset figures show initial change in profile. Plots show CO<sub>2</sub> has quickest initial rate at all three pressures, but experiences a much slower rate at the 'step' in the isotherm. CH<sub>4</sub> and N<sub>2</sub> do not show the same change in profile**

The presence of a step in the 333 K isotherm was considered by analysis of the kinetic profiles from the adsorption measurement. Figure 7.12 shows the raw data of the kinetic profiles for CO<sub>2</sub> at 333 K in the pressure region 200 – 350 kPa. Of the three pressure steps recorded in the region, the 250 – 300 kPa pressure step is much longer than the steps on either side. This pressure step corresponds to a filling of one CO<sub>2</sub> molecule per unit cell at 333 K.

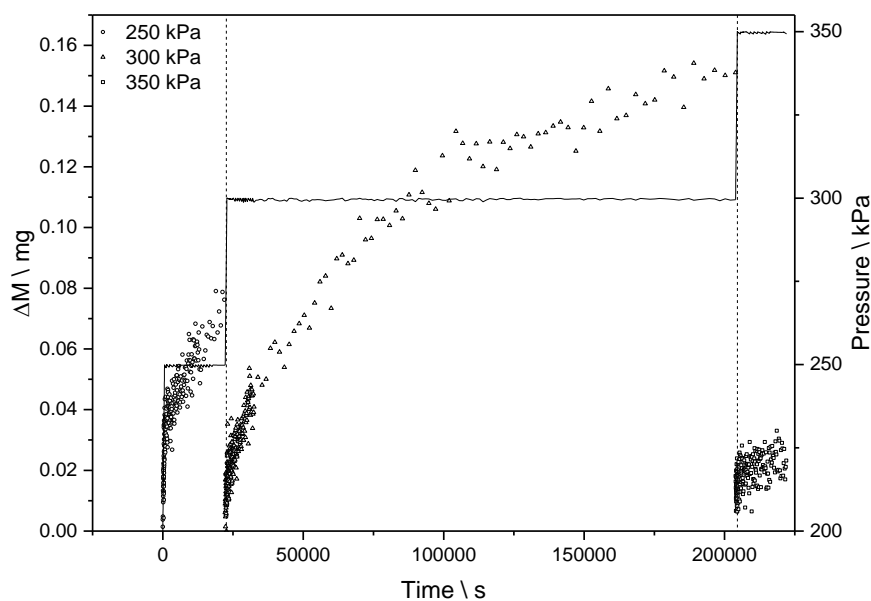


**Figure 7.12: Mass Profiles for CO<sub>2</sub> at 333 K over pressure range 200 – 350 kPa. Profiles show a long equilibration time for 250 and 300 kPa, which is not witnessed during pressures before or after, suggesting the ‘step’ in 333 K isotherm may occur at higher pressure, which corresponds to one CO<sub>2</sub> molecule per unit cell.**

To determine the presence of a step in the adsorption isotherms, the equilibrium times for pressure steps above and below the volume filling criteria of one CO<sub>2</sub> molecule per unit cell was analysed.

**Table 7.2: Equilibration times (s) before, during, and after the ‘step’ for temperature range 273 – 333 K**

Temperature (K)	Equilibrium Times (s)		
	Step Before	Step During	Step After
273*	-	-	2000
298	30000	200000	25000
318	61000	87000	74000
328	10000	11000	10500
333	25000	200000	20000

\*First pressure step is above one CO<sub>2</sub> molecule

### 7.1.5 COMPETITIVE ADSORPTION ISOTHERMS

To analyse the adsorption under more realistic conditions, when two of the competing gases are present, a dynamic isothermal experiment was performed using CO<sub>2</sub> and N<sub>2</sub> at varying flow rates from 0 – 200 cm<sup>3</sup> min<sup>-1</sup> in a maximum pressure of 100 kPa. By varying the flow rates of the two gases, the partial pressure of each component could be determined by the ratio of the gas contributing to the total flow. The plots in Figure 7.13 show the adsorption isotherms of the competitive measurement under a flow of CO<sub>2</sub> and N<sub>2</sub>, and the adsorption of pure CO<sub>2</sub> at a constant flow rate of 200 cm<sup>3</sup> min<sup>-1</sup> and varying the pressure from 0 – 100 kPa.

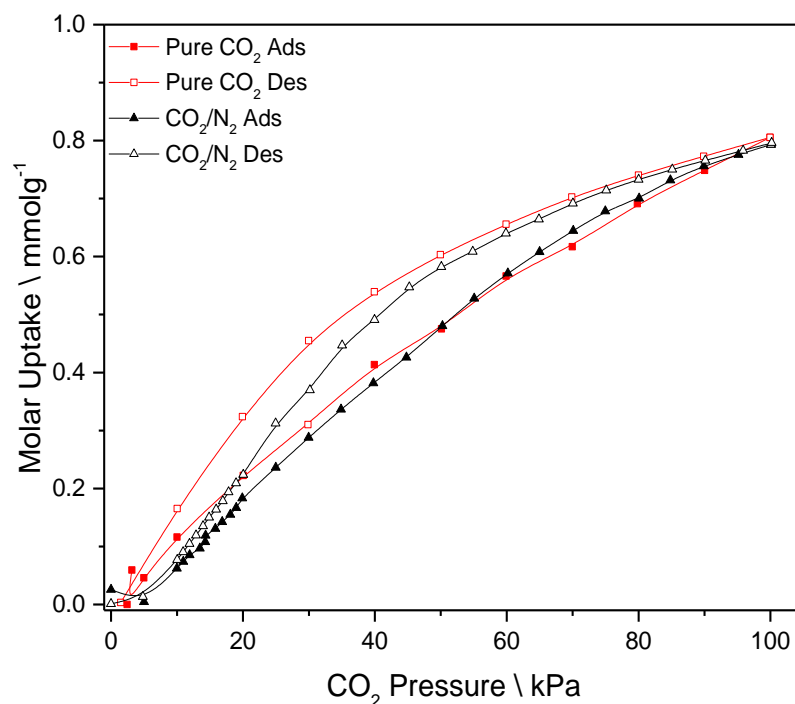


**Figure 7.13: Competitive adsorption isotherm for CO<sub>2</sub> vs. N<sub>2</sub> at 333 K (black ▲), with desorption curve (black △). Pressure was maintained at 100 kPa with a total flow of gas of 200 ml min<sup>-1</sup>. Ratio of flow rates was changed to alter the partial pressure of CO<sub>2</sub> within the system. Second curve shows pure component adsorption (red ●) and desorption (red ○) isotherm for CO<sub>2</sub> at 333 K under flowing conditions to compare with competitive adsorption uptake. Plots show mixed flow has similar uptake to pure CO<sub>2</sub> indicating minimal uptake of N<sub>2</sub>. Presence of N<sub>2</sub> causes a suppression of the isotherm at low CO<sub>2</sub> partial pressures, suggesting mean free path is altered.**

In considering the adsorption performance of  $\text{Cu}(\text{bpetha})_2\text{SiF}_6$  in the context of post-combustion capture using pressure swing adsorption (PSA) processing, the equilibration times of  $\text{CO}_2$  and  $\text{N}_2$  were considered for pressures of 10 kPa ( $\text{CO}_2$ ) and 90 kPa ( $\text{N}_2$ ). Figure 7.14 shows the normalized adsorbed mass based on equilibrated uptake ( $M_e$ ) for single component isotherms of  $\text{CO}_2$  (0–10 kPa) and  $\text{N}_2$  (0–90 kPa) at 333 K, over a 10 min period. The equilibrium uptake of  $\text{CO}_2$  at 10 kPa is far quicker than  $\text{N}_2$  at 90 kPa, indicating a selective separation of  $\text{CO}_2$  using the kinetic capabilities of  $\text{Cu}(\text{bpetha})_2\text{SiF}_6$ . Moreover, the completion of equilibrium uptake is approximately 90 % of the total capacity for  $\text{CO}_2$  at 10 kPa within the first 3 mins of exposure to pressure, putting  $\text{Cu}(\text{bpetha})_2\text{SiF}_6$  well within the limits of most PSA cycling times. The non-linear nature of the curve below 3 min is a result of the pressure ingress during the adsorption measurement.

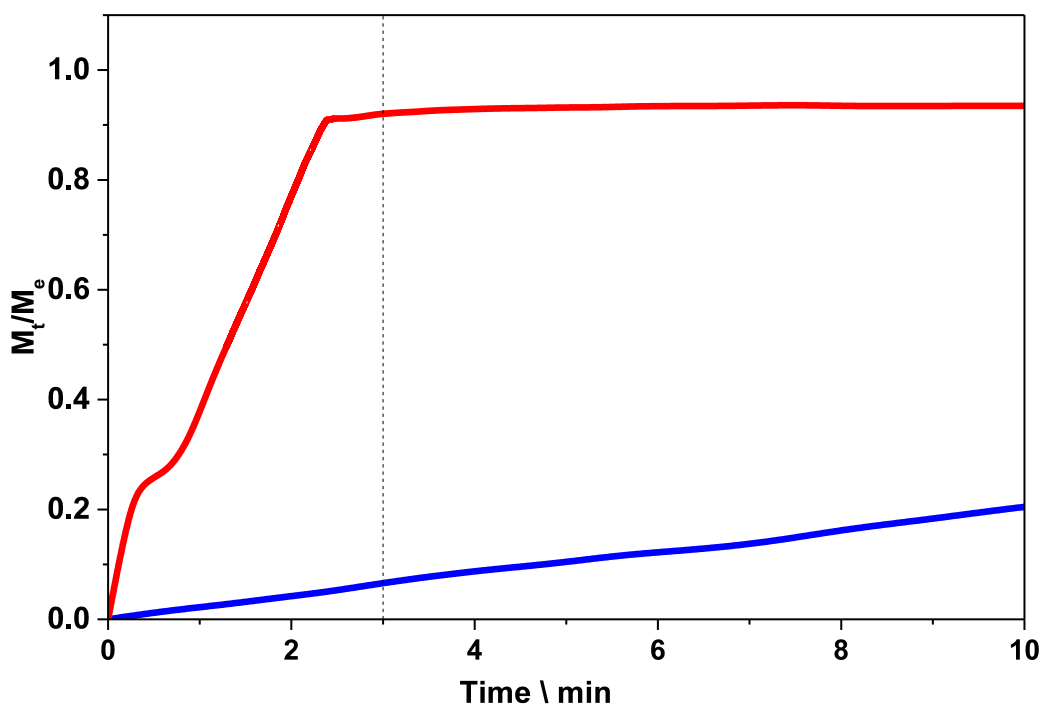


**Figure 7.14: Pure component mass profiles vs. equilibration time (min) for  $\text{CO}_2$  (red) and  $\text{N}_2$  (blue) at 333 K.  $\text{CO}_2$  plot shown for a pressure step of 10 kPa, and  $\text{N}_2$  plot shown for a pressure step of 90 kPa. Plots show  $\text{CO}_2$  reaches 90 % of the equilibrated mass uptake within 3 min, with  $\text{N}_2$  having very low uptake at this time.**

## 7.2 ADSORPTION ON [Cu(TPT)]BF<sub>4</sub>·0.75H<sub>2</sub>O

### 7.2.1 ADSORPTION ISOTHERMS

The adsorption of gases CO<sub>2</sub>, CH<sub>4</sub> and N<sub>2</sub> were studied on [Cu(TPT)]BF<sub>4</sub>·0.75H<sub>2</sub>O, to consider its suitability for carbon capture processes. Figure 7.15 shows the equilibrium uptake of CO<sub>2</sub>, CH<sub>4</sub>, and N<sub>2</sub> at 333 K up to 100 kPa. The adsorption capacity of all three gases within this MOF is extremely low, with maximum uptakes at 100 kPa going in order CH<sub>4</sub> > CO<sub>2</sub> > N<sub>2</sub>. All three gases experience wide hysteresis loops, showing a strong retention of adsorbate molecules on reducing pressure. At a pressure of 10 kPa, it is observed that the uptakes for CO<sub>2</sub> and N<sub>2</sub> are similar in value (0.02 and 0.012 mmol g<sup>-1</sup>), therefore appreciable separation would be insignificant. At this pressure, methane is shown to have an uptake of 0.04 mmol g<sup>-1</sup>; although double the capacity of CO<sub>2</sub>, it is still well below a value which makes it capable of separations of CH<sub>4</sub> from CO<sub>2</sub>.

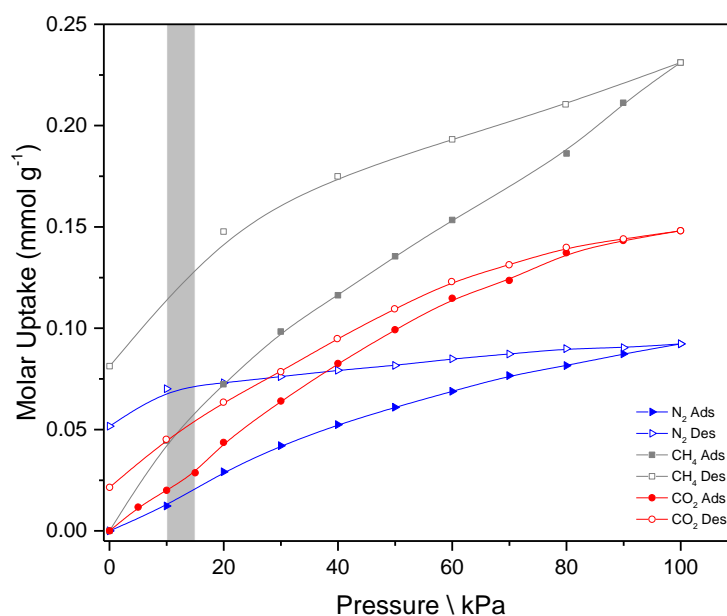


**Figure 7.15: Adsorption isotherms for CO<sub>2</sub> (red), CH<sub>4</sub> (grey), and N<sub>2</sub> (blue) on [Cu(TPT)]BF<sub>4</sub>·0.75H<sub>2</sub>O at 333 K from 0 – 100 kPa. Grey band shows pressure range between 10 – 15 kPa which indicates the concentration of CO<sub>2</sub> within a post-combustion flue gas stream, showing adsorption of CH<sub>4</sub> is higher in this region.**

## 7.2.2 ADSORPTION KINETICS

The kinetics were used to further probe the adsorption performance of  $[\text{Cu}(\text{TPT})]\text{BF}_4 \cdot 0.75\text{H}_2\text{O}$ , to give a better understanding of the process which governs the minimal equilibrium capacity. The set of nested models, using the double stretched exponential as a basis, was used to analyse the kinetics of adsorption. The best fit was assumed based upon the least number of variables required to give residuals from linear regression of less than  $\pm 0.02 - 0.04$ . Figure 7.16(a) shows a comparison between the rate constants of  $\text{CO}_2$ ,  $\text{CH}_4$  and  $\text{N}_2$ , plotted with their exponents. All three gases were found to fit the stretched exponential (SE) model.  $\text{CH}_4$  was found to have a constant trend in adsorption, whereas  $\text{CO}_2$  showed a minimum adsorption rate at 40 kPa, and  $\text{N}_2$  experienced a linear increase and levelled off at a rate comparable to  $\text{CH}_4$ .  $\text{CO}_2$  could not be modelled at pressures above 70 kPa, as the resolution for the mass-time profile was reduced due to the low uptake quantities. All models showed differences in the  $\beta$  exponent of the model, with  $\text{CO}_2$  and  $\text{N}_2$  showing a typical stretched model, whereas  $\text{CH}_4$  was more accurately modelled by an Avrami model above pressures of 30 kPa.

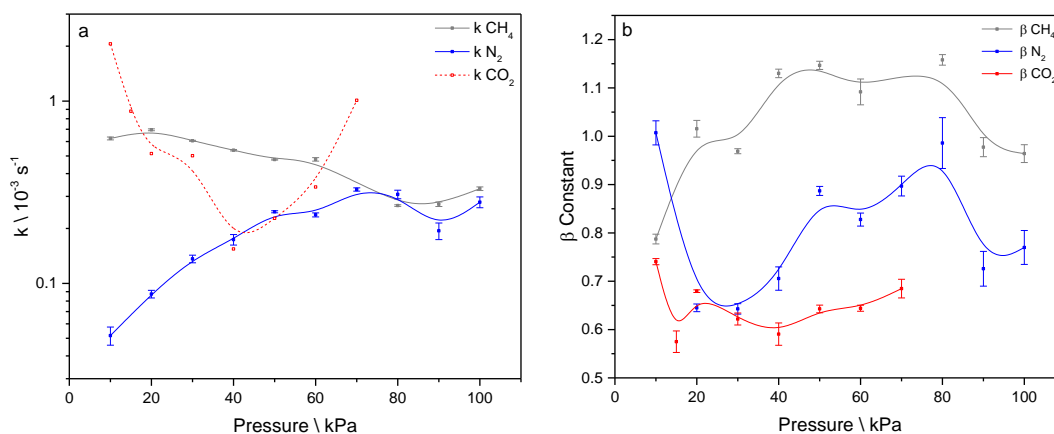


**Figure 7.16: Adsorption kinetic parameters, (a) rate constant,  $k$  ( $\text{s}^{-1}$ ), against pressure (kPa) and (b) exponent  $\beta$  against pressure (kPa) for  $\text{CO}_2$  (red),  $\text{CH}_4$  (grey), and  $\text{N}_2$  (blue) at 333 K.**

Further analysis of this structure was not carried out, as it was deemed inadequate for the purposes of this investigation. The aims of this thesis were to determine the properties of Metal-Organic Framework materials which were suitable for carbon capture processes and/or the removal of CO<sub>2</sub> from natural gas streams. As such the uptake of CO<sub>2</sub> in this material, at conditions simulated for carbon capture, was insignificant compared to current capture methods, and was lower than methane.

## 7.3 ADSORPTION ON [Cu(TPT)]NO<sub>3</sub>.MeOH

### 7.3.1 ADSORPTION ISOTHERMS

Adsorption analysis of [Cu(TPT)]NO<sub>3</sub>.MeOH, the analogous material to [Cu(TPT)]BF<sub>4</sub>.0.75H<sub>2</sub>O, was performed to determine its capabilities for CO<sub>2</sub> capture. The material was studied at 298 K for CO<sub>2</sub> and CH<sub>4</sub> and 333 K for CO<sub>2</sub>, CH<sub>4</sub> and N<sub>2</sub>; the results of these measurements are shown in Figure 7.17. The results show that at 298 K the uptake for methane is 2.04 mmol g<sup>-1</sup>, compared with CO<sub>2</sub> whose uptake is 1.09 mmol g<sup>-1</sup>; the desorption curves show hysteretic behaviour, however the uptake when outgassed is approximately zero shown from the final data point collected on the desorption curves. At 333 K, the isotherms follow the same trend in maximum uptakes resulting in maximum uptakes at 100 kPa of, CH<sub>4</sub> 1.58 mmol g<sup>-1</sup>, CO<sub>2</sub> 0.64 mmol g<sup>-1</sup>, and N<sub>2</sub> 0.24 mmol g<sup>-1</sup>. The results of this material are comparable to [Cu(TPT)]BF<sub>4</sub>.0.75H<sub>2</sub>O, and must result from a structural component within the framework. Comparison of the uptakes at 10 kPa shows very little difference in uptakes, showing the same trend of CH<sub>4</sub>>CO<sub>2</sub>>N<sub>2</sub>; at such low uptake values, it is possible the resolution of the instrument means that these values overlap and there is no separation ability of the material at 333 K.

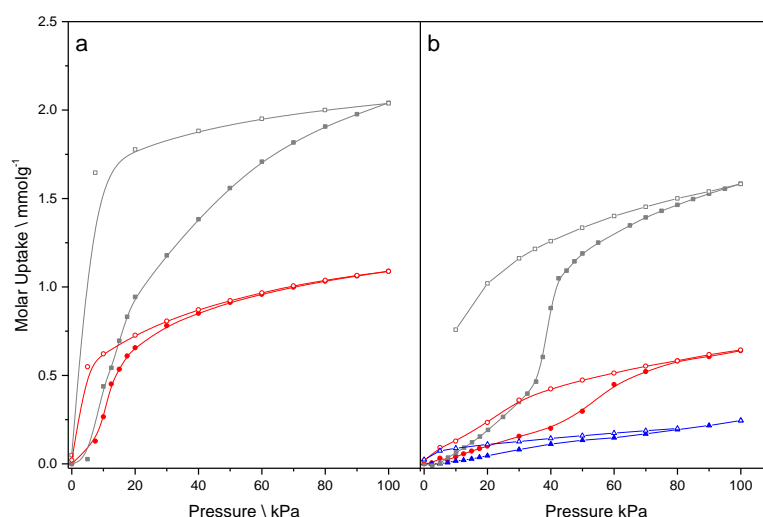


**Figure 7.17: Adsorption isotherms for (a) CO<sub>2</sub> (red) and CH<sub>4</sub> (grey) at 298 K, and (b) CO<sub>2</sub> (red), CH<sub>4</sub> (grey), and N<sub>2</sub> (blue) at 333 K.**

Further analysis of the methane adsorption capacity was studied for different temperatures between 298 – 333 K. Figure 7.18 shows the adsorption results for CH<sub>4</sub> up to a maximum of 100 kPa. The results show a decreasing trend in uptake with temperature, showing a physisorptive process. Similarities in the maximum uptake of 318 and 323 K, and 328 and 333 K suggest limiting thermal threshold exists for volume filling within the microporous structure. The isotherm also undergoes a ‘step’, corresponding to ~0.3 - 0.4 mmol g<sup>-1</sup> in all temperatures studied, and approximately corresponds to 1 molecule of CH<sub>4</sub> per unit cell of [Cu(TPT)]NO<sub>3</sub>.MeOH.

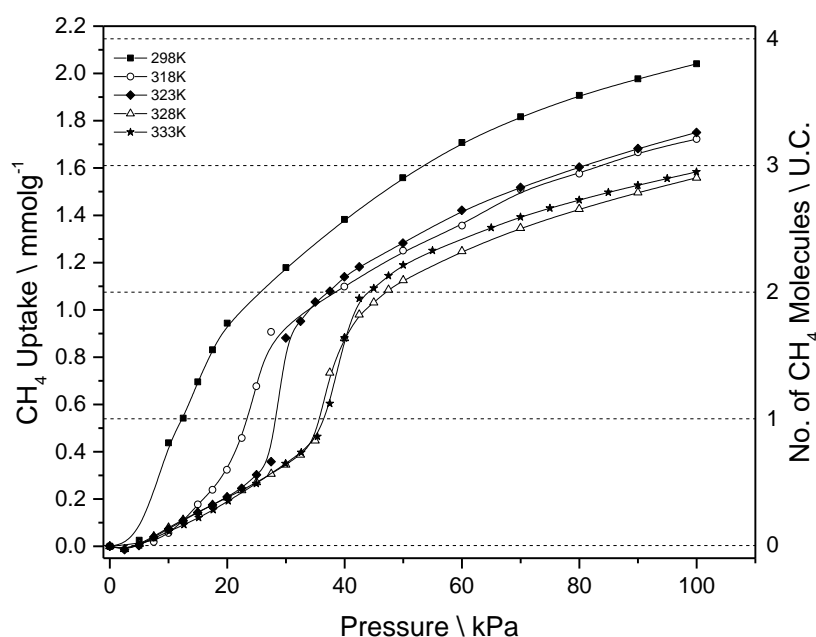


**Figure 7.18: CH<sub>4</sub> adsorption isotherms measured at 298 – 333 K, over pressure range 0 – 100 kPa. Second axis given showing number of CH<sub>4</sub> molecules per unit cell. Isotherm ‘step’ observed for volume filling of one CH<sub>4</sub> molecule per unit cell**

### 7.3.2 THERMODYNAMICS OF ADSORPTION

The isosteric heats of adsorption of the CH<sub>4</sub> uptakes were calculated by fitting of the virial equation to the isotherm plots. The virial graphs for [Cu(TPT)]NO<sub>3</sub>.MeOH for temperatures from 298 – 333 K are shown in Figure 7.19; the parameters obtained from the linear fits are shown in Table 7.3. Linear plots were fit at positions before and after the step in the isotherms which corresponds to filling to one molecule of CH<sub>4</sub> and filling after two molecules of CH<sub>4</sub> have adsorbed.

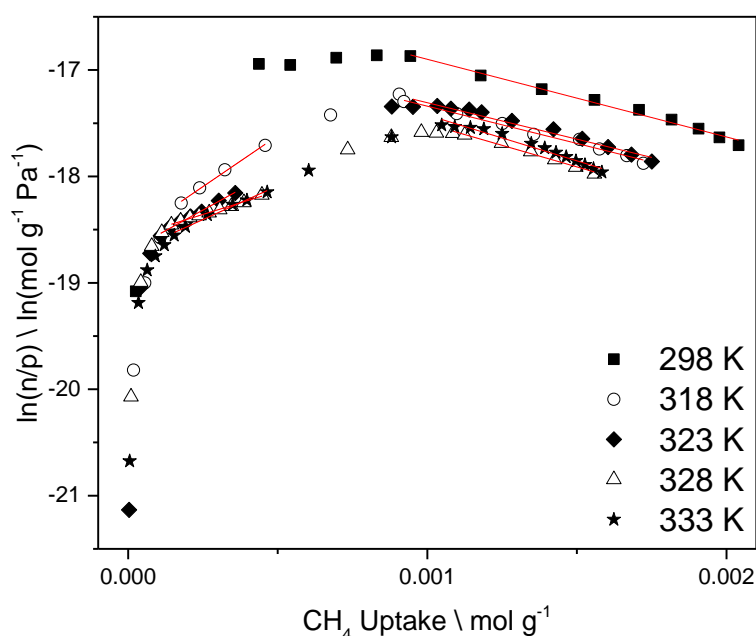


**Figure 7.19: Virial plot of  $\ln(n/p)$  ( $\ln \text{mol g}^{-1} \text{Pa}^{-1}$ ) vs.  $n$  ( $\text{mol g}^{-1}$ ) for CH<sub>4</sub> uptake over temperature range 298 – 333 K. Two measured linear plots were taken at positions before and after the ‘step’ in the isotherm**

**Table 7.3: Virial parameters for CH<sub>4</sub> adsorption at temperatures 298 – 333 K**

Temperature (K)	Pressure range (kPa)	$A_0 \setminus \ln(\text{mol g}^{-1} \text{Pa})$	$A_1 \setminus (\text{g mol}^{-1})$	$K_H (\text{g mol}^{-1} \text{Pa}^{-1})$
333	17.5 – 35	$-18.723 \pm 0.026$	$1269 \pm 80$	$7.39 \times 10^{-9}$
	42.5 – 100	$-16.564 \pm 0.067$	$-860 \pm 49$	$8.11 \times 10^{-8}$
328	15 – 35	$-18.576 \pm 0.007$	$873 \pm 24$	$8.56 \times 10^{-9}$
	42.5 – 100	$-16.695 \pm 0.053$	$-810 \pm 40$	$5.76 \times 10^{-8}$
323	12.5 – 27.5	$-18.704 \pm 0.016$	$1550 \pm 67$	$7.53 \times 10^{-9}$
	30 – 100	$-16.622 \pm 0.055$	$-685.0 \pm 41$	$7.08 \times 10^{-8}$
318	15 – 22.5	$-18.58 \pm 0.03$	$1915 \pm 93$	$8.53 \times 10^{-9}$
	30 – 100	$-16.639 \pm 0.045$	$-700 \pm 32$	$5.91 \times 10^{-8}$
298	-	-	-	-
	20 – 100	$-16.169 \pm 0.047$	$-730 \pm 29$	$9.07 \times 10^{-8}$

Calculation of the heats of adsorption at zero coverage were possible by plotting values of  $A_0$  against  $1/T$ , where the gradient provides values of  $\Delta H/R$  and intercept gives  $\Delta S/R$ . Figure 7.20 shows the plots of  $A_0$  vs.  $1/T$ . This gave heats of adsorption of  $5.29 \pm 6.60 \text{ kJ mol}^{-1}$  and  $11.16 \pm 3.66 \text{ kJ mol}^{-1}$  before and after the 'step', respectively. The entropy values for both linear plots were found to be  $-0.17 \pm 0.02 \text{ kJ mol}^{-1}$  and  $-0.17 \pm 0.01 \text{ kJ mol}^{-1}$  for before and after the step, respectively.

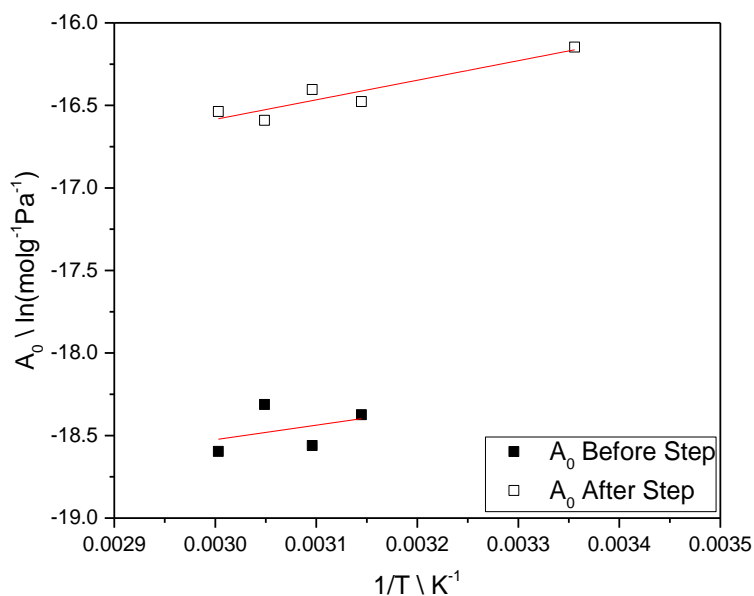


**Figure 7.20:** Plot of virial function constant  $A_0$  ( $\text{ln mol g}^{-1}\text{ Pa}^{-1}$ ) vs  $1/T$  ( $\text{K}^{-1}$ ) for  $\text{CH}_4$  adsorption on  $[\text{Cu}(\text{TPT})]\text{NO}_3 \cdot \text{MeOH}$ . Shows values before step (■) and after the step (□) giving enthalpy values from the gradient of the lines of  $5.29 \pm 6.60 \text{ kJ mol}^{-1}$  and  $11.16 \pm 3.66 \text{ kJ mol}^{-1}$ , respectively.

### 7.3.3 ADSORPTION KINETICS

The adsorption kinetics were analysed to give more detail into the transformation which was occurring within the framework. Results for adsorption of CH<sub>4</sub> and CO<sub>2</sub> at 298 K were compared, alongside kinetics from CH<sub>4</sub>, CO<sub>2</sub>, and N<sub>2</sub> at 333 K. Figure 7.21 shows the results of these analyses; all kinetic profiles were fit to a stretched exponential model, which allowed the exponent term to vary between 0.5 and 4, giving a combination of stretched exponential and Avrami models. The plot of the rate constants shows adsorption of CO<sub>2</sub> at 298 K has similar rates of adsorption at pressures up to 20 kPa, with faster kinetics than CH<sub>4</sub> above this pressure. In the case of 333 K, the kinetic rate constants are comparable between CH<sub>4</sub>, CO<sub>2</sub>, and N<sub>2</sub>. CH<sub>4</sub> experiences a decrease in rate at pressures of 7.5 kPa and 40 kPa at temperatures of 298 K and 333 K, respectively. CO<sub>2</sub> shows this decrease at a temperature of 333 K but at a higher pressure of 50 kPa compared with the rate measured for CH<sub>4</sub> adsorption; N<sub>2</sub> does not show a reduction in rate over the pressure range recorded.

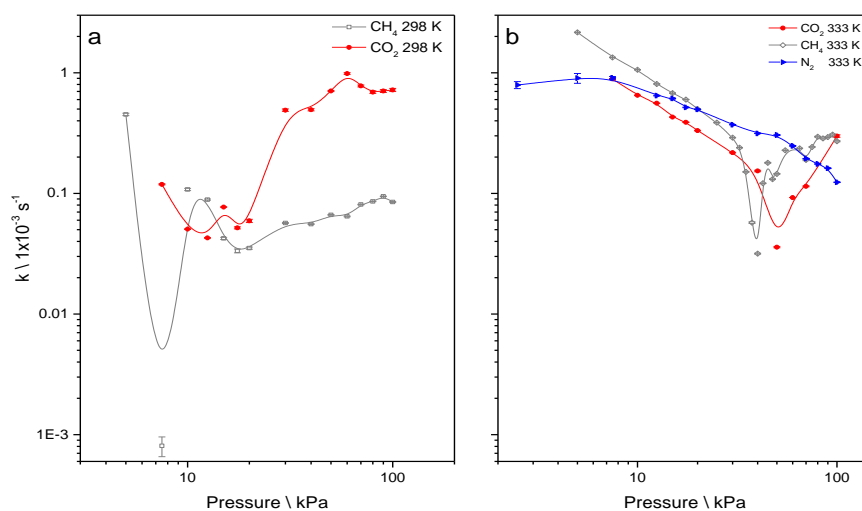


**Figure 7.21: Comparison of adsorption kinetic rate constants vs. Pressure (kPa) for (a) CO<sub>2</sub> (red) and CH<sub>4</sub> (grey) at 298 K, and (b) CO<sub>2</sub> (red), CH<sub>4</sub> (grey), and N<sub>2</sub> (blue) at 333 K**

The variation in the exponent is plotted in Figure 7.22, and shows CH<sub>4</sub> starts as an LDF model ( $\beta = 1$ ) and decreases to a value of  $\beta = 0.8$  at ~40 kPa, the exponent of

CO<sub>2</sub> adsorption varies between 0.75 and 1.05, and N<sub>2</sub> initially starts at  $\beta = 0.5$ , and increases to an LDF model at ~20 kPa.

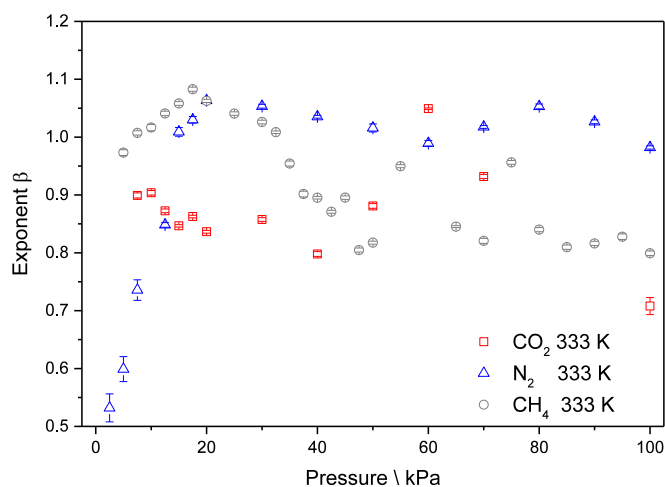


**Figure 7.22: Adsorption kinetic exponent,  $\beta$ , vs pressure (kPa) for SE model of CO<sub>2</sub> (□), CH<sub>4</sub> (○), and N<sub>2</sub> (△) at a temperature of 333 K for material [Cu(TPT)]NO<sub>3</sub>.MeOH. Values vary between 0.8 – 1.1 for all three gases, with the exception of N<sub>2</sub> below 10 kPa where the value decreases to 0.5.**

Closer inspection of the kinetic profiles at the stated pressures for CH<sub>4</sub> shows that the adsorption undergoes a change in diffusion process. Figure 7.23 shows the kinetic profiles of the pressure steps 2.5 – 5 kPa, 5 – 7.5 kPa, and 7.5 – 10 kPa, where the decrease in rate occurs during the 5 – 7.5 kPa at 298 K.

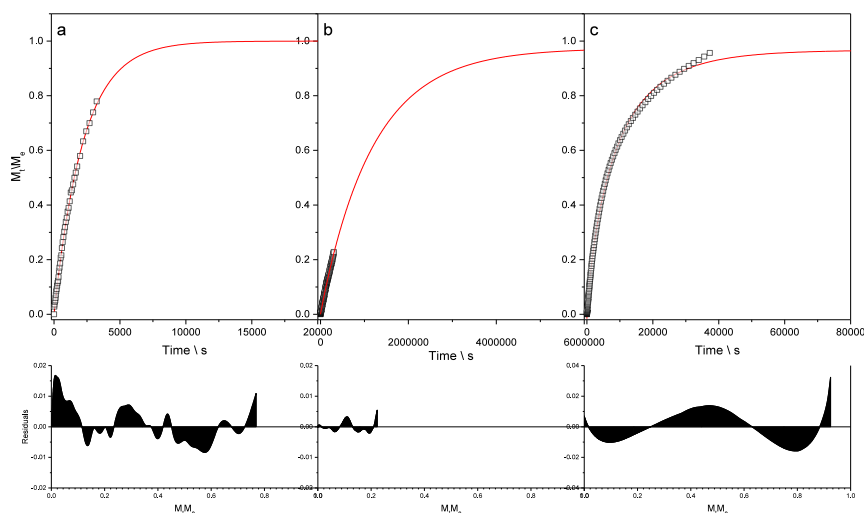


**Figure 7.23: Mass profiles vs. time (s) for CH<sub>4</sub> adsorption at 298 K for pressure steps (a) 2.5 – 5 kPa, (b) 5 – 7.5 kPa, and (c) 7.5 – 10 kPa, where the ‘step’ occurs in (b). The corresponding residual plots show the accuracy of the fit, the red lines show the projection of the equilibrated uptake.**

Analysis of the CH<sub>4</sub> kinetics over the temperature 298 – 333 K was performed to study the structural change in more detail. Figure 7.24 shows the plot of rate constants for the temperatures 298 – 333 K against pressure (a), and in plot (b) the rates are compared on a molar uptake basis. The graph shows at all studied temperatures, a slow kinetic process occurs within the pressure range 10 – 40 kPa, and this reduction in rate occurs at a molar uptake of 0.8 – 1 mmol g<sup>-1</sup>.

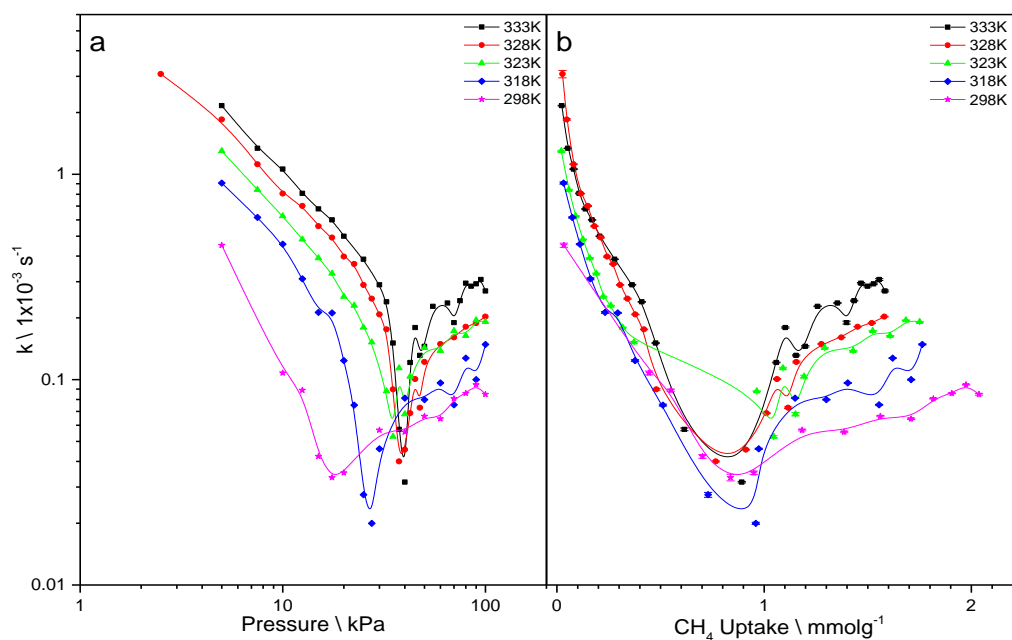


**Figure 7.24: Kinetic rate constant,  $k$ , for CH<sub>4</sub> adsorption at temperatures from 298 – 333 K, using the SE model. (a) shows kinetic plots on a pressure basis, (b) shows kinetic plots on a molar uptake basis. A reduction in rate occurs within the region 0.8 – 1 mmol g<sup>-1</sup>, with the exception of the plot for 323 K, which does not show a decrease as the isotherm shows a large increase in uptake between 0.4 – 1 mmol g<sup>-1</sup>.**

The plot of exponent,  $\beta$ , against pressure is plotted in Figure 7.25. Although the value of  $\beta$  was allowed to vary during analysis of the kinetic profiles, the trend shows that the values centre around 1, indicating that this is likely a LDF model.

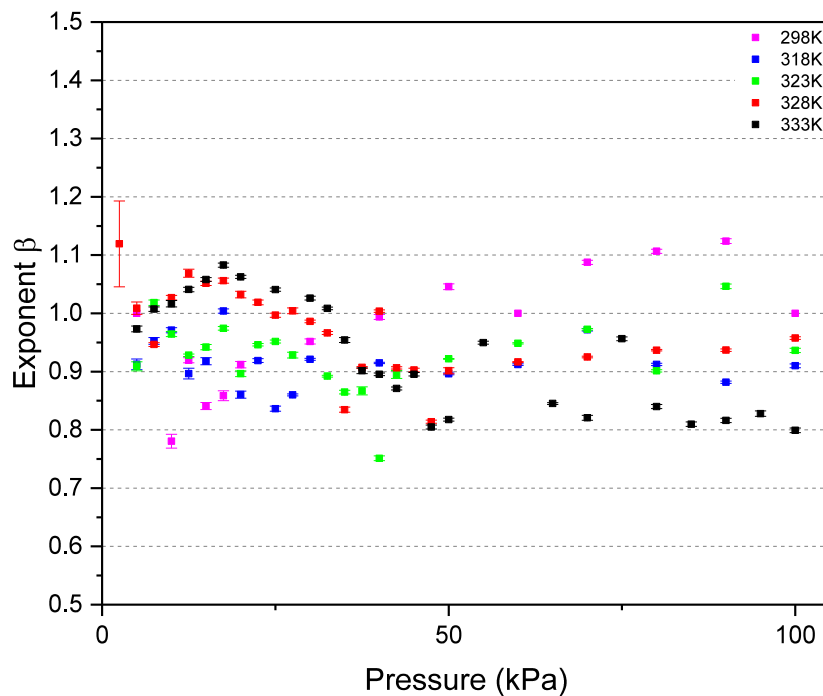


**Figure 7.25: Kinetic exponent parameter,  $\beta$ , plotted against pressure for  $\text{CH}_4$  at temperatures from 298 – 333 K. Plot shows exponent varies between 0.8 – 1.1, suggesting the kinetics follow a linear driving force process.**

Plots of different pressure steps within each of the temperatures studied are shown in Figure 7.26. The plots show that the pressure of the step shifts higher with temperature.

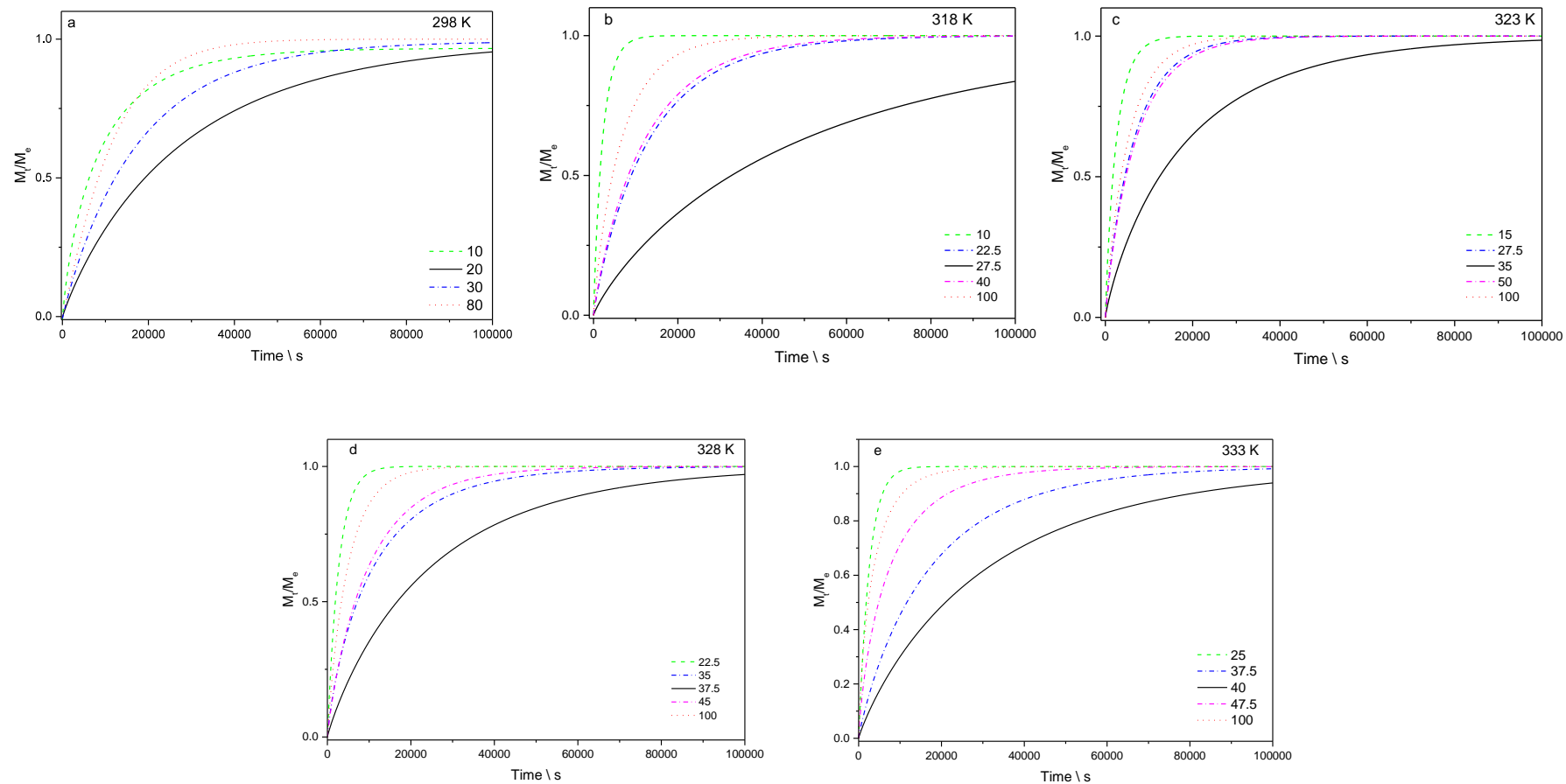


**Figure 7.26: Mass profiles of CH<sub>4</sub> adsorption at temperatures from 298 – 333 K, showing five pressure steps at points along the adsorption isotherms. The plots in black show that the pressure at which the step occurs shows an increasing trend from 298 – 333 K, at pressures ranging from 20 – 40 kPa.**

Analysis of some of the kinetic profiles was not fully possible, as additional steps were seen in the profile shape, which could not be fit directly to one of the models used in this study. Figure 7.27 shows the step 32.5 – 35 kPa for 328 K, this shows how the first curve could be fit to a stretched exponential model, but further fitting to the rest of the profile would produce insufficient  $R^2$  values. The step shown in Figure 7.27 was recorded over a longer time scale, but was still insufficient to reach equilibrium uptake.

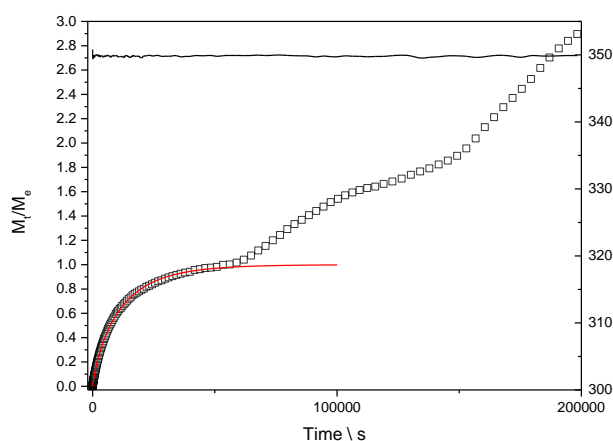


**Figure 7.27: Mass profile for CH<sub>4</sub> adsorption at 328 K for pressure step 32.5 – 35 kPa, and shows the uptake within the step increasing in successive levels . The consecutive steps in the kinetic plot were not modelled as this mechanism cannot be adequately fit to the nested set of kinetic equations**

### 7.3.4 ACTIVATION ENERGIES

The barriers to diffusion in terms of the activation energy of the process were determined through analysis of the kinetic rate constants at different temperatures using the Arrhenius equation (3-45). By taking values of constant volume filling and determining the rate constant at each temperature a linear plot of  $\ln(k)$  vs.  $1/T$  could be analysed from the Arrhenius equation in the linear form;

$$\ln k = \ln A - \frac{E_a}{R} \frac{1}{T} \quad (7-2)$$

This gives the intercept of  $\ln A$  and gradient  $-E_a/R$ . These are plotted against the amount adsorbed which is shown in Figure 7.28(a) for  $\text{CH}_4$  adsorption on  $[\text{Cu}(\text{TPT})]\text{NO}_3 \cdot \text{MeOH}$ . The data shows two distinct regions before and after the isotherm ‘step’, where there is a high activation barrier at low pressures (low surface coverage), and a lower activation energy at higher surface coverage after the ‘step’. Data in Figure 7.28(b) shows the  $\ln A$  values against the activation energy, showing high  $\ln A$  values at high activation energies, decreasing to low values at low activation energies.

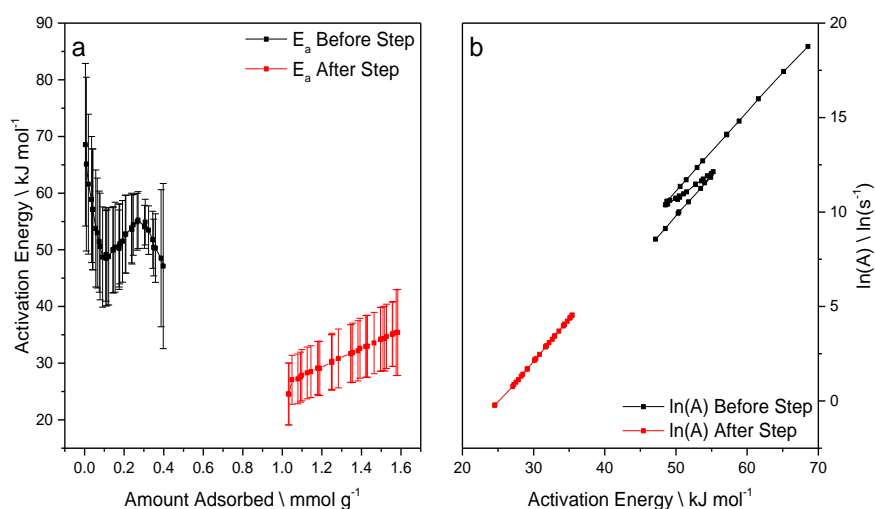


**Figure 7.28: (a) Plot of Activation Energy ( $\text{kJ mol}^{-1}$ ) against amount adsorbed ( $\text{mmol g}^{-1}$ ), (b) plot of frequency factor  $\ln(A)$  ( $\ln(\text{s}^{-1})$ ) against activation energy ( $\text{kJ mol}^{-1}$ ), for  $\text{CH}_4$  adsorption on  $[\text{Cu}(\text{TPT})]\text{NO}_3 \cdot \text{MeOH}$ . Activation energy shows decrease in value with increasing uptake, large change in energy after ‘step’ in the isotherm, energy experiences gradual increase after this point. Pre-exponential factor decreases with decreasing activation energy, which corresponds to a larger frequency of molecules at the pore opening when the barrier to activation is high.**

## 7.4 DISCUSSION

### 7.4.1 ADSORPTION ON $\text{Cu}(\text{BPETHA})_2\text{SiF}_6$

Adsorption properties of  $\text{Cu}(\text{bpetha})_2\text{SiF}_6$  showed interesting potential for carbon capture and storage applications. Initial studies of the low temperature isotherms (273 K and 298 K) showed moderate uptake capacities for  $\text{CO}_2$ , however, these were lower than expected, when compared with the literature SIFSIX materials. Findings from the structural analysis suggested that the material, which was synthesised from batch crystallisation methods, was in fact interpenetrated, as seen from the activated diffusion effects observed for  $\text{N}_2$  adsorption at 77 K in Figure 6.22, indicative of a pore size which is within the ultramicroporous region, and from comparison of the pore volume with SIFSIX-2-Cu-i. Nugent *et al.*<sup>2</sup> performed a t-plot analysis of both the non-interpenetrated and interpenetrated versions of  $\text{Cu}(\text{dpa})_2\text{SiF}_6$  (dpa = 1,2-Bis(4-pyridyl)ethyne), and found that the pore volume decreased from  $1.15 \text{ cm}^3 \text{ g}^{-1}$  to  $0.26 \text{ cm}^3 \text{ g}^{-1}$ ; having obtained a value of  $0.1298 \text{ cm}^3 \text{ g}^{-1}$  for  $\text{Cu}(\text{bpetha})_2\text{SiF}_6$ , this was of a similar magnitude to the interpenetrated form. While these structural phenomena will affect the adsorption properties, we actually expect that the interesting effects observed during the adsorption of  $\text{CO}_2$  on  $\text{Cu}(\text{bpetha})_2\text{SiF}_6$  are generated from the flexibility of the bpetha ligand, which has  $\text{sp}^3$  hybridisation of the central carbon-carbon bond, allowing significant rotation of the ligand. The isotherms are characterised as Type I(a) and Type I(b) for  $\text{CO}_2$  adsorption into a microporous material at temperatures of 298 K and 273 K, respectively. The possible Type I(b) character, which is witnessed in the measurement at 273 K is the result of a higher relative pressure range being studied at this temperature as a consequence of the maximum pressure of the instrument used and the lower saturation pressure of  $\text{CO}_2$ ; therefore, it is likely that some of the wider microporosity which fills at higher pressures is being probed. Porosity is often

described as a distribution of pore sizes, therefore, micropores that are wider than the crystalline pore size that can be analysed by X-ray diffraction are considered to be a result of the macro structure of the crystal; these are generated by defects as a result of the dislocations during crystal growth and grain boundaries between crystallites.

As indicated in Figure 7.1(b), a step in the 298 K isotherm is observed at 7.5 kPa. The change in the isotherm's projected direction (as shown from the dashed line in Figure 7.1(b)) from the expected profile is ascribed to a gate opening phenomenon, as seen previously for some flexible MOFs. This step is not observed for the 273 K isotherm, however, the uptake measured for the first pressure step recorded during the experiment (2.5 kPa) represents approximately 35 % of the maximum uptake and, therefore, the data suggest that the gate opening pressure is lower than 2.5 kPa at this temperature. The 2.5 kPa pressure step is used as the minimum resolution that the pressure can be controlled using the pressure gauge (2000 kPa gauge) supplied with the instrument (IGA). Pressure gauges were available for ranges 10 kPa and 100 kPa, however, the measurements collected at 273 K were acquired to maximise the relative pressure range studied, hence, the pressure range of 2000 kPa was used.

The CO<sub>2</sub> isotherms measured at different temperatures (Figure 7.2) show a physisorptive process occurs for all CO<sub>2</sub> adsorption on the Cu(bpetha)<sub>2</sub>SiF<sub>6</sub> material, as confirmed by a reduction in capacity with an increase in temperature. Only the data at 298 K shows a significant step in the isotherm at 7.5 kPa, corresponding to one CO<sub>2</sub> molecule per unit cell. As will be explained in detail later in this section, the kinetics of adsorption analysed for each of the temperatures shown (Figure 7.6) indicates a significant drop in the rate of adsorption around the pressure corresponding to a filling of one molecule of CO<sub>2</sub> per unit cell. This is more difficult to distinguish for the higher temperatures due to the reduced available adsorption capacity that occurs for

physisorption. This, in effect, reduces the resolution of the adsorption uptake, and therefore the 'step' in the equilibrium isotherm is likely to produce minimal changes in uptake at these conditions. As seen from the kinetic data, the isotherm at 333 K shows a significant lag in equilibrium time at 300 kPa, when compared with the pressure steps before and after; this could signify a step occurring as the rate of adsorption reduces to accommodate the slower processes associated with a change in structure (Figure 7.12).

The data for N<sub>2</sub> adsorption, shown in Figure 7.4, confirms that the material does not uptake large quantities of N<sub>2</sub> at any of the temperatures studied. The results, so far, have indicated that a collapse of the structure has reduced the pore size to a level of similar magnitude to the kinetic diameter of N<sub>2</sub>; this limits the adsorption potential via activated diffusion, but, by contrast, enhances the CO<sub>2</sub> selectivity, which exhibits a Type I isotherm, therefore, resulting in higher uptakes at low pressure, and a more selective interaction. Similar differences in adsorption behaviour between CO<sub>2</sub> and N<sub>2</sub> were observed for [Cu<sub>2</sub>(Glu)<sub>2</sub>(bpetha).(CH<sub>3</sub>CN)]<sub>n</sub>, where adsorption of N<sub>2</sub> showed no significant uptake at either 77 K, 273 K or 298 K, whereas CO<sub>2</sub> was reported to have a higher than expected uptake at 273 K. It was suggested that the unpredicted results were attributable to the fact that N<sub>2</sub> has a small quadrupole moment, reducing its adsorption interactions<sup>3</sup>. While this is an expected result with MOF materials exhibiting specific surface interactions for the quadrupole moment of CO<sub>2</sub>, [Cu<sub>2</sub>(Glu)<sub>2</sub>(bpetha).(CH<sub>3</sub>CN)]<sub>n</sub> does not have any exposed heteroatoms which could induce such behaviour; many materials have been shown to have limited capacity for N<sub>2</sub> at temperatures of 273 K and 298 K, regardless of the stronger interaction sites<sup>4</sup>. It is possible that the adsorption behaviour of [Cu<sub>2</sub>(Glu)<sub>2</sub>(bpetha).(CH<sub>3</sub>CN)]<sub>n</sub> is the result of the flexible nature of bpetha as has been shown in this study.

CO<sub>2</sub> shows significant uptake capacity at both 298 K and 333 K, this is typical of the Type I isotherms which are seen in most MOF materials where strong interactions occur, through unsaturated metal centres, exposed functional groups with pore structures, or those materials having small pore size through shortening of the ligand or interpenetration<sup>5</sup>. Cu(bpetha)<sub>2</sub>SiF<sub>6</sub> also has the potential to offer specific surface sites from the fluorine atoms in [SiF<sub>6</sub>]<sup>2-</sup>. The enhanced adsorption of CO<sub>2</sub> could be a result of the quadrupole moment, through potential interactions with the free equatorial fluorine atoms of the [SiF<sub>6</sub>]<sup>2-</sup> moiety<sup>6</sup>. Noro *et al.*<sup>7</sup> suggested that [SiF<sub>6</sub>]<sup>2-</sup> is a weak Lewis base, allowing it to interact with the metal atoms of the framework in forming 3-dimensional structures. The electronegative equatorial atoms of the [SiF<sub>6</sub>]<sup>2-</sup> unit can interact with the positive dipole on the carbon atom of CO<sub>2</sub> in a Lewis acid-Lewis base interaction, thus enhancing selectivity for CO<sub>2</sub> in a similar fashion to amine scrubbing technologies, but with a reduced enthalpy of adsorption. Results for the enthalpy of adsorption were determined for isosteres taken through the CO<sub>2</sub> isotherms. The data shown in Figure 7.3, shows the enthalpy of adsorption at zero coverage can be extrapolated to approximately -40 kJ mol<sup>-1</sup>. As shown in Table 3.2, the energy of a physisorptive process can be between 20 – 40 kJ mol<sup>-1</sup>, and chemisorptive processes are above 80 kJ mol<sup>-1</sup>; the results of the enthalpy of adsorption calculation suggest the interaction of the material is similar to a physisorptive process, with the interaction strength increasing as coverage increases up to 0.8 mmol g<sup>-1</sup>. The presence of fluorine atoms within the anionic species are likely to result in this enhanced interaction, as results from the adsorption of CH<sub>4</sub> and N<sub>2</sub> show no enhancement at low pressure. The data also shows a reduction in enthalpy to a value of -15 kJ mol<sup>-1</sup>, at 1.2 mmol g<sup>-1</sup>; the reduction in enthalpy is expected when the flexibility of the material is considered, as increasing the pore volume will reduce the interaction strength of the surface by increasing the pore size, which is shown to reduce adsorption potential. As previously stated, the calculation of enthalpy values at coverage above 1.2 mmol g<sup>-1</sup> was

performed using only two temperature points, 273 K and 298 K; the values obtained should therefore be considered with caution, as an accurate estimation of the enthalpy requires that more data points be used, and this analysis gives only an estimate of the results.

The uptake of CH<sub>4</sub> is an unexpected result; several MOFs have been studied which have shown high selectivity for CO<sub>2</sub> over CH<sub>4</sub>, however, contradictory evidence has been put forward on materials similar to Cu(bpetha)<sub>2</sub>SiF<sub>6</sub>, showing both high and low uptakes for CH<sub>4</sub><sup>8,9</sup>. Analysis of the kinetic data from adsorption experiments (Figure 7.10) shows that long equilibration times are necessary for a completely equilibrated isotherm, and it is possible that previous studies of CH<sub>4</sub> uptake in other materials have not considered the kinetic profiles of the adsorption data. However, when considering Cu(bpetha)<sub>2</sub>SiF<sub>6</sub> on a kinetic selectivity basis between all three gases studied, it is evident that CO<sub>2</sub> has a much faster rate of adsorption into the porous structure at the low pressures necessary for post-combustion capture, and the trapping of CO<sub>2</sub> from natural gas streams.

The study of the kinetics for adsorption can provide a detailed analysis of the processes governing the diffusion of gases into a porous material. The results from Figure 7.5 show that CO<sub>2</sub> follows a DE model, with both a fast and slow rate process occurring. As evidenced by the rate constants from CH<sub>4</sub> and N<sub>2</sub> at 298 K and 333 K (Figure 7.10), only CO<sub>2</sub> experiences this two-step process, and the k<sub>2</sub> rate constant for CO<sub>2</sub> is of a similar magnitude to the rate constants of CH<sub>4</sub> and N<sub>2</sub>. Comparing the slow process rate constants, it can be seen that these are in the order of N<sub>2</sub>>CO<sub>2</sub>>CH<sub>4</sub> (except for instances in the CO<sub>2</sub> data where a reduction in the rate is the effect of structural changes in the MOF). This coincides with the minimum molecular dimensions of the molecules, calculated by Webster *et al.*<sup>10</sup>; these are shown in Table 7.4. The

differences in the overlapping rate show little variation, most likely due to the almost equivalent dimensions of the gas molecules.

**Table 7.4: Minimum molecular dimensions of adsorptives** <sup>10</sup>

Molecule	MIN-1 (Å)	MIN-2 (Å)	MIN-3 (Å)
CO <sub>2</sub>	3.189	3.339	5.361
CH <sub>4</sub>	3.829	3.942	4.101
N <sub>2</sub>	2.991	3.054	4.046

Due to the difference outlined above, it is, therefore proposed that the adsorption of gases into Cu(bpetha)<sub>2</sub>SiF<sub>6</sub> is controlled by two possible diffusional processes:

1) for gases which have an electronic interaction with the framework, a high rate constant is observed for the quick diffusion of adsorbate molecules to the enhanced interaction sites, once in close proximity, such as for CO<sub>2</sub> molecules interacting with the fluorine atoms of [SiF<sub>6</sub>]<sup>2-</sup>. This is not observed for CH<sub>4</sub> or N<sub>2</sub> as they either have no quadrupole moment, or a very weak quadrupole moment, which does not enhance uptake.

2) The second rate determining process is that of the porous structure. All gases probed experience similar rate constants for the slow rate process, indicating that this must be an effect associated with the overall porous structure. On approaching the pore opening of the microporous material, the molecules must orient themselves in the correct orientation for their molecular dimensions to allow diffusion through the pore; this explains the increase in rate constant with decrease in molecular dimension of the adsorbate. N<sub>2</sub> has very similar dimensions for MIN-1 and MIN-2; therefore it has very little difficulties associated with diffusion. CO<sub>2</sub> and CH<sub>4</sub> have larger MIN values, which leads to slower rate constants. In the case of CO<sub>2</sub>, this slow process occurs concurrently with the first process outlined above, hence, DE behaviour is observed.

The reduction in rate constant for CO<sub>2</sub> can be explained as follows. Initially, the small pore size of the 'closed' form is beneficial to adsorption, as it creates a high potential, in addition to the high energy sites of the fluorine atoms. Before the gate opening pressure, the 'closed' pore begins to limit diffusion as the pore volume becomes filled. As the volume filling constraint is fulfilled (one CO<sub>2</sub> molecule per unit cell) the porous structure opens, opening the pore structure to the 'open' form, and allowing diffusion of more molecules through the pore opening. This results in an increase in the rate to levels similar to the initial rates of adsorption in the 'closed' pore. The final stage is the slow reduction in rate as the volume begins to reach total filling, and diffusion is once again limited by restriction of the mean free path within the pore by the larger number of molecules at higher pressures. Although described as being two separate processes,  $k_1$  and  $k_2$  occur concurrently within the diffusion process, as stated above. At low pressures, the number of molecules surrounding the material will be low, and therefore adsorption towards the high potential sites of the fluorine atoms is quick and impedance at the pore opening does not impact adsorption; due to the speed of this process, analysis of the low pressure kinetic profiles was difficult. As the pressure was increased, the slow diffusion process became dominant.

Thus, it is seen that during the gate opening process (Figure 7.11(b)), the rate of process  $k_2$  is reduced significantly in comparison to CH<sub>4</sub> and N<sub>2</sub>, resulting in a longer equilibration time. The process  $k_1$  remains unaffected by the structural change, as access to the fluorine sites is unaltered. CH<sub>4</sub> and N<sub>2</sub> experience no interaction with the fluorine atoms, and their diffusion process varies little, except for the decrease in rate with pressure, as fewer adsorption sites are available, and the mean free path is restricted by the larger number of molecules within the pore.

The difference in CH<sub>4</sub> adsorption, as opposed to both CO<sub>2</sub> and N<sub>2</sub>, is likely due to the molecular diameter of the adsorbate. As shown in Figure 7.4, adsorption experiences no enhancement at low pressure (linear uptake of CH<sub>4</sub>), therefore there are no specific interactions between the adsorbate and the adsorbent surface. It is likely that adsorption of CH<sub>4</sub> causes the same structural change, as seen for CO<sub>2</sub>, but through a more gradual process caused by the larger molecular size. This explains the slow rates seen for CH<sub>4</sub>, and gives a suggested mechanism for the incongruous results compared with the other gases studied. Further analysis is required to elucidate the mechanism of adsorption, and understand the structural changes occurring within the material.

In order to further probe the selectivity of Cu(bpetha)<sub>2</sub>SiF<sub>6</sub>, in an industrial processing context, experiments were performed to analyse the adsorption of CO<sub>2</sub> under flowing conditions and in the presence of a competing gas, N<sub>2</sub>. Figure 7.13 shows the molar uptakes measured for CO<sub>2</sub> in N<sub>2</sub> (black curve) and pure CO<sub>2</sub> (red curve), under dynamic conditions. The IGA-003 is capable of measuring adsorption under static and dynamic (flowing) conditions; in the measurement of liquid vapours (such as water) and mixtures of gases, it is more appropriate to perform these using a flowing set-up. Very few experiments have been carried out using competitive mixtures in a flowing configuration using a gravimetric based set-up, therefore information is limited<sup>11</sup>. The mixed isotherm was performed by initially dosing the chamber with N<sub>2</sub> at 100 kPa, and altering the ratio of flow rates to produce a partial pressure curve<sup>11</sup> of CO<sub>2</sub> adsorption into Cu(bpetha)<sub>2</sub>SiF<sub>6</sub> from 0 – 100 kPa. The pure component isotherm of CO<sub>2</sub> was performed at 333 K in order to differentiate between alterations in the isotherm from the new dynamic conditions, and those caused by the presence of N<sub>2</sub>. The isotherms show that uptake of CO<sub>2</sub> at low pressures is suppressed in the mixed measurement, compared to the pure flowing measurement; at maximum pressure, the uptakes of CO<sub>2</sub> for both isotherms are approximately equal. The suppression of the isotherm at low pressure is

the influence of N<sub>2</sub> being present in higher quantities, which will alter the mean free path of the CO<sub>2</sub> molecules, and reduce the rate at which diffusion occurs. The similarity in CO<sub>2</sub> uptake at 100 kPa suggests that the material does not adsorb N<sub>2</sub> at high energy sites. Had strong interactions occurred between N<sub>2</sub> and the surface, these molecules would result as impurities on the surface, blocking adsorption and reducing the number of free adsorption sites for CO<sub>2</sub>.

Kinetic separation is considered an important attribute for industrial adsorption processes<sup>12</sup>, as they often require much shorter timescales than is possible for equilibrium uptakes; it has been stated that cycle times for Pressure Swing Adsorption (PSA) should not exceed 10 min<sup>13</sup>, ideally working towards even shorter times to increase productivity<sup>14</sup>. In contrast to the equilibrium isotherms, the results in Figure 7.14 show that CO<sub>2</sub> adsorption is a much faster process, having reached ~90 % of its equilibrated uptake in 3 min; adsorbed N<sub>2</sub> only reaches ~20% of its overall uptake within 10 min. The kinetic plots for CO<sub>2</sub> and N<sub>2</sub> are shown to simulate a 10%/90% flue gas mixture, which is similar to measured post-combustion flue gas compositions<sup>15</sup>. Even at nine times the pressure of CO<sub>2</sub>, the adsorption process of pure N<sub>2</sub> is significantly slower; kinetic selectivities have been calculated on a mol/mol basis (at 3 min) for CO<sub>2</sub>/N<sub>2</sub> of 36, which is in contrast with the selectivity calculated for the equilibrium amount adsorbed; by taking molar uptakes of CO<sub>2</sub> and N<sub>2</sub> at the specified pressure of 10 kPa and 90 kPa, the selectivity is reduced to 2.57. Hence, [Cu(bpetha)<sub>2</sub>(SiF<sub>6</sub>)<sub>n</sub>] can kinetically separate gas mixtures of CO<sub>2</sub>/N<sub>2</sub> or CO<sub>2</sub>/CH<sub>4</sub>; it is unlikely that mixtures of N<sub>2</sub>/CH<sub>4</sub> would be possible to separate kinetically due to the similar kinetic profiles of both gases.

## 7.4.2 ADSORPTION ON [Cu(TPT)]BF<sub>4</sub>·0.75H<sub>2</sub>O

[Cu(TPT)]BF<sub>4</sub>·0.75H<sub>2</sub>O was initially synthesised with the intention of producing a material similar to Cu(bpetha)<sub>2</sub>SiF<sub>6</sub>, by incorporating both the nitrogen functionality of the TPT triazine ring and the electronegative fluorine atoms of [SiF<sub>6</sub>]<sup>2-</sup>. Syntheses of this material were unsuccessful; however the material discussed here was formed during experiments to test the synthesis without [SiF<sub>6</sub>]<sup>2-</sup> present in the system. Given the adsorption behaviour of Cu(bpetha)<sub>2</sub>SiF<sub>6</sub>, the material was studied in order to determine whether the fluorine atoms of [BF<sub>4</sub>]<sup>-</sup> could be used in a similar fashion to [SiF<sub>6</sub>]<sup>2-</sup>.

As described in Section 6.5.2, the porosity of the resultant material was restricted due to the [BF<sub>4</sub>]<sup>-</sup> anions being situated within the central channels of the pores. The anions experienced weak interactions with the Cu<sup>+</sup> atoms in the framework, having no formal bonds, and acted to balance the overall charge of the framework. The adsorption capacities of the three gases studied are shown in Figure 7.15, and the adsorption capacity is seen to be severely restricted by the anionic species present. In general, adsorption was low for all gas species, however the higher uptake of CH<sub>4</sub> was unexpected from initial predictions, as the additional Lewis basic sites were expected to enhance adsorption of CO<sub>2</sub>. Although CH<sub>4</sub> adsorption is enhanced within this material, N<sub>2</sub> is still lower in adsorption potential than either CH<sub>4</sub> or CO<sub>2</sub>. The ability of N<sub>2</sub> to adsorb in sufficient quantities at higher temperatures is often only possible in the presence of chemisorption, or through enhancement by another co-adsorbing species<sup>16</sup>.

Studies of the kinetics (Figure 7.16) showed that adsorption was slow for all gases, with CH<sub>4</sub> showing a consistently high rate. CO<sub>2</sub> shows a higher rate constant at high and low pressures within the range studied, however analysis was limited by the

low uptake experienced, such that the model failed at pressures above 70 kPa due to no discernable adsorption. The kinetics of CO<sub>2</sub> follow an SE model, where the exponent is often close to 0.6 – 0.65; this suggests that there is a distribution of rates, and the proximity to an exponent value of 0.5 suggests that the diffusion process is 3-dimensional. Consequently, the positioning of the [BF<sub>4</sub>]<sup>-</sup> anion within the centre of the pore impacts on the diffusion in the parallel axis to the pore direction, and diffusion perpendicular to this axis will have a different rate, which could infer that diffusion to the pore wall (and interaction with the nitrogen sites) is much faster than diffusion into the pore, which requires passing the anion. CH<sub>4</sub> and N<sub>2</sub> appear less affected by the presence of the anion, as their diffusion is largely 1-dimensional (having exponent values at ~1). The impact on the diffusion of CO<sub>2</sub> is likely caused by the quadrupole moment of the adsorbing molecule; in orienting itself to pass through the pore entrance, the molecule must arrange itself with its long axis parallel to the walls, due to the small pore size, and the minimum molecular dimensions which govern entry of an adsorptive into a porous structure (See Section 7.4.1, Table 7.4). This orients the negative dipole directly towards the anion within the pore, and reduces the rate of diffusion by electrostatic repulsion of the gas molecules. Walton *et al.*<sup>17</sup> examined the effect of cationic size on CO<sub>2</sub> adsorption within zeolite X and Y-type materials. They found that increasing cation size decreased the CO<sub>2</sub> adsorption capacity; although not studying anions, it is likely that a large anion would have a more pronounced effect due to the charge repulsion between the molecules, something which is not observed for CH<sub>4</sub> or N<sub>2</sub> (which has a much weaker quadrupole moment).

It is, therefore, suggested that due to the weak interaction strength of the anion within [Cu(TPT)]BF<sub>4</sub>·0.75H<sub>2</sub>O, it would be possible to exchange [BF<sub>4</sub>]<sup>-</sup> with smaller anions, which could have a potential benefit towards increasing the adsorption capacity. Studies of anion exchange within a MOF material have been performed by Fei *et al.*<sup>18</sup>,

which allowed tuning of the pore structure through templating around an organosulfonate anion. The structure of  $[\text{Cu}(\text{TPT})]\text{BF}_4 \cdot 0.75\text{H}_2\text{O}$  may lend itself to being a highly stable and  $\text{CO}_2$  selective MOF, as  $[\text{BF}_4]^-$  generates pores of a sufficiently small size through templating around the anion. By exchanging the material with a smaller anion, such as chloride, the material may be useful as a carbon capture material, and allow use of the nitrogen functionality within the organic ligand.. Initial studies of anion exchange were performed under mild conditions, but these did not lend themselves to exchanging the  $[\text{BF}_4]^-$  anion. It is likely that harsher conditions at increased temperature and stirring of the solution would be required to provide the energy needed to exchange the MOF from its current stable arrangement, however further testing was required to assess the thermal stability of the MOF under the harsh conditions necessary, and due to time constraints this route was not investigated.

### 7.4.3 ADSORPTION ON [Cu(TPT)]NO<sub>3</sub>.MeOH

Adsorption on [Cu(TPT)]NO<sub>3</sub>.MeOH was performed as previous studies detailing its synthesis had not looked further into studies of its properties<sup>19</sup>. Due to the inadequate results of [Cu(TPT)]BF<sub>4</sub>.0.75H<sub>2</sub>O for CCS applications, it was decided to synthesise the former structure to analyse the adsorption characteristics and elucidate the main properties governing its behaviour. The results of adsorption on [Cu(TPT)]NO<sub>3</sub>.MeOH showed a large uptake of CH<sub>4</sub> compared with CO<sub>2</sub> and N<sub>2</sub> (Figure 7.17). The result is consistent with the measurements performed on [Cu(TPT)]BF<sub>4</sub>.0.75H<sub>2</sub>O, so could suggest that they are not solely attributed to the larger [BF<sub>4</sub>]<sup>-</sup> anion; the smaller [NO<sub>3</sub>]<sup>-</sup> anion and stronger coordination with the metal centre results in reduced pore blocking. The results in Figure 7.17 show that both CH<sub>4</sub> and CO<sub>2</sub> exhibit a change in structure with the presence of a large ‘step’ in the isotherm. Additionally, the isotherms experience a large hysteresis loop on desorption, however this is not the effect of capillary condensation, as the pore size characterised from X-ray diffraction results show that the material is microporous, and CH<sub>4</sub> is above its critical temperature, therefore has no saturation pressure. Although these are disappointing results for separation of gas mixtures at low pressures, the properties of this material mean it may lend itself to separation or gas storage of CH<sub>4</sub> at higher pressures. Analysis was then performed for CH<sub>4</sub> to analyse the interesting adsorption behaviour resulting from the stepped isotherm. CH<sub>4</sub> isotherms were collected at various temperatures, from 298 K – 333 K (Figure 7.18), showing a physisorptive process occurred, where increasing temperature reduces the uptake, and the recurrence of a ‘step’ in the isotherm was found at a similar loading value of 0.4 mmol g<sup>-1</sup>. Long *et al.* observed similar adsorption isotherms for CH<sub>4</sub> uptake into MOF materials Co(bdp) and Fe(bdp), which they suggested could be used for natural gas storage, due to the flexible and reversible phase transition of the adsorbent allowing for much larger working

capacities through adsorption/desorption cycles. The ‘step’ observed for their material was over a much larger pressure range, showing uptake values of  $7 \text{ mmol g}^{-1}$  at 323 K and 35 bar<sup>20</sup>. This provides an advantageous result from a gas storage perspective, but the ‘stepped’ isotherm experienced in  $[\text{Cu}(\text{TPT})]\text{NO}_3 \cdot \text{MeOH}$  occurs on a scale more beneficial to separations from gas streams at atmospheric pressures. Thus it can be seen that the choice of components for the MOF structure can lead to properties which are beneficial for one particular application; nonetheless, through the application of MOF rational design, this could lead to structures which contain the beneficial properties of both materials.

The isosteric heats of adsorption were determined using a virial equation, shown in Figure 7.19, with Table 7.3 showing the data collected from the linear plots of each of the isotherms, and Figure 7.20 showing the linear plots of  $A_0$  vs  $1/T$ . The isosteric heat value obtained for zero coverage before the ‘step’ in the isotherm, taken from the intercept of the line with the x-axis, is unrealistic due to the large error associated with the linear regression of the line of  $A_0$  vs.  $1/T$ . The result obtained after the ‘step’ is fairly reasonable, showing values within a similar magnitude to heats of adsorption for  $\text{CH}_4$  on a range of materials<sup>20-22</sup>. The values for  $A_1$  are indicative of adsorbate-adsorbate interactions; these values compare well with those previously stated for  $\text{CH}_4$  adsorption on a carbon molecular sieve<sup>21</sup>. Compared with MOF NPC-4, the  $A_1$  values are in the range  $-85$  to  $-120 \text{ g mol}^{-1}$  at temperatures of 280 K, and are attributed to the weak interaction strength of  $\text{CH}_4$  with a material of pore size  $16 \text{ \AA}$ <sup>22</sup>. The values obtained here for  $[\text{Cu}(\text{TPT})]\text{NO}_3 \cdot \text{MeOH}$  compared well with a carbon molecular sieve (CMSA), which has a pore distribution in the ultramicroporous region which, from crystallographic results, is similar to the pore size of the MOF studied<sup>22</sup>.

---

<sup>2</sup> And references 29-34 within Reid *et al.*

Coupled with the value of  $11.16 \text{ kJ mol}^{-1}$  for the surface interaction strength at zero coverage, this suggests that the adsorbate-adsorbate interactions dominate after the step, and there is no strong interaction of the gas with the pore surface. Comparing the results before the 'step' in the  $\text{CH}_4$  isotherm, the values for  $A_1$  are positive; such values have not been reported in the literature for virial analysis of adsorbents, and are not considered to be representative of adsorbate-adsorbate interactions. It is suggested that below the 'step' in the isotherm there are large differences in the structural transformation of the material to accommodate  $\text{CH}_4$  into the framework, therefore, the structures at different temperatures are not comparable, resulting in the erroneous result from the heats of adsorption calculation. It is noted that good agreement of the entropic heats of adsorption between both of the sections analysed was obtained, suggesting that the gas molecules are more ordered within the porous structure, yet since the value remains unaltered between the initial and final sections of the isotherm, this process is not entropically driven.

The adsorption kinetics showed a similar trend for the three gases analysed at 333 K, with both  $\text{CH}_4$  and  $\text{CO}_2$  demonstrating similar decreases in rate at the step in the isotherm, around 40 – 50 kPa. Analysis of the kinetic profiles for  $\text{CH}_4$  shows a dramatic slowing of the adsorption kinetics, with the model showing a 300x increase in the equilibration times at the adsorption 'step'. Caution is advised in the analysis of such kinetic profiles, as only 20 % of the equilibrated profile was recorded for this pressure, it is difficult to determine an exact point for equilibration; however it is easy to see that an alteration of the kinetic process is occurring as shown by the linear progression of the kinetic profile (Figure 7.23). It was shown through measurement and analysis of several temperatures for  $\text{CH}_4$  that this was a prominent occurrence in all temperatures measured. A single kinetic profile, shown in Figure 7.27, shows the unusual behaviour of the adsorption profile for a pressure step of 25 – 35 kPa of the

328 K isotherm. This adsorption process is similar to a Type VI isotherm classification<sup>23</sup>, as it shows distinct adsorption steps before another increase in adsorption occurs. Analysis of the pressure and temperature during the run shows that there is no influence of either condition that would have caused the behaviour seen, and this is attributed to the adsorption of CH<sub>4</sub> onto the MOF material. It is possible that during the transition between the two structural phases, adsorption occurs in distinct layers, similar to Type VI adsorption behaviour, however this occurs only during a single pressure step and at distinct volume filling within each isotherm.

The isotherm obtained at 318 K appears to show the lowest rate, for the pressure step recorded between either of the temperatures studied. This could have been a limitation of the study, in that the pressure for the measurement resulted in an uptake that corresponded to the point at which the 'step' in the isotherm occurred, allowing the rate to be probed at the lowest point of the curve. In general, the adsorption 'step' is seen to increase in pressure with increasing temperature. The phenomenon of physisorption causes adsorbed amount to decrease with increasing temperature, due to the process being exothermic. As all isotherms appear to reach the 'step' in the isotherm at a similar uptake, this leads us to assume that the process of inducing the structural change is due to volume filling of the microporosity. Thus, it is a consequence of the lower adsorption uptakes at higher temperatures, resulting from the thermodynamics of physisorption, that results in a shift to higher pressures in order for the required volume filling (one molecule of CH<sub>4</sub> per unit cell) to be reached.

Analysis of the kinetic data for determination of the activation energies was performed as shown in Figure 7.28. As kinetic constants are a measure of the rates of diffusion, the activation energies determined at constant filling gives a measure of the energy associated with the barriers to diffusion. As can be seen from the data,

activation energy is high before the 'step' in the isotherm occurs, which results from the large barrier to diffusion at the pore opening. After the 'step' in the isotherms, the activation energy decreases by  $\sim 25 \text{ kJ mol}^{-1}$  to  $25 \text{ kJ mol}^{-1}$ , which progresses in a decreasing trend as adsorbed amount increases. The much lower activation energy is the impact of increasing the pore opening as the material flexes, and reduces the barrier to diffusion into the pore. The decreasing trend to high activation energy occurs as the adsorption sites begin to fill and there are less available sites for adsorption. The pre-exponential factor,  $A$ , is plotted against activation energy to show the relationship between the two results. At high activation energy, the value of  $\ln A$  is high; this suggests a high frequency of adsorbate molecules at the pore opening, due to the large barrier. As a consequence of reducing the activation energy after opening of the structure, the frequency factor decreases, therefore there are fewer molecules at the pore entrance.

As was observed for  $[\text{Cu}(\text{TPT})]\text{NO}_3 \cdot \text{MeOH}$ , the low selectivity towards  $\text{CO}_2$  is juxtaposed to the potential interaction with the Lewis base sites of nitrogen in the organic ligand TPT. A number of factors impact the results of the adsorption kinetics within this material, namely; the effect of the anion  $[\text{NO}_3]^-$  in pore blocking; the nitrogen sites; and the structural transition of the framework. Analyses of the crystal structure through powder diffraction data can be performed under atmospheres of the adsorbate being studied<sup>24</sup>. This would allow structural characterisation of the transition to determine the possible source of the 'step' within the isotherm. Similarly, monitoring guest loss through heating studies similar to the measurement performed on  $\text{Cu}(\text{bpetha})_2\text{SiF}_6$  would help to determine whether the structural change is related to a collapse of the open structure, and subsequent reopening on reaching the required volume filling.

## 7.5 REFERENCES

1. Metz, B., Davidson, O., de Coninck, H., Loos, M. & [Working Group III of the Intergovernmental Panel on Climate Change]. *IPCC: Special Report on Carbon Dioxide Capture and Storage.*, (Cambridge University Press, 2005).
2. Nugent, P., Belmabkhout, Y., Burd, S. D., Cairns, A. J., Luebke, R., Forrest, K., Pham, T., Ma, S., Space, B., Wojtas, L., Eddaoudi, M. & Zaworotko, M. J. Porous materials with optimal adsorption thermodynamics and kinetics for CO<sub>2</sub> separation. *Nature* **495**, 80-4 (2013).
3. Hwang, I. H., Bae, J. M., Kim, W. S., Jo, Y. D., Kim, C., Kim, Y., Kim, S. J. & Huh, S. Bifunctional 3D Cu-MOFs containing glutarates and bipyridyl ligands: selective CO<sub>2</sub> sorption and heterogeneous catalysis. *Dalton Transactions* **41**, 12759-65 (2012).
4. McDonald, T. M., Lee, W. R., Mason, J. A., Wiers, B. M., Hong, C. S. & Long, J. R. Capture of Carbon Dioxide from Air and Flue Gas in the Alkylamine-Appended Metal-Organic Framework mmen-Mg<sub>2</sub>(dobpdc). *Journal of the American Chemical Society* **134**, 7056-65 (2012).
5. Belmabkhout, Y., Guillerm, V. & Eddaoudi, M. Low concentration CO<sub>2</sub> capture using physical adsorbents: Are metal-organic frameworks becoming the new benchmark materials? *Chemical Engineering Journal* **296**, 386-97 (2016).
6. Dan-Hardi, M., Serre, C., Frot, T., Rozes, L., Maurin, G., Sanchez, C. & Férey, G. A new photoactive crystalline highly porous titanium (IV) dicarboxylate. *JACS* **131**, 10857 (2009).
7. Noro, S.-i. Rational synthesis and characterization of porous Cu(II) coordination polymers. *Physical Chemistry Chemical Physics* **12**, 2519-31 (2010).
8. Noro, S., Kitagawa, S., Kondo, M. & Seki, K. A new, methane adsorbent, porous coordination polymer {CuSiF<sub>6</sub>(4,4'-bipyridine)<sub>2</sub>}(n). *Angewandte Chemie-International Edition* **39**, 2082-4 (2000).
9. Burd, S. D., Ma, S., Perman, J. A., Sikora, B. J., Snurr, R. Q., Thallapally, P. K., Tian, J., Wojtas, L. & Zaworotko, M. J. Highly Selective Carbon Dioxide Uptake by Cu(bpy-n)<sub>2</sub>(SiF<sub>6</sub>) (bpy-1=4,4'-Bipyridine; bpy-2=1,2-Bis(4-pyridyl)ethene). *Journal of the American Chemical Society* **134**, 3663-6 (2012).
10. Webster, C. E., Drago, R. S. & Zerner, M. C. Molecular Dimensions for Adsorptives. *Journal of the American Chemical Society* **120**, 5509-16 (1998).
11. Fletcher, A. J., Kennedy, M. J., Zhao, X. B., Bell, J. B. & Thomas, K. M. in *Recent Advances in Adsorption Processes for Environmental Protection and Security* (eds José Paulo Mota & Svetlana Lyubchik) pp. 29-54 (Springer Netherlands, 2008).
12. Feng, D., Chung, W.-C., Wei, Z., Gu, Z.-Y., Jiang, H.-L., Chen, Y.-P., Darensbourg, D. J. & Zhou, H.-C. Construction of ultrastable porphyrin Zr metal-organic frameworks through linker elimination. *JACS* **135**, 17105 (2013).

13. Grande, C. A. Advances in Pressure Swing Adsorption for Gas Separation. *ISRN Chemical Engineering* **2012**, 13 (2012).
14. Hobday, C. L., Marshall, R. J., Murphie, C. F., Sotelo, J., Richards, T., Allan, D. R., Düren, T., Coudert, F.-X., Forgan, R. S., Morrison, C. A., Moggach, S. A. & Bennett, T. D. A Computational and Experimental Approach Linking Disorder, High-Pressure Behavior, and Mechanical Properties in UiO Frameworks. *Angew. Chem. Int. Ed.* **55**, 2401 (2016).
15. Drage, T. C., Snape, C. E., Stevens, L. A., Wood, J., Wang, J., Cooper, A. I., Dawson, R., Guo, X., Satterley, C. & Irons, R. Materials challenges for the development of solid sorbents for post-combustion carbon capture. *Journal of Materials Chemistry* **22**, 2815-23 (2012).
16. Schmidt, M., Masson, A. & Bréchnignac, C. Enhancement of nitrogen physisorption in coadsorption with oxygen on free, positively charged silver clusters. *The Journal of Chemical Physics* **122**, 134712 (2005).
17. Walton, K. S., Abney, M. B. & Douglas LeVan, M. CO<sub>2</sub> Adsorption in Y and X Zeolites Modified by Alkali Metal Cation Exchange. *Microporous and Mesoporous Materials* **91**, 78-84 (2006).
18. Fei, H., Rogow, D. L. & Oliver, S. R. J. Reversible Anion Exchange and Catalytic Properties of Two Cationic Metal-Organic Frameworks Based on Cu(I) and Ag(I). *Journal of the American Chemical Society* **132**, 7202-9 (2010).
19. Feng, M., Tian, H.-J., Mi, H.-F. & Hu, T.-L. Poly[[ $(\mu_3$ -2,4,6-tri-4-pyridyl-1,3,5-triazine)copper(I)] nitrate monohydrate]. *Acta Crystallographica Section E-Structure Reports Online* **67**, M515-U1143 (2011).
20. Mason, J. A., Oktawiec, J., Taylor, M. K., Hudson, M. R., Rodriguez, J., Bachman, J. E., Gonzalez, M. I., Cervellino, A., Guagliardi, A., Brown, C. M., Llewellyn, P. L., Masciocchi, N. & Long, J. R. Methane storage in flexible metal-organic frameworks with intrinsic thermal management. *Nature* **527**, 357-61 (2015).
21. Reid, C. R. & Thomas, K. M. Adsorption kinetics and size exclusion properties of probe molecules for the selective porosity in a carbon molecular sieve used for air separation. *Journal of Physical Chemistry B* **105**, 10619-29 (2001).
22. Li, L., Bell, J. G., Tang, S., Lv, X., Wang, C., Xing, Y., Zhao, X. & Thomas, K. M. Gas Storage and Diffusion through Nanocages and Windows in Porous Metal-Organic Framework Cu<sub>2</sub>(2,3,5,6-tetramethylbenzene-1,4-diisophthalate)(H<sub>2</sub>O)<sub>2</sub>. *Chemistry of Materials* **26**, 4679-95 (2014).
23. Thommes, M., Kaneko, K., Neimark, A. V., Olivier, J. P., Rodriguez-Reinoso, F., Rouquerol, J. & Sing, K. S. W. Physisorption of gases, with special reference to the evaluation of surface area and pore size distribution (IUPAC Technical Report). *Pure and Applied Chemistry* **87**, 1051-69 (2015).
24. Carrington, E. J., Vitorica-Yrezabal, I. J. & Brammer, L. Crystallographic studies of gas sorption in metal-organic frameworks. *Acta Crystallographica Section B-Structural Science Crystal Engineering and Materials* **70**, 404-22 (2014).



# Chapter VIII

## 8 CONCLUSIONS

---

The study of Metal-Organic Frameworks (MOFs) has developed rapidly over the last twenty years, with breakthroughs in the development of structures in a carbon capture context with incredibly large surface areas, high selectivity for carbon dioxide (CO<sub>2</sub>), flexible frameworks with enhanced adsorption properties, and thermally stable frameworks for multiple cycling regimes during pressure swing adsorption processing.

Amine scrubbing is the most advanced technology available for carbon capture processing within industry, due to its learned knowledge from historic use. The development of materials that use the strong binding ability of amines with CO<sub>2</sub> through Lewis acid-Lewis base interactions should generate MOF structures with improved capture efficiencies through stronger binding between electrostatic interactions; the ability to tailor the MOF structure distinguishes it from other adsorbent materials like activated carbons and zeolites, which either have difficulty in generating a reproducible structure, or are too rigid making tailoring of the structure difficult <sup>1,2</sup>.

The objective of this study was to investigate MOF materials that included inherent Lewis base functionality, to test their ability to selectively capture CO<sub>2</sub> in a carbon capture context. The materials studied, Cu(bpetha)<sub>2</sub>SiF<sub>6</sub>, [Cu(TPT)]BF<sub>4</sub>·0.75H<sub>2</sub>O, and [Cu(TPT)]NO<sub>3</sub>·MeOH all showed distinct adsorption properties, and in the perspective of the overall objective, only Cu(bpetha)<sub>2</sub>SiF<sub>6</sub> proved suitable for the purposes of CO<sub>2</sub> capture from post-combustion process streams, where CO<sub>2</sub> is in low concentration (10 – 15 %) <sup>3</sup>. Conclusive evidence of the MOF structure was unobtainable from single crystal X-ray diffraction, however it was predicted, from similar materials in the literature <sup>4</sup>, that the [SiF<sub>6</sub>]<sup>2-</sup> anion coordinates to the Cu<sup>2+</sup> metal

centres which forms 2-dimensional layers with bpetha ligands, allowing the extension of the structure in 3-dimensions. This creates a microporous material which is doubly interpenetrated, and allows the exposed equatorial fluorine atoms to interact with CO<sub>2</sub> molecules during adsorption via Lewis acid-Lewis base interactions. The study of the adsorption kinetics revealed that CO<sub>2</sub> was adsorbed at higher rates than the studied gases, with interaction of the fluorine atoms generating a fast adsorption rate, which was not observed for either of the other gases, and a second rate due to diffusion through the porous structure, which was slower and comparable for all gases studied. Flexibility of the material was also observed as a result of the MOF structure. The  $\sigma$ -bond character of 1,2-bis(4-pyridyl)ethane, showed a change in structure on removal of guest species, which allowed CO<sub>2</sub> to be adsorbed at higher concentrations, under lower temperature conditions, due to the effects of activated diffusion which was a result of closure of the porous framework. Although equilibrium capacities were not highly selective between CO<sub>2</sub> and CH<sub>4</sub> or N<sub>2</sub> at conditions of industrial flue gas streams, the adsorption kinetics showed that on short timescales, advantageous for pressure swing adsorption processing, CO<sub>2</sub> could be selectively captured at much higher selectivity. Under dynamic flowing conditions, where both CO<sub>2</sub> and N<sub>2</sub> are introduced to the material, no appreciable change in uptake was witnessed compared to pure CO<sub>2</sub> measurements under the same conditions. Materials containing [SiF<sub>6</sub>]<sup>2-</sup> have already been shown to have excellent potential for CO<sub>2</sub> selective capture <sup>5</sup>, and this study shows that the combination of [SiF<sub>6</sub>]<sup>2-</sup> with flexible structures can lead to other interesting adsorption applications, and opens the way for further investigation into the chemistry behind their unique properties.

The production of [Cu(TPT)]BF<sub>4</sub>·0.75H<sub>2</sub>O and Cu(TP)NO<sub>3</sub> materials aimed to study the interaction of nitrogen functional groups contained within the tertiary setting of a triazine ring, to assess the selective nature of the interaction of this site with CO<sub>2</sub>

through a Lewis acid-Lewis base interaction. The use of primary amine functionalities is extensive within the literature, which offers high capture efficiencies, but often leads to high heats of adsorption through chemisorption of CO<sub>2</sub> to the amine group (in a manner akin to amine scrubbing). This requires high temperatures to regenerate the sorbents and, from an economic point-of-view, leads to no improvement over current technologies. The tertiary amine offers a reduced interaction with CO<sub>2</sub>, which was expected to result in a stronger and more selective physisorptive interaction. Both materials displayed a similarly poor uptake of CO<sub>2</sub>, and resulted in a more selective adsorbent for CH<sub>4</sub>. The large anion in [Cu(TPT)]BF<sub>4</sub>·0.75H<sub>2</sub>O was concluded to reduce the volume available for adsorption, and the negative charge results in a repulsive interaction with CO<sub>2</sub>, limiting its access to the porous structure; this was not witnessed for CH<sub>4</sub> which is a non-polar molecule. The results from [Cu(TPT)]NO<sub>3</sub>·MeOH again showed selectivity for CH<sub>4</sub> over CO<sub>2</sub>, but with a much larger capacity than was observed for [Cu(TPT)]BF<sub>4</sub>·0.75H<sub>2</sub>O. The stronger coordinated [NO<sub>3</sub>]<sup>-</sup> anion is possibly responsible for the increased uptake, as the pore blocking mechanism of [BF<sub>4</sub>]<sup>-</sup> is reduced. The isotherm experiences a 'step' which could be the result of a flexible nature of the structure, or collapse of the pores on guest removal; further investigations are required for this to be clarified. It is possible to determine from the results that the initiation of the 'step' is due to a volume filling mechanism, which results in a large decrease in the adsorption rate and equilibration times which are not practicable to measure.

Using the materials [Cu(TPT)]BF<sub>4</sub>·0.75H<sub>2</sub>O and [Cu(TPT)]NO<sub>3</sub>·MeOH to study the effects of inherent nitrogen functionality in the MOF ligand structure, it was not possible to distinguish between the impact of the anion, which was present to balance the charge of the framework, and that of the nitrogen sites. The overall conclusion is that in this configuration, the framework is not selective towards CO<sub>2</sub>,

despite its Lewis basic character. The frameworks do experience moderate capacity for CO<sub>2</sub> at low temperatures, showing the same 'step' behaviour witnessed for CH<sub>4</sub>.

In conclusion, the individual materials presented here, have been synthesised to investigate their potential for CO<sub>2</sub> adsorption, by including inherent functionalities within the ligand moieties. The presence of fluorine atoms was shown to impact the adsorption properties of MOFs, tailoring them towards CO<sub>2</sub> capture. The impact of inherent nitrogen functionalities on CO<sub>2</sub> adsorption properties was probed within this study. MOFs with nitrogen functionality have been shown to have beneficial properties towards CO<sub>2</sub> capture; however, additional complexities of the materials studied here made differentiation of individual contributions to the adsorption properties difficult. This study indicates that nitrogen functionality may prove useful for CCS materials in the future, but this must be taken into consideration with the influence of factors including, ligand flexibility, interpenetration, topology and steric effects. Further research into the effects of nitrogen fixed within the structure of the framework is required to elucidate the effects of potential Lewis acid-Lewis base interactions.

## REFERENCES

1. Sumida, K., Rogow, D. L., Mason, J. A., McDonald, T. M., Bloch, E. D., Herm, Z. R., Bae, T.-H. & Long, J. R. Carbon Dioxide Capture in Metal-Organic Frameworks. *Chemical Reviews* **112**, 724-81 (2012).
2. Bae, Y.-S. & Snurr, R. Q. Development and Evaluation of Porous Materials for Carbon Dioxide Separation and Capture. *Angewandte Chemie-International Edition* **50**, 11586-96 (2011).
3. Metz, B., Davidson, O., de Coninck, H., Loos, M. & [Working Group III of the Intergovernmental Panel on Climate Change]. *IPCC: Special Report on Carbon Dioxide Capture and Storage.*, (Cambridge University Press, 2005).
4. Burd, S. D., Ma, S., Perman, J. A., Sikora, B. J., Snurr, R. Q., Thallapally, P. K., Tian, J., Wojtas, L. & Zaworotko, M. J. Highly Selective Carbon Dioxide Uptake by Cu(bpy-n)<sub>2</sub>(SiF<sub>6</sub>) (bpy-1=4,4'-Bipyridine; bpy-2=1,2-Bis(4-pyridyl)ethene). *Journal of the American Chemical Society* **134**, 3663-6 (2012).
5. Nugent, P., Belmabkhout, Y., Burd, S. D., Cairns, A. J., Luebke, R., Forrest, K., Pham, T., Ma, S., Space, B., Wojtas, L., Eddaoudi, M. & Zaworotko, M. J. Porous materials with optimal adsorption thermodynamics and kinetics for CO<sub>2</sub> separation. *Nature* **495**, 80-4 (2013).

# Chapter IX

## 9 FURTHER WORK

---

Several suggestions are made for the continuation of this study to develop materials similar to those analysed here, and additional work which would be required to unambiguously distinguish the effects of functionalisation of these materials.

### 9.1 FURTHER WORK ON $\text{Cu}(\text{BPETHA})_2\text{SiF}_6$

- The evaluation of the single crystal structure is necessary for the complete analysis of the material. Methods of determining the structure by simulated annealing from the powder diffraction data may be considered; however, this requires much more detailed data collection, the simple fine-tuning of the synthesis method could yield crystals capable of single crystal X-ray diffraction, or different treatment of the crystals when running the measurement <sup>1</sup>
- As it was concluded that the structure was interpenetrated, most typically a result of the fast synthesis approach using batch crystallisation, the synthesis and analysis of the structure in its non-interpenetrated form would be advantageous to determine if there are large differences in the adsorption properties.
- Additional to the previous point, synthesis of the non-interpenetrated framework could be obtained from the reduction of the 1,2-bis(4-pyridyl)ethene, or 1,2-bis(4-pyridyl)ethyne ligand structures by hydrogenation of the internal bond. The possibility of this method for selective bond reduction would need further investigation.

- Studies of the *in-situ* adsorption of CO<sub>2</sub> during X-ray diffraction experiments would yield advantageous results to the discussion of the adsorption of adsorbate molecules into the framework structure, and provide information regarding the extent of the framework flexibility<sup>2-5</sup>
- Studies of the competitive adsorption of CO<sub>2</sub> in the presence of methane to analyse the impact on its adsorption capacity in mixed flows. In addition, studies of water vapour and competitive measurements with water to test its stability
- Cyclic studies to determine the repeatability of adsorption/desorption cycles

## 9.2 FURTHER WORK ON [Cu(TPT)]BF<sub>4</sub>·0.75H<sub>2</sub>O

- Further analysis of the adsorption properties via *in-situ* X-ray diffraction techniques to evaluate the flexible nature of the structure
- Anion exchange of the [BF<sub>4</sub>]<sup>-</sup> anion for smaller ions, such as Cl<sup>-</sup>, to determine the effects of the anion on the adsorption properties.
- Due to the small pore size and electrostatic effects reducing the CO<sub>2</sub> adsorption capabilities, it is possible that this material could lend itself to hydrogen (H<sub>2</sub>) adsorption and storage. A simulation study using density functional theory found that adding nitrogen sites onto a benzene ring (pyrazine) enhanced the adsorption energy of H<sub>2</sub><sup>6</sup>, which could lead to enhanced selectivity of hydrogen. Although not performed during this study, the adsorption of H<sub>2</sub> could be utilised for pre-combustion capture technologies.

## 9.3 FURTHER WORK ON [Cu(TPT)]NO<sub>3</sub>·MEOH

- Analysis of the adsorption capacity of methane (CH<sub>4</sub>) at higher pressures to investigate the extent of the structural flexibility of the framework.

- Analysis of the adsorption properties via *in-situ* X-ray diffraction to elucidate the large framework flexibility and determine its origin
- As stated previously, analysis of the H<sub>2</sub> adsorption capabilities for pre-combustion capture, to compare with the analogous BF<sub>4</sub> structure.

## 9.4 REFERENCES

1. Harris, K. D. M. & Cheung, E. Y. How to determine structures when single crystals cannot be grown: opportunities for structure determination of molecular materials using powder diffraction data. *Chemical Society Reviews* **33**, 526-38 (2004).
2. Carrington, E. J., Vitorica-Yrezabal, I. J. & Brammer, L. Crystallographic studies of gas sorption in metal-organic frameworks. *Acta Crystallographica Section B-Structural Science Crystal Engineering and Materials* **70**, 404-22 (2014).
3. Carrington, E. J., McAnally, C. A., Fletcher, A. J., Thompson, S. P., Warren, M. & Brammer, L. Solvent-switchable continuous-breathing behaviour in a diamondoid metal-organic framework and its influence on CO<sub>2</sub> versus CH<sub>4</sub> selectivity. *Nature Chemistry* (2017).
4. Bon, V., Senkovska, I., Wallacher, D., Heerwig, A., Klein, N., Zizak, I., Feyerherm, R., Dudzik, E. & Kaskel, S. In situ monitoring of structural changes during the adsorption on flexible porous coordination polymers by X-ray powder diffraction: Instrumentation and experimental results. *Microporous and Mesoporous Materials* **188**, 190-5 (2014).
5. Yakovenko, A. A., Wei, Z., Wriedt, M., Li, J.-R., Halder, G. J. & Zhou, H.-C. Study of Guest Molecules in Metal-Organic Frameworks by Powder X-ray Diffraction: Analysis of Difference Envelope Density. *Crystal Growth & Design* **14**, 5397-407 (2014).
6. Samanta, A., Furuta, T. & Li, J. Theoretical Assessment of the Elastic Constants and Hydrogen Storage Capacity of Some Metal-Organic Framework Materials. *The Journal of Chemical Physics* **125**, 084714 (2006).

# Chapter X

# 10 APPENDIX

## 10.1 BOND VALENCE CALCULATIONS

Constants	Cu(I) - N (3-Coord)	Cu(I) - N (4-Coord)	Cu(II) - N (3-Coord)	Cu(II) - N (4-Coord)	Cu(I) - F	Cu(II) - F
Ro (Å)	1.52	1.63	1.704	1.763	1.6	1.594
B (Å)	0.37	0.37	0.37	0.37	0.37	0.37

Cu1	Bond Length	Cu(I) 3cN	Cu(I) 4cN	Cu(II) 3cN	Cu(II) 4cN
N4	1.9817	0.2871	0.3865	0.4721	0.5537
N5	1.9812	0.2875	0.3871	0.4727	0.5545
N6	1.9903	0.2805	0.3777	0.4613	0.5410
<b>Sum</b>		<b>0.8552</b>	<b>1.1512</b>	<b>1.4061</b>	<b>1.6492</b>

Cu2	Bond Length	Cu(I) 3cN	Cu(I) 4cN	Cu(II) 3cN	Cu(II) 4cN
N10	1.9881	0.2822	0.3799	0.4640	0.5442
N12	1.9793	0.2890	0.3890	0.4752	0.5573
N11	1.9824	0.2866	0.3858	0.4712	0.5527
<b>Sum</b>		<b>0.8578</b>	<b>1.1548</b>	<b>1.4104</b>	<b>1.6542</b>

Cu3	Bond Length	Cu(I) 3cN	Cu(I) 4cN	Cu(II) 3cN	Cu(II) 4cN
N16	1.9755	0.2920	0.3931	0.4801	0.5631
N18	1.9613	0.3034	0.4084	0.4989	0.5851
N17	1.9721	0.2947	0.3967	0.4845	0.5683
<b>Sum</b>		<b>0.8900</b>	<b>1.1982</b>	<b>1.4635</b>	<b>1.7165</b>

Cu4	Bond Length	Cu(I) 3cN	Cu(I) 4cN	Cu(II) 3cN	Cu(II) 4cN
N24	1.9770	0.2908	0.3915	0.4781	0.5608
N23	1.9907	0.2802	0.3772	0.4608	0.5404
N22	1.9970	0.2755	0.3709	0.4530	0.5313
<b>Sum</b>		0.8465	1.1396	1.3919	1.6325

	Cu(I) - N (3-Coord)	Cu(I) - N (4-Coord)	Cu(II) - N (3-Coord)	Cu(II) - N (4-Coord)	Cu(I) - O	Cu(II) - O
Ro (Å)	1.52	1.63	1.704	1.763	1.504	1.655
$\beta$ (Å)	0.37	0.37	0.37	0.37	0.37	0.37

Cu1	Bond Length	Cu1 3cN	Cu1 4cN	Cu2 3cN	Cu2 4cN
N1	2.0202	0.2588	0.3483	0.4255	0.4990
N2	1.9643	0.3010	0.4051	0.4948	0.5804
N3	1.9829	0.2862	0.3853	0.4706	0.5519
O1	2.5438	0.0602	0.0602	0.0905	0.0905
<b>Sum</b>		<b>0.9061</b>	<b>1.1989</b>	<b>1.4814</b>	<b>1.7219</b>

## 10.2 DETERMINATION OF COMPONENTS LOST DURING TGA

### 10.2.1 $\text{Cu}(\text{BPETHA})_2\text{SiF}_6$

	<b>Units</b>	<b>Mass</b>	<b>%Atoms</b>
<b>Unit Cell Mass</b>	<b>1</b>	<b>7619.62</b>	
<b>Cu</b>	16	63.55	13.34
<b>C</b>	288	12.01	45.40
<b>H</b>	192	1.01	2.54
<b>B</b>	16	10.81	2.27
<b>F</b>	64	19.00	15.96
<b>N</b>	96	14.01	17.65
<b>H<sub>2</sub>O</b>	12	18.02	2.84
<b>Total</b>			99.99
	<b>Units</b>	<b>Mass</b>	<b>%Components</b>
<b>Cu</b>	16	63.55	13.34
<b>TPT</b>	16	312.33	65.58
<b>BF<sub>4</sub></b>	16	86.81	18.23
<b>H<sub>2</sub>O</b>	12	18.02	2.84
<b>Total</b>			99.99
	<b>Units</b>	<b>Mass</b>	<b>%Components</b>
<b>CuBF<sub>4</sub></b>	16	150.35	31.57
<b>Pyridine</b>	48	78.09	49.19
<b>Triazine</b>	16	78.05	16.39
<b>H<sub>2</sub>O</b>	12	18.02	2.84
<b>Total</b>			99.99

### 10.2.2 $[\text{Cu}(\text{TPT})]\text{BF}_4 \cdot 0.75\text{H}_2\text{O}$

	<b>Units</b>	<b>Mass</b>	<b>%Atoms</b>
<b>Unit Cell Mass</b>	<b>1</b>	<b>7619.62</b>	
<b>Cu</b>	16	63.55	13.34
<b>C</b>	288	12.01	45.40
<b>H</b>	192	1.01	2.54
<b>B</b>	16	10.81	2.27
<b>F</b>	64	19.00	15.96
<b>N</b>	96	14.01	17.65
<b>H<sub>2</sub>O</b>	12	18.02	2.84
<b>Total</b>			99.99
	<b>Units</b>	<b>Mass</b>	<b>%Components</b>
<b>Cu</b>	16	63.55	13.34
<b>TPT</b>	16	312.33	65.58
<b>BF<sub>4</sub></b>	16	86.81	18.23
<b>H<sub>2</sub>O</b>	12	18.02	2.84
<b>Total</b>			99.99
	<b>Units</b>	<b>Mass</b>	<b>%Components</b>
<b>CuBF<sub>4</sub></b>	16	150.35	31.57
<b>Pyridine</b>	48	78.09	49.19
<b>Triazine</b>	16	78.05	16.39
<b>H<sub>2</sub>O</b>	12	18.02	2.84
<b>Total</b>			99.99

10.2.3 [Cu(TPT)]NO<sub>3</sub>.MEOH

	<b>Units</b>	<b>Mass</b>	<b>%Atoms</b>
<b>Unit Cell Mass</b>	<b>1</b>	<b>1879.75</b>	
<b>Cu</b>	4	63.55	13.52
<b>C</b>	72	12.01	46.00
<b>H</b>	48	1.01	2.57
<b>N</b>	28	14.01	20.86
<b>O</b>	12	16.00	10.21
<b>CH<sub>3</sub>OH</b>	4	32.04	6.82
<b>Total</b>			100
	<b>Units</b>	<b>Mass</b>	<b>%Components</b>
<b>Cu</b>	4	63.55	13.52
<b>TPT</b>	4	312.33	66.46
<b>NO<sub>3</sub></b>	4	62.01	13.19
<b>CH<sub>3</sub>OH</b>	4	32.04	6.82
<b>Total</b>			100
	<b>Units</b>	<b>Mass</b>	<b>%Components</b>
<b>CuNO<sub>3</sub></b>	4	125.55	26.72
<b>Pyridine</b>	12	78.09	49.85
<b>Triazine</b>	4	78.05	16.61
<b>CH<sub>3</sub>OH</b>	4	32.04	6.82
<b>Total</b>			100

### 10.3 SINGLE CRYSTAL X-RAY DIFFRACTION STRUCTURAL DATA OF [Cu(BPETHA)(OH<sub>2</sub>)<sub>3</sub>(NO<sub>3</sub>)]SiF<sub>6</sub>·(H<sub>2</sub>O)·0.5(CH<sub>3</sub>OH)

**Table 10.1: Crystal data and structure refinement for [Cu(bpetha)(OH<sub>2</sub>)<sub>3</sub>(NO<sub>3</sub>)]SiF<sub>6</sub>·(H<sub>2</sub>O)·0.5(CH<sub>3</sub>OH)**

Empirical formula	C12.5 H22 Cu F6 N3 O7.5 Si	
Formula weight	539.946	
Temperature	123(2) K	
Wavelength	0.71073 Å	
Crystal system	Monoclinic	
Space group	C2/c	
Unit cell dimensions	a = 17.5309(10) Å	α = 90°.
	b = 15.8396(9) Å	β = 90.156(3)°.
	c = 12.9996(8) Å	γ = 90°.
Volume	3609.75(37) Å <sup>3</sup>	
Z	4	
Density (calculated)	1.644 Mg/m <sup>3</sup>	
F(000)	1856	
Crystal size	0.25 x 0.08 x 0.02 mm <sup>3</sup>	
Theta range for data collection	2.8 to 29.1°.	
Index ranges	-22 ≤ h ≤ 22, -17 ≤ k ≤ 20, -17 ≤ l ≤ 13	
Reflections collected	12684	
Independent reflections	4274 [R(int) = 0.090]	
Absorption correction	Semi-empirical from equivalents	
Max. and min. transmission	1.000 and 0.622	
Refinement method	Full-matrix least-squares on F <sup>2</sup>	
Data / restraints / parameters	4274 / 12 / 265	
Goodness-of-fit on F <sup>2</sup>	0.81	
Final R indices [I > 2σ(I)]	R1 = 0.049, wR2 = 0.105	
Largest diff. peak and hole	0.64 and -0.60 e.Å <sup>-3</sup>	

**Table 10.2: Fractional atomic coordinates and isotropic or equivalent isotropic displacement parameters ( $\text{\AA}^2$ ) for  $[\text{Cu}(\text{bpetha})(\text{OH}_2)_3(\text{NO}_3)]\text{SiF}_6 \cdot (\text{H}_2\text{O}) \cdot 0.5(\text{CH}_3\text{OH})$**

	x	y	z	Uiso/Ueq
Cu1	0.26587(3)	0.26769(4)	0.22067(5)	0.02816(17)
Si1	0.0000	0.22751(13)	0.2500	0.0296(5)
F1	0.06047(15)	0.15367(17)	0.2946(2)	0.0368(8)
F2	0.04638(16)	0.2271(2)	0.1372(2)	0.0463(8)
F3	0.05867(16)	0.30295(18)	0.2966(3)	0.0549(11)
O1	0.2099(2)	0.4760(2)	0.1015(3)	0.0439(10)
O2	0.2785(2)	0.3717(2)	0.0470(3)	0.0389(10)
O3	0.2570(3)	0.4799(2)	-0.0505(3)	0.0531(11)
O1W	0.1928(2)	0.2072(2)	0.1343(3)	0.0433(11)
H1W	0.1439(12)	0.213(3)	0.127(4)	0.065
H2W	0.204(3)	0.176(3)	0.082(3)	0.065
O2W	0.2119(2)	0.2050(2)	0.3578(3)	0.0358(10)
H3W	0.235(2)	0.185(3)	0.410(3)	0.054
H4W	0.1642(11)	0.196(3)	0.370(4)	0.054
O3W	0.19110(18)	0.3585(2)	0.2471(3)	0.0314(9)
H5W	0.1443(14)	0.348(3)	0.258(4)	0.047
H6W	0.189(3)	0.394(3)	0.196(3)	0.047
O4W	0.1956(2)	0.6450(2)	-0.0065(3)	0.0412(10)
H7W	0.196(3)	0.671(3)	-0.065(3)	0.062
H8W	0.210(3)	0.5951(17)	-0.026(4)	0.062
N1	0.3460(2)	0.1862(3)	0.1756(3)	0.0269(11)
N2	0.3440(2)	0.3345(2)	0.2961(3)	0.0243(10)
N3	0.2484(2)	0.4440(3)	0.0322(4)	0.0345(12)
C1	0.3523(3)	0.1084(3)	0.2138(5)	0.0367(14)
H1	0.3188	0.0919	0.2676	0.044
C2	0.4052(3)	0.0507(3)	0.1786(4)	0.0392(15)
H2	0.4086	-0.0039	0.2090	0.047
C3	0.4531(3)	0.0725(3)	0.0995(4)	0.0287(13)
C4	0.4466(3)	0.1535(3)	0.0611(4)	0.0327(13)
H4	0.4792	0.1717	0.0071	0.039
C5	0.3929(3)	0.2080(3)	0.1009(4)	0.0331(13)
H5	0.3895	0.2636	0.0734	0.040
C6	0.5100(3)	0.0112(3)	0.0550(4)	0.0322(13)
H6A	0.5107	-0.0411	0.0971	0.039
H6B	0.5618	0.0365	0.0574	0.039
C7	0.3844(3)	0.3017(3)	0.3734(4)	0.0310(13)
H7	0.3742	0.2448	0.3930	0.037
C8	0.4399(3)	0.3452(3)	0.4266(4)	0.0326(13)
H8	0.4660	0.3192	0.4825	0.039
C9	0.4572(3)	0.4271(3)	0.3978(4)	0.0285(12)
C10	0.4148(3)	0.4624(3)	0.3192(4)	0.0306(13)
H10	0.4242	0.5191	0.2984	0.037
C11	0.3586(3)	0.4154(3)	0.2707(4)	0.0299(12)
H11	0.3293	0.4411	0.2176	0.036
C12	0.5174(3)	0.4772(3)	0.4539(4)	0.0340(14)
H12A	0.5403	0.5193	0.4065	0.041
H12B	0.5586	0.4388	0.4776	0.041
C1S	0.03062	0.15759	0.19853	0.0706
C1S	-0.03062	0.15759	0.30147	0.0706
O1S	0.03230	0.23203	0.25630	0.0473
O1S	-0.03230	0.23203	0.24370	0.0473

## 10.4 SINGLE CRYSTAL X-RAY DIFFRACTION STRUCTURAL DATA OF [Cu(TPT)]BF<sub>4</sub>·0.75H<sub>2</sub>O

**Table 10.3: Crystal data and structure refinement for [Cu(TPT)]BF<sub>4</sub>·0.75H<sub>2</sub>O**

Identification code	sbac008	
Empirical formula	C18 H13.50 B Cu F4 N6 O0.75	
Formula weight	476.20	
Temperature	123(2) K	
Wavelength	0.71073 Å	
Crystal system	Monoclinic	
Space group	Cc	
Unit cell dimensions	a = 19.6546(8) Å	α = 90°.
	b = 17.9133(6) Å	β = 112.816(5)°.
	c = 24.0581(11) Å	γ = 90°.
Volume	7807.6(5) Å <sup>3</sup>	
Z	16	
Density (calculated)	1.620 Mg/m <sup>3</sup>	
Absorption coefficient	1.178 mm <sup>-1</sup>	
F(000)	3832	
Crystal size	0.22 x 0.18 x 0.10 mm <sup>3</sup>	
Theta range for data collection	3.82 to 27.00°.	
Index ranges	-25 ≤ h ≤ 25, -22 ≤ k ≤ 21, -30 ≤ l ≤ 30	
Reflections collected	26295	
Independent reflections	14509 [R(int) = 0.0284]	
Completeness to theta = 27.00°	99.2 %	
Absorption correction	Semi-empirical from equivalents	
Max. and min. transmission	1.00000 and 0.93598	
Refinement method	Full-matrix least-squares on F <sup>2</sup>	
Data / restraints / parameters	14509 / 96 / 1148	
Goodness-of-fit on F <sup>2</sup>	1.037	
Final R indices [I > 2σ(I)]	R1 = 0.0509, wR2 = 0.1222	
R indices (all data)	R1 = 0.0665, wR2 = 0.1336	
Absolute structure parameter	-0.002(11)	
Largest diff. peak and hole	0.770 and -0.507 e.Å <sup>-3</sup>	

**Table 10.4: Atomic coordinates (  $\times 10^4$ ) and equivalent isotropic displacement parameters ( $\text{\AA}^2 \times 10^3$ ) for  $[\text{Cu}(\text{TPT})]\text{BF}_4 \cdot 0.75\text{H}_2\text{O}$ .  $U(\text{eq})$  is defined as one third of the trace of the orthogonalized  $U^{ij}$  tensor.**

	x	y	z	$U(\text{eq})$
Cu(1)	2434(1)	-8776(1)	-7379(1)	25(1)
Cu(2)	-1625(1)	-8864(1)	-4682(1)	32(1)
Cu(3)	4879(1)	-6173(1)	-2022(1)	26(1)
Cu(4)	4598(1)	-11238(1)	-2902(1)	24(1)
F(1)	3468(3)	-5954(3)	-5293(2)	80(2)
F(2)	4195(2)	-5046(2)	-4709(2)	50(1)
F(3)	3995(2)	-6111(2)	-4280(2)	55(1)
F(4)	4708(3)	-6137(3)	-4827(2)	95(2)
F(6)	-500(3)	-8795(2)	-2458(2)	61(1)
F(5)	92(3)	-8947(3)	-1471(2)	72(1)
F(9)	6484(4)	-9406(4)	-1590(4)	168(4)
F(10)	6250(4)	-9137(4)	-764(2)	130(3)
F(7)	-1027(3)	-8432(2)	-1833(2)	63(1)
F(11)	6536(4)	-8247(3)	-1253(3)	97(2)
F(12)	5453(3)	-8885(4)	-1685(3)	119(2)
F(13)	3453(12)	-11140(10)	-5180(5)	95(3)
F(14)	3686(10)	-10778(8)	-5988(8)	116(3)
F(15)	2599(7)	-11133(9)	-6123(7)	91(3)
F(16)	3521(11)	-12012(7)	-5905(11)	78(3)
F(8)	-894(2)	-9667(2)	-1970(2)	61(1)
O(1)	2574(3)	-7008(3)	-4892(3)	69(2)
O(2)	-3767(4)	-5990(4)	-4620(3)	92(2)
O(3)	7445(4)	-8744(4)	-2154(3)	83(2)
N(1)	3437(2)	-11011(2)	-9292(2)	22(1)
N(2)	4317(2)	-11449(2)	-8364(2)	19(1)
N(3)	4309(2)	-11931(2)	-9284(2)	21(1)
N(4)	2830(2)	-9517(2)	-7787(2)	23(1)
N(5)	6513(2)	-13196(2)	-7778(2)	23(1)
N(6)	2929(3)	-11346(2)	-11489(2)	28(1)
N(7)	-3607(2)	-8156(2)	-7756(2)	22(1)
N(8)	-2757(2)	-9071(2)	-7784(2)	20(1)
N(9)	-3644(2)	-8606(2)	-8694(2)	19(1)
N(10)	-2103(3)	-8776(3)	-5575(2)	34(1)
N(11)	-2122(3)	-10498(2)	-9280(2)	30(1)
N(12)	-5737(3)	-6754(2)	-9266(2)	25(1)
N(13)	1939(2)	-8693(2)	-3000(2)	19(1)
N(14)	1920(2)	-8251(2)	-3938(2)	20(1)
N(15)	1056(2)	-9161(2)	-3920(2)	21(1)
N(16)	4020(2)	-6817(2)	-2451(2)	25(1)
N(17)	355(3)	-8775(2)	-6135(2)	26(1)
N(18)	366(2)	-10515(2)	-2407(2)	24(1)
N(19)	1489(2)	-13570(2)	-3885(2)	21(1)
N(20)	1441(2)	-13065(2)	-4815(2)	26(1)
N(21)	587(2)	-13996(2)	-4810(2)	25(1)
N(22)	3687(2)	-11846(2)	-3308(2)	24(1)
N(23)	39(2)	-13647(3)	-7009(2)	27(1)
N(24)	6(2)	-15497(2)	-3299(2)	22(1)
C(1)	3740(3)	-11027(3)	-8699(2)	19(1)
C(2)	4573(3)	-11892(3)	-8684(2)	21(1)
C(3)	3738(3)	-11479(3)	-9568(2)	21(1)
C(4)	3435(3)	-10511(3)	-8364(2)	19(1)
C(5)	2850(3)	-10041(3)	-8695(2)	22(1)
C(6)	2570(3)	-9560(3)	-8393(3)	27(1)

C(7)	3386(3)	-9989(3)	-7472(3)	24(1)
C(8)	3701(3)	-10484(3)	-7745(2)	22(1)
C(9)	5236(3)	-12370(3)	-8355(2)	20(1)
C(10)	5620(3)	-12309(3)	-7730(2)	24(1)
C(11)	6262(3)	-12730(3)	-7459(2)	24(1)
C(12)	6119(3)	-13247(3)	-8375(2)	32(1)
C(13)	5491(3)	-12845(3)	-8678(2)	24(1)
C(14)	3455(3)	-11448(3)	-10230(2)	23(1)
C(15)	3597(3)	-12017(3)	-10571(3)	32(1)
C(16)	3311(4)	-11952(3)	-11196(3)	38(1)
C(17)	2811(4)	-10810(4)	-11155(3)	43(2)
C(18)	3055(4)	-10850(4)	-10538(3)	43(2)
C(19)	-3036(3)	-8622(3)	-7484(3)	26(1)
C(20)	-3061(3)	-9038(3)	-8381(3)	21(1)
C(21)	-3884(3)	-8175(3)	-8357(2)	20(1)
C(22)	-2703(3)	-8665(3)	-6817(3)	25(1)
C(23)	-2885(4)	-8160(4)	-6470(3)	42(2)
C(24)	-2559(4)	-8217(4)	-5854(3)	42(2)
C(25)	-1942(4)	-9263(4)	-5913(3)	47(2)
C(26)	-2234(4)	-9221(4)	-6538(3)	42(2)
C(27)	-2747(3)	-9546(3)	-8702(2)	20(1)
C(28)	-2186(3)	-10023(3)	-8381(3)	29(1)
C(29)	-1901(3)	-10485(3)	-8681(3)	34(1)
C(30)	-2661(3)	-10026(3)	-9596(3)	30(1)
C(31)	-2989(3)	-9551(3)	-9328(3)	27(1)
C(32)	-4530(3)	-7689(3)	-8678(2)	20(1)
C(33)	-4893(3)	-7709(3)	-9295(2)	25(1)
C(34)	-5495(3)	-7255(3)	-9571(3)	28(1)
C(35)	-5371(3)	-6731(3)	-8665(3)	26(1)
C(36)	-4776(3)	-7191(3)	-8354(3)	25(1)
C(37)	2186(3)	-8264(3)	-3342(2)	19(1)
C(38)	1343(3)	-8713(3)	-4213(2)	19(1)
C(39)	1373(3)	-9123(3)	-3316(2)	20(1)
C(40)	2825(3)	-7769(3)	-3022(2)	19(1)
C(41)	3184(3)	-7771(3)	-2401(2)	24(1)
C(42)	3789(3)	-7287(3)	-2122(3)	25(1)
C(43)	3664(3)	-6820(3)	-3048(2)	23(1)
C(44)	3067(3)	-7275(3)	-3361(2)	24(1)
C(45)	1016(3)	-8743(3)	-4875(3)	22(1)
C(46)	1275(3)	-8290(3)	-5219(2)	36(1)
C(47)	934(4)	-8322(4)	-5838(3)	42(2)
C(48)	124(4)	-9217(3)	-5790(3)	36(1)
C(49)	420(3)	-9207(4)	-5168(3)	38(2)
C(50)	1045(3)	-9602(3)	-2982(2)	22(1)
C(51)	435(4)	-10047(3)	-3315(3)	37(2)
C(52)	119(3)	-10482(3)	-3013(3)	35(1)
C(53)	950(3)	-10073(3)	-2093(3)	29(1)
C(54)	1297(3)	-9611(3)	-2370(2)	25(1)
C(55)	1731(3)	-13113(3)	-4210(2)	23(1)
C(56)	881(3)	-13519(3)	-5091(2)	24(1)
C(57)	913(3)	-13989(3)	-4208(3)	21(1)
C(58)	2401(3)	-12665(3)	-3883(3)	23(1)
C(59)	2769(3)	-12707(3)	-3274(2)	24(1)
C(60)	3413(3)	-12282(3)	-2995(2)	24(1)
C(61)	3312(3)	-11812(3)	-3905(2)	30(1)
C(62)	2689(3)	-12204(3)	-4211(2)	27(1)
C(63)	576(3)	-13548(3)	-5755(2)	25(1)
C(64)	493(3)	-12914(3)	-6103(2)	30(1)

C(65)	219(3)	-12975(3)	-6725(2)	32(1)
C(66)	125(3)	-14254(3)	-6666(2)	30(1)
C(67)	369(4)	-14241(3)	-6054(3)	34(1)
C(68)	603(3)	-14502(3)	-3887(3)	20(1)
C(69)	15(3)	-14963(3)	-4207(3)	25(1)
C(70)	-268(3)	-15440(3)	-3904(3)	25(1)
C(71)	585(3)	-15051(3)	-2984(3)	23(1)
C(72)	890(3)	-14551(3)	-3260(2)	21(1)
B(1)	4085(5)	-5820(5)	-4783(4)	54(2)
B(2)	-581(5)	-8965(4)	-1928(3)	43(2)
B(3)	6168(7)	-8901(6)	-1315(5)	70(3)
B(4)	3324(6)	-11321(5)	-5763(4)	91(3)
F(18)	1929(10)	-11596(8)	-5592(7)	78(3)
F(17)	3023(10)	-10912(12)	-5112(8)	95(3)
F(19)	1763(13)	-10434(12)	-5442(10)	116(3)
B(5)	2285(10)	-10909(10)	-5510(9)	91(3)
F(20)	2395(12)	-10717(10)	-6027(9)	91(3)
F(14A)	3864(8)	-10867(8)	-5373(7)	116(3)
F(13A)	3026(8)	-11650(8)	-5361(6)	95(3)
F(15A)	2834(8)	-10996(8)	-6274(6)	91(3)
F(16A)	3707(11)	-11897(7)	-5900(11)	78(3)

---

## 10.5 SINGLE CRYSTAL X-RAY DIFFRACTION STRUCTURAL DATA OF [Cu(TPT)]BF<sub>4</sub> AFTER CO<sub>2</sub> ADSORPTION

**Table 10.5: Crystal data and structure refinement for [Cu(TPT)]BF<sub>4</sub>afterCO<sub>2</sub>.**

Identification code	shelx	
Empirical formula	C18 H13.25 B Cu F4 N6 O0.625	
Formula weight	1895.78	
Temperature	123(2) K	
Wavelength	0.71073 Å	
Crystal system	Monoclinic	
Space group	Cc	
Unit cell dimensions	a = 19.1986(17) Å	α = 90°.
	b = 18.2767(15) Å	β = 112.221(9)°.
	c = 23.9060(17) Å	γ = 90°.
Volume	7765.3(12) Å <sup>3</sup>	
Z	16	
Density (calculated)	1.622 Mg/m <sup>3</sup>	
Absorption coefficient	1.184 mm <sup>-1</sup>	
F(000)	3812	
Crystal size	0.20 x 0.12 x 0.04 mm <sup>3</sup>	
Theta range for data collection	3.761 to 26.998°.	
Index ranges	-24<=h<=24, -23<=k<=23, -29<=l<=30	
Reflections collected	35407	
Independent reflections	16126 [R(int) = 0.0638]	
Completeness to theta = 26.998°	98.3 %	
Absorption correction	Semi-empirical from equivalents	
Max. and min. transmission	1.00000 and 0.85987	
Refinement method	Full-matrix least-squares on F <sup>2</sup>	
Data / restraints / parameters	16126 / 201 / 1200	
Goodness-of-fit on F <sup>2</sup>	1.036	
Final R indices [I>2sigma(I)]	R1 = 0.0767, wR2 = 0.1586	
R indices (all data)	R1 = 0.1458, wR2 = 0.1937	
Absolute structure parameter	0.035(8)	
Extinction coefficient	n/a	
Largest diff. peak and hole	0.921 and -0.561 e.Å <sup>-3</sup>	

**Table 10.6: Atomic coordinates (  $\times 10^4$ ) and equivalent isotropic displacement parameters ( $\text{\AA}^2 \times 10^3$ ) for [Cu(TPT)]BF<sub>4</sub>afterco2. U(eq) is defined as one third of the trace of the orthogonalized U<sup>ij</sup> tensor.**

	x	y	z	U(eq)
Cu(1)	2448(2)	-8750(1)	-7386(1)	35(1)
Cu(2)	-1602(2)	-8867(1)	-4703(1)	41(1)
Cu(3)	4922(2)	-6132(1)	-2038(1)	39(1)
Cu(4)	4619(2)	-11263(1)	-2877(1)	36(1)
F(1)	3380(7)	-5920(6)	-5271(4)	91(4)
F(2)	4224(5)	-5096(5)	-4734(4)	61(2)
F(3)	3951(6)	-6085(6)	-4274(4)	65(3)
F(4)	4606(7)	-6215(7)	-4868(5)	104(4)
F(6)	-501(6)	-8778(6)	-2462(4)	75(3)
F(5)	86(7)	-8930(6)	-1456(5)	91(4)
F(7)	-1064(6)	-8426(6)	-1841(4)	86(3)
F(8)	-884(6)	-9639(6)	-1970(5)	83(3)
O(1)	2531(12)	-6968(12)	-4931(9)	76(7)
O(2)	-3820(8)	-6091(8)	-4601(5)	97(5)
O(3)	7407(8)	-8814(10)	-2107(6)	125(6)
N(1)	3437(6)	-10995(5)	-9312(4)	27(2)
N(2)	4321(6)	-11430(6)	-8362(5)	32(2)
N(3)	4314(5)	-11915(5)	-9284(4)	30(2)
N(4)	2826(6)	-9503(6)	-7800(4)	29(3)
N(5)	6516(6)	-13171(6)	-7781(4)	31(2)
N(6)	2949(6)	-11359(6)	-11494(5)	35(3)
N(7)	-3585(6)	-8159(6)	-7774(4)	30(3)
N(8)	-2749(6)	-9067(6)	-7809(5)	33(3)
N(9)	-3610(6)	-8616(6)	-8707(5)	31(3)
N(10)	-2074(7)	-8766(7)	-5590(5)	42(3)
N(11)	-2113(6)	-10506(6)	-9309(5)	33(3)
N(12)	-5721(6)	-6753(6)	-9280(5)	34(3)
N(13)	1985(6)	-8644(6)	-3018(4)	28(2)
N(14)	1974(6)	-8213(6)	-3967(4)	29(2)
N(15)	1085(6)	-9128(6)	-3946(4)	31(2)
N(16)	4067(6)	-6790(6)	-2470(5)	38(3)
N(17)	395(7)	-8798(7)	-6145(5)	40(3)
N(18)	377(6)	-10450(7)	-2428(5)	38(3)
N(19)	1493(6)	-13580(6)	-3855(4)	30(2)
N(20)	1446(6)	-13078(5)	-4789(4)	31(2)
N(21)	597(5)	-14000(6)	-4791(4)	30(2)
N(22)	3716(6)	-11859(6)	-3283(5)	39(3)
N(23)	63(6)	-13631(6)	-6983(5)	31(3)
N(24)	18(6)	-15521(6)	-3273(5)	33(3)
C(1)	3739(6)	-11016(7)	-8715(6)	27(3)
C(2)	4588(7)	-11884(7)	-8675(6)	27(3)
C(3)	3748(8)	-11455(7)	-9566(5)	33(3)
C(4)	3419(7)	-10483(7)	-8376(5)	28(3)
C(5)	2855(8)	-10002(7)	-8712(6)	29(3)
C(6)	2562(8)	-9547(8)	-8419(6)	35(3)
C(7)	3363(7)	-9961(7)	-7496(6)	30(3)
C(8)	3693(7)	-10445(7)	-7758(6)	27(3)
C(9)	5229(6)	-12354(7)	-8360(5)	23(3)
C(10)	5634(8)	-12272(7)	-7732(5)	34(3)
C(11)	6260(7)	-12683(7)	-7467(5)	31(3)
C(12)	6103(7)	-13252(8)	-8369(6)	41(3)
C(13)	5494(8)	-12839(7)	-8652(5)	34(3)
C(14)	3464(7)	-11452(8)	-10226(5)	35(3)

C(15)	3602(7)	-12004(7)	-10584(6)	42(3)
C(16)	3334(8)	-11951(7)	-11190(6)	40(3)
C(17)	2819(8)	-10838(8)	-11173(6)	43(4)
C(18)	3069(9)	-10852(10)	-10538(7)	53(5)
C(19)	-3021(8)	-8618(8)	-7507(6)	36(3)
C(20)	-3070(7)	-9041(7)	-8404(5)	22(3)
C(21)	-3876(7)	-8178(7)	-8373(5)	29(3)
C(22)	-2687(8)	-8678(8)	-6828(6)	30(3)
C(23)	-2826(8)	-8119(8)	-6473(6)	40(4)
C(24)	-2513(8)	-8192(8)	-5860(6)	45(4)
C(25)	-1916(10)	-9280(9)	-5948(7)	54(4)
C(26)	-2215(10)	-9231(9)	-6558(6)	50(4)
C(27)	-2739(7)	-9542(7)	-8731(6)	30(3)
C(28)	-2175(8)	-10041(7)	-8402(6)	34(3)
C(29)	-1876(8)	-10486(8)	-8703(6)	35(3)
C(30)	-2660(8)	-10023(8)	-9625(6)	38(3)
C(31)	-2997(8)	-9550(7)	-9376(6)	31(3)
C(32)	-4520(7)	-7695(7)	-8693(6)	27(3)
C(33)	-4861(7)	-7717(7)	-9314(5)	32(3)
C(34)	-5470(8)	-7253(8)	-9589(6)	41(4)
C(35)	-5354(7)	-6742(8)	-8681(6)	39(4)
C(36)	-4754(7)	-7200(7)	-8372(6)	35(3)
C(37)	2230(7)	-8233(7)	-3352(6)	33(3)
C(38)	1404(8)	-8668(8)	-4229(5)	35(3)
C(39)	1407(8)	-9084(8)	-3344(6)	36(3)
C(40)	2873(7)	-7717(8)	-3044(5)	33(3)
C(41)	3240(7)	-7737(8)	-2437(6)	36(3)
C(42)	3848(8)	-7258(8)	-2152(6)	38(3)
C(43)	3714(7)	-6771(7)	-3062(5)	31(3)
C(44)	3118(7)	-7221(7)	-3375(6)	30(3)
C(45)	1073(8)	-8700(8)	-4896(6)	36(3)
C(46)	1270(8)	-8239(9)	-5243(6)	47(4)
C(47)	923(9)	-8292(9)	-5867(6)	55(4)
C(48)	225(9)	-9260(9)	-5817(6)	52(4)
C(49)	558(9)	-9263(9)	-5176(6)	50(4)
C(50)	1067(7)	-9556(7)	-3003(5)	31(3)
C(51)	488(9)	-9997(10)	-3317(6)	54(5)
C(52)	158(8)	-10421(9)	-3019(6)	53(4)
C(53)	951(8)	-10017(8)	-2110(6)	41(4)
C(54)	1309(8)	-9553(9)	-2406(6)	39(4)
C(55)	1737(7)	-13130(7)	-4188(6)	33(3)
C(56)	885(7)	-13536(7)	-5065(5)	28(3)
C(57)	916(8)	-14019(7)	-4180(6)	33(3)
C(58)	2408(7)	-12687(7)	-3862(5)	32(3)
C(59)	2808(8)	-12724(8)	-3241(6)	40(4)
C(60)	3449(7)	-12317(7)	-2978(5)	28(3)
C(61)	3322(8)	-11835(8)	-3881(6)	43(4)
C(62)	2682(8)	-12216(8)	-4197(6)	40(3)
C(63)	581(7)	-13535(8)	-5736(6)	32(3)
C(64)	538(7)	-12918(7)	-6069(6)	38(3)
C(65)	261(7)	-12994(7)	-6687(5)	36(3)
C(66)	120(7)	-14230(7)	-6649(5)	37(3)
C(67)	361(9)	-14196(9)	-6031(7)	40(4)
C(68)	618(7)	-14513(8)	-3857(6)	34(3)
C(69)	16(8)	-14978(8)	-4176(6)	35(3)
C(70)	-246(8)	-15472(9)	-3875(6)	41(4)
C(71)	599(7)	-15096(8)	-2960(6)	30(3)
C(72)	920(8)	-14587(8)	-3233(6)	34(3)

B(1)	4028(11)	-5844(11)	-4797(8)	50(5)
B(2)	-626(13)	-8918(11)	-1946(8)	62(4)
B(3)	1058(13)	-6096(13)	-6318(10)	110(6)
F(9)	1521(16)	-6721(9)	-6237(8)	92(6)
F(10)	1433(15)	-5545(11)	-6506(10)	111(8)
F(11)	1054(15)	-5856(12)	-5766(9)	83(7)
F(12)	305(14)	-6061(14)	-6726(9)	102(7)
B(4)	-2586(16)	-5987(19)	-5515(12)	146(7)
F(13)	-2970(20)	-6640(20)	-5531(15)	153(10)
F(14)	-3070(20)	-5477(17)	-5402(16)	200(10)
F(15)	-2458(19)	-5890(16)	-6051(10)	144(9)
F(16)	-1838(17)	-6040(17)	-5109(10)	169(9)
B(6)	-2490(30)	-6090(20)	-5511(15)	146(7)
F(24)	-2690(40)	-5590(30)	-5993(18)	136(14)
F(21)	-2470(30)	-5660(20)	-5019(17)	172(13)
F(22)	-1870(20)	-6550(30)	-5238(18)	169(9)
F(23)	-3110(30)	-6570(40)	-5680(30)	142(13)
B(5)	9(14)	-6320(14)	-6043(13)	110(6)
F(17)	714(19)	-6139(17)	-5604(14)	154(11)
F(18)	-558(15)	-5776(12)	-6205(11)	176(11)
F(19)	291(19)	-6570(20)	-6482(13)	167(9)
F(20)	-362(16)	-6849(11)	-5828(7)	136(8)

---

## 10.6 BUOYANCY CORRECTION OF GRAVIMETRIC ADSORPTION DATA

Information regarding the buoyancy correction of data was interpreted from the Hiden Isochema manual (Appendix B) <sup>1</sup>.

In accordance with Archimedes' Principle, an object of mass,  $M_s$ , suspended within a fluid of density,  $\rho_g$ , experiences forces acting on the object, as shown in Figure 10.1. The object exerts a downwards force,  $f_w$ , corresponding to the weight of the mass, and the fluid in which it is suspended enacts a force onto the object that results in an upthrust (upwards) force, due to the displacement of an equivalent volume of fluid to the volume of the object; the force is therefore equal to the mass of fluid.

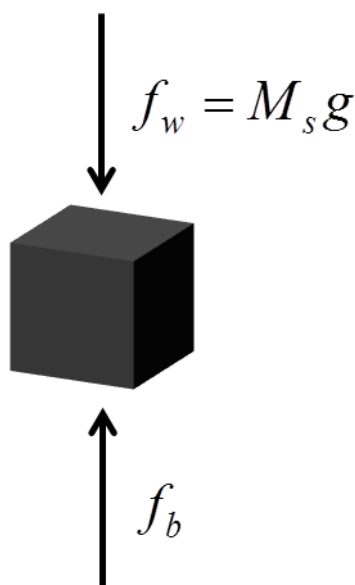


**Figure 10.1:** Forces acting on an object of mass,  $M_s$ , in a fluid of density,  $\rho_g$ . Force contributions are from weight of sample,  $f_w$ , and buoyancy due to displacement of fluid by volume of object,  $f_b$ , and outlined in Equation (10-2)

Mathematically, the buoyancy force is represented as:

$$\begin{aligned}
 f_b &= -M_f g \\
 f_b &= -\rho_f V g \\
 V &= \frac{M_s}{\rho_s} \\
 f_b &= -M_s g \left( \frac{\rho_f}{\rho_s} \right) \tag{10-1}
 \end{aligned}$$

Therefore, the total force acting on the object is the sum of the forces:

$$\begin{aligned}
 f_T &= f_w - f_b \\
 f_T &= M_s g - M_s g \left( \frac{\rho_f}{\rho_s} \right) \\
 f_T &= M_s g \left( 1 - \frac{\rho_f}{\rho_s} \right) \tag{10-2}
 \end{aligned}$$

Calculations of the forces during adsorption measurements are complicated by the adsorption of gas onto the adsorbent surface. Thus, a second term is included in the total force on the sample to account for the adsorbed weight,  $M_a$ , and the associated buoyancy effect this creates in the fluid,  $\rho_f$ :

$$\begin{aligned}
 f_w &= f_s - f_a \\
 f_T &= f_s + f_a - f_{bs} - f_{ba} \\
 f_T &= M_s g + M_a g - M_s g \left( \frac{\rho_f}{\rho_s} \right) - M_a g \left( \frac{\rho_f}{\rho_a} \right) \\
 f_T &= M_s g \left( 1 - \frac{\rho_f}{\rho_s} \right) + M_a g \left( 1 - \frac{\rho_f}{\rho_a} \right) \tag{10-3}
 \end{aligned}$$

Consequently, if a total force,  $f_T$ , is measured, the adsorbed mass can be determined from the other known quantities.

The set up for the Intelligent Gravimetric analyser (IGA) balance is one which has the sample suspended from one arm, with a counterweight suspended from the opposite arm. Changes in mass are recorded through analysis of the increased force

acting on the sample side of the balance head, which corresponds to a weight loss or gain in addition to the initial mass of adsorbent. However, as gas is added to the system, the sample experiences a buoyancy force. Additionally, the various components connecting the sample to the balance head, and the matching components of the counterweight also experience the same (but not equivalent) effects of buoyancy, which must be considered when performing the buoyancy correction of a set of adsorption data. The various components that were used within the IGA set up are given in **Table 10.7**.

**Table 10.7: Balance components and their associated weights, densities, and temperatures as used in the buoyancy correction calculations**

Object	Description	Weight	Density	Temperature
$s$	Dry sample	$M_s$	$\rho_s$	$T_s$
$a$	Adsorbed mass	$M_a$	$\rho_a$	$T_s$
$i_1$	Sample container	$w_{i=1}$	$\rho_1$	$T_{i=1}$
$i_2$	Upper sample hang-down	$w_{i=2}$	$\rho_2$	$T_{i=2}$
$i_3$	Lower sample hang-down	$w_{i=2}$	$\rho_3$	$T_{i=3}$
$j_1$	Counterweight Upper	$w_{j=1}$	$\rho_1$	$T_{j=1}$
$j_2$	counterweight hang-down	$w_{j=2}$	$\rho_2$	$T_{j=2}$

Each component gives a contribution to the measured mass of the system, and also contributes to the displacement of fluid. Therefore the resultant force acting on each component is summed for the downwards and upwards forces, to give an expression for the buoyancy correction of the entire system.

As each of the instrument components is initially weighed in air, a correction for the objects mass in air, of density,  $\rho_{air}$ , must be applied, and is shown in Equation (10-4); substituting this equation to replace the mass of object  $m_i$  and applying the buoyancy correction for the mass in fluid of density,  $\rho_{gi}$ , gives the resultant force shown in Equation (10-5).

$$\begin{aligned}
w_{bi} &= -m_i g \left( \frac{\rho_{air}}{\rho_i} \right) \\
w_i &= m_i g - m_i g \left( \frac{\rho_{air}}{\rho_i} \right) \\
m_i g &= \frac{w_i}{\left( 1 - \frac{\rho_{air}}{\rho_i} \right)}
\end{aligned} \tag{10-4}$$

The mass of  $M_s$  and  $M_a$  do not require correction for weighing in air, as they are not measured until the sample has been dried of any guest species, and this is performed by evacuation of the system, therefore, taking the measurement of mass in a vacuum ( $\rho_g = 0$ ), and subsequent measurements are performed in the adsorbing fluid. Additionally, as gravity,  $g$ , is assumed not to vary between the distances of the components, it is removed from the calculation as an arbitrary constant.

$$f_b = - \left[ \sum_i w_i \left( \frac{\rho_{gi}}{\rho_i - \rho_{air}} \right) - \sum_j w_j \left( \frac{\rho_{gj}}{\rho_j - \rho_{air}} \right) + M_s \left( \frac{\rho_{gs}}{\rho_s} \right) + M_a \left( \frac{\rho_{gs}}{\rho_a} \right) \right] \tag{10-5}$$

Thus, the total force over the balance head is the sum of each of the components suspended from the balance, and their associated buoyancy corrections, giving Equation (10-6):

$$\begin{aligned}
f_T &= f_w - f_b \\
f_T &= \left( \sum_i \frac{w_i}{\left( 1 - \frac{\rho_{air}}{\rho_i} \right)} - \sum_j \frac{w_j}{\left( 1 - \frac{\rho_{air}}{\rho_j} \right)} + M_s + M_a \right) - f_b \\
f_T &= \sum_i w_i \left( \frac{\rho_i - \rho_{gi}}{\rho_i - \rho_{air}} \right) - \sum_j w_j \left( \frac{\rho_j - \rho_{gj}}{\rho_j - \rho_{air}} \right) + M_s \left( 1 - \frac{\rho_{gs}}{\rho_s} \right) + M_a \left( 1 - \frac{\rho_{gs}}{\rho_a} \right)
\end{aligned} \tag{10-6}$$

The IGA, as part of the initial experimental set up, records a force for the unloaded system,  $f_U$ , which is a measure of the force generated by the balance components in the absence of sample. The measured force when the sample has been

dried under vacuum is given as  $f_D$ , by assuming  $M_a$  to be zero, and gas densities are zero as the measurement of  $f_D$  is made under vacuum.

$$\begin{aligned}
f_T &= f_U \cdot M_s = 0 \cdot M_a = 0 \cdot \rho_{gi} = \rho_{gj} = \rho_{gs} = \rho_{air} \\
f_U &= \sum_i w_i - \sum_j w_j \\
f_T &= f_D \cdot M_a = 0 \cdot \rho_{gi} = \rho_{gj} = \rho_{gs} = 0 \\
f_D &= \sum_i w_i \left( \frac{\rho_i}{\rho_i - \rho_{air}} \right) - \sum_j w_j \left( \frac{\rho_j}{\rho_j - \rho_{air}} \right) + M_s \quad (10-7)
\end{aligned}$$

The difference between the dry sample force and the unloaded force can provide the dry sample mass,  $M_s$ , before the adsorption experiment, and from which all subsequent measurements are taken.

$$\begin{aligned}
f_D - f_U &= \left[ \sum_i w_i \left( \frac{\rho_i}{\rho_i - \rho_{air}} \right) - \sum_j w_j \left( \frac{\rho_j}{\rho_j - \rho_{air}} \right) + M_s \right] - \left[ \sum_i w_i - \sum_j w_j \right] \\
f_D - f_U &= \left[ \sum_i w_i \left( \frac{\rho_i}{\rho_i - \rho_{air}} \right) - \sum_i w_i \left( \frac{\rho_i - \rho_{air}}{\rho_i - \rho_{air}} \right) \right] - \left[ \sum_j w_j \left( \frac{\rho_j}{\rho_j - \rho_{air}} \right) - \sum_j w_j \left( \frac{\rho_j - \rho_{air}}{\rho_j - \rho_{air}} \right) \right] + M_s \\
M_s &= f_D - f_U - \left[ \sum_i w_i \left( \frac{\rho_{air}}{\rho_i - \rho_{air}} \right) - \sum_j w_j \left( \frac{\rho_{air}}{\rho_j - \rho_{air}} \right) \right] \quad (10-8)
\end{aligned}$$

As  $\rho_{air} \ll \rho_i$  the corrective terms for the density in air of each of the balance components is assumed to be zero, therefore  $M_s$  is the difference between  $f_D$  and  $f_U$ .

Adsorbate measurements are taken in successive steps where the pressure is increased to a defined set-point. The force generated by the system with increased mass due to the adsorbed mass,  $M_a$ , is equal to the difference in the measured force and the unloaded force,  $f_U$ .

$$\begin{aligned}
f_T - f_U &= \left[ \sum_i w_i \left( \frac{\rho_i - \rho_{gi}}{\rho_i - \rho_{air}} \right) - \sum_j w_j \left( \frac{\rho_j - \rho_{gj}}{\rho_j - \rho_{air}} \right) + M_s \left( 1 - \frac{\rho_{gs}}{\rho_s} \right) + M_a \left( 1 - \frac{\rho_{gs}}{\rho_a} \right) \right] - \left[ \sum_i w_i - \sum_j w_j \right] \\
M_a &= \frac{f_T - f_U + \sum_i w_i \left( \frac{\rho_{gi} - \rho_{air}}{\rho_i - \rho_{air}} \right) - \sum_j w_j \left( \frac{\rho_{gj} - \rho_{air}}{\rho_j - \rho_{air}} \right) - M_s \left( 1 - \frac{\rho_{gs}}{\rho_s} \right)}{\left( 1 - \frac{\rho_{gs}}{\rho_a} \right)} \quad (10-9)
\end{aligned}$$

The value of  $f_T - f_U$  is recorded experimentally and is output by the IGASwin software as a measureable weight in milligrams, shown in Equation (10-10).

$$M_a = \frac{M_{s+a} + \sum w_i \left( \frac{\rho_{gi} - \rho_{air}}{\rho_i - \rho_{air}} \right) - \sum w_j \left( \frac{\rho_{gj} - \rho_{air}}{\rho_j - \rho_{air}} \right) - M_s \left( 1 - \frac{\rho_{gs}}{\rho_s} \right)}{\left( 1 - \frac{\rho_{gs}}{\rho_a} \right)} \quad (10-10)$$

As stated, measurements performed on a sample within the IGA system experience a range of pressures set by the user. The components of the balance are situated at different positions and, therefore, experience different temperatures within the instrument; for example, the sample and sample bulb are at the experiment temperature, whereas the balance head is fixed at a temperature of 328 K. This affects the density of the gas used, and its value must be calculated for each segment of the instrument, using the ideal gas law:

$$\rho_g = \frac{m_g}{V_g} = \frac{M_w \cdot P}{z_{(P,T)} \cdot R \cdot T} \quad (10-11)$$

The density must be calculated for each component in the balance system, and this requires the compressibility factor ( $z$ ) of the gas at each pressure and temperature to be determined.

The compressibility factor is found from data obtained from NIST<sup>2</sup> for each gas used, at a specific temperature and for the range of pressures used within the measurement. Compressibility values are calculated by rearrangement of Equation (10-11), and the information given in the NIST database for pressure, temperature and density. The values of  $z$  vs. pressure are plotted on a graph and a cubic trend line fitted to the data. Accurate values for each of the pressures recorded in the experiment can then be

obtained from the cubic equation. Using this information, gas densities for each of the components is found, and used to calculate the buoyancy corrective terms.

During measurement of the equilibrium uptake, at a set pressure, it is not always feasible to wait the total time for complete equilibration; therefore, the kinetic models can be used to predict the asymptote of equilibrium uptake,  $M_{s+a}$ , which is used in the calculation for the adsorbed mass, and is determined from the parameter,  $A$ , within the kinetic model used (where  $A$  can be the combination of  $A_1+A_2$  for double exponential and double stretched exponential models). Figure 10.2 shows an example where the mass profile reaches a maximum of  $M_t$ , but its fully equilibrated uptake,  $M_e$ , is at a position further in time.

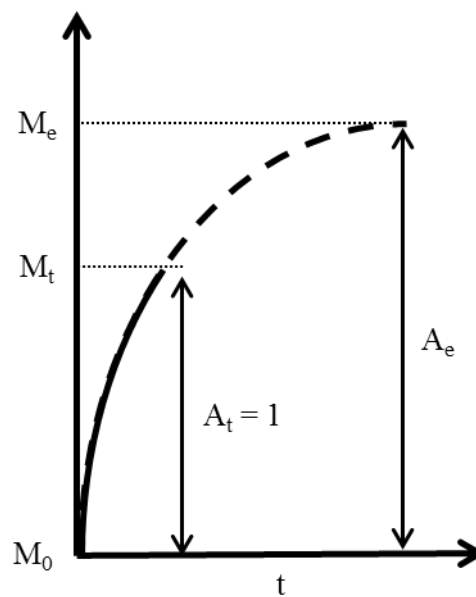


**Figure 10.2: Example of unequilibrated mass profile. Data is normalise from 0 to 1 in the range  $M_0$  to  $M_t$ , calculation using the kinetic models provides a value for parameter  $A$  which is  $>1$  if equilibrium is not reached during the experiment. A correction is made to find the maximum uptake  $M_e$  using the information from the graph**

The data collected is initially normalised from 0 to 1, such that  $M_t$  is at a value of  $A$  equal to 1, and the  $A$  parameter for  $M_e$  is  $>1$ . The normalisation of the data is determined by the equation

$$A_t = \frac{M - M_0}{M_t - M_0} \quad (10-12)$$

Where at  $M = M_t$ ,  $A_t = 1$ .

It then follows that for a value of  $A_e$  the mass  $M = M_e$ ; rearranging Equation (10-12) corrects the maximum uptake for the equilibrated point on the graph.  $M_e$  is therefore equivalent to  $M_{s+a}$ .

$$M_e = A_e \cdot (M_t - M_0) + M_0 \quad (10-13)$$

Once all the information is gathered, new concentrations for the adsorption experiment can be obtained from calculation of Equation (10-10), and using a simple equation for the conversion to moles, and divided by the dry mass of sample.

$$conc = \frac{M_a}{M_w \cdot M_s} \quad (10-14)$$

### 10.6.1 ERROR ANALYSIS

From the estimation of equilibrium uptake from a kinetic profile of a single pressure point, errors are introduced as a result of the fraction of the total equilibrated profile which is collected. To estimate the error, a fully equilibrated data point was analysed using percentages of the collected data from 10 – 90 %; the rate constants were fixed at the values determined from the calculation using 100 % of the data, and the parameters  $A_1$  and  $A_2$  were allowed to vary to determine the final value of the equilibrated mass. Figure 10.3 shows the fitted curves to a fully equilibrated dataset.

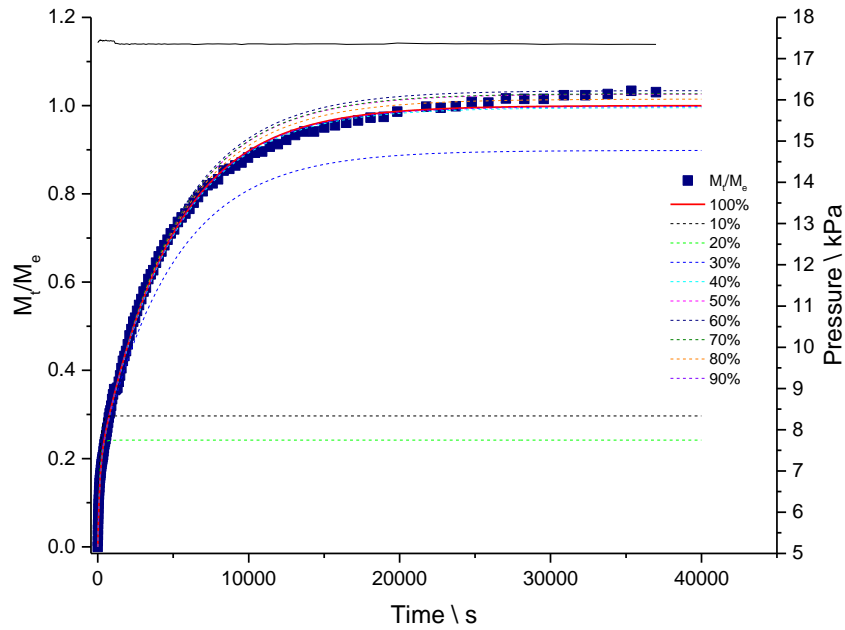


**Figure 10.3: Plot of  $M_t/M_e$  against time (s) for a fully equilibrated pressure step. Analysis of the profile was performed using a DE model, taking percentages of the total equilibrated profile data between 10 – 100 %. The values of  $A$  from the kinetic model gave an indication of the deviation from the calculated equilibrium mass using 100 % of the profile data**

The values of  $A_1$  and  $A_2$  were plotted against the percentage of data used to calculate the kinetic model fit, as shown in Figure 10.4. The results show that when the collected data is below 40 % of the equilibrated uptake, the errors in calculating the equilibrium mass are unreasonable. At values above 40 – 70 %, there is an overestimation of the equilibrium uptake, with errors of 2 – 3 %; at 80 – 100 %, the errors are negligible. Visual analysis of the data collected showed that all isotherm data points were collected to a minimum of 40 %, therefore all equilibrated isotherm data is assumed to be within reasonable errors of the actual uptake value.

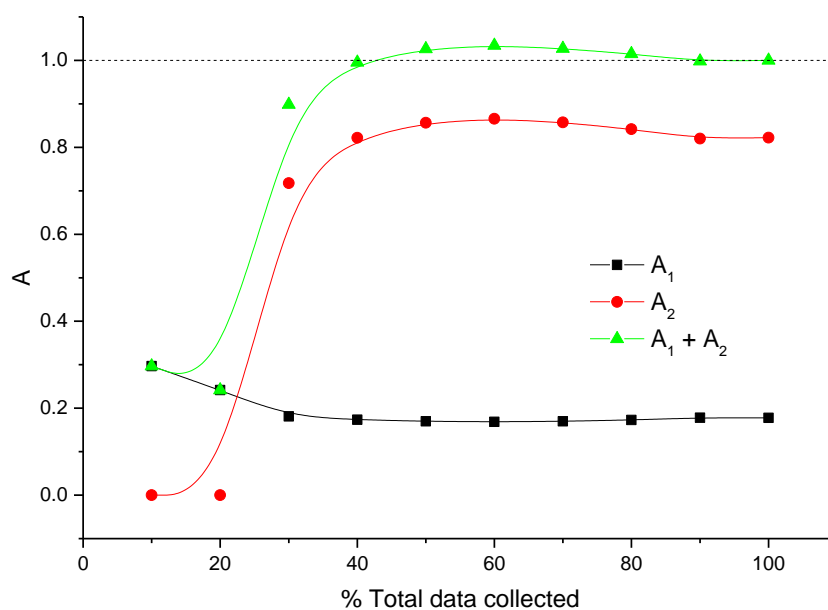


**Figure 10.4: Plot of the values of  $A_1$ ,  $A_2$ , and  $A_1 + A_2$  against the percentage of collected data used to determine the kinetic fit. Plot shows that reasonable errors are achieved when a minimum of 40 % of the equilibrium curve data is collected**

Results from this analysis give an appreciation of the errors associated with the analysis and correction of isotherm data; however, other sources of error are present from experiment. Therefore it is not appropriate to use the values calculated here as the precise value of the error in the molar uptake, and a more rigorous analysis of the combined errors would be required. Additionally, analysis of each of the kinetic models would be required to determine if there is variation in the relationship between the model and resultant errors.

<b>Symbol</b>	<b>Description</b>
$f_w$	Force due to weight of object
$M_s$	Mass of object
$g$	Gravitational constant
$f_b$	Buoyant force due to displacement of fluid by object
$M_f$	Mass of fluid
$\rho_f$	Density of fluid
$V$	Volume of object
$\rho_s$	Density of object
$f_T$	Measured resultant force acting on object
$f_s$	Force due to weight of sample
$f_a$	Force due to weight of adsorbate
$f_{bs}$	Buoyant force acting on sample
$f_{ba}$	Buoyant force acting on adsorbate
$M_a$	Mass of adsorbate
$\rho_a$	Density of adsorbate
$w_i$	Force due to weight of component i
$w_{bi}$	Buoyant force acting on component i
$w_j$	Force due to weight of component j
$m_i$	Mass of component i
$\rho_i$	Density of component i
$\rho_j$	Density of component j
$\rho_{air}$	Density of air
$\rho_{gi}$	Density of fluid surrounding component i
$\rho_{gj}$	Density of fluid surrounding component j
$\rho_{gs}$	density of fluid surrounding sample
$f_U$	Unloaded force
$f_D$	Dry sample force
$M_{s+a}$	Mass of sample and adsorbate
$\rho_g$	Density of gas
$m_g$	Mass of gas
$V_g$	Volume of gas
$M_w$	Molecular weight
$P$	pressure
$z_{(P,T)}$	Compressibility factor
$R$	Universal gas constant (8.314 J mol <sup>-1</sup> K <sup>-1</sup> )
$T$	Temperature
$A$	Kinetic parameter
$M_t$	Mass at end of adsorption
$M_0$	Initial mass at start of adsorption
$M_e$	Fully equilibrated mass

## 10.7 REFERENCES

1. Hiden Analytical Ltd. *IGA Systems User Manual*. (2002).
2. Lemmon, E. W., McLinden, M. O. & Friend, D. G. *Thermophysical Properties of Fluid Systems in NIST Chemistry WebBook, NIST Standard Reference Database Number 69*. (National Institute of Standards and Technology).